Department of Mechanical Engineering
Imperial College London

Development of optimised compact chemical kinetic mechanisms to support the transition to net zero

Daniel Greenblatt

March 2023

Supervised by Professor R. P. Lindstedt
and Professor P. G. Aleiferis

Submitted in part fulfilment of the requirements for the degree of Doctor of Philosophy in Mechanical Engineering of Imperial College London and the Diploma of Imperial College London

Declaration of Originality

This is to certify that the present thesis is in full the work of the author, with the work of others appropriately acknowledged.

Copyright Declaration

Abstract

Attitudes towards energy sources and any pollutant emissions as a result of their use are rapidly changing in a world seeking to reduce the rate of climate change. Renewable electricity generation is beginning to displace the legacy fossil fuel combustion based devices. However, due to intermittency issues with these renewable sources in the power generation sector and the scale and diversity of the transportation sector, combustion devices will linger in the mix, perhaps even indefinitely through the use of renewable fuels. Therefore, it is paramount that ever more stringent pollutant emission regulations are set and met and in order to achieve this, further understanding and computational modelling capabilities of the fuels to be used is required. In this work, chemical kinetic models are further developed and refined and comprehensive validation used to assess their ability to predict both global (burning velocities, ignition delay times) and detailed (speciation) properties. The fuel components studied in this work include the primary reference fuels, iso-octane and n-heptane, which represent the base level chemicals used to approximate real fuels in both laboratory-based research and computational surrogates. Additionally, with the advent of green hydrogen and its formation into green ammonia the study of fuel alternatives, such as ammonia, and fuel enhancers, such as nitromethane, have been included in this work. The chemical kinetic models are compact to allow for their direct implementation in computing dynamic systems. All mechanisms provide good to excellent agreement with experimental data for burning velocities and ignition delay times, and an assessment of their ability to predict speciation results with key sensitivities and uncertainties is outlined. Finally, these mechanisms have been implemented to consider the key trends at conditions of practical relevance, with a focus on the characteristic timescales within flames.

Acknowledgements

My sincerest gratitude to Prof. Peter Lindstedt for guiding and supporting me, even from before the PhD began during my final year of undergraduate studies, through the many ups and downs of this process especially with the significant uncertainties of the past few years. It has been a pleasure, and I'm grateful for our many and varied conversations and all the wisdom shared on and off the topic of my research. I look forward to the next chapter working together. Thanks also to Prof. Pavlos Aleiferis for co-supervising this project and Dr. Konstantinos Gkagkas at Toyota Motor Europe for his and their support.

To my colleagues in 674, thank you for creating a welcoming working environment (which you often left all for me, especially in the mornings). Thank you to Drs. Fabian Hampp and Seyedhamed Shariatmadar for the help and support in the laboratory and in particular to Dr. Panagiotis Simatos for teaching me about computational research. Their help was truly invaluable. Thanks also to Dr. Lu Tian, Dr. Aliki Tsopelakou and Mr. Sam Hughes for the support and friendship and to Stephen Winn, Monal Patel and Omer Rathore for all the good times. Also, thanks to the support throughout from Ms. Serena Dalrymple, Ms. Agnes Lam and Ms. Kate Lewis. A mention to Tom Readshaw, who kept me sane with our morning chats, regular badminton sessions, crosswords and general procrastination. Thanks to my old friends, Michael and Max, who made me feel a little less ancient.

To my family, I know no words are required here, nor would they be sufficient. Thank you for the encouragement and the space to grow, and for the patience and understanding to falter. To Annie, all the same applies. Thank you for your company, patience and kindness, particularly through the more challenging times. Finally, to my friends, thank you for the escapes, laughter and always keeping me in my place.

For my mother, Lisa Eve Greenblatt z"l,
who first stood me on the steps of Imperial twenty years ago.

Contents

List of Tables

List of Figures

Nomenclature

Acronyms / Abbreviations

ANN	Artificial neural network
ATcT	Active thermochemical tables
BEV	Battery electric vehicle
CAI	Controlled autoignition
CCS	Carbon capture and storage
CFD	Computational fluid dynamics
CI	Compression ignition
CSP	Computational singular perturbation
DNS	Direct numerical simulation
DRG	Direct relation graph
EGR	Exhaust gas recirculation
FAA	Federal Aviation Administration
GHG	Greenhouse gas
HCCI	Homogeneous charge compression ignition
HCP	Hot combustion product
HyChem	Hybrid Chemistry approach developed at Stanford University
ICE	Internal combustion engine
IDT	Ignition delay time
ILDM	Intrinsic low-dimensional manifolds
IPCC	Intergovernmental Panel on Climate Change
ISAT	In-situ adaptive tabulation
JSR	Jet stirred reactor
LBV	Laminar burning velocity
LIF	Laser induced fluorescence

MILD	Moderate or intense low-oxygen dilution
MON	Motor octane number
NTC	Negative temperature coefficient
ODE	Ordinary differential equation
PDF	Probability density function
PE	Partial equilibrium
PRF	Primary reference fuel
QSS	Qausi-steady state
QSSA	Quasi-steady state approximation
RON	Research octane number
SAF	Sustainable aviation fuel
SI	Spark ignition
SNCR	Selective non-catalytic reduction
STP	Standard temperature and pressure (298 K and 1 atm)
SVUV-PIMS	Synchrotron vacuum ultraviolet photoionisation mass spectrometry
UQ	Uncertainty quantification

Chemical species

Ar	Argon
C_2H_2	Acetylene
C_2H_4	Ethylene
C_4H_8	Iso-butene
C_4H_9	Iso-butyl radical
$C_5H_{11}CHO$	Hexanal
C_7H_{16}	n-Heptane
C_8H_{17}	Iso-octyl radical
C_8H_{18}	Iso-octane
CH_3NO_2	Nitromethane
CH_3	Methyl radical
CH_4	Methane
CH	Methylidyne radical
CO_2	Carbon dioxide
CO	Carbon monoxide
H_2NO	Aminoxyl radical
H_2O	Water (g)

HO_2	Hydroperoxy radical
H	Hydrogen radical
JP-10	Exo-tetrahydrodicyclopentadiene
N_2	Nitrogen
NH_2	Amidogen
NH_3	Ammonia
NH	Imidogen
NO_x	Oxides of nitrogen
O_2	Oxygen
OH	Hydroxyl radical
O	Oxygen radical

Greek symbols

δ	Reaction zone thickness
δ_{ij}	Kronecker delta (2D)
ϵ_r	Turbulence dissipation rate
λ	Thermal conductivity
μ	Dynamic viscosity
ν_r	Kinematic viscosity
$\nu_{k,i}$	Net stoichiometric coefficient of species k in reaction i
ϕ	Equivalence ratio
ρ	Density
τ	Residence time
τ_c	Chemistry timescale
τ_I	Flow timescale
τ_{ign}	Ignition time (IDT)
τ_{ij}	Viscous stress tensor

Dimensionless numbers

Da	Damköhler number
Ka	Karlovitz number
Ka_δ	Karlovitz number (based on the inner flame thickness)
Re	Reynolds number
Re_t	Turbulent Reynolds number

Roman symbols

A_i	Pre-exponential factor in Arrhenius expression for reaction i
C_p	Mixture specific heat capacity
C_{p_a}	Specific heat capacity at constant pressure of species a
D	Nozzle diameter
D_a	Diffusion coefficient for species a
D_{th}	Thermal diffusivity
$E_{a,i}$	Activation energy barrier of reaction i
F	Broadening factor (for pressure dependent reactions)
F_{cent} / F_c	Troe or SRI form of F
g_i	Body force per unit volume vector
h	Enthalpy
h	Mixture enthalpy
ΔH_i^0	Change in standard state molar enthalpy for reaction i
h_a	Specific enthalpy of species a
$\Delta h_{a,f}$	Standard enthalpy of formation of species a
J_j^a	Molecular diffusion flux of species a
$J_{q,j}$	Heat flux vector
K	Total number of species in reaction i
k	Reaction rate
k_0	Low pressure limit reaction rate
k_∞	High pressure limit reaction rate
$K_{c,i}$	Equilibrium constant in concentration terms for reaction i
$k_{f,i}$	Forward reaction rate for reaction i
$K_{p,i}$	Equilibrium constant in pressure terms for reaction i
$k_{r,i}$	Reverse reaction rate for reaction i
L_η	Kolmogorov length scale
l_F	Laminar flame thickness
L_I	Integral length scale
$[M]$	Third body species concentration
$\dot{m}$	Mass flow rate
$\overline{M_w}$	Mean molecular weight
n	Mole number
n_i	Temperature dependence in Arrhenius expression for reaction i
NS	Total number of species

p / P	Pressure
P_r	Reduced pressure (for pressure dependent reactions)
P_{atm}	Atmospheric pressure
q_R	Heat transfer due to radiation
R	Universal gas constant (8.314 J mol^{-1} K^{-1})
ΔS_i^0	Change in standard state molar entropy for reaction i
S_a	Chemical reaction source term of species a
S_L	Laminar flame speed
T	Temperature
t	Time
T^0	Inner layer temperature
T_C	Cold reactant temperature
t_c	Flame characteristic timescale
T_H	Hot product temperature
T_{HCP}	Hot combustion products temperature
T_{in}	Inlet temperature
U_b	Bulk velocity
u_i	Cartesian velocity vector [u,v,w]
u_{rms}	Turbulence velocity fluctuations
V	Volume (of reactor)
V_c	Correction velocity for species a
W_a	Molecular weight of species a
x_i	Cartesian coordinate vector [x,y,z]
Y_a	Mole fraction of species a
ΔY_a	Change of mole fraction of species a in a reactor
Y_a^{in}	Mole fraction of species a flowing into a reactor
Y_a^{out}	Mole fraction of species a flowing out a reactor

Subscripts and superscipts

$1, 2$	Coordinate directions
b / u	burnt/unburnt
i, j, k	Coordinate indices

Chapter 1 | Introduction

1.1 Background

Anthropogenic climate change has come to the centre of the attention of policymakers and the general public in addition to the previously niche ‘climate scientists’. Since the 2015 Paris Agreement, the Intergovernmental Panel on Climate Change (IPCC) assessed the impact of global warming of $1.5\,^{\circ}\mathrm{C}$ above pre-industrial levels [1] as a means of strengthening the global response. By 2017, already $1\,^{\circ}\mathrm{C}$ of warming could be attributed to human activities with an increase of $0.2\,^{\circ}\mathrm{C}$ per decade forecast at current rates. This spotlight, in particular on the emissions released through the combustion of fossil fuels and their impact on the the global climate, has spurred an array of policies aimed at curtailing the human impact on the climate and maintaining global warming below $2\,^{\circ}\mathrm{C}$, but ideally below $1.5\,^{\circ}\mathrm{C}$ above pre-industrial levels [2]. This is an ambitious target, one which the nature and scale of the problem warrants. However, even when avoiding criticisms of stated ambitions and policies of countries all around the world [3], the future looks unclear. The roadmap towards this goal is highly dependent on geopolitics, quality of life considerations and the availability and implementation of renewable resources. As such, seemingly legacy technology may well linger amongst the mix for longer than anticipated and, furthermore, feature in the diverse solution to local and global climate change issues.

In the UK today, the transportation sector is the largest emitter of greenhouse gases (GHGs) at approximately 25%, with energy production only accounting for slightly less [4]. Considering the global picture, fossil fuels account for over 80% of primary energy, a reduction of only 3% in the last half decade [5]. The BP Energy Outlook in 2022 [6] presented possible scenarios for future energy trends up to 2050 which met the IPCC recommendations for maintaining warming to 1.5 °C. Three pathways are shown in Fig. 1.1, where for the current purposes 'new-momentum' could be interpreted as an optimistic business-as-usual case, 'accelerated' an attempt to limit global warming to below 2 °C and 'net-zero' to limit global warming to below 1.5 °C. Even with the most aggressive 'net-zero' approach, around 20-30% of energy is still generated from the combustion of fossil fuels by the middle of century, as shown in Fig. 1.1, with technologies such as carbon capture and storage (CCS) implemented to remove carbon emissions. Other scenarios, also predicted to achieve below 2 °C warming, still rely on fossil fuels for up to 70% of energy generation. For the transportation sector the change is more extreme, with about a factor five reduction in oil usage for light- and heavy-duty road transport, aviation and marine sectors, the latter two currently approximately 100% powered by oil. Furthermore, contrary to popular belief, over 60% of the reduction in oil consumption in road transport over the next decade can be attributed to improvements in fossil fuel powered vehicle efficiency and not their displacement by battery electric vehicles (BEVs). Alternative sources to the BP report [6] paint a similar, but more conservative, picture. The IPCC Sixth Assessment Report [7] calls for a "substantial reduction in overall fossil fuel use". Riahi et al. [8], in work performed for the IPCC, considered a number of scenarios based on limiting warming to 1.5 and 2 °C with and without an overshoot over the remainder of this century. To limit the peak temperature rise to 2 °C by 2100, slightly under 20% of energy came from fossil fuels. To achieve 1.5 °C, but with an overshoot (of 0.1 – 0.3 °C over several decades), still about two thirds of the total global energy supply came from fossil fuels by 2050, reducing to about 10% by 2100. Carbon abatement technologies, such as CCS, would be implemented in this scenario. For the most stringent scenarios, limiting warming to 1.5 °C with no or limited overshoot (< 0.1 °C), reduced total global energy consumption was typically required with the proportion of global energy production from fossil fuels reduced to < 50% by 2050 and close to 0% by 2100. The IEA [9] also presented a net-zero emissions by 2050 pathway where unabated fossil fuels for energy uses accounts for only 5%. In the scenario fossil fuels used with CCS and for non-energy uses (e.g. chemicals industry) raises the total value to just under 20%.

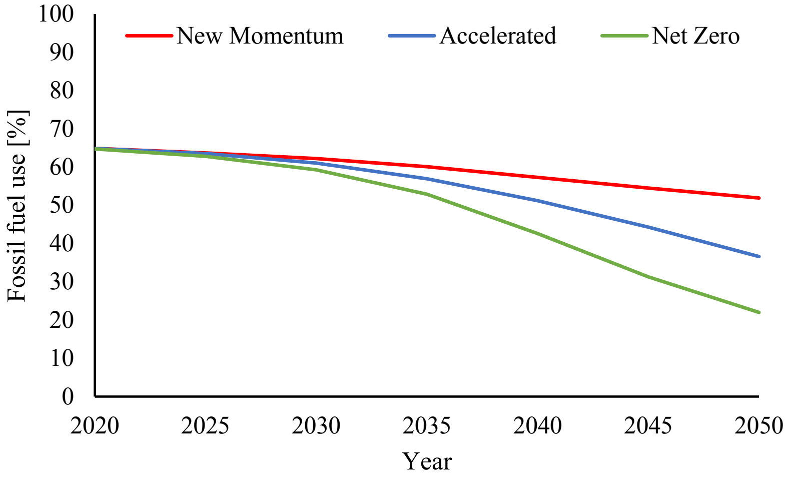

Figure 1.1: The percentage share of final energy consumption generated from fossil fuels comparing three scenarios of increasing aggression for maintaining global warming at least below 2 °C adapted from [6].

Switching away from hydrocarbon fuel combustion is not simple, or perhaps even optimum. Considering the aviation sector, the average age of an aircraft is in excess of 10 years [10] with the average retirement age upwards of 20 years [11] with more than half of the fleet still in use after 25 years [12]. Simultaneously, the Federal Aviation Administration (FAA) timeline for approval of a new aircraft type can take up to about a decade [13]. Compounding these facts, it is clear that any change to an electric propulsion aircraft, rather than just electrification of accessories such as fuel pumping or aileron actuation as is often discussed in the context of electrification of the aircraft fleet [14], would take at the very least a decade to be first used for commercial flights, with a further decade to proliferate throughout the sector. Instead, carbon abatement technologies being developed for imminent implementation are a shift towards biofuels. In 2023, Rolls-Royce aims for its jet engines to be able to accept 100% sustainable aviation fuel (SAF) [15]. Sustainable aviation fuels can originate from used cooking oil and animal waste, as is the case for those developed by Air BP, which result in up to an 80% reduction in carbon emissions over the lifetime [16]. Other sources of SAF include the conversion of landfill waste via gasification to syngas and the Fischer-Tropsch process into a drop-in fuel [17]. It is important to note, that any replacement bio-derived fuels must be fully compatible with a wide range of new and legacy combustion engines for immediate and direct use. In the aviation sector all biofuels must be "drop-in" and meet the general ASTM jet fuel specifications when not blended, with a separate standard for up to 50% blends of biofuel [18, 19]. Combustion of biofuels, unless carbon neutral, would still require carbon offsetting techniques, such as direct air capture (where CO_2 is extracted from the atmosphere), in order for net-zero to be achieved.

There remains an imperative to decarbonise. Pragmatically, in the transportation and power sectors, combustion will remain relevant for the foreseeable future [20]. This is largely due to the superior qualities of liquid fuels as energy carriers which when compared to batteries, their most serious challenger, are more energy dense and offer convenient and stable long-term storage of energy. Furthermore, with the accumulated knowledge and legal requirements established from their use over the last century, they are well characterised and relatively safe. In the realm of combustion processes, carbon emission reductions are possible through two techniques primarily: fuel side changes, such as the use of carbon neutral fuels, and efficiency gains through novel combustion modes.

Firstly, replacing fossil fuels which release previously locked-up carbon with reduced carbon fuels like hydrogen and ammonia, or carbon neutral fuels such as biofuels which release biogenic carbon. In this context green hydrogen, formed using no fossil fuels and its storage as ammonia is a potential technology. The so called 'ammonia economy' would facilitate a shift towards greater hydrogen use [21] as ammonia is easier to store and transport than hydrogen and is more hydrogen dense than pure hydrogen when stored. Furthermore, ammonia is one of the most ubiquitous chemicals worldwide [22]. Projects to ultimately supply green ammonia, formed from green hydrogen, have already begun in Australia [23]. Additionally, biofuels (produced from biomass stores) can be processed to resemble current fuels or are already sufficiently similar to current fuels to only require minor modifications to combustion devices, as in the case of SAFs, before being used directly [24]. However, biofuels may contain other contaminant species such as ammonia, hydrogen sulphides and siloxanes [25] which may have a negative impact on combustion efficiency and more critically lead to the formation of harmful pollutants such as elevated levels of oxides of nitrogen and acidic oxides of sulphur [26]. Additionally, the fuel itself may be damaging to the combustion device, especially if used directly, therefore requiring device modifications. When alcohol biofuels like ethanol, which is perhaps the most common biofuel globally, are used directly, as is the case in Brazil, modifications to the design and materials used in engines are necessary due to their corrosive nature but also to achieve the greatest thermal efficiencies and minimise pollutant emissions [19, 27]. To combat these issues and ensure maximum efficiencies are reached, a fuel-flexible combustion process is required.

This highlights the second carbon abatement strategy, by the efficiency gains of new combustion modes. For example, the novel moderate or intense low oxygen dilution (MILD) combustion process as defined by Cavaliere and de Joannon [28] is characterised by high reactant preheat and a low combustion temperature rise resulting in greatly reduced pollutant emissions. Other examples of combustion methods that can achieve reduced emissions include flameless oxidation [29], two-stage combustion [30] and high-temperature air combustion [31]. While it is technically feasible, if not challenging, to remove carbon from the exhaust emissions of vehicles, the technology would require a dedicated storage tank for the scrubbed CO_2 and unless permanently stored would not prevent emissions of previously locked-up carbon in fossil fuels. Biofuels used in current devices offer only the improvements from displacing the fossil fuel alternative, however when combined with a combustion mode such as MILD dual benefits of fuel choice and combustion mode can be achieved. Such designed fuels match the emerging philosophy of coupling the design of combustion devices with their fuels in order to achieve these dual and amplified benefits of increased efficiencies and reduced pollutant emissions. In so doing, efforts to tackle the unfolding climate crisis can be more swiftly and widely implemented with reduced sacrifices by people and industries in both developed and developing countries.

In order to achieve a coupled design of combustion devices and fuels, a greater understanding of, and ability to, predict the behaviour of fuels is a prerequisite. The development of comprehensively validated chemical kinetic models for fuels, fuel components and additives offers the opportunity to model these molecules and mixtures thereof under conditions relevant to novel combustion modes and make recommendations for practical optimisations. The aim of this work is to further develop such kinetic models.

1.2 Approach

Through chemical kinetic modelling, the combustion characteristics of a fuel and system can be defined. This allows for optimisation, both through increased efficiency and reduced pollutant emissions. The use of simplified surrogate fuel models to approximate the highly complex real-world fuel provides a powerful tool for understanding the impact and nature of alternative fuels and fuel blends [32]. These chemical kinetic models must accurately reproduce the behaviour of their target chemical evaluated through their ability to reproduce experimental data for both global and detailed flame properties. In this work, the ignition delay time, laminar burning velocity, speciation and other unique properties (such as cool flames and Thermal DeNO$_x$), which represent a broad range of fuel oxidation properties and are discussed in more detail later, have been used to comprehensively analyse and validate chemical kinetic models presented herein.

The chemicals considered in this work include primary reference fuels (PRFs) which are a crucial starting point in building surrogate fuels for theoretical and experimental studies. An alternative fuel, ammonia, and fuel additives, including nitromethane, are also considered in this work. Furthermore, a characteristic flame timescale was defined using flame properties (burning velocity and flame thickness). This allowed comparisons between the flame structure of the fuels mentioned above at varied and elevated inlet temperatures and pressures, matching those experienced in real-world combustion applications, with those achievable in experiments in order to inform choices in the latter.

1.3 Objectives and thesis structure

In this work chemical kinetic models for iso-octane, n-heptane, ammonia and nitromethane will be further developed and validated using recent reaction kinetic studies and experimental data for global and detailed combustion properties. Subsequently, these models will be implemented to further understand the relationship between key control parameters related to inlet and combustion conditions and flame properties. Through the use of a characteristic flame timescale, different combustion conditions will be compared in order to match extreme real-world conditions, characterised by high pressures and pre-heat temperatures, with laboratory conditions constrained to atmospheric pressure and lower pre-heating temperatures.

The fundamental theory for modelling combustion systems using chemical kinetic models in addition to its shortcomings, as well as the key parameters used to validate these mechanisms are discussed in Chapter 2. In Chapter 3 the chemical kinetic models for the PRFs, iso-octane and n-heptane are validated and refined. A similar process is applied in Chapter 4, considering an alternative fuel and additive with ammonia and nitromethane. Finally, these chemical kinetic models are applied to conditions of relevance in practical devices and the relationship between global properties and various control parameters are discussed in Chapter 5.

Chapter 2 | Theory

This chapter discusses the theoretical grounding for the computational modelling of combustion systems, including the geometries applied and the mathematical formulation of the physical system and chemical kinetics. In addition, the fuel performance parameters used to describe fuel combustion characteristics and, by extension, evaluate chemical kinetic mechanism efficacy against experimentally obtained values is discussed.

2.1 Computational geometries

To validate chemical kinetic mechanisms various experimentally obtained data sets are used for comparison. Evaluation data includes unstretched laminar burning velocities, ignition delay times and species profiles, both spatial and temporal, obtained from a variety of devices. A comprehensive analysis and mechanism validation relies on such data coming from a variety of sources and having been obtained over a broad range of experimental conditions. Throughout this work three computational geometries have been applied to calculate global properties such as the laminar burning velocity and ignition delay time, and detailed properties including chemical species profiles.

Ignition delay times (IDTs) are predominantly measured in shock tubes and rapid compression machines [33, 34]. Similarly, jet stirred reactors (see also well- or perfectly-stirred reactors) are used for gas phase kinetic studies, primarily the oxidation and pyrolysis of fuels [35], although some ignition studies have been conducted using these devices too, notably by Baulch et al. [36] and co-workers. Both shock tubes and stirred reactors, shown in Figs. 2.1a and 2.1c respectively, can also be used to study the evolution of chemical species with time at conditions that may include high temperatures and pressures, and the measurement of the chemiluminescence of hydroxyl and methylidyne radicals is ubiquitous for IDT identification [37, 38]. The nature of stirred reactors means that there is no molecular diffusion. All of these devices can be modelled using a zero-dimensional approach, with a gas mixture at a specified initial temperature and pressure allowed to evolve over time. The approach for experimentally measuring and computationally defining IDTs is discussed in Section 2.4.3. The foundational equations for this geometry are presented in Section 2.2.1. Modelling systems without reactive-diffusive interactions greatly reduces the state space and means computations are faster. As computational power has increased the modelling of reactive-diffusive systems has become increasingly possible.

The other two geometries are for modelling one-dimensional laminar flames. The rate of propagation of a flame, the laminar burning velocity (LBV), provides information on the overall reactivity of a mixture and can be measured in a number of devices. The methodology for doing so is discussed in greater detail in Section 2.4.2. Common techniques involve spherically expanding [43], counterflow and stagnation flow geometries [44], in addition to the so called heat flux method [45, 46]. The latter method allows for the measurement of unstrained LBVs while the former methods require an extrapolation to zero-strain, but also provide information on the response of the flame structure to the rate of strain. Additionally, the spatially resolved species profiles can be measured in such devices. To do so, a one-dimensional freely propagating or burner stabilised flame setup (Fig. 2.1b) and an axi-symmetric (pseudo) one-dimensional counterflow burner geometry (taken along the burner centreline, Fig. 2.1d) have been used to model flames and calculate laminar burning

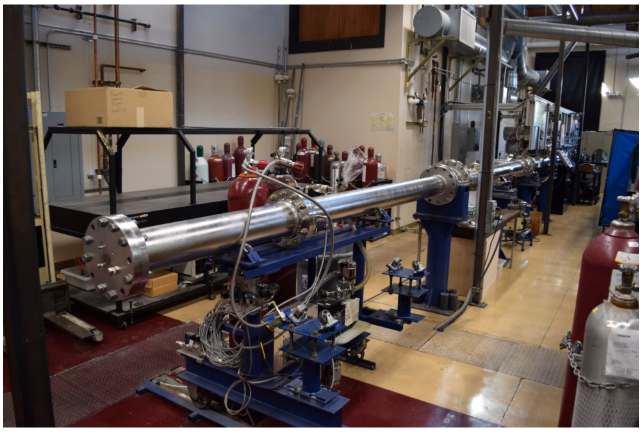

(a) Shock tube at Stanford university [39].

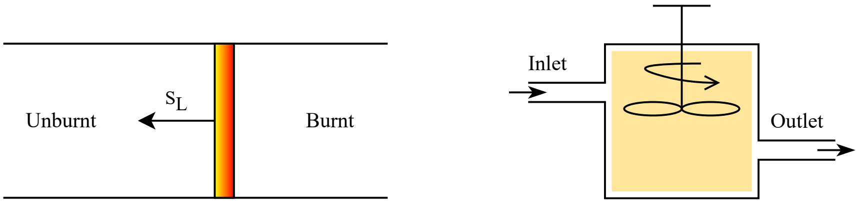

(b) Schematic of a freely propagating flame. (c) Schematic of a well-stirred reactor.

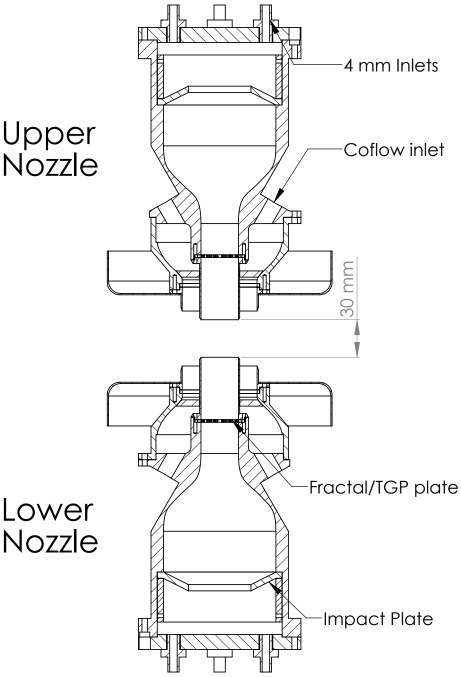

(d) Counterflow geometry at the Imperial College London laboratory and used in prior work [40–42]. The laminar flow equivalent requires the removal of the fractal turbulence generating plate (TGP).

Figure 2.1: Images for the combustion devices used and the equivalent computational geometry applied in this study.

velocities and, in the case of the counterflow burner geometry, the impact of strain. The computations for the latter geometry were based on the dimensions of the Imperial College London counterflow burner, which has a 30 mm nozzle separation.

The methodology for ascertaining chemical species profiles in all the above devices is discussed in Section 2.4.5 and images or schematics of the devices discussed above are shown in Fig. 2.1.

2.2 Instantaneous equations

To describe premixed combustion the governing equations for the conservation of mass, momentum, enthalpy and species mass fractions, respectively, are:

$$\frac{\partial \rho}{\partial t} + \frac{\partial \rho u_i}{\partial x_i} = 0 \tag{2.1}$$

$$\frac{\partial \rho u_i}{\partial t} + \frac{\partial \rho u_j u_i}{\partial x_j} = -\frac{\partial p}{\partial x_i} - \frac{\partial \tau_{ij}}{\partial x_j} + \rho g_i \tag{2.2}$$

$$\frac{\partial \rho h}{\partial t} + \frac{\partial \rho u_j h}{\partial x_j} = \frac{Dp}{Dt} - \frac{\partial J_{q,j}}{\partial x_j} + q_R \tag{2.3}$$

$$\frac{\partial \rho Y_a}{\partial t} + \frac{\partial \rho u_j Y_a}{\partial x_j} = -\frac{\partial J_j^a}{\partial x_j} + S_a W_a \tag{2.4}$$

where u is the velocity in the i or j direction and ρ is the fluid density, In the momentum conservation equation, Eq. 2.2, g_i is the body force and τ_{ij} is the viscous stress tensor which for Newtonian fluids can be expressed as:

$$\tau_{ij} = \mu \left(\frac{\partial u_i}{\partial x_j} + \frac{\partial u_j}{\partial x_i} \right) - \frac{2}{3} \mu \frac{\partial u_k}{\partial x_k} \delta_{ij} \tag{2.5}$$

where μ is the dynamic viscosity of the mixture and δ_{ij} is the Kronecker delta.

In the enthalpy conservation equation, Eq. 2.3, the pressure is p, the heat transfer due to radiation is q_R and the mixture enthalpy, h, is the sum of the specific enthalpy contributions from each species (where NS is the total number of species),

$$h = \sum_{a=1}^{NS} Y_a h_a \tag{2.6}$$

where Y_a is the mass fraction of species a and the specific enthalpy for the respective species, h_a, is given by the summation of the standard enthalpy of formation and the sensible enthalpy:

$$h_a = \Delta h_{a,f} + \int_{T_0}^{T} C_{p_a} dT \tag{2.7}$$

where $\Delta h_{a,f}$ is the standard enthalpy of formation for species a and C_{p_a} is the specific heat capacity at constant pressure for the respective species. Additionally, the heat flux, $J_{q,j}$, is given by:

$$J_{q,j} = -\lambda \frac{\partial T}{\partial x_j} + \sum_{a=1}^{NS} h_{a,f} J_j^a \tag{2.8}$$

where λ is the thermal conductivity and T is the temperature. The heat flux (Eq. 2.8) is expressed in terms of enthalpy, which is a conservative scalar, to do so the mixture specific heat capacity, C_p, is used and is expressed as:

$$C_p = \sum_{a=1}^{NS} Y_a C_{p_a} \tag{2.9}$$

therefore, this allows the enthalpy (Eq. 2.6), to be expressed as:

$$h = \int_{T_0}^{T} C_p dT + \sum_{a=1}^{NS} Y_a h_{a,f} \tag{2.10}$$

Differentiation of Eq. 2.10 with respect to x_j gives:

$$\frac{\partial h}{\partial x_j} = C_p \frac{\partial T}{\partial x_j} + \sum_{a=1}^{NS} h_a \frac{\partial Y_a}{\partial x_j} \tag{2.11}$$

which allows the heat flux (Eq. 2.8) to be re-expressed as:

$$J_{q,j} = -\frac{\lambda}{C_p} \frac{\partial h}{\partial x_j} + \sum_{a=1}^{NS} h_a \left(\frac{\lambda}{C_p} \frac{\partial Y_a}{\partial x_j} + J_j^a \right) \tag{2.12}$$

In the species mass fraction conservation equation, Eq. 2.4, S_a is the chemical reaction source term for species a, in units of $\mathrm{kmol\,m^{-3}\,s^{-1}}$, and $S_a W_a$ is subsequently referred to as S_a^* has units of $\mathrm{kg\,m^{-3}\,s^{-1}}$. The molecular diffusion flux, J_j^a, also appearing in the heat flux equation, Eq. 2.8, for the respective species is defined as:

$$J_j^a = -\rho D_a \left(\frac{\partial Y_a}{\partial x_j} - Y_a \frac{1}{n} \frac{\partial n}{\partial x_j} \right) - \rho V_c Y_a \tag{2.13}$$

where D_a is the diffusion coefficient of species a , n is the number of moles and V_c is a correction velocity to ensure all the diffusive fluxes sum to zero.

The variation of pressure with time (Dp/Dt) must be included in the case of compressible flows but can be removed for systems with constant pressure. Finally, for ideal gases the above equations are closed using the equation of state:

$$p = \rho R T \sum_{a=1}^{NS} \frac{Y_a}{W_a} \tag{2.14}$$

where the universal gas constant, R = 8.314 J mol^{-1} K^{-1}, W_a is the molecular weight of species a and for very low Mach numbers: $\rho = \rho(Y_a, h, p)$.

2.2.1 Application of transport equations

The computational models applied in this work to study the geometries discussed in Section 2.1 assume laminar flow, for simplicity, and additionally, the appropriate dimensionality must be applied. For the one-dimensional, and quasi-unidimensional approach used for the counterflow geometry, the transport equations can in principle be simplified to variants of:

$$\frac{\partial \rho}{\partial t} + \frac{\partial \rho u_1}{\partial x_1} = 0$$

$$\frac{\partial \rho u_1}{\partial t} + \frac{\partial \rho u_1 u_1}{\partial x_1} = -\frac{\partial p}{\partial x_1} + \frac{4}{3}\mu \frac{\partial u_1}{\partial x_1} + \rho g_1$$

$$\frac{\partial \rho h}{\partial t} + \frac{\partial \rho u_1 h}{\partial x_1} = \frac{Dp}{Dt} + \frac{\partial J_{q,1}}{\partial x_1} + q_R$$

$$\frac{\partial \rho Y_a}{\partial t} + \frac{\partial \rho u_1 Y_a}{\partial x_1} = -\frac{\partial J_1^a}{\partial x_1} + S_a^*$$

For the two zero-dimensional geometries outlined in Section 2.1 there are different governing equations applied. For the well-stirred reactor, since the mixture is homogeneous all spatial gradients can be removed and assuming constant pressure (i.e. $\frac{Dp}{Dt} = 0$) and adiabatic conditions ($q_R = 0$) the fundamental equations reduce to:

$$\rho \frac{\partial h}{\partial t} = 0$$

$$\rho \frac{\partial Y_a}{\partial t} = S_a^* + \frac{\dot{m}}{V}(Y_a^{in} - Y_a^{out})$$

where $\dot{m}$ is the mass flow rate through the reactor and V is the volume of the reactor. The residence time, τ, can be defined as $\tau = (\rho V)/\dot{m}$. The equation can be integrated to steady-state for the given residence time:

$$\frac{\partial Y_a}{\partial t} = 0 = \frac{S_a^*}{\rho} - \frac{\Delta Y_a}{\tau}$$

$$\Delta Y_a = \frac{S_a^*}{\rho}\tau$$

where $\Delta Y_a = Y_a^{out} - Y_a^{in}$. It follows that reaction progress is dependent on the residence time.

The governing equations for a shock tube or plug flow reactor are derived in a slightly different manner. The common assumptions include steady state flow, no axial mixing, uniform flow properties perpendicular to the flow, frictionless (no boundary layers) and the ideal gas law applies. This means that time derivatives can be removed, and assuming adiabatic conditions the governing equations reduce to

$$\frac{\partial \rho u_1}{\partial x_1} = 0$$

$$\rho u_1 \frac{\partial u_1}{\partial x_1} = -\frac{\partial p}{\partial x_1}$$

$$\rho u_1 \frac{\partial h}{\partial x} = 0$$

$$\rho u_1 \frac{\partial Y_a}{\partial x_1} = S_a^*$$

Rewriting the species conservation equation using $u = \partial x / \partial t$

$$\rho \frac{\partial Y_a}{\partial t} = S_a^*$$

recalling the species conservation equation for the well-stirred reactor, it can be shown to be equivalent to the above equation as $\tau \to \infty$. Therefore, solving the well-stirred reactor with an infinite residence time (or in computational codes, a very large value) will produce the result for a shock tube or plug flow reactor. In this way, both geometries can be solved using a zero-dimensional numerical model.

If isothermal conditions are assumed instead, the temperature can be found using the current mixture state and properties (composition, enthalpy, heat capacities etc.) and an iterative method.

2.2.2 Solution methods

In order to compute flames a numerical model is required to solve the governing equations, outlined above, including the chemical kinetic model. One of the first attempts to solve the governing equations of a premixed flame was conducted by Hirschfelder et al. [47], who used linear asymptotic analysis and a numerical shooting method. Spalding [48] presented a theory connecting the flame speed and inflammability limit, where the former was solved for one-dimensional, laminar and steady combustion in a premixed gas. Dixon-Lewis [49] built on the method proposed by Spalding [50] and solved the time-dependent continuity equations for a one-dimensional fuel rich hydrogen/oxygen/nitrogen flame. Numerous computational simplifications were employed for expediency, including the one-dimensional approach and assuming all mixture components had the same specific heat capacities. By modern standards only a simple system of equations were solved, containing up to six species and 14 reactions, in time using finite difference methods until convergence at steady-state. The work of Spalding et al. [51] applied the previously developed computational procedure for solving the steady two-dimensional boundary layer equations [52] to solve an unsteady one-dimensional laminar flame. This marked a turning point where increasingly complex reaction mechanisms could be solved and allowed for their subsequent refinement for improved predictions of experimental data. For example, Tsatsaronis and co-workers [53, 54] applied the approach of Spalding et al. [51] and incorporated a diffusion model to solve a methane-air flame using a reaction mechanism containing 13 species and 29 reactions and predict hydroxyl radical and temperature profiles, as well as the impact of equivalence ratio and pressure on these parameters.

In the 1980s Smooke [55] presented a numerical technique developed for integrating one-dimensional steady-state premixed laminar flames. It used a global finite difference method with non-linear equations solved using a damped-modified Newton method. The so-called block solver along with increased computing power and capacity has allowed the more efficient and economic solving of ever increasingly complex systems using larger kinetic mechanisms, containing hundreds or even thousands of distinct chemical species. In 1988, Jones and Lindstedt [56] formulated the equivalent time dependent solution method with the time derivative used to ensure diagonal dominance of the block solver in order to also provide improved computational stability. Further developments include work by Lindstedt and Sakthitharan [57] extending the above technique to studies of transient effects on premixed laminar flames, including code parallelisation by domain decomposition to allow for more detailed chemical kinetics. This approach has recently been applied to transient spherical flames of fuel blends with hydrogen to explore the impact of the rate of strain and non-unity Lewis numbers [58].

Commercial software based on the outcomes of the work of Smooke [55], such as CHEMKIN and Cantera, now exists for conducting gas phase kinetic studies. All that is required is a kinetic model and the initial conditions of temperature, pressure and mixture composition before the differential equations can be solved. In this work, the above [56] in-house code is used, which solves the implicit time dependent PDEs using a variety of linear equation solvers, such as block LU decomposition and Newton linearisation techniques with derivatives evaluated analytically.

2.3 Chemical kinetic modelling

The fuels evaluated in this work were studied by considering their change from reactants to products to occur through a system of elementary and global reactions. The reaction rate constant is modelled using the modified Arrhenius expression:

$$k_{f,i} = A_i T^{n_i} \mathrm{e}^{-E_{a,i}/RT} \tag{2.15}$$

where $k_{f,i}$ is the forward rate constant for reaction i, A is a pre-exponential factor, n is a temperature dependence and E_a is the activation energy barrier.

To compute the reverse rate constant, k_r, for elementary reactions the equilibrium constant is calculated according to:

$$k_{r,i} = \frac{k_{f,i}}{K_{c,i}} \tag{2.16}$$

where $K_{c,i}$ is the equilibrium constant in concentration terms for reaction i. It is calculated using the species thermodynamic properties in pressure units which are related by:

$$K_{c,i} = K_{p,i} \left(\frac{P_{atm}}{RT} \right)^{\sum\limits_{k=1}^{K} \nu_{k,i}} \tag{2.17}$$

where the exponent is the sum of the stoichiometric coefficients and the equilibrium constant in pressure terms, $K_{p,i}$ for reaction i is defined as:

$$K_{p,i} = \exp \left(\frac{\Delta S_i^0}{R} - \frac{\Delta H_i^0}{RT} \right) \tag{2.18}$$

where ΔS_i^0 and ΔH_i^0 are the change in standard state molar entropy and enthalpy in changing from reactants to products by reaction i, respectively.

2.3.1 Pressure dependent reactions

Some reactions may be pressure dependent. For such reactions two rate constant expressions are specified, the high pressure limit, k_∞, and the low pressure limit, k_0 with any third bodies present. The two rate constants are typically combined using the Lindemann approach [59]:

$$k = k_\infty \left(\frac{P_r}{1 + P_r} \right) F \tag{2.19}$$

where F is the broadening factor, P_r is the reduced pressure and is defined as

$$P_r = \frac{k_0[M]}{k_\infty}$$

and $[M]$ is the concentration of the mixture, including any chaperon efficiencies to enhance or diminish the impact of specific species as third body collision partners. In the Lindemann form $F = 1$, the more complex Troe [60] form is described below:

$$\log F = \left[1 + \left(\frac{\log P_r + c}{n - d(\log P_r + c)} \right)^2 \right]^{-1} \log F_{cent} \tag{2.20}$$

where the constants are

$$c = -0.4 - 0.67 \log F_{cent}$$

$$n = 0.75 - 1.27 \log F_{cent}$$

$$d = 0.14$$

and

$$F_{cent} = (1 - \alpha) \exp(-T/T^{***}) + \alpha \exp(-T/T^{*}) + \exp(-T^{**}/T)$$

where α, T^{***}, T^{*} and T^{**} are constants determined for a specific reaction. Frequently T^{**} is not used. The constant, F_{cent}, is sometimes referred to by the abbreviated F_c and other approximations, in addition to the Troe form, exist [61].

2.3.2 Reduction methods

Highly detailed reaction mechanisms exist, some containing over 1000 distinct chemical species and up to 100,000 reactions. Figure 2.2 is taken from Lu and Law [62] and shows the general trend towards mechanisms of increasing size and complexity over time as computational power has increased. Curran [63] discusses the development of these detailed mechanisms and the creation of community-wide core hydrogen and carbon (C_1-C_4) mechanisms, such as those in AramcoMech, JetSurf, San Diego Mech and USC Mech II, in addition to in-house mechanisms such as the CRECK mechanism, also known as POLIMI. Detailed mechanisms also exist for heavier ($>C_4$) hydrocarbons, such as the primary reference fuels (PRFs), n-heptane and iso-octane, for example the early work of Lindstedt and Maurice [64] and those developed and updated by Curran and co-workers [65–68].

However, such large mechanisms are impractical for computations of real world systems where both turbulence and multi-dimensional effects need to be considered. Lindstedt [69] outlined three tiers of mechanisms, each occupying a smaller state space: detailed, skeleton and reduced reaction mechanisms. In order to achieve these reductions a variety of techniques are available to the chemical kinetics researcher. Lu and Law [62] discuss a comprehensive collection of these techniques in their paper: *Toward accommodating realistic fuel chemistry in large-scale computations*. Broadly speaking they identify four categories. Firstly, skeletal reduction where reactions and species are removed from a detailed mechanism, where each simplification method is its own subcategory of the skeletal reduction approach. This approach leaves a subset of the detailed mechanism including only that which is relevant to the current study. Secondly, lumping methods where similar species

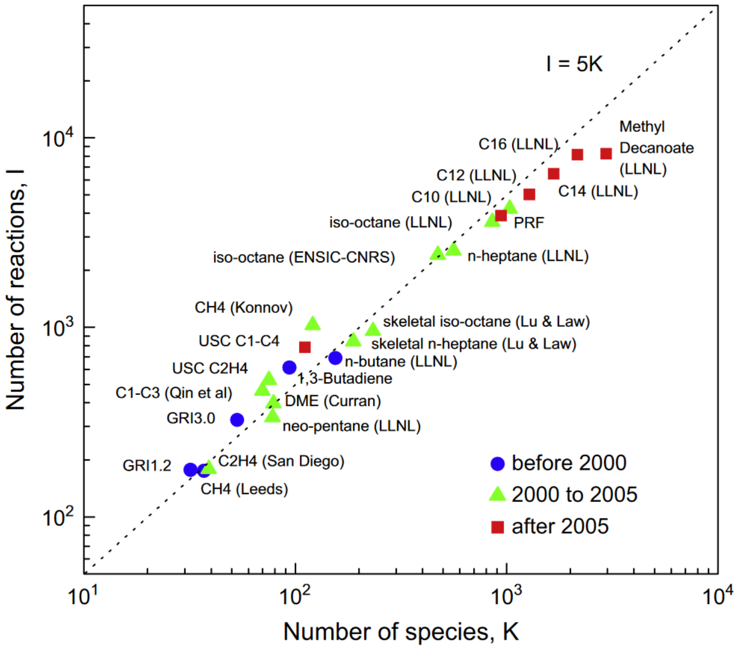

Figure 2.2: Collection of mechanisms, collated by year up to 2009, showing the number of chemical species and reactions contained within them, from [62].

and reaction pathways are combined. Thirdly, a time-scale analysis which identifies quasi-steady state (QSS) species and partial equilibrium (PE) reactions. Mathematically more advanced techniques may be utilised here to formalise the process, such as intrinsic low-dimensional manifolds (ILDM) [70] and computational singular perturbation (CSP) [71]. Finally, on the fly procedures such as in-situ adaptive tabulation (ISAT) to speed-up computations and other tabulation methods such as the use of artificial neural networks (ANNs) [72].

Skeletal approaches offer the fundamental reduction technique for detailed mechanisms. Warnatz [73] noted that above the negative temperature coefficient (NTC) region large hydrocarbon fuels first undergo pyrolysis and then subsequent oxidation of those products. Building on this, Warnatz [74] suggested the rapid decomposition hypothesis whereby the dominant route for fuel consumption is hydrogen abstraction (by radicals) and the subsequent alkyl radical decomposition to C_1- and C_2-fragments occurs quickly such that these reactions are not rate-limiting. Therefore, the elementary reactions from the fuel alkyl radical towards the fragments can be collected into a simplified reaction and the alkyl isomeric species disregarded. This has the dual benefit of species and reaction number reduction. Varatharajan et al. [75] applied this technique to acetylene, ethylene, propane and JP-10 using a two-step mechanism for hydrocarbon-air detonations. This built on prior work for JP-10 [76] using a similar rapid decomposition approach.

The Hybrid Chemistry (HyChem) approach developed at Stanford University incorporates the ideas from the rapid decomposition hypothesis [74] and lumped reaction models (discussed below) but with experimental constraints applied. Wang et al. [77] and Xu et al. [78] describe and demonstrate the HyChem approach, designed to address the issues of using surrogate fuels as simplifications for variable multicomponent real-world fuels due to the significant difficulties in the development of a surrogate that matches physiochemical properties of the real-world fuel [77]. Seven lumped fuel thermal decomposition and oxidative pyrolysis reaction steps to C_1-C_5, one $C-C$ fission and six hydrogen abstraction steps, are built using experimental data. It was shown that foundational chemistry uncertainties dominate [78] and that the approach was able to predict global combustion properties well for a range of typical fuels and blends thereof [77–79], including for JP-10 (a single-component fuel) [80].

Isomer lumping combines similar molecules into single species, greatly reducing the number of reactions and of species included in a mechanism. This also requires alterations to the fundamental kinetic rates to consider the reaction of multiple isomers represented by the lumped species, and as such does not account for the reaction pathways associated with individual isomers. The rigour with which this is done can vary. Ranzi et al. [81] introduced lumping for pyrolysis products of normal and branched alkanes. This was further developed by Ranzi et al. [82], who generalised the process to be applied to oxidation reactions where the reaction of intermediate radicals with oxygen must be accounted for. Lumped species for the alkyl radicals (pyrolysis products) and the remaining intermediate radicals (oxidation products) were defined for the n-alkane example. This approach was later reviewed by Ranzi et al. [83] who identified the core mechanism as the crucial and fundamental step with the most significant sensitivities arising from it. The widest range of experimental data was therefore needed to conduct comprehensive validation of the core scheme. Ranzi et al. [84] applied this approach, building on prior work [85], to produce the lumped POLIMI pyrolysis and oxidation mechanism for producing several skeletal mechanisms for surrogate transportation fuels, from n-heptane to heavy diesel fuels. This procedure was automated and tested for n-heptane and n-dodecane, in combination with reduction techniques, by Stagni et al. [86]. However, the multidimensional real-world CFD applications only extended to steady-state, axisymmetric, laminar diffusion flames. The n-dodecane work was then further extended by Frassoldati et al. [87] using an updated detailed mechanism (POLIMI-TOT-1407) to produce a reduced mechanism containing 96 species and 993 reactions for high- and low-temperature behaviour.

Further reductions on skeletal mechanisms may still be necessary in the computation of multi-dimensional and turbulent computations, especially for large and multi-component real-world fuels. The quasi-steady state approximation (QSSA) approach was first developed by Bodenstein [88] and Chapman and Underhill [89]. It gained popularity following further publications by Bodenstein and Lütkemeyer [90] and Semenov [91, 92, 93]. At first the method was used for approximating analytical solutions and make conversions to non-stiff differential equations, but as computer power increased and the study of more complex systems came to the fore its use as a reduction technique became of interest [94]. In combustion systems, the QSSA approach was initially applied to reactive systems only, where diffusivity was neglected. For flames this assumption relied on very fast diffusion. The approach was notably applied to other combustion systems by Peters [95] from the mid-1980s. In such systems, the QSSA approach suggests that there exist chemical species, typically reactive intermediates, which reach a quasi-steady state much faster than the major reactants and products. As such, these chemical species can be considered at quasi-steady state after a very short (relatively) initial transient. This allows QSS species to be removed from the solver, greatly reducing computational cost, and their concentrations be calculated using algebraic relationships. A book on reduction technique applications by Peters and Rogg [96], included a collection of relevant research for the QSSA approach applied to unstretched premixed and counterflow diffusion flames. For example, this included a 2-step mechanism for premixed hydrogen flames [97]. Notable, foundational work on the QSSA applications includes the work on methane oxidation by Paczko et al. [98] which was later extended by Glarborg et al. [99] with the addition of reduced nitrogen chemistry. Turányi et al. [94] developed comprehensive error analysis tools for QSSA applications. Lindstedt and Louloudi [100] applied the approach for the computation of turbulent methanol jet diffusion flames using a transported joint probability density function approach and a systematically reduced mechanism which was still able to predict local extinction near to the burner nozzle and reignition downstream.

Other ad hoc methods exist for reduction and aiding this process. Computational singular perturbation (CSP) was first presented by Lam [71] and used as a diagnostic tool or stiff ODE solver. The technique uses timescale analysis to separate into fast and slow subspaces, identifying PE and rate-controlling reactions and which species can be considered "radicals" (in the CSP context). The approach is further discussed by Lam [101]. Massias et al. [102] demonstrates the methodology for application of CSP in identifying PE reactions and QSS species in aiding the usage of the QSSA approach. The intrinsic low-dimensional manifolds (ILDM) method, developed by Maas and Pope [70], offers a fundamentally similar methodology to the CSP approach, but with the express purpose of a reduction in the degrees of freedom (the number of reaction steps). Both CSP and ILDM methods offer a systematic and automatable method that reduces the need for intuition in the selection of QSS species when simplifying mechanisms with the QSSA approach. Pope [103] developed the in-situ adaptive tabulation (ISAT) approach for speeding up computations. A look-up table is built during the reactive flow computation with each entry referring to a composition, with adaptive local error control. A speed-up of three orders of magnitude was achieved [103] in a test case, but significant storage space is required. Lu and Law [104] used graph theory for the direct relation graph (DRG) method which identifies unneeded species for skeletal reduction. The approach was further applied to n-heptane in combination with isomer lumping based on thermal and diffusive properties and CSP to reduce a detailed mechanism containing 561 species to a reduced mechanism containing 55 solved species (13 QSS species) [105]. Finally, artificial neural network (ANN) techniques to allow varied degree of mechanism tabulation. Christo et al. [72] applied an integrated pdf/ANN approach for turbulent flames, where the training set for the ANN was generated using statistical mapping. More recent examples include the work from Franke et al. [106] and Readshaw et al. [107] demonstrating an 18-fold reduction in reaction source term computation time. However, the accuracy of such techniques is heavily dependent on the type and scope of the data sets used for training.

In this work, multiple approaches from above have been applied for the larger chemical mechanisms used to model the primary reference fuels, in particular. Both the rapid decomposition hypothesis and isomer lumping have been used and their implementation is discussed further below. Further reductions are possible by systematic applications of the QSSA.

2.4 Performance parameters and combustion descriptors

A fuel can be described using global and detailed combustion properties. Global properties describe combustion using a restricted number of values and primarily focus on two key aspects: the rate of propagation of a flame or chemical processes and the species evolution. The former leads to definitions of the burning velocity and the ignition delay time and the latter to the flame thickness and different zones within it. Detailed properties, by contrast, consider the chemistry by measuring the evolution of species from reactants to products. Measurements can be temporal or spatial, depending on the device type. Both types of properties provide crucial metrics for the comprehensive validation of chemical kinetic models discussed in Section 2.3. While in the past mechanisms that were tailored to the prediction of only certain quantities [63] could be of primary relevance, the increased computational power and need to model systems where chemical understanding becomes crucial, a more general approach is now favoured. This section explores the fundamentals of flames and how they can be classified according to dimensionless numbers. In addition, the definitions applied experimentally and computationally for global combustion properties, including the laminar burning velocity, ignition delay time and flame thickness, as well as the methodologies used for measuring and predicting the evolution of species are discussed.

2.4.1 Flame classification

Real-world combustion devices function in the turbulent regime and those with premixed fuel/oxidiser reactants are ubiquitous. Examples of such devices include the spark-ignition engine in the automotive industry and modern stationary industrial gas turbines for power generation [108]. Turbulent combustion models can include the assumption that the turbulent flames are formed from an ensemble of laminar flamelets [109]. Such models can be conditionally used to compute turbulent flame properties and require an understanding of laminar flame behaviour. A planar laminar premixed flame is composed of two major zones:

- *Preheat zone* - the temperature of the reactants increases, some thermal decomposition of the fuel will occur but temperatures remain too low to initiate major heat release.

- *Reaction zone* - temperatures are sufficient to overcome activation barriers and most of the chemical reactions occur here, releasing heat which is diffused towards the cool reactant side.

The preheat and reaction zones are flanked on either side by fresh reactants, as long as they are supplied, and hot combustion products, respectively. Therefore, practical premixed combustion devices with high levels of turbulence exhibit complex relationships between reaction chemistry and turbulent transport, of energy (heat), reactants, products and intermediate species. Various non-dimensional parameters are used to categorise the flow and reaction state. The Reynolds number (Re) and turbulent Reynolds number (Re_t) describe turbulence levels and are evaluated as shown in Eq. 2.21:

$$\mathrm{Re} = D \cdot U_b \cdot \nu_r^{-1} \tag{2.21a}$$

$$\mathrm{Re}_t = L_I \cdot u_{rms} \cdot \nu_r^{-1}, \tag{2.21b}$$

where D is the nozzle diameter, U_b the bulk velocity, L_I the integral length scale, u_{rms} the turbulence velocity fluctuations and ν_r the kinematic viscosity. In addition to the integral length scale, the size of most energetic eddies, the Kolmogorov length scale (L_η), the size of smallest eddies where turbulent kinetic energy is dissipated, is defined as shown in Eq. 2.22:

$$L_\eta = (\nu_r^3 \cdot \epsilon_r^{-1})^{1/4}, \tag{2.22}$$

where ϵ_r is the dissipation rate and is approximated as, $\epsilon_r \simeq u_{rms}^3 \cdot L_I^{-1}$.

Most crucially, the ratio of the turbulence timescale (by various definitions) and the chemical timescale are described by the Damköhler (Da) number and two Karlovitz (Ka and Ka_δ) numbers (based on the Kolmogorov scale and inner flame thickness, respectively), found as shown in Eq. 2.23:

$$\mathrm{Da} = \frac{\tau_I}{\tau_c} = \frac{L_I \cdot S_L}{u_{rms} \cdot l_F}; \tag{2.23a}$$

$$\mathrm{Ka} = \frac{\tau_c}{\tau_\eta} = \frac{l_F}{S_L}\left(\frac{\nu_r}{\epsilon_r}\right)^{-1/2}; \tag{2.23b}$$

$$\mathrm{Ka}_\delta = \delta^2 \cdot \mathrm{Ka}, \tag{2.23c}$$

where τ is a characteristic timescale, S_L the laminar flame speed and l_F the laminar flame thickness and δ the reaction zone thickness. These parameters, in addition to the Klimov-Williams criterion [40] allow the definition of combustion regime diagrams. First proposed by Williams [110] and then expanded on by Borghi [111] and Peters [112]. Peters [113] defined the combustion regime diagram depicted in Figure 2.3.

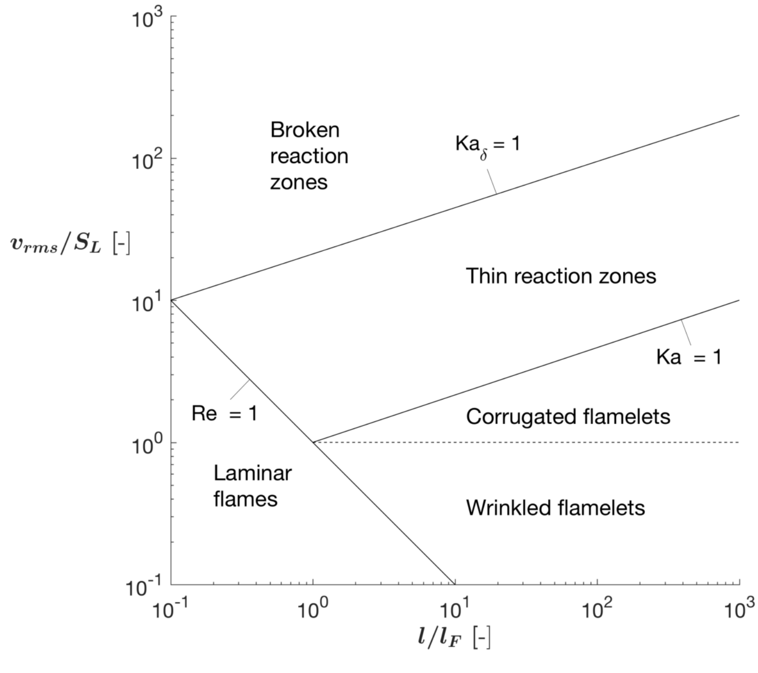

Figure 2.3: Combustion regime diagram according to Peters [113].

Novel proposed combustion regimes, with increased turbulence levels and leaner mixtures, exhibit flow and chemical timescales of increasingly comparable order, even with Kolmogorov eddies sizes below the reaction zone or inner zone thickness [114]. These combustion modes occupy the 'thin reaction zone' and 'broken reaction zone' regions of Figure 2.3, providing lower overall temperatures. However, in these modes the common flamelet model for turbulent combustion proposed by Bray-Moss-Libby [115] breaks down. Furthermore, flames can become difficult to sustain and prone to extinction. Therefore, experimental characterisation of these modes is required to aid the evaluation of computational models for them. Suggested practical combustion modes that operate in this regime, which often require external enthalpy support, include: (a) Moderate or low-oxygen dilution (MILD) combustion [28] (b) Flameless oxidation [29] (c) High-temperature air combustion [31]. Hampp and Lindstedt [116, 117] studied and quantified the existence of reacting fluid states for MILD combustion. All these modes are characterised by a broadening of the reaction zone, which results in lower maximum temperatures reducing the appearance of hot spots. Therefore, the associated benefits are reduced pollutant production and, in the case of fuel lean mixtures, no soot emissions.

2.4.2 Laminar burning velocity

Premixed combustion is characterised by its rate of propagation, which indicates the rate that reactants are converted into products exothermically. The rate of propagation is directly analogous to the burning velocity, which is unique for each reactant composition but is typically between 30 - 60 cm/s at standard conditions for hydrocarbon/air mixtures [108]. The velocity can be defined for laminar and turbulent regimes, but in both cases the same definition is applied: it represents the speed of propagation of a (effectively planar) flame in a direction normal to itself and towards the reactants. Unlike the laminar burning velocity (LBV), the turbulent burning velocity is also dependent on turbulent flow properties, as well as thermochemical quantities. Both velocities are also highly dependent on equivalence ratio and temperature, with maximum values observed around stoichiometric conditions (slightly to the rich side) and at elevated temperatures.

The laminar burning velocity has been extensively studied and shown to be related to flame stretch and instability [118] and is thus of relevance to combustion phenomena including flame flashback and extinction [119, 120]. This means that the LBVs are relevant in multiple industrial applications where a flamelet structure exists including some engine types, gas turbine combustors and furnaces [119]. Therefore, validation of chemical mechanism against laminar burning velocity data is crucial for their subsequent application to real-world scenarios.

The experimental techniques have been discussed and evaluated in prior work by Egolfopoulos et al. [121] and Konnov et al. [120]. The more ubiquitous techniques are presented only briefly here. The spherical flame method [122] creates an expanding flame and evaluates the LBV from measurements of the pressure-time history [123] or the flame radius [124]. The counterflow or stagnation flame technique measure the minimum velocity near the stabilised flame, ahead of the flame front, and correct for strain effects [125]. The methods and relevance of these correction techniques are discussed later including their relevance to computational methods and the evaluation of chemical mechanisms. The heat-flux method directly obtains stretch-free burning velocity measurements by stabilising the flame on a perforated plate [126, 127]. Other methods are discussed by Konnov et al. [120] that use mass conservation across the flame front to infer the LBV. Computational methods utilise approaches consistent with the experimental techniques. The velocity profile across the flame can be used to infer the LBV and rate of strain, based on the minimum velocity ahead of the flame front and from the negative of the maximum velocity gradient upstream of the LBV measurement location [128], respectively. Additionally, the reaction rate integral of a defined species can also be used to evaluate the LBV, Bradley et al. [118] describe this as the rate of disappearance of reactants and/or the rate of appearance of products. All these methodologies give convergent results at zero strain.

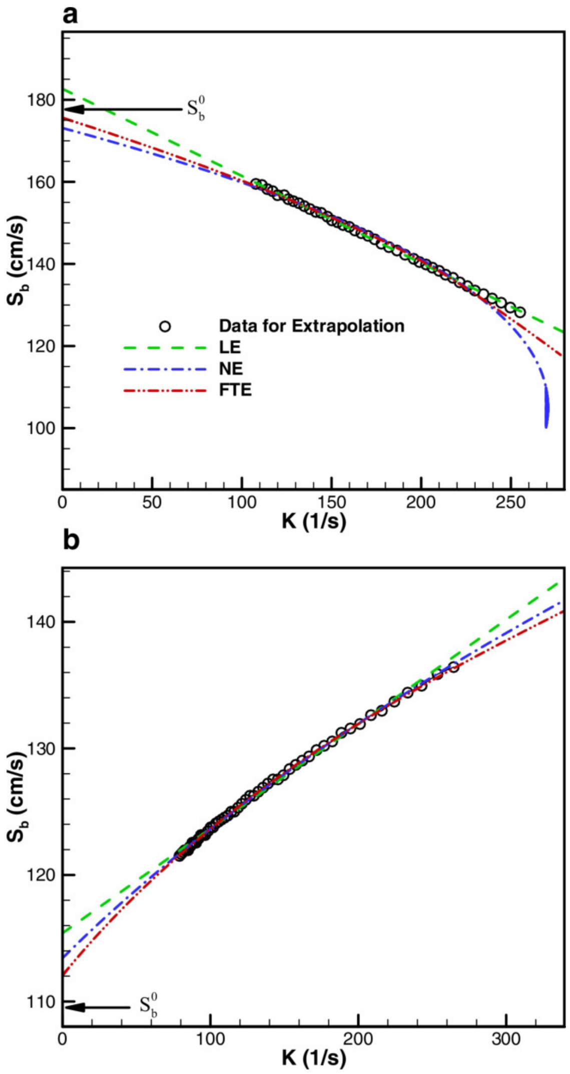

Figure 2.4: Typical laminar burning velocity at varied strain plot for (a) lean conditions, ϕ = 0.8 and (b) rich conditions, ϕ = 1.7 for n-heptane/air mixtures. Linear (LE), non-linear (NE) and flame thickness expressions (FTE) for the extrapolation are included [129].

Dealing with non-zero strain rates in the prediction of the unstrained LBV has been the subject of much research [118, 124, 130]. This issue is especially relevant to the counterflow and stagnation flame techniques for measuring LBV and to computations that apply these geometries. Wu and Law [125] suggested the use of a linear extrapolation, after measurements at a range of strain rates had been collected, to zero rate of strain. However, others have criticised this approach, which tends to over-predict LBVs when compared to the results obtained from the heat-flux method. Therefore, Tien and Matalon [131] suggested a non-linear stretch model which was applied by van Maaren and de Goey [127] and was able to account for the differences between the counterflow and heat-flux measurements [132] over a range of stoichiometries for methane- and propane-air flames. Mittal et al. [128] assessed the validity of the assumption of a one dimensional system along the centreline of the counterflow flame using direct numerical simulations (DNS) computations. They showed that this assumption only worked well if the nozzle exit velocity had a top hat profile, and that therefore experimentalists needed to ensure a uniform velocity exit profile. Furthermore, another non-linear extrapolation model was proposed relying only on computed values to account for the break down of non-linear models in the presence of non-uniformities in the nozzle exit velocity profile. Up to a 10% change was seen when compared with a linear extrapolation, a recent study measuring burning velocities in spherical flames stated that uncertainties in the measurement could be up to 6.5% [133]. Liang et al. [129] compared a linear, non-linear [134, 135] and finite flame thickness [136] extrapolations and the results for a fuel lean and rich n-heptane-air mixture are shown in Fig. 2.4. Similar uncertainties are discussed for spherical flames by Wu et al. [137].

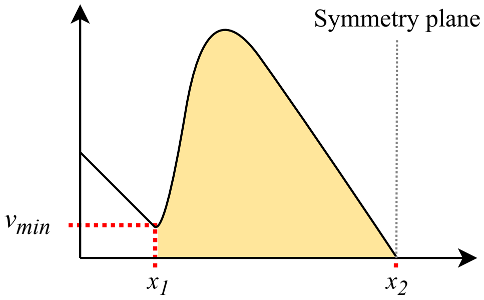

Figure 2.5: A typical axial velocity profile for a counterflow flame. The position of the minimum velocity ahead of the flame front is indicated at x_1 and the stagnation point at x_2. The shaded area shows the region in which the reaction rate is integrated.

In this work, considering the uncertainties in measurements and variety of non-linear extrapolation models in the literature with no clear consensus, linear extrapo-

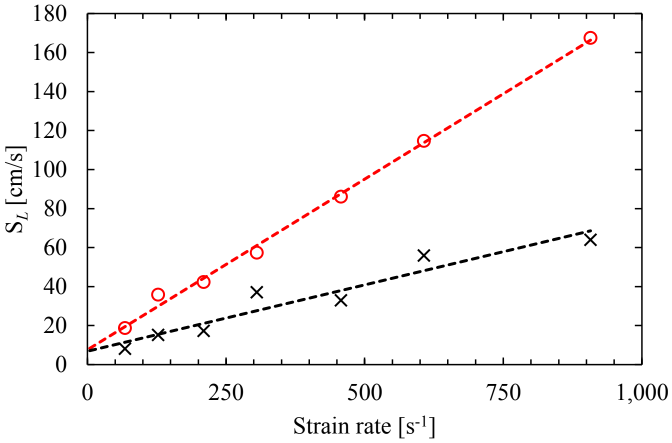

Figure 2.6: Comparison of velocity definitions at varied rate of strain and the linear extrapolation to zero strain for a ϕ = 1.0 iso-octane flame at 28 atm and inlet temperature 300 K. Red circles are for the minimum velocity in the reaction zone and black crosses are for the reaction rate integral velocities for iso-octane.

lations of both the reaction rate integral of the fuel consumption and the minimum velocity ahead of the flame front were used and the values compared at zero strain. Figure 2.5 shows a typical axial velocity profile for a counterflow flame and is used to portray these two definitions graphically. The minimum velocity ahead of the flame front is taken directly at x_1. The reaction rate integral for a specific species integrates the net production rate of that species within the shaded region, between x_1 and x_2. The rate of strain, as mentioned above, is taken from the absolute value of the steepest velocity gradient between 0 and x_1. The strain rate dependency for a stoichiometric iso-octane/air flame at 28 atm and with an in inlet temperature of 300 K is shown in Fig. 2.6 comparing the results using both computational burning velocity definitions. Both definitions are linearly extrapolated to zero strain and it is shown that at this point both definitions converge within narrow uncertainty bounds.

2.4.3 Ignition delay time

The ignition delay time (IDT) is an important fuel performance descriptor. It can be described as the time taken for a fuel-oxidiser mixture to react and release heat at a specific temperature and pressure. It has strong links to autoignition phenomena such as knock and superknock [138], which are damaging or catastrophic events in compression ignition (CI) engines. The octane rating is used to describe the autoignition resistance of a fuel and as such numerous researchers have related IDTs with octane ratings: motor and research octane number (MON and RON) and the octane index (OI) [139–141]. These metrics provide convenient points of comparison between real-world fuels and PRFs with direct applicability to the engines. However, Kalghatgi et al. [142, 143] has suggested the inclusion of toluene in PRF blends which allow for a higher sensitivity and allow for both RON and MON matching, where MON measurements of pure PRFs tend to be impacted by NTC behaviour not present in real-world fuels tested under similar conditions [144]. Most crucially in this work, IDTs provide a measure for assessing the validity of a chemical kinetic model. In particular it tests the ability of a chemical mechanism to reproduce oxidation behaviour at elevated pressures across a wide range of temperatures.

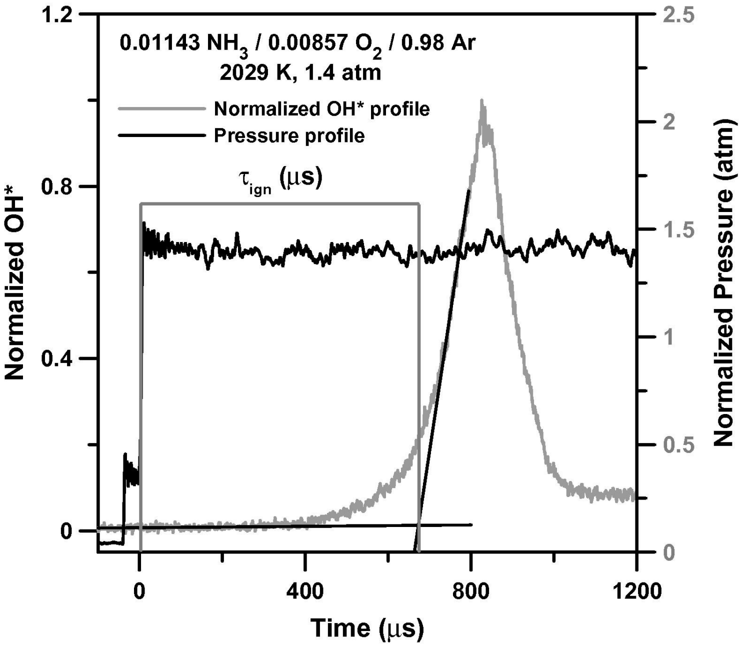

Figure 2.7: Typical temporal pressure and OH* chemiluminescence plot including the back tangent extrapolation and definition of the ignition delay time (τ_{ign}). From [37].

Shock tubes and rapid compression machines are the primary apparatus used in measuring ignition delay times experimentally. Many high quality recent IDT measurements have been obtained using shock tubes [37, 38], therefore the experimental procedure for these is described briefly. A shock wave is created when a diaphragm separating an inert, low molecular weight gas (on the driver side) perforates, which then propagates through the test mixture (on the driven side) raising the temperature and pressure almost instantaneously. When this shock reaches the end wall it reflects back further raising the temperature and pressure and effectively stagnating the test gas [39]. The shock tube is capable of operating over a wide temperature (500 to over 10,000 K) and pressure (0.01 to over 1000 atm) range. It is in the end wall region that measurement apparatus are located, for collecting the temporal pressure signal and the concentrations of key species. Such an approach is adopted in the implementation of HyChem (see Section 2.3.2) [77], where the time dependent evolution of species is used to define global reaction rates. The IDT is subsequently determined based on the time between the arrival of the reflected shock and the intersection of the tangent to the steepest gradient of the chemiluminescence signal and the zero-concentration level [37, 38]. Common species' profiles to track include the hydroxyl (OH^*) and the methylidyne (CH^*) radicals [140]. A typical temporal plot used for defining the IDT is shown in Fig. 2.7, where the aforementioned definition of the IDT is shown by τ_{ign}. Recent work by Davidson et al. [38] has measured IDTs, with uncertainties of ±15%, for gasoline relevant fuels at very high pressures, up to 250 atm, of relevance to modern light- and heavy-duty diesel engines. Studies built on previous work that considered peak pressures around 60 atm [139–141].

The current shock tube computations (see Section 2.1) the instantaneous equations described in Section 2.2 are applied and two definitions are commonly used to determine the IDT. The first approach considers the heat release, defining the IDT as the time at which the rate of change of temperature is the highest. The second approach tracks the evolution of the species mole fraction and defines the IDT as the time at which the maximum fraction of that species, typically OH, is reached [61]. A process replicating that used experimentally where the steepest gradient of the species profile is extrapolated to zero concentration, as discussed above, can also be implemented computationally.

2.4.4 Flame thickness

The laminar flame thickness (l_F) provides a useful reference parameter for identifying the spatial distribution of a reaction zone. Definitions of l_F can be ambiguous, one approach is to define a thermal thickness. A simple and compact mathematical definition of the flame thickness is:

$$l_F = \frac{D^u_{th}}{S_L} = \frac{\lambda_u}{c_p \rho_u S_L} \tag{2.24}$$

where D_{th} is the thermal diffusivity, which can be re-expressed in terms of the thermal conductivity, λ_u, the specific heat capacity at constant pressure for the unburnt reactants, c_p, and the density of the unburnt reactants, ρ_u. While Eq. 2.24 only requires knowledge of the burning velocity, the result is normally an underprediction by a factor of five [145]. Peters [146] derives a similar relationship from a dimensional argument or from the temperature profile (discussed below) and the flamelet ODE describing it, where the thermal conductivity of the burnt mixture is used instead, λ_b. However, Peters [146] discusses a further improvement using properties determined at the inner layer temperature (T^0):

$$l_F = \frac{(\lambda / c_p)_{T^0}}{\rho_u S_L} \tag{2.25}$$

In the flamelet model, the inner layer occurs after the preheat zone and is where the fuel has been consumed and intermediates are formed, in a subsequent layer their oxidation occurs.

More informative interpretations of the flame thickness use the temperature profile. The simplest application of this approach defines the thickness as the

1-99% temperature rise layer, although in principle the selection of the limits is arbitrary, from the cold reactant temperature (T_C) to the hot product temperature (T_H). This definition is not particularly useful since it provides an overestimate as slow reactions occurring after the reaction zone create a wide temperature profile. A more useful application takes the maximum temperature gradient and the distance between its intersection with T_C and T_H [145, 146]. However, this approach assumes a flamelet structure. As discussed in Section 2.4.1, this assumption breaks down as flow and chemical timescales become comparable and reaction zone broadening is observed, so another flame thickness definition is required. Furthermore, as some flames would be supported by hot combustion products (HCPs) in this study, in order to more clearly define the reaction zone, the 5-95% fuel consumption layer thickness [40] is preferred here, providing a more conservative value for l_F. A selection of these flame thickness definitions is shown in Fig. 2.8.

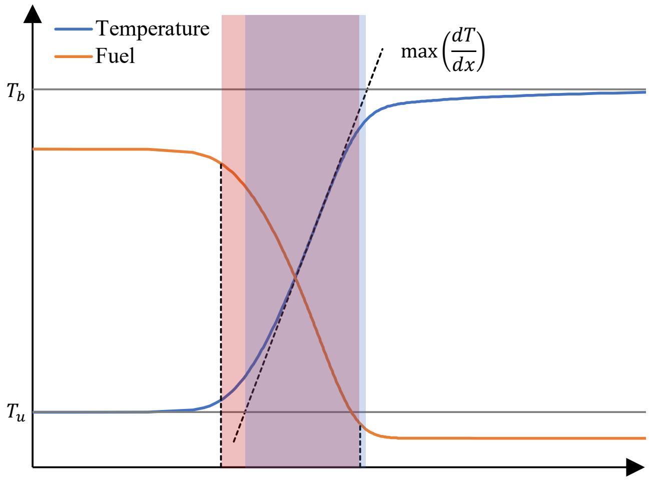

Figure 2.8: Fuel and temperature axial profiles with the 5–95% fuel consumption thickness and the maximum temperature gradient flame thickness portrayed.

Some work [129, 136] has suggested for the inclusion of the flame thickness in the function for burning velocity extrapolation to zero strain. Additionally, the flame thickness is useful for defining the appropriate mesh resolution a priori, sometimes requiring a first computation of the flame or the equilibrium state of the reactants [145] to be applied to the methods discussed above.

2.4.5 Species profiles

Chemical species involved in combustion processes include the reactants, products and intermediates such as unstable radicals. These intermediates are important markers of reaction progress and the state of the flame. As discussed in Section 2.4.1, a flame consists of different zones and within each differing proportions of chemical species are likely to appear; this distinguishes a spatial distribution of chemistry. More generally, as any oxidation process occurs there will be a temporal variation of species, for instance as a fuel is consumed through thermal decomposition and abstraction reactions its concentration will decrease. Quantitative chemical analysis through measuring species profiles is a useful technique for reaction rate determination and more broadly for the validation of chemical mechanisms and their ability to predict emissions of combustion processes. The real-world importance of quantitative chemical analysis has become increasingly relevant over the past half century as pollutant emissions from combustion devices have come under increasing scrutiny.

Experimental techniques can be divided into two categories: invasive and non-invasive measurements. An invasive technique, such as sampling, may interfere with flow and chemistry either through local quenching or impeding the flow. Whereas, a non-invasive technique, such as laser induced fluorescence (LIF), is able to extract information without altering the system. The direct sampling technique has a long history with comprehensive reviews on the technique dating back to the 1960s [147] and molecular beams first suggested in the 1950s by Kantrowitz and Grey [148]. The process involves extracting a sample directly from the position of interest in the form of a so called molecular beam. Before some of this sample is injected into a mass spectrometer for analysis it must in effect be frozen so as to create a snapshot and the molecules spatially distributed. This is achieved by reducing the pressure and temperature in the work of McLean and Sawyer [149] or through aerodynamic quenching and dilution with an inert gas in the more recent work of Shariatmadar et al. [42, 150]. This general technique has been extended to complex extractions of soot particles in turbulent fuel-rich ethylene combustion in order to measure soot particle size distributions [42]. The alternative non-invasive approach uses lasers, LIF, tuned to a specific chemical species excitation energy. The excited species subsequently de-excites and the emission is measured using photodetectors. The method was developed in the 1960s [151, 152] and a comprehensive review for LIF in combustion analysis was presented by Daily [153] in the late 1990s and again more recently by Hanson [154] who discusses the impact of laser diagnostic techniques on chemical kinetic, propulsion and practical energy system studies. The review by Daily [153] on LIF included a discussion on the fundamental physics and experimental considerations and implementation methods. Early uses in combustion applications by Hanson et al. [155] studied nitric oxide absorption for a broad temperature range, 300-4000 K, for combustion studies and the reactions of oxides of nitrogen. Recent applications of LIF were used to measure hydroxyl and formaldehyde concentrations and, along with the velocity field, a multi-fluid statistical analysis was applied to distinguish chemically active fluid states in highly strained, low Damköhler number premixed DME-air flames with external enthalpy support [41]. Other applications involve the measurement of species concentrations for ignition delay time experiments (see Section 2.4.3) and in the development of chemical kinetics by fundamental studies or for global reactions (see HyChem approach in Section 2.3.2).

There are advantages and disadvantages of each method. While laser based diagnostics do not impact the flow and chemistry conditions in the way that sampling may, in order to obtain values for concentrations of species a correlation model must be applied to the signal. This correlation model tends to produce the most significant errors in the stated concentration value [153], whereas sufficiently quenched and diluted samples obtained via a probe technique provide absolute values. In addition, laser based diagnostic techniques can only be used for a limited selection of species both in number and simultaneously, whereas many more components of a sample can in principle be detected in a mass spectrometer. Therefore, both apparatus have inherent uncertainties and both are of significant value in combustion studies and provide validation data for chemical kinetics.

The computation of species profiles comes as a direct result of solving the chemical source term and instantaneous equation discussed in Section 2.2. By solving the time dependent partial differential equations, the species temporal evolution can also be described.

2.5 Shortcomings of kinetic modelling

Chemical kinetic modelling of combustion processes has made significant progress over the last half century and mechanisms for increasingly complex hydrocarbons have been developed (see Section 2.3.2). However, models are not without their limitations. These can be divided into two groups: reaction uncertainties and physicochemical uncertainties.

Large collations and reviews of reaction rate suggestions, both theoretical and experimental, with recommendations made have been conducted by Cohen and Westberg [156, 157], Tsang and co-workers [158–161] and others [162, 163], but arguably most notably by Baulch et al. [164–166]. These have provided an invaluable resource for the development of chemical mechanisms. However, reactions that have not been studied in detail are often inferred by analogy, in the case of large hydrocarbons by using the so called rate rule as discussed by Prager et al. [167]. Wang and Sheen [168] highlight the need for elementary reactions to be studied in well defined experiments and using high-level ab initio theoretical computations. The state of computational chemistry in combustion was reviewed by Klippenstein [169]. He notes the progress in the field over the past two decades and the reduction in uncertainties, for a limited selection of reaction types now as low as 20-30%. Additionally, pressure dependent reactions using the Troe parameterisation [60], discussed in Section 2.3.1, is by design limited and typically incurs deviation from the data of 10-20% [169]. The PLOG method, using logarithmic interpolation, is an improvement with tabulated fits for a range of pressures. However, third body collisions are unaccounted for which can introduce errors [63, 169].

The thermodynamic properties have been collected in databases such as the Third Millennium Ideal Gas and Condensed Phase Database for Combustion originally developed by Burcat [170]. These continue to be updated using the Active Thermochemical Tables (ATcT) which compute high accuracy enthalpies of formation. However, entropies and heat capacities are also requirements for calculating the Gibbs energy and finding the equilibrium constant (see Eqs. 2.16 - 2.18). To this end, more progress is required. Furthermore, modelling reactive-diffusive systems requires knowledge of transport properties such as diffusivity and viscosity. Brown et al. [171] reviewed approximations for various transport properties and outlined recommendations. However, currently comprehensive databases and transport data for radical species remains limited.

As uncertainties in kinetic models prevail analysing these is of key importance to ascertain the reliability of their predictions. To do so, sensitivity analyses are conducted, as reviewed by Turányi [172]. A 'brute-force' technique involves altering one or more parameters in order to determine which reactions are the most critical. Numerically efficient methods exist and that of Stewart and Sørensen [173] was implemented in the ubiquitous combustion modelling software package CHEMKIN. A more advanced approach is the use of formal uncertainty quantification (UQ). Wang and Sheen [168] presented a comprehensive review on UQ methodology and theory. Uncertainty quantification includes the identification and quantification of uncertainties, as well as their minimisation using computational techniques. The overall aim is to reduce the size of the uncertainty surface, or in other words to improve the statistical predictability of the mechanism. Calculating the uncertainties can be done using intrusive or non-intrusive techniques, where intrusive techniques modify the governing equations. The uncertainty minimisation can be done in two ways. The first approach is through experimental and theoretical improvements in rate predictions. However, some uncertainties will prevail with the current best-in-class uncertainty still around $\pm15\%$ [168]. The alternative is the inverse problem approach where parameters, such as IDTs and LBVs, are used to constrain uncertain pathways. However, the experimental data consistency must then be considered [174]. This causes issues in dealing with possible anomalous results as these data points could contain vital information or be genuine outliers due to systematic or other errors.

The most renowned application of combustion kinetic mechanism uncertainty quantification and subsequent mechanism optimisation is GRI-Mech [175] for the combustion of methane. This was achieved using solution mapping, an approach pioneered by Frenklach [176, 177] and discussed in the context of UQ by Wang and Sheen [168]. Different versions were derived for GRI-Mech (2.11 and 3.0, for example) which indirectly highlighted the importance of accurate target data in avoiding optimisation errors, including over-fitting for outliers or inaccurate data [178]. The latter was responsible for the withdrawal of GRI-Mech 2.11, though it continues to see use. However, the application of UQ to more complex hydrocarbons presents a significant challenge due to the increase in the size of the parameter space and the reduction in data availability.

In this work, in-house chemical kinetic mechanisms [64, 179–187] are further developed and refined using recent kinetic evaluations and new experimental data, for the variety of validation parameters discussed above. The kinetic mechanisms rely on best available independent datasets and have not been optimised to target limited data points, such as LBVs and IDTs, in order to avoid bias and errors associated with individual datasets. However, the key sensitivities have been identified and adjustments within the uncertainty bounds have been made as deemed necessary.

Chapter 3 | Primary reference fuels

This chapter evaluates a mechanism for both primary reference fuels (PRFs), iso-octane and n-heptane. Sub-mechanisms for both fuels were appended to a detailed H/C_1-C_2 sub-mechanism and validated using ignition delay time, laminar burning velocity and speciation experimental data. Fundamental species and assumptions are discussed alongside the key reactions and sensitivities.

3.1 Background

Primary reference fuels provide a crucial starting point for the development of surrogate fuels to be studied experimentally and numerically as chemical or physical simplifications of a fully-blended fuel, such as petrol or diesel [188, 189]. Such surrogate fuels may be single component or significantly larger and more complex. Iso-octane is a primary reference fuel (PRF) and has been used as a benchmark for comparing the autoignition properties of fuels through the use of the octane number, for which iso-octane is assigned a value of 100 indicating its high autoignition resistance. By contrast, n-heptane, another PRF, was assigned an octane number of zero or a cetane number of 54 to indicate its high propensity to auto-ignite [190]. Both PRFs provide useful and frequent base components for surrogate fuels, in particular for binary blends to achieve variable octane number surrogates [191].

Historically, two ignition methods have been utilised in internal combustion engines (ICEs): the use of a pilot in the spark ignition (SI) engine and autoignition under high compression ratios in the compression ignition (CI) engine. Within SI internal combustion engines, prevention of autoignition is paramount to avoid the destructive processes of knock and super knock [138]. Both are autoignition phenomena but occur under differing conditions. Knock occurs during the expansion stroke, where the end gas ignites before the flame brush has reached it, which may not cause engine damage. Whereas, super knock is a pre-ignition phenomena where the charge ignites during the compression stroke resulting in a pressure spike and causing guaranteed engine damage [138, 192]. Willand et al. [193] identified three contributing factors to super knock: oil droplets or deposits (lubricants), hot spots in the cylinder and the reaction kinetics of the fuel and lubricants. In an effort to increase engine efficiency and reduce pollutant emissions, current SI engine trends show increased use of downsizing, turbocharging and the use of exhaust gas recirculation (EGR). However, all these create more favourable conditions for autoignition [192]. Uncontrolled autoignition events can lead to excessive component wear or catastrophic engine failure, as outlined above. By contrast, CI internal combustion engines operate at higher thermal efficiencies than SI engines as a direct result of the higher compression ratios used [194]. As no piloting is used, the autoignition properties of the fuel are crucial to control to ensure ignition when the fuel is sprayed into the cylinder near the top of the compression stroke.

Novel engine technologies, such as homogeneous charge compression ignition (HCCI), combine aspects of SI and CI engines relying on a premixed charge and controlled autoignition (CAI) event. HCCI engines can achieve CI engine-like efficiencies but with reduced production of nitrogen oxides and particulate matter [195] due to lower in-cylinder temperatures and a lean premixed charge. CAI engine technologies necessitate an understanding of fuel properties and chemistry-flow interactions impacted by pressure and temperature histories within the cylinder. Therefore, through coupled design of fuels and engines the greatest scope for future improvements in efficiencies and emissions is possible [196]. This process requires fully validated accurate chemical kinetic models for the PRFs of a size that can be applied using accurate computational methods. Such mechanisms serve as underpinning components in surrogate fuels capable of being used in the modelling of highly dynamic systems.

3.2 Iso-octane

3.2.1 Introduction

Iso-octane (C_8H_{18}), is a primary reference fuel and the basis for fuel metrics relevant to SI engine selection. It has been used in surrogate fuels for modelling petrol and will continue to be a significant component in the modelling of future alternative automotive fuels, particularly within engines relying on CAI technologies. Therefore, the accurate prediction of the thermal behaviour of iso-octane under engine specific operating conditions is critical. In particular, the reactivity of the fuel, assessed via the prediction of global variables, burning velocities and ignition delay times, must first be validated for a range of temperatures, pressures and stoichiometries. This must be supplemented with the ability to accurately predict species profiles for the quantification and subsequent limitation of engine emissions. Additionally, a compact chemical kinetic mechanism is crucial for turbulent flame computations of realistic engine conditions when utilising a transported probability density function (PDF) method [197] which includes the chemistry without approximations.

Large and detailed iso-octane kinetic models, encapsulating both high and low temperature behaviour, have been developed extensively [67, 68, 198], containing over 2500 chemical species. Such mechanisms provide a useful framework for the development of simplified schemes through the identification and extraction of key reaction steps while still maintaining accurate prediction of fuel behaviour. However, they are inappropriate for rapid calculation of key parameters such as laminar burning velocities, or to be applied in more complex computations including turbulence-chemistry interactions. To meet the dual requirements of accurate chemical modelling and computational efficiency, reduced iso-octane mechanisms were initially explored by Davis and Law [199] who focused on high temperature elementary iso-octane reactions. More recently, Ra and Reitz [200] developed a skeletal mechanism for PRFs and the iso-octane sub-mechanism contained 36 species and 54 reactions. This kinetic reduction was conducted using isomer lumping and reaction elimination. Reaction kinetics were then tuned to fit ignition delay times. An alternative approach, HyChem (Hybrid Chemistry), pioneered by Wang et al. [77], creates compact chemical mechanisms for the high temperature combustion of large hydrocarbons through the use of experimentally determined lumped reaction steps producing fuel pyrolysis products. The method has been applied to a range of fuels, including gasoline surrogates. This work applies a similar methodology, using the rapid decomposition hypothesis [74], to remove almost all C_3 to C_7 species and isomer lumping of iso-octane pyrolysis products such as the iso-octyl (C_8H_{17}) and butyl (C_4H_9) radicals in order to create a compact mechanism which will provide time efficient computations, without negatively impacting prediction performance.

This work aims to produce an iso-octane sub-mechanism compact enough to feasibly be used in turbulent flame computations under engine relevant conditions. In addition, with new low temperature and high pressure shock tube data available [201] the mechanism is extended and validated at lower temperatures, where the effects of high preheat conditions, such as those produced by EGR, are relevant. The key kinetic sensitivities within the sub-mechanism will also be highlighted.

3.2.2 Iso-octane chemical mechanism

An iso-octane sub-mechanism containing 57 reactions and 18 chemical species, shown in Table 3.1 was used within a mechanism containing a total of 383 reactions and 68 chemical species. A rapid-decomposition approach [74], discussed previously in Section 2.3.2, was adopted in order to remove (almost all) higher hydrocarbons with between three and seven carbon atoms as the hypothesis states that higher hydrocarbons exist only in low concentrations. Propene is a possible addition and related work (e.g. HyChem [78]) includes a sub-mechanism for it. Only the thermal decomposition, abstraction and low temperature products of iso-octane were considered down to species still containing eight carbon atoms, with the exception of the butyl radical (C_4H_9), iso-butene (i-C_4H_8) and hexanal ($C_5H_{11}CHO$). A detailed C_1, C_2 and hydrogen sub-mechanism was used alongside the simplified iso-octane mechanism (shown in Appendix A). The former can also be reduced for greater compactness, or an alternative selected. The simplified PRF mechanisms were developed on the basis of the work pursued by Curran et al. [65, 67] with revisions and simplifications introduced by Lindstedt [202, 203] for heavy alkanes and lightly branched Gas to Liquid (GTL) fuels. The mechanisms were subsequently revised by Pimentel de Lamo and Lindstedt [204] for PRF fuels with the intention of modelling proprietary IQT data provided by BP.

Table 3.1: Final simplified iso-octane sub-mechanism applied in the current work. Forward rate constants as $k_f = AT^n e^{-E_a/RT}$. Units: kg, m, s, kmol, kJ, K.

No.	Reaction	A	n	E_a	Ref.
3.1	$C_8H_{18} \rightleftharpoons$ 4-C_8H_{17} + H	3.348×10^{19}	-0.94	3.992×10^{5}	adj. [198]
3.2	$C_8H_{18} \rightleftharpoons$ 1-C_8H_{17} + H	1.724×10^{18}	-0.36	4.234×10^{5}	adj. [198]
3.3a	$C_8H_{18} \rightarrow 2\,C_2H_5 + 2\,C_2H_4$	2.346×10^{30}	-3.92	3.521×10^{5}	adj. [198]
3.3b	$C_8H_{18} \rightarrow C_4H_9 + C_2H_5 + C_2H_4$	2.346×10^{30}	-3.92	3.521×10^{5}	adj. [198]
3.3c	$C_8H_{18} \rightarrow 2\,C_4H_9$	2.346×10^{30}	-3.92	3.521×10^{5}	adj. [198]
3.4	C_8H_{18} + H $\rightleftharpoons$ 4-C_8H_{17} + H_2	6.020×10^{2}	2.40	1.081×10^{4}	[198]
3.5	C_8H_{18} + H $\rightleftharpoons$ 1-C_8H_{17} + H_2	7.341×10^{2}	2.76	3.409×10^{4}	[198]
3.6	C_8H_{18} + OH $\rightleftharpoons$ 4-C_8H_{17} + H_2O	1.700×10^{3}	1.90	-6.070×10^{3}	[198]
3.7	C_8H_{18} + OH $\rightleftharpoons$ 1-C_8H_{17} + H_2O	2.630×10^{4}	1.80	6.067×10^{3}	[198]
3.8	C_8H_{18} + O $\rightleftharpoons$ 4-C_8H_{17} + OH	3.830×10^{2}	2.41	4.770×10^{3}	[198]
3.9	C_8H_{18} + O $\rightleftharpoons$ 1-C_8H_{17} + OH	8.550	3.05	1.307×10^{4}	[198]
3.10	C_8H_{18} + CH_3 $\rightleftharpoons$ 4-C_8H_{17} + CH_4	6.010×10^{-12}	6.36	3.736×10^{3}	[198]
3.11	C_8H_{18} + CH_3 $\rightleftharpoons$ 1-C_8H_{17} + CH_4	4.257×10^{-16}	8.06	1.738×10^{4}	[198]
3.12	C_8H_{18} + O_2 $\rightleftharpoons$ 4-C_8H_{17} + HO_2	7.000×10^{9}	0.00	1.930×10^{5}	[198]
3.13	C_8H_{18} + O_2 $\rightleftharpoons$ 1-C_8H_{17} + HO_2	1.320×10^{11}	0.00	2.124×10^{5}	adj. [198]
3.14	C_8H_{18} + HO_2 $\rightleftharpoons$ 4-C_8H_{17} + H_2O_2	4.332	3.01	5.059×10^{4}	[198]

Table 3.1 (Continued)

No.	Reaction	A	n	E_a	Ref.
3.15	$C_8H_{18} + HO_2 \rightleftharpoons 1\text{-}C_8H_{17} + H_2O_2$	0.612	3.59	7.180×10^4	[198]
3.16	$4\text{-}C_8H_{17} \rightarrow C_4H_9 + C_2H_4 + C_2H_4$	7.500×10^{21}	-2.70	1.354×10^5	adj. [205]
3.17	$1\text{-}C_8H_{17} \rightarrow C_4H_8 + C_2H_5 + C_2H_4$	9.000×10^{16}	-1.30	1.249×10^5	adj. [205]
3.18	$4\text{-}C_8H_{17} \rightleftharpoons C_8H_{16} + H$	8.995×10^{11}	0.59	1.554×10^5	[198]
3.19	$1\text{-}C_8H_{17} \rightleftharpoons C_8H_{16} + H$	3.000×10^{13}	0.00	1.691×10^5	[202, 203]
3.20	$1\text{-}C_8H_{17} \rightleftharpoons 4\text{-}C_8H_{17}$	3.710×10^{11}	0.00	8.535×10^4	[198]
3.21	$4\text{-}C_8H_{17} + O_2 \rightleftharpoons C_8H_{16} + HO_2$	1.000×10^6	0.00	1.465×10^4	[202, 203]
3.22	$1\text{-}C_8H_{17} + O_2 \rightleftharpoons C_8H_{16} + HO_2$	4.000×10^6	0.00	1.465×10^4	[202, 203]
3.23	$4\text{-}C_8H_{17} + O_2 \rightleftharpoons 4\text{-}C_8H_{17}OO$	1.300×10^{10}	0.00	0	adj. [198]
3.24	$1\text{-}C_8H_{17} + O_2 \rightleftharpoons 1\text{-}C_8H_{17}OO$	4.520×10^9	0.00	0	[198]
3.25	$4\text{-}C_8H_{17}OO \rightleftharpoons 4\text{-}C_8H_{16}OOH$	1.406×10^{10}	0.00	9.184×10^4	[198]
3.26	$4\text{-}C_8H_{16}OOH \rightleftharpoons C_8H_{16} + HO_2$	4.500×10^{12}	0.00	1.088×10^5	[202, 203]
3.27	$4\text{-}C_8H_{16}OOH \rightleftharpoons C_8H_{16}O + OH$	1.800×10^{12}	0.00	9.205×10^4	[198]
3.28	$4\text{-}C_8H_{16}OOH \rightarrow C_2H_4 + C_5H_{11}CHO + OH$	5.567×10^{21}	-2.40	1.135×10^5	adj. [198]
3.29	$4\text{-}C_8H_{16}OOH + O_2 \rightleftharpoons 4\text{-}C_8H_{17}O_4$	4.520×10^9	0.00	0	[198]
3.30	$4\text{-}C_8H_{17}O_4 \rightleftharpoons C_8H_{16}O_4H$	2.000×10^{11}	0.00	4.650×10^4	[202, 203]
3.31	$1\text{-}C_8H_{17}OO \rightleftharpoons 1\text{-}C_8H_{16}OOH$	1.000×10^{10}	0.00	1.004×10^5	adj. [198]
3.32	$1\text{-}C_8H_{16}OOH \rightleftharpoons C_8H_{16} + HO_2$	4.500×10^{12}	0.00	1.088×10^5	adj. [206]
3.33	$1\text{-}C_8H_{16}OOH \rightleftharpoons C_8H_{16}O + OH$	3.000×10^{11}	0.00	5.963×10^4	adj. [67, 206]
3.34	$1\text{-}C_8H_{16}OOH \rightarrow C_2H_4 + C_5H_{11}CHO + OH$	1.000×10^{13}	0.00	1.067×10^5	adj. [206]
3.35	$1\text{-}C_8H_{16}OOH + O_2 \rightleftharpoons 1\text{-}C_8H_{17}O_4$	4.520×10^9	0.00	0	[198]
3.36	$1\text{-}C_8H_{17}O_4 \rightleftharpoons C_8H_{16}O_4H$	2.000×10^{11}	0.00	4.650×10^4	[202, 203]
3.37	$C_8H_{16}O_4H \rightleftharpoons C_8H_{15}O_3H + OH$	1.250×10^{10}	0.00	7.301×10^4	[198]
3.38	$C_8H_{15}O_3H \rightarrow CH_2CHO + C_5H_{11}CHO + OH$	1.500×10^{16}	0.00	1.632×10^5	adj. [198]
3.39	$C_8H_{16}O \rightarrow C_2H_4 + C_5H_{11}CHO$	3.400×10^{13}	0.00	2.419×10^5	adj. [207]
3.40	$C_8H_{16}O + H \rightarrow C_4H_8 + C_2H_4 + CH_2CHO + H_2$	2.740×10^4	2.00	2.092×10^4	[202, 203]
3.41	$C_8H_{16}O + O \rightarrow C_4H_8 + C_2H_4 + CH_2CHO + OH$	7.800×10^{10}	0.00	2.176×10^4	[202, 203]
3.42	$C_8H_{16}O + OH \rightarrow C_4H_8 + C_2H_4 + CH_2CHO + H_2O$	7.800×10^3	2.00	-3.201×10^3	[202, 203]
3.43	$C_8H_{16}O + HO_2 \rightarrow C_4H_8 + C_2H_4 + CH_2CHO + H_2O_2$	1.200×10^9	0.00	6.485×10^4	[202, 203]
3.44	$C_8H_{16}O + CH_3 \rightarrow C_4H_8 + C_2H_4 + CH_2CHO + CH_4$	6.000×10^8	0.00	4.602×10^4	[202, 203]
3.45	$C_8H_{16} \rightarrow C_4H_8 + C_4H_8$	1.000×10^{15}	0.00	3.420×10^5	[202, 203]
3.46	$C_8H_{16} + H \rightleftharpoons C_8H_{15} + H_2$	8.000×10^{10}	0.00	1.423×10^4	adj. [67, 206]

Table 3.1 (Continued)

No.	Reaction	A	n	E_a	Ref.
3.47	$C_8H_{16} + O \rightleftharpoons C_8H_{15} + OH$	4.000×10^{10}	0.00	1.674×10^{4}	adj. [67]
3.48	$C_8H_{16} + O \rightarrow C_2H_4 + C_5H_{11}CHO$	3.620×10^{3}	1.88	7.600×10^{4}	[202, 203]
3.49	$C_8H_{16} + OH \rightleftharpoons C_8H_{15} + H_2O$	2.000×10^{10}	0.00	1.088×10^{4}	adj. [206]
3.50	$C_8H_{16} + CH_3 \rightleftharpoons C_8H_{15} + CH_4$	2.000×10^{8}	0.00	2.847×10^{4}	adj. [67, 206]
3.51	$C_8H_{16} + HO_2 \rightleftharpoons C_8H_{16}O + OH$	1.000×10^{9}	0.00	6.025×10^{4}	adj .[67]
3.52	$C_8H_{16} + HO_2 \rightarrow C_2H_4 + C_5H_{11}CHO + OH$	1.000×10^{9}	0.00	6.000×10^{4}	[202, 203]
3.53	$C_8H_{15} \rightarrow C_4H_9 + C_2H_4 + C_2H_2$	2.000×10^{13}	0.00	1.681×10^{5}	[202, 203]
3.54	$C_8H_{15} + O_2 \rightarrow 2\,CH_2CHO + C_2H_4 + C_2H_5$	1.640×10^{18}	-2.78	1.056×10^{4}	[202, 203]
3.55	$C_5H_{11}CHO \rightarrow CH_2CHO + C_4H_9$	1.000×10^{13}	0.00	1.208×10^{5}	adj. [208]
3.56a	$2\,C_4H_9 \rightarrow 3\,C_2H_4 + 2\,CH_3$	2.000×10^{13}	0.00	1.253×10^{5}	adj. [159]
3.56b	$2\,C_4H_9 \rightarrow 3\,C_2H_4 + 2\,CH_3$	9.504×10^{10}	0.77	1.284×10^{5}	adj. [209]
3.56c	$C_4H_9 \rightarrow C_2H_5 + C_2H_4$	3.504×10^{11}	0.46	1.233×10^{5}	[198]
3.57	$C_4H_8 \rightarrow C_2H_4 + C_2H_4$	1.000×10^{13}	0.00	2.573×10^{5}	[210]

Iso-octane thermal decomposition: Iso-octane thermally decomposes to form the iso-octyl radicals (C_8H_{17}) and a hydrogen radical in (R3.1) and (R3.2), in addition to the irreversible rapid decomposition global steps included in (R3.3), with all rates increased by a factor of three from those in the work of Mehl et al. [198]. The rates adapted from Mehl et al. [198] in all cases use only the forward rate constants with the reverse rates calculated *in-situ* using the equilibrium constant, as discussed in Section 2.3. The increased rates were justified due to the use of isomer lumping for the various forms of the iso-octyl radicals, as discussed below. The rapid decomposition approach was tested to varying extents, as shown in Reactions (R3.3a-c). Three different product distributions were studied with increased proportion of butyl radical (C_4H_9) formation, which will subsequently be referred to by their corresponding reaction number as they appear in Reaction (R3.3) below and in Table 3.1. The rate expression used for (R3.3a)-(R3.3c) was adapted from Mehl et al. [198] for the reaction: $C_8H_{18} \rightleftharpoons$ i-C_4H_9 + t-C_4H_9. The various isomers of the butyl radical, iso- and tert-, were lumped together and will subsequently be referred to as the butyl radical (C_4H_9).

$$C_8H_{18} \longrightarrow 2\,C_2H_5 + 2\,C_2H_4 \tag{R3.3a}$$

$$C_8H_{18} \longrightarrow C_4H_9 + C_2H_5 + C_2H_4 \tag{R3.3b}$$

$$C_8H_{18} \longrightarrow 2\,C_4H_9 \tag{R3.3c}$$

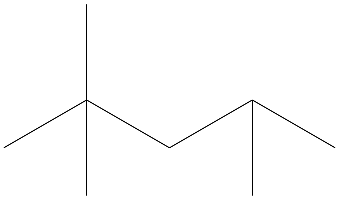

Figure 3.1: Iso-octane (2,2,4-trimethylpentane, C_8H_{18}).

The functional form of iso-octane (C_8H_{18}), 2,2,4 trimethylpentane, is shown in Figure 3.1. The thermal decomposition of C_8H_{18} in (R3.3) involves breaking the C−C bond (β-scission) between carbon 2 and 3 to form two molecules of the butyl radical. Both the iso- and tert-butyl radical would be formed, shown in Figure 3.2. For simplicity and reduced computational cost, this model uses isomer lumping and only includes one species for both C_4H_9 isomers. For the product distributions in reactions (R3.3a) and (R3.3b), subsequent rapid decomposition of the butyl radical produces ethylene (C_2H_4) and the ethyl radical (C_2H_5), shown in Figure 3.3. Physically, this would proceed via two steps, possibly requiring internal rearrangement, but was selected for expediency in the fuel decomposition to lighter hydrocarbon products. The thermal decomposition products of C_4H_9 are discussed in greater detail later.

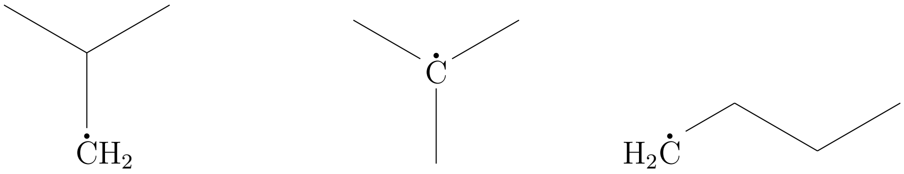

(a) Iso-butyl radical (i-C_4H_9). (b) Tert-butyl radical (t-C_4H_9). (c) 1-butyl radical (1-C_4H_9).

Figure 3.2: Butyl radicals.

(a) Ethylene (C_2H_4). (b) Ethyl radical (C_2H_5).

Figure 3.3: Thermal decomposition products.

Iso-octane hydrogen abstraction: Additionally, fuel consumption via hydrogen abstraction was included in (R3.4)–(R3.15) with rate expressions taken from Mehl et al. [198] and for (R3.13) increased by a factor of two. Abstractors included are H, OH, O, CH_3, O_2 and HO_2 and the iso-octyl radical is produced in each case. There are four possible isomers of the iso-octyl radical, shown in Figure 3.4. Structurally, there are similarities between a-C_8H_{17} and d-C_8H_{17} with the methyl radical group, and between b-C_8H_{17} and c-C_8H_{17} with the free radical site protected on a primary chain carbon. Therefore, only a-C_8H_{17} and c-C_8H_{17} were included in the scheme as lumped species, which are subsequently referred to as 1-C_8H_{17} and 4-C_8H_{17}, respectively.

Iso-octyl radical consumption: In reactions (R3.16)–(R3.19) the thermal decomposition of 1-C_8H_{17} and 4-C_8H_{17} is included. Reactions (R3.16) and (R3.17) are irreversible rapid decomposition reactions and were adapted from the work conducted by Kelley et al. [205]. Reactions (R3.16) and (R3.17) were based on 4-C_8H_{17} $\rightleftharpoons$ t-C_4H_9 + i-C_4H_8 and 1-C_8H_{17} $\rightleftharpoons$ x-C_7H_{14} + CH_3 respectively, where i-C_4H_8 is iso-butene and x-C_7H_{14} is 2,4-dimethyl-1-pentene, shown in Figure 3.6. Since the rapid decomposition hypothesis is applied here, these reactions were selected as a placeholder for a more complete sub-mechanism that could include C_3–C_7 species. In order to achieve this, a reaction rate in literature with a similar product distribution to the desired global step was selected so that activation energy barriers would remain appropriate for the isomer lumped and altered, irreversible rapid decomposition step. Iso-butene has an enthalpy of formation of -17.9 kJ/mol, the most exothermic and therefore favourable of the C_4H_8 isomers [211]. The decomposition of iso-butene to two ethylene molecules, while not physically realistic without internal rearrangement, was selected for expediency. Refinement can be introduced via an appropriate sub-mechanism, if desired. The iso-butyl radical, i-C_4H_9, is the least stable of the butyl radicals [161] and as such the rapid decomposition approach was utilised and the product distribution was adapted to include its decay into C_2H_4 and C_2H_5 as was also applied with reactions (R3.3a) and (R3.3b), in accordance with the rapid decomposition hypothesis [73, 212].

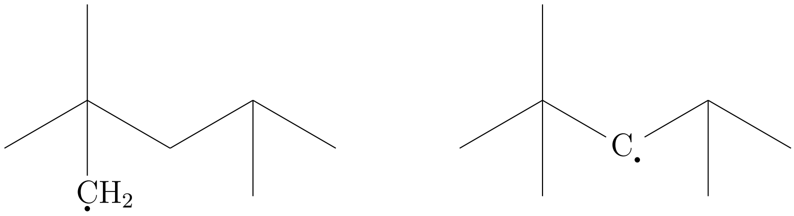

(a) (1) a-C_8H_{17}. (b) b-C_8H_{17}.

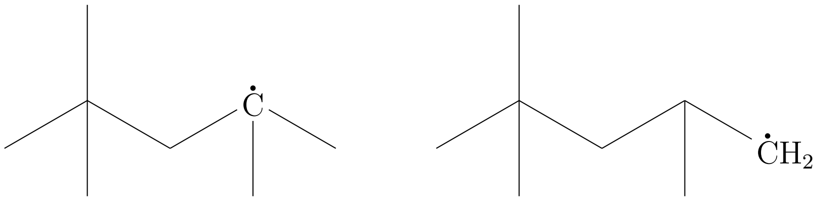

(c) (4) c-C_8H_{17}. (d) d-C_8H_{17}.

Figure 3.4: Iso-octyl radicals

$$\text{4-}C_8H_{17} \longrightarrow C_4H_9 + 2\,C_2H_4 \tag{R3.16}$$

$$\text{1-}C_8H_{17} \longrightarrow C_4H_8 + C_2H_5 + C_2H_4 \tag{R3.17}$$

$$\text{1-}C_8H_{17} \rightleftharpoons \text{4-}C_8H_{17} \tag{R3.20}$$

Two further thermal decomposition reactions of the iso-octyl radicals were included. Reactions (R3.18) and (R3.19) both produce octene (C_8H_{16}) and a hydrogen radical. The rate expression for 4-C_8H_{17} thermal decomposition in (R3.18) was taken from [198], while the equivalent reaction was not included for 1-C_8H_{17} and was added in the work of Lindstedt [202, 203]. Reaction (R3.19) is approximately a factor of ten slower than (R3.18) at 1000 K. The primary consumption pathway of 1-C_8H_{17} is its isomerisation reaction, (R3.20), to form 4-C_8H_{17} using the rate from Mehl et al. [198]. The remaining iso-octyl radical consumption pathways include its reaction with molecular oxygen to form octene and the hydroperoxyl radical (HO_2) (R3.21) and (R3.22) in addition to the low temperature oxidation reactions discussed below.

Consumption of other C_8 species: Octyl species with 16 or fewer hydrogen atoms produced either from iso-octyl radical thermal decomposition or abstraction reactions rapidly thermally decompose to C_4H_8 (R3.45) or form C_8H_{15} in an abstraction reaction with H, O, OH or CH_3 forming H_2, OH, H_2O or CH_4 in addition, respectively (R3.46-47), (R3.49-50). A consumption reaction of C_8H_{16} with atomic oxygen (R3.48) and HO_2 (R3.52) is included forming C_2H_4, $C_5H_{11}CHO$ and OH. Another reaction with HO_2 forms an ether ($C_8H_{16}O$) and OH (R3.52), the consumption of ether chemical species is discussed below. The C_8H_{15} formed from the abstraction of C_8H_{16} rapidly decomposes to C_4H_9, C_2H_4 and C_2H_2 (R3.53) or reacts with molecular oxygen to form CH_2CHO, C_2H_4 and C_2H_5 (R3.54).

Low temperature chemistry: The low temperature chemistry occurs almost independently of the high temperature scheme accounting for different ignition stages. It is of crucial importance for accurate prediction of the negative temperature coefficient (NTC) region, where reduction in temperature results in reduced ignition delay times and sustained ignition down to temperatures as low as a few hundred kelvin. The relevant low temperature oxidation reactions were based on the work of Curran et al. [67] and reduced and applied by Lindstedt [202, 203]. Reactions (R3.23) – (R3.44) encapsulate the simplified low temperature chemistry included in the iso-octane sub-mechanism. Reactions (R3.23,R3.24) are the oxidation of the iso-octyl radicals to form the respective alkylperoxy radicals ($Q-O_2$, where Q represents an alkyl chain). These in turn isomerise to form hydroperoxy-alkyl radicals (Q-OOH) in reactions (R3.25,R3.31). The hydroperoxy-alkyl radicals can be consumed in a variety of reactions, including: thermal decomposition to form an olefin (octene) (R3.26,R3.32), a cyclic ether (R3.27,R3.33) or with the rapid decomposition hypothesis to form C_2H_4, $C_5H_{11}CHO$ and OH (R3.28,R3.34) or by reacting with molecular oxygen to form an peroxy-alkyl hydroperoxide radical (OOQOOH or QO_4) (R3.29,R3.35). The peroxy-alkyl hydroperoxide radical isomerises to form a alkyl-dihydroperoxides species QO_4H (R3.30,R3.36), which can be considered as an intermediate in the $QO_4 \rightleftharpoons QO_3H + OH$ reaction. The alkyl-dihydroperoxide species decomposes to form a ketohydroperoxide (QO_3H) and a hydroxyl radical (R3.37). The ketohydroperoxide rapidly decomposes to form CH_2CHO, $C_5H_{11}CHO$ and OH (R3.38). The ether formed from decomposition of the hydroperoxy-alkyl radical can rapidly decompose to C_2H_4 and $C_5H_{11}CHO$ (R3.39) or abstract with H, O, OH, HO_2 or CH_3 to form a combination of C_4H_8, C_2H_4, CH_2CHO, H_2, OH, H_2O, H_2O_2 and CH_4 (R3.39-44). The naming convention for the low temperature species has drawn on the work of Curran et al. [65, 67] and Atef et al. [68].

(a) Alkylperoxy radical ($C_8H_{17}OO$).

(b) Hydroperoxy-alkyl radical ($C_8H_{16}OOH$).

(c) Peroxy-alkyl hydroperoxide radical ($C_8H_{17}O_4$).

(d) Alkyl dihydroperoxide ($C_8H_{16}O_4H$).

Rapid decomposition intermediates consumption: Three rapid decomposition intermediates, i.e. species with fewer than eight but greater than two carbon atoms,

(e) Ketohydroperoxide ($C_8H_{15}O_3H$).

(f) Cyclic ether ($C_8H_{16}O$).

Figure 3.5: Example iso-octane low temperature oxidation species, showing the defining functional group in each case.

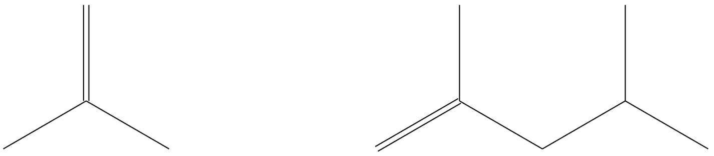

(a) Iso-butene (i-C_4H_8)

(b) 2,4-dimethyl-1-pentene (x-C_7H_{14})

Figure 3.6: Iso-octyl radical thermal decomposition products.

are included in the sub-mechanism. Hexanal rapidly decomposes to CH_2CHO and the butyl radical (R3.55). Two different pathways were explored for butyl radical thermal decomposition, as shown in reactions (R3.56) and three different rates were explored [159, 198, 209]. For reaction R3.56c the isomer of C_4H_9 quoted in literature was 1-butyl radical, in contrast to reaction R3.56a (and also (R3.56b)) which describes the thermal decomposition of the iso-butyl radical. All butyl radical isomers are shown in Figure 3.2. To form C_2H_4 and C_2H_5, the 1-butyl radical would split at the C−C bond between the second and third carbon. Whereas, the decomposition product distribution was altered for reaction R3.56a. The original product distribution described by Tsang [159] and Curran [209] was: i-$C_4H_9 \rightleftharpoons C_3H_6 + CH_3$. Propene ($C_3H_6$) was removed from the mechanism for similar computational benefits to the lumping of butyl radical isomers into a single species. A complete propane and propene combustion and pyrolysis mechanism was developed by, for example, Westbrook and Pitz [213] which contained 163 elementary reactions and 41 chemical species, of which 12 species contained three or more carbon atoms and were therefore amongst the chemical species excluded from this study. Additionally, as discussed by Warnatz [73, 212], the only relevant reaction of the alkyl radical product of an alkane hydrogen abstraction reaction is its subsequent thermal decomposition via an alkene to ultimately form methyl and ethyl radicals. Thus, for simplicity the lumped iso- and tert-butyl radicals were decomposed to C_2H_4 and CH_3 according to R3.56a, which physically would require internal rearrangement to proceed. The various rate constants are shown in Table 3.1. The rapid decomposition of C_4H_8 follows the recommendation of Bryce and Kebarle [210] and forms two molecules of ethylene (R3.57). The above approximations can be directly replaced by sub-mechanisms including more detailed C_3 - C_7 chemistry.

$$\text{i-C}_4\text{H}_9 \longrightarrow 1.5\,\text{C}_2\text{H}_4 + \text{CH}_3 \tag{R3.56a}$$

$$\text{1-C}_4\text{H}_9 \longrightarrow \text{C}_2\text{H}_5 + \text{C}_2\text{H}_4 \tag{R3.56c}$$

3.2.3 Computational methods

The calculation methods applied to compute the shock tube, stirred reactor and the counterflow and freely propagating flames data sets have been described in Section 2.2.1 and in past work (e.g. [56, 180, 214–216]) and are discussed only briefly. The shock tube and stirred reactor data sets were computed as zero-dimensional, homogeneous, adiabatic and isobaric [217] using time steps in the range 10 to 100 ns. Premixed counterflow flames were used for the laminar burning velocity computations. Rates of strain were maintained below 150 s^{-1} to minimise the impact of stretch effects. Local grid refinement according to the derivative of the heat release was used, resulting in cell sizes from 2 μm in the reaction zone up to 5 mm at the inlets.

3.2.4 Iso-octane mechanism sensitivities

3.2.4.1 Iso-octane thermal decomposition

The laminar burning velocity was compared for three equivalence ratios - fuel lean, stoichiometric and rich - for flames with an inlet temperature of 358 K and pressure of 1 atm. The results are presented in Table 3.2. All three mechanisms were identical, with the exception of the product distribution for the thermal decomposition of iso-octane according to reactions (R3.3a-c), and included C_4H_9 thermal decomposition according to reaction (R3.56a) using the adjusted rate from Curran [209]. The laminar burning velocities for iso-octane, presented in Table 3.2, were calculated in a counterflow burner geometry and computed from the average of the reaction rate integral velocity for iso-octane and the minimum velocity ahead of the flame front at each stoichiometry.

Table 3.2: Laminar burning velocities of iso-octane/air flames at atmospheric pressure with inlet temperature of 358 K at different stoichiometric conditions comparing the mechanisms with differing iso-octane thermal decomposition products. Experiment data from: [218–222].

Equivalence ratio, ϕ	Laminar burning velocity [cm/s]			
	Experiments	(R3.3a)	(R3.3b)	(R3.3c)
0.7	22 - 27	23.2	23.3	23.4
1.0	44 - 48	44.1	44.8	45.3
1.3	35 - 42	38.5	39.4	39.4

All product distributions resulted in good agreement within the range of experimental data from literature. The formation of C_4H_9, produced by the thermal decomposition of iso-octane, effectively acts as a buffer to the subsequent production of lighter C_2 hydrocarbons. However, the burning velocity tends to remain very similar or increase somewhat for richer mixtures depending on the choice made. The radical pool size has a significant impact on the burning velocity. Since the butyl radical decomposed to form the methyl radical in addition to ethylene, its concentration was impacted by the fuel thermal decomposition product distribution. Considering $\phi = 1.0$, when compared to reaction (R3.3a) the concentration of C_4H_9 in the flame increased by 7% and 23% for reactions (R3.3b) and (R3.3c), respectively. This directly impacted the methyl radical production and concentrations were 4 and 10% higher for the models using reactions (R3.3b) and (R3.3c) than for that using reaction (R3.3a), respectively. This contributed to compensating for the increased buffer for the thermal decomposition into C_2 hydrocarbons and ultimately resulted in higher burning velocity predictions with reactions (R3.3b) and (R3.3c) compared to reaction (R3.3a) for all stoichiometries, as shown in Table 3.2.

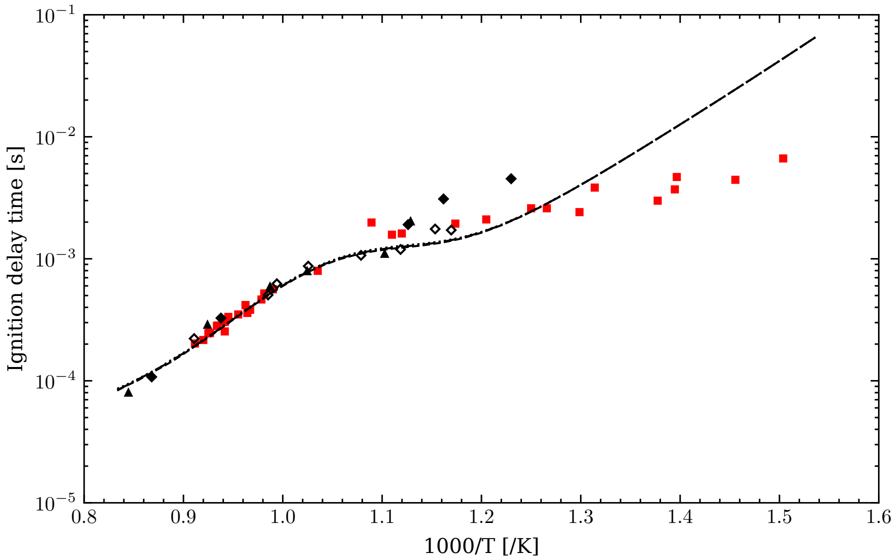

Figure 3.7: Ignition delay times for $\phi = 1.0$ iso-octane/air shock tube experiments near 50 atm comparing the mechanisms with differing iso-octane thermal decomposition products according to (R3.3a)-(R3.3c). Computed data: dashed line - (R3.3a); dot-dashed line - (R3.3b); dotted line - (R3.3c). Experimental data: red squares - Shao et al. [201]; filled black diamond - Fieweger et al. [139]; hollow black diamond - Davidson et al. [223]; black triangle - Shen et al. [224].

The ignition delay time for $\phi = 1.0$ iso-octane/air mixtures at 50 atm was calculated and compared to literature values from Shao et al. [201], Fieweger et al. [139, 225], Shen et al. [224] and Davidson et al. [223] for comparable pressures. Amongst all the available experimental data for IDTs a higher weighting was given to the 50 atm results for dual reasons of applicability and accuracy. The highest pressures are present in ICEs and the data extends across a wider range of temperatures without being limited by the need for accurate measurement of long ignition delay times [226]. Therefore, subsequent sensitivity analyses are restricted to the 50 atm data. The results demonstrating the sensitivity to (R3.3) are shown in Fig. 3.7. All computations show a deviation from the experimental data at lower temperatures (particularly from below approximately 750 K), as seen in Figure 3.7. However, for all product distributions variations (R3.3a-c) the computed IDTs appear to be coincident and only deviate very slightly from each other for temperatures above 900 K. For all possible pathways, at approximately 1000 K the thermal decomposition reaction of iso-octane, (R3.3), contributed around 78% of the consumption of iso-octane, suggesting that subsequent reaction pathways are rate determining, as discussed by Warnatz [74]. As expected, the fuel rapid thermal decomposition reaction has a more significant impact on the laminar burning velocity predictions than on the ignition delay time predictions. In addition, the discrepancies for temperatures below 750 K highlights the importance of (very) low temperature chemistry, discussed in further detail later, and that it is conservative in its rates, aligned with the views expressed by Atef et al. [68] and the motivation for their work. Removing the barrier to decomposition of C_4H_9 (R3.56) had no impact on the IDT predictions, but resulted in numerical stiffness for temperatures below about 800 K. This insensitivity supports the matching of the rate here for (R3.56b) with the rate alteration made with the n-heptane sub-mechanism, discussed later, to allow compatibility with both sub-mechanisms when applied for PRF fuel mixtures.

Reaction (R3.3b) provides a middle ground with burning velocity predictions and identical ignition delay time behaviour with the other product distributions for (R3.3). Therefore, this pathway was selected for the final iso-octane sub-mechanism and is used in all subsequent analyses. This selection is relevant to the butyl radical thermal decomposition, discussed later, as a direct result of the product distribution of (R3.3b), with the alternative (R3.3a) producing up to 50% less C_4H_9.

3.2.4.2 Iso-octyl radical thermal decomposition

The iso-octyl radicals are a primary product of the thermal decomposition of iso-octane (R3.1-3.2). At 1000 K, approximately 20% of iso-octane consumption produces an iso-octyl radical. A high sensitivity to the irreversible rapid thermal decomposition of 4-C_8H_{17} and 1-C_8H_{17}, reactions (R3.16) and (R3.17) respectively, can be seen in Figure 3.8. The original rate expressions from Kelley et al. [205] of: $k_{3.16} = 3.78 \times 10^{22} T^{-2.7} e^{(-1.354\times10^5/RT)}$ s^{-1} and $k_{3.17} = 3.62 \times 10^{17} T^{-1.3} e^{(-1.243\times10^5/RT)}$ s^{-1} were used with the pre-exponential factor reduced by about a factor of five and four for each pathway respectively. The ignition delay time prediction improved for all temperatures above approximately 700 K, and good agreement was seen for temperatures greater than 800 K, as shown in Fig. 3.8.

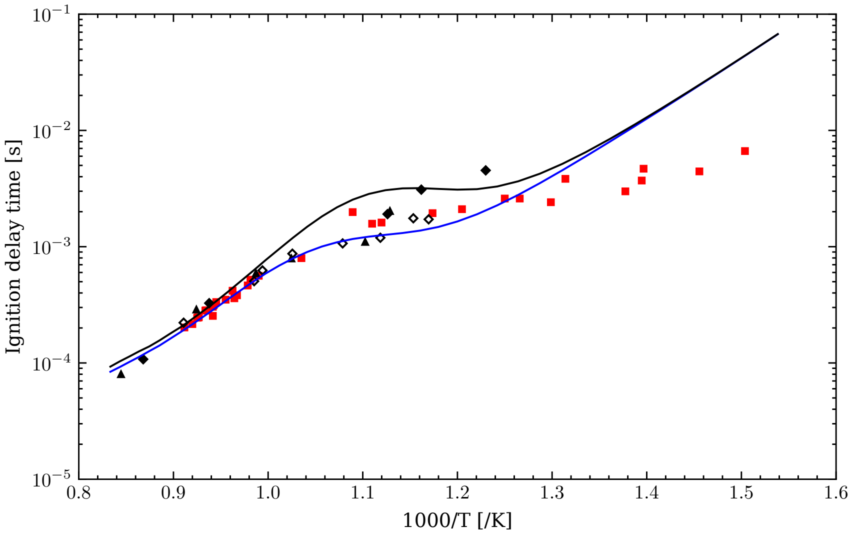

Figure 3.8: Ignition delay times for ϕ = 1.0 iso-octane/air shock tube experiments near 50 atm comparing the mechanisms with systematically reduced 1-C_8H_{17} and 4-C_8H_{17} thermal decomposition pathways. Computed data: blue line - with reductions to (R3.16) and (R3.17), as shown in Table 3.1; black line - using the rates from Kelley et al. [205] for (R3.16) and (R3.17). Experimental data as defined in Fig. 3.7.

Specifically, it can be seen in Fig. 3.9 that reaction (R3.16) exhibits a higher

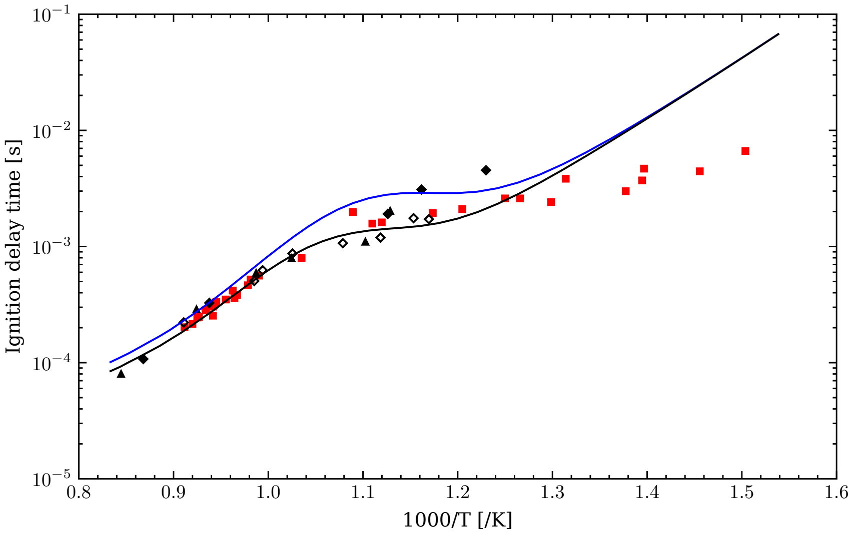

Figure 3.9: As in Fig. 3.8 but comparing the individual sensitives of each of the iso-octyl thermal decomposition pathways. Computed data: blue line - (R3.16) from Kelley et al. [205] with (R3.17) as in Table 3.1; black line - (R3.17) from Kelley et al. [205] with (R3.16) as in Table 3.1. Experimental data as defined in Fig. 3.7.

sensitivity than reaction (R3.17), particularly around the intermediate temperature range of 800–1000 K. This is consistent with the larger concentrations of 4-C_8H_{17} than 1-C_8H_{17} at almost every temperature point. Therefore, almost the entire change demonstrated in Fig. 3.8 can be attributed to the decomposition of 4-C_8H_{17}. However, for temperatures above approximately 900 K the combination of adjustments to both reactions (R3.16) and (R3.17) produced the best agreement with the experimental data.

The reduction in thermal decomposition rates resulting in reduced IDTs is counter-intuitive and suggests the significant impact of other iso-octyl radical consumption pathways, in particular the role the low temperature chemistry (oxygen addition) plays across all temperatures, as discussed later.

3.2.4.3 Low temperature chemistry

A distinctive feature for stoichiometric iso-octane/air oxidation at 50 atm at temperatures below 1000 K is the negative temperature coefficient (NTC) region where reactivity becomes inversely proportional to temperature, this is most evident in Fig. 3.7 between 770 - 910 K. This is due to the competition of chain branching and propagation reactions of low temperature chemistry species, in particular alkyl-hydroperoxide radicals (QO_4H) and hydroperoxy-alkyl radicals (QOOH) [68]. Further analysis of the low temperature chemistry sub-mechanism highlighted a high sensitivity to the isomerisation reaction (R3.31).

$$\text{1-}C_8H_{17}OO \rightleftharpoons \text{1-}C_8H_{16}OOH \tag{R3.31}$$

Oxygen addition to the iso-octyl radicals produces alkylperoxy radicals (QOO), both 1-$C_8H_{17}OO$ and 4-$C_8H_{17}OO$ are included in this work. As seen in Fig. 3.9, the sensitivities of the decomposition of each iso-octyl radical differed, as such the isomerisation reaction sensitivity of the species directly produced through oxygen addition to the iso-octyl radicals was explored. Figure 3.10, shows the results when the rate from the work of Mehl et al. [198] for the isomerisation reactions (R3.25) and (R3.31) were reduced by a factor of about four. The reduction to both reactions results in increased ignition delay time predictions. It is clear that while both demonstrate similar insensitivity at temperatures above about 1100 K, below this temperature the isomerisation of 4-$C_8H_{17}OO$ has a greater sensitivity and leads to more significant reduction of IDTs with this arguably modest rate reduction, particularly in the intermediate temperature region of 800-1000 K where predictions move to the upper end of the experimental data. For this reason, only the isomerisation of 1-$C_8H_{17}OO$, shown in reaction (R3.31), was reduced to provide improved intermediate temperature behaviour without compromising the low temperature predictions too much.

There remains scope for further improvement to the prediction of IDTs for the lowest temperatures, below 750 K at 50 atm, however data remains scarce and other reaction kinetics may come to the fore [227].

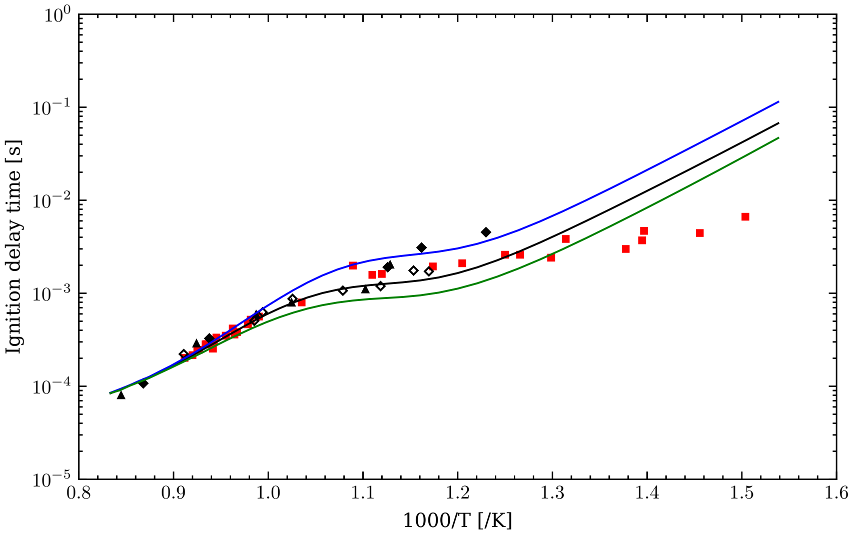

Figure 3.10: Ignition delay times for $\phi = 1.0$ iso-octane/air shock tube experiments near 50 atm comparing the sensitives of the $C_8H_{17}OO$ isomers isomerisation pathways, (R3.25) and (R3.31), to a factor of about four rate alteration. Computed data: green line - original rates from [198] for both (R3.25) and (R3.31); black line - final mechanism shown in Table 3.1 with reduction to (R3.31) only; blue line - reduction to (R3.25) only. Experimental data as defined in Fig. 3.7.

3.2.4.4 Butyl radical thermal decomposition

The various pathways explored for the thermal decomposition of the butyl radical (C_4H_9) were discussed in Section 3.2.2. The two pathways and three rates are shown in Table 3.1 and the laminar burning velocities are shown in Table 3.3. All mechanisms provide adequate agreement with the experimental values. Reactions (R3.56a) and (R3.56b) have identical product distributions and provide the closest agreement for the range of stoichiometries, while reaction (R3.56c) predicts at the lower end of the range of literature values for the stoichiometric conditions.

The ignition delay times for 50 atm shock tube experiments using the rate expressions for (R3.56a-c) are shown in Figure 3.11, in addition to the original rate for (R3.56b) from [209] which was a factor of ten larger. The impact of the different rate expressions for (R3.56a) [159] and (R3.56b) [209] is minor and the lines appear coincident in Fig. 3.11, including with the rate adjustment to (R3.56b) mentioned

Table 3.3: Laminar burning velocities of iso-octane/air flames at different stoichiometric conditions comparing the mechanisms with differing butyl radical (C_4H_9) thermal decomposition rates and pathways (R3.56) (see Table 3.1). Experiment data from: [218–222].

Equivalence ratio, ϕ	Laminar burning velocity [cm/s]			
	Experiments	(R3.56a)	(R3.56b)	(R3.56c)
0.7	22 - 27	23.2	23.3	23.4
1.0	44 - 48	44.9	44.8	43.4
1.3	35 - 42	39.0	39.4	38.1

above. The impact of the different decomposition products according to (R3.56c) is modest, with a reduction of IDTs at all temperatures. However, the general trend is better matched by (R3.56a) and (R3.56b), particularly for higher temperatures from about 1000 K. This discrepancy follows from the (R3.56c) reaction pathway describing the decomposition of the 1-butyl radical which, considering the functional form of iso-octane, is not a direct thermal decomposition product. The more recent rate expression from [209] adjusted to be consistent with the adjustment made for the n-heptane sub-mechanism was selected for the recommended iso-octane sub-mechanism (R3.56b) for compatibility with a full PRF sub-mechanism.

3.2.5 Results and discussion

The following results for ignition delay times, laminar burning velocities and time histories in a shock tube were computed using the mechanism outlined in Table 3.1, with the selection of (R3.3b) and (R3.56b).

3.2.5.1 Ignition delay times

The ignition delay time prediction using the updated iso-octane sub-mechanism for a stoichiometric iso-octane/air mixture and a range of pressures, 13, 28 and 50 atm, are shown in Fig. 3.12. Very good agreement with the experimental data [139, 201, 223–225] is shown with all pressures and for temperatures above approximately 770 K.

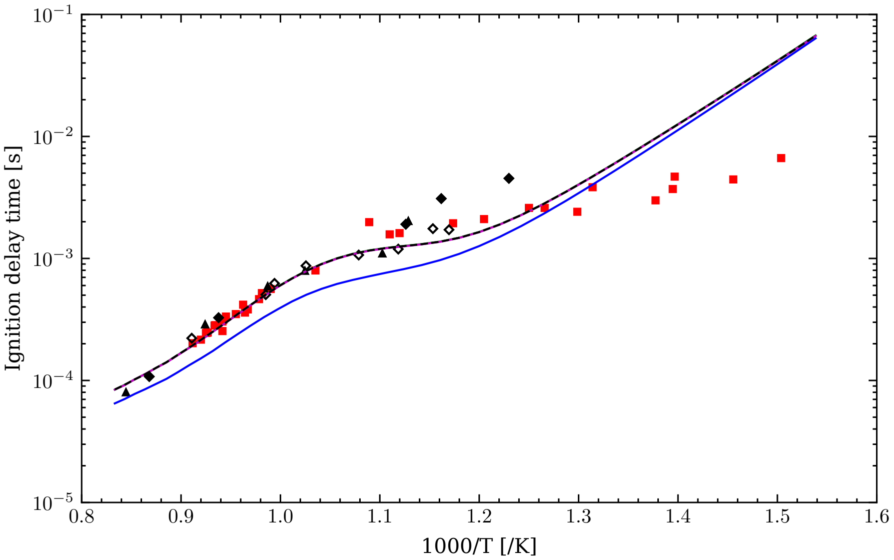

Figure 3.11: Ignition delay times for ϕ = 1.0 iso-octane/air shock tube experiments near 50 atm comparing the differing butyl radical thermal decomposition pathways, (R3.56a-c). Computed data: black dashed line - (R3.56a) [159]; green line - rate adjusted (R3.56b) [209]; blue line - (R3.56c) [198]; magenta line - (R3.56b) with the original rate expression [209]. Experimental data as defined in Fig. 3.7.

Experimental data for temperatures below this exists for the 50 atm case where the mechanism tends to overpredict the IDT and also the rate at which further temperature reduction increases the IDT. However, for intermediate and high temperatures the prediction provides very good agreement with the trend of the experimental data with only a moderate overprediction at the very highest temperatures. For the 13 and 28 atm cases the IDT predictions provide very good agreement with the experimental data.

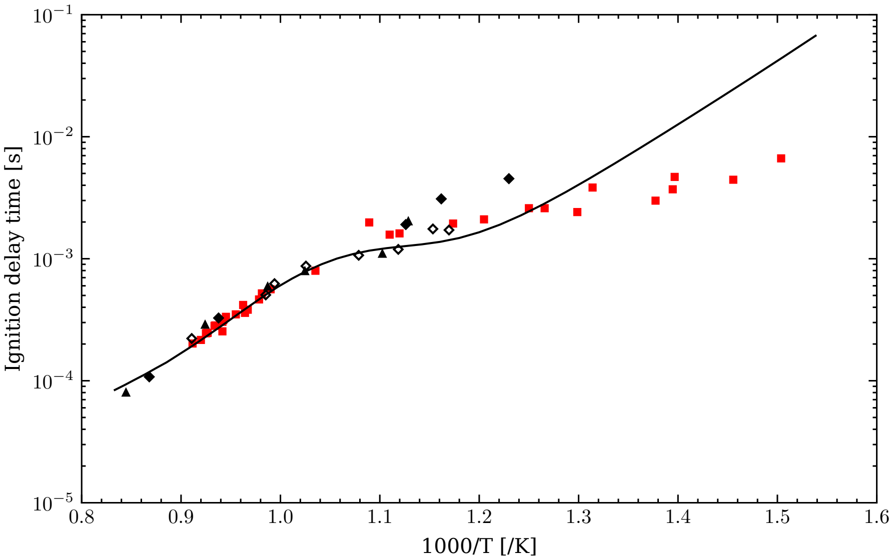

(a) 50 atm.

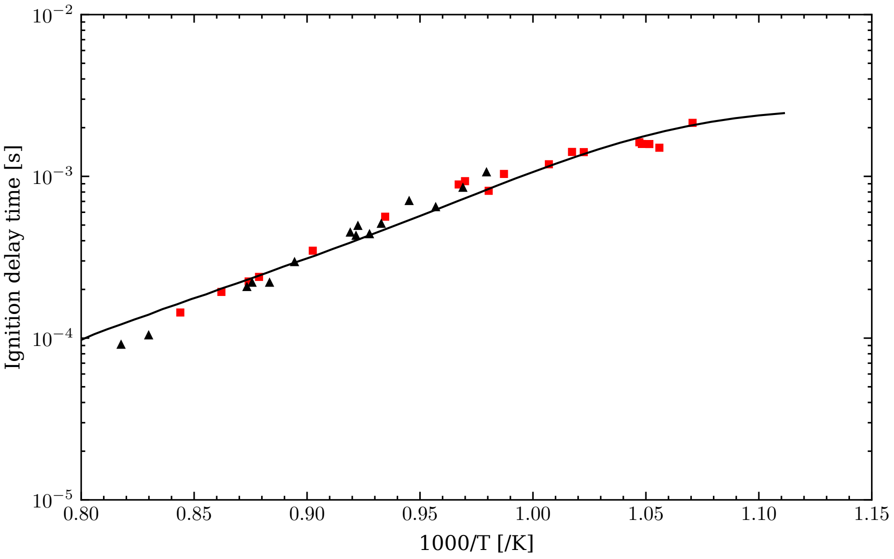

(b) 28 atm.

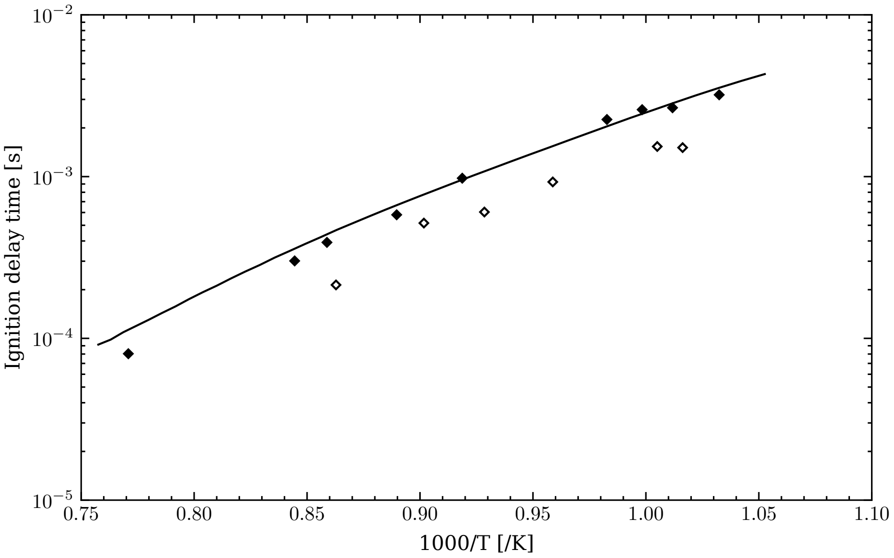

(c) 13 atm.

Figure 3.12: Ignition delay times for ϕ = 1.0 iso-octane/air shock tube experiments near 50, 28 and 13 atm. Experimental data: red squares - Shao et al. [201]; filled black diamond - Fieweger et al. [139, 225]; hollow black diamond - Davidson et al. [223]; black triangle - Shen et al. [224].

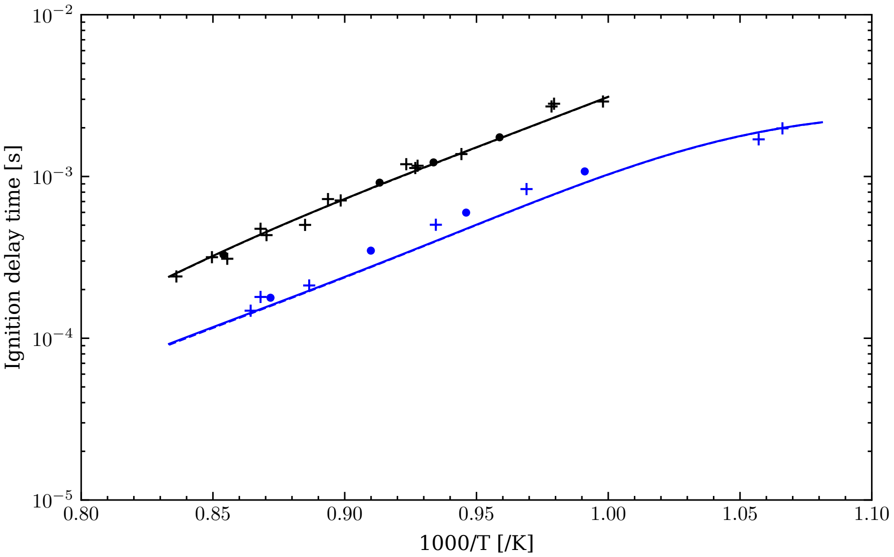

Figure 3.13: Ignition delay times for ϕ = 0.5 iso-octane/air shock tube experiments near 15 (black lines and markers) and 50 atm (blue lines and markers). Experimental data: dots - Shen et al. [224]; pluses - Davidson et al. [223].

Figure 3.13 shows the ignition delay time predictions for 15 and 50 atm for a ϕ = 0.5 iso-octane/air mixture compared with the experimental data close to these pressures from Davidson et al. [223] and Shen et al. [224]. The predictions are in very good agreement with the data across the full range of temperatures.

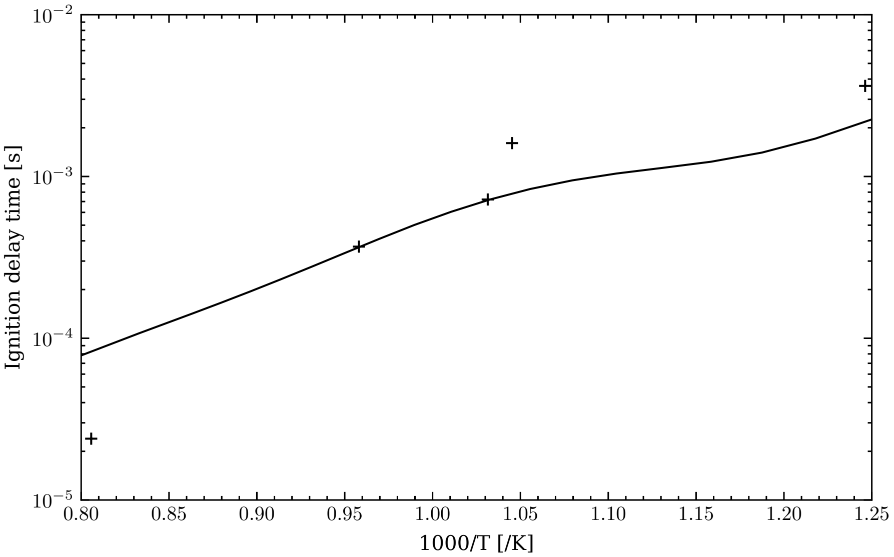

Figure 3.14: Ignition delay times for ϕ = 2.0 iso-octane/air shock tube experiments near 36 atm. Experimental data: pluses - Fieweger et al. [225].

The ignition delay time computations at 36 atm for a fuel-rich (ϕ = 2.0) shock tube computation are shown in Fig. 3.14. Little data and data points are available, however the mechanism provides good agreement with the measured values around 1000 K with slightly more deviation at the highest temperatures. The rapid fuel (thermal) decomposition step (R3.3) contributes 100% to the consumption of iso-octane at 1250 K and therefore could indicate that the rate is too fast for fuel-rich mixtures. However, due to the age and scarcity of data for fuel-rich iso-octane IDTs, in addition to becoming less relevant to practical applications, a reduced weighting is given to these results.

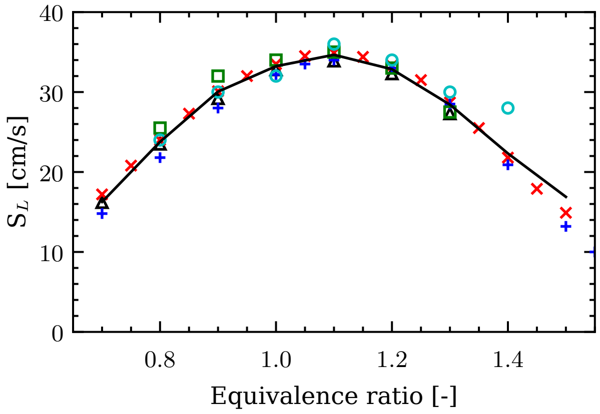

Figure 3.15: Laminar burning velocities for iso-octane/air flames at 1 atm and 298 K inlet temperature as a function of equivalence ratio. Experimental data from: black triangle - [221]; red cross - [220]; blue plus - [222]; green square - [218]; cyan circle - [219].

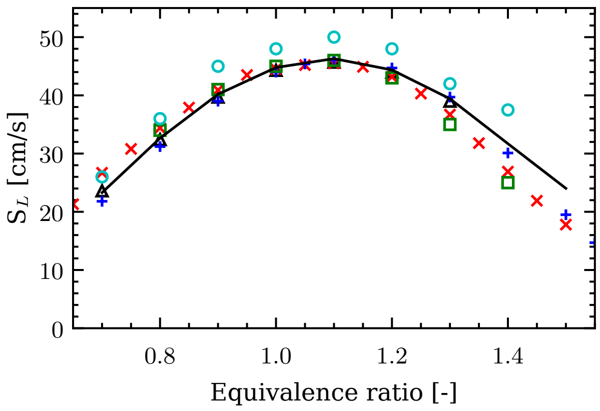

Figure 3.16: Laminar burning velocities for iso-octane/air flames at 1 atm and 358 K inlet temperature as a function of equivalence ratio. Experimental data as defined in Fig. 3.15.

3.2.5.2 Laminar burning velocities

The laminar burning velocity predictions at atmospheric pressure with inlet temperature of 298 K and 358 K are shown in Figs. 3.15 and 3.16, respectively. The mechanism shows excellent agreement with the experimental data, especially for lean stoichiometries where more coherence in the experimental data is also demonstrated. The burning velocity is predicted slightly high for fuel rich flames, but still within the range of experimental data. The key fuel consumption reactions are the hydrogen abstraction reaction with the hydrogen radical forming the 1-C_8H_{17}

iso-octyl radical (R3.5) and the rapid decomposition reaction (R3.3b), each accounting for approximately 30% of the iso-octane consumption. About 50% of 1-C_8H_{17} formed rapidly decomposes (R3.17) and the other half isomerises to form 4-C_8H_{17} of which about 80% rapidly decomposes according to (R3.16). This highlights the implementation of the rapid decomposition hypothesis and how the unadjusted elementary reactions in the hydrogen and C_1–C_2 sub-mechanism are rate determining, with the balance achieving excellent LBV predictions.

3.2.5.3 Time histories in a shock tube

Measurement of the time histories of key radicals, such as the hydroxyl and methyl radicals, can allow for more accurate determination of the ignition delay time of a mixture than relying solely on the pressure trace. Davidson et al. [228, 229] measured time histories for a fuel lean mixture containing 0.05% iso-octane, 0.625% oxygen and balanced with argon at pressures slightly above atmospheric. For the hydroxyl radical traces and model prediction shown in Fig. 3.17 a large discrepancy is shown between the experimental trace and the computed trace for intermediate times between the first and second peaks. The final and initial states are well reproduced, as well as the ignition delay times for both the high and low temperatures. A reaction pathway analysis was conducted at 30 μs and the major production pathway for the hydroxyl radical was by $H + O_2 \rightleftharpoons O + OH$ (71%). This highlighted the importance of the hydrogen radical, rather than intermediate hydrocarbon species resulting from fuel decomposition. The most significant contributor to H radical formation at this time was the low-pressure limit rate for CHO thermal decomposition ($CHO + M \rightleftharpoons CO + H + M$), accounting for about 36%. The sensitivity to the chaperon efficiency of argon for this reaction was explored and its impact on the hydroxyl radical prediction is shown in Fig. 3.17 for a high and low initial temperature and on the methyl radical in Fig. 3.18. As the mixture was very dilute (>99% Ar), the sensitivity to the chaperon efficiency of argon is non-trivial. Reducing the efficiency improves the prediction of a trough in the OH profile for the 1511 K inlet temperature experiments and also reduces the discrepancy between the predicted and measured time to reach steady state. All the mechanisms explored for the 1511 K initial temperature experiment by Davidson et al. [228] overpredicted the initial OH peak and were able to capture the trough to varying degrees. With a variation of the argon chaperon efficiency for the CHO thermal decomposition reaction, comparable performance with the current mechanism can be achieved.

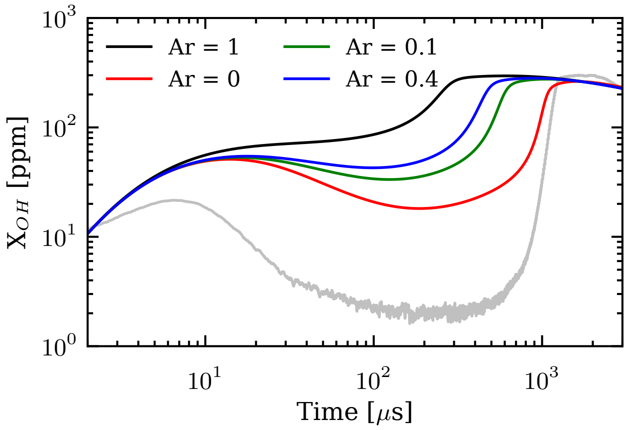

(a) T = 1511 K; P = 1.511 atm

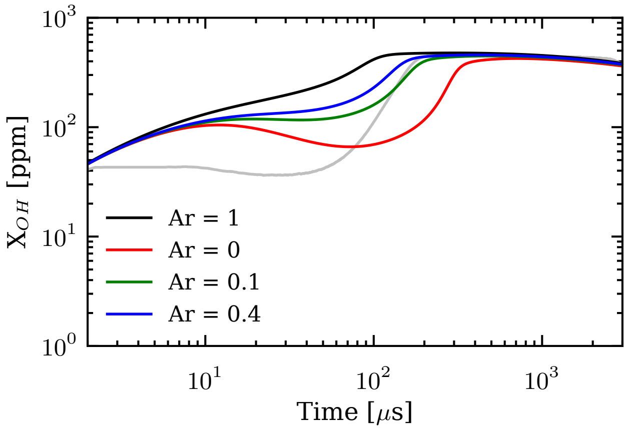

(b) T = 1736 K; P = 1.399 atm

Figure 3.17: Hydroxyl radical time histories for fuel lean mixtures containing 0.05% iso-octane, 0.625% oxygen and balanced with argon. The key defines the argon chaperon efficiency used for $CHO + M \rightleftharpoons CO + H + M$ in the mechanism in Table 3.1 and the grey lines are the experimental data of Davidson et al. [228].

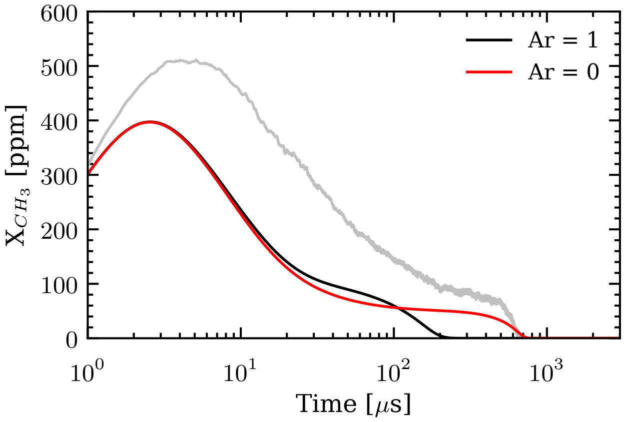

Figure 3.18: Methyl radical time history for the same mixture composition as in Fig. 3.17. Inlet conditions are 1559 K and 1.55 atm. The key is as defined in Fig. 3.17 with the experimental data of Davidson et al. [229].

For the methyl radical measurements and predictions shown in Fig. 3.18, the computed values follow the trend of the experimental data excellently with a fairly constant under-prediction. This discrepancy can be viewed as caused by an earlier onset of ignition, consistent with the trends in Fig. 3.17, where the final steady-state value is reached earlier in the computations than in the experimental data. This early onset reduces with increased temperature. Further fine tuning of the fuel rapid decomposition reactions may reduce this discrepancy for the CH_3 radical computations, but will not significantly impact intermediate OH radical predictions. Furthermore, the selection of the chaperon efficiency for argon in the CHO thermal decomposition reaction has no impact on the CH_3 radical prediction until approximately 0.1 ms.

3.3 n-Heptane

3.3.1 Introduction

Similarly to iso-octane, n-heptane is relevant as a simple surrogate and surrogate fuel component for practical fuels. Notably, n-heptane is used as a diesel surrogate due to its autoignition properties, assigned a cetane number of 54 (and an octane number of zero). It has been studied in a variety of devices to elucidate its chemical phenomena, including its autoignition properties, cool flame and negative temperature coefficient (NTC) behaviour.

These studies extend to numerous ignition based studies in shock tubes [140, 201, 225, 230–232], laminar burning velocity studies [120, 219–222] and low temperature and speciation studies [233, 234]. This experimental data provides critical validation points for any n-heptane mechanism. Westbrook et al. [235] developed a detailed mechanism for the oxidation of n-heptane and iso-octane building on previous sub-mechanisms for lower carbon species. The mechanism contained 212 chemical species and 765 reactions and was validated using experimental data obtained in shock tubes, flow reactors and stirred reactors. Other early detailed chemical modelling of n-heptane was conducted by Lindstedt and Maurice [64] validated with laminar burning velocities, in addition to speciation in counterflow diffusion flames and stirred reactors. The developed n-heptane sub-mechanism consisted of 21 chemical species and 201 elementary reactions appended to a H/C_1-C_6 mechanism to produce a mechanism containing a total of 109 chemical species and 659 elementary reactions. Further work on detailed n-heptane modelling by Curran et al. [65] produced a mechanism containing a total of 550 chemical species and 2450 elementary reactions. This work was comprehensively validated using a range of speciation data and ignition delay times. This work was recently updated by Zhang et al. [66] using revised sub-mechanisms for lower carbon species and a broad range of validation data. The mechanism contained 1268 chemical species and 5336 reactions. As discussed previously, such large chemical schemes are prohibitive for computations of highly dynamical systems and restrictive even for simple one-dimensional computations.

Ranzi et al. [236] developed a semi-detailed n-heptane mechanism that used a detailed H/C_1–C_4 mechanism with the use of kinetic lumping to reduce the quantity of intermediate steps. Other reduced mechanisms have been developed. Work by Lu and Law [105] utilised DRG, isomer lumping and CSP to produced a reduced mechanism containing 55 solved species and 13 QSS species. Work by Stagni et al. [86] and Ranzi et al. [84] applied isomer lumping and systematic removal of species and reactions to create a mechanism containing 100 species. This study applies a similar process, both to the aforementioned literature and the iso-octane sub-mechanism discussed in Section 3.2. A n-heptane mechanism simplified through isomer lumping and the rapid decomposition hypothesis appended to an updated H/C_1–C_2 base mechanism, which was also used with the iso-octane sub-mechanism, is validated with ignition delay times, laminar burning velocities and speciation in a stirred reactor.

Table 3.4: Simplified n-heptane oxidation sub-mechanism applied in the current work. Forward rate constants as $k_f = AT^n e^{-E_a/RT}$. Units: kg, m, s, kmol, kJ, K.

No.	Reaction	A	n	E_a	Ref.
3.60	$C_7H_{16} \rightleftharpoons 1\text{-}C_7H_{15} + H$	2.020×10^{17}	-0.36	4.234×10^{5}	adj. [198]
3.61	$C_7H_{16} \rightleftharpoons 2\text{-}C_7H_{15} + H$	7.890×10^{18}	-0.88	4.046×10^{5}	adj. [198]
3.62	$C_7H_{16} \rightarrow CH_3 + C_2H_5 + 2\,C_2H_4$	7.203×10^{25}	-2.55	3.695×10^{5}	adj. [198]
3.63	$C_7H_{16} + H \rightleftharpoons 1\text{-}C_7H_{15} + H_2$	9.330×10^{3}	2.00	3.224×10^{4}	adj. [64]
3.64	$C_7H_{16} + H \rightleftharpoons 2\text{-}C_7H_{15} + H_2$	1.820×10^{4}	2.00	2.092×10^{4}	[64]
3.65	$C_7H_{16} + OH \rightleftharpoons 1\text{-}C_7H_{15} + H_2O$	4.400×10^{6}	0.97	6.650×10^{3}	adj. [64]
3.66	$C_7H_{16} + OH \rightleftharpoons 2\text{-}C_7H_{15} + H_2O$	7.840×10^{4}	1.61	0	adj. [64]
3.67	$C_7H_{16} + O \rightleftharpoons 1\text{-}C_7H_{15} + OH$	1.920×10^{3}	2.40	2.303×10^{3}	adj. [237]
3.68	$C_7H_{16} + O \rightleftharpoons 2\text{-}C_7H_{15} + OH$	9.400×10^{2}	2.50	9.331×10^{3}	adj. [206]
3.69	$C_7H_{16} + CH_3 \rightleftharpoons 1\text{-}C_7H_{15} + CH_4$	2.500×10^{9}	0.00	4.853×10^{4}	adj. [238]
3.70	$C_7H_{16} + CH_3 \rightleftharpoons 2\text{-}C_7H_{15} + CH_4$	5.320×10^{9}	0.00	3.975×10^{4}	adj. [238]
3.71	$C_7H_{16} + O_2 \rightleftharpoons 1\text{-}C_7H_{15} + HO_2$	2.090×10^{10}	0.00	2.181×10^{5}	adj. [206]
3.72	$C_7H_{16} + O_2 \rightleftharpoons 2\text{-}C_7H_{15} + HO_2$	1.320×10^{11}	0.00	2.040×10^{5}	adj. [206]
3.73	$C_7H_{16} + HO_2 \rightleftharpoons 1\text{-}C_7H_{15} + H_2O_2$	1.870×10^{9}	0.00	8.120×10^{4}	adj. [238]
3.74	$C_7H_{16} + HO_2 \rightleftharpoons 2\text{-}C_7H_{15} + H_2O_2$	1.680×10^{10}	0.00	7.120×10^{4}	adj. [238]
3.75	$1\text{-}C_7H_{15} \rightarrow C_5H_{10} + C_2H_5$	2.009×10^{20}	-1.80	1.395×10^{5}	adj. [198]
3.76	$2\text{-}C_7H_{15} \rightarrow C_5H_{10} + C_2H_5$	4.440×10^{21}	-2.06	1.359×10^{5}	adj. [198]
3.77	$1\text{-}C_7H_{15} \rightleftharpoons C_7H_{14} + H$	5.612×10^{14}	-0.29	1.441×10^{5}	[198]
3.78	$2\text{-}C_7H_{15} \rightleftharpoons C_7H_{14} + H$	1.437×10^{13}	0.23	1.577×10^{5}	[198]
3.79	$1\text{-}C_7H_{15} \rightleftharpoons 2\text{-}C_7H_{15}$	2.000×10^{11}	0.00	8.400×10^{4}	[64]
3.80	$1\text{-}C_7H_{15} + O_2 \rightleftharpoons C_7H_{14} + HO_2$	1.000×10^{6}	0.00	1.465×10^{4}	[202, 203]
3.81	$2\text{-}C_7H_{15} + O_2 \rightleftharpoons C_7H_{14} + HO_2$	4.000×10^{6}	0.00	1.465×10^{4}	[202, 203]

Table 3.4 (Continued)

No.	Reaction	A	n	E_a	Ref.
3.82	$1\text{-}C_7H_{15} + O_2 \rightleftharpoons C_7H_{15}OO$	2.000×10^{9}	0.00	0	adj. [206]
3.83	$2\text{-}C_7H_{15} + O_2 \rightleftharpoons C_7H_{15}OO$	6.000×10^{9}	0.00	0	adj. [206]
3.84	$C_7H_{15}OO \rightleftharpoons C_7H_{14}OOH$	2.000×10^{10}	0.00	7.120×10^{4}	adj. [198]
3.85	$C_7H_{14}OOH \rightleftharpoons C_7H_{14} + HO_2$	4.500×10^{12}	0.00	1.088×10^{5}	adj. [206]
3.86	$C_7H_{14}OOH \rightleftharpoons C_7H_{14}O + OH$	3.000×10^{10}	0.00	5.900×10^{4}	adj. [67, 206]
3.87	$C_7H_{14}OOH \rightarrow CH_2CHO + C_4H_8 + CH_3 + OH$	1.000×10^{13}	0.00	1.067×10^{5}	adj. [206]
3.88	$C_7H_{14}OOH + O_2 \rightleftharpoons C_7H_{15}O_4$	2.000×10^{9}	0.00	0	[236]
3.89	$C_7H_{15}O_4 \rightleftharpoons C_7H_{14}O_4H$	2.000×10^{11}	0.00	4.650×10^{4}	[202, 203]
3.90	$C_7H_{14}O_4H \rightleftharpoons C_7H_{13}O_3H + OH$	2.500×10^{10}	0.00	7.469×10^{4}	[198]
3.91	$C_7H_{13}O_3H \rightarrow 2\,CH_2CHO + C_2H_4 + CH_3 + OH$	7.000×10^{15}	0.00	1.757×10^{5}	adj. [206]
3.92	$C_7H_{14}O \rightarrow CH_2CHO + C_4H_8 + CH_3$	3.400×10^{13}	0.00	2.419×10^{5}	adj. [207]
3.93	$C_7H_{14} + H \rightleftharpoons C_7H_{13} + H_2$	8.000×10^{10}	0.00	1.423×10^{4}	adj. [67, 206]
3.94	$C_7H_{14} + O \rightleftharpoons C_7H_{13} + OH$	4.000×10^{10}	0.00	1.674×10^{4}	adj. [67]
3.95	$C_7H_{14} + OH \rightleftharpoons C_7H_{13} + H_2O$	2.000×10^{10}	0.00	1.088×10^{4}	adj. [206]
3.96	$C_7H_{14} + CH_3 \rightleftharpoons C_7H_{13} + CH_4$	2.000×10^{8}	0.00	2.847×10^{4}	adj. [206]
3.97	$C_7H_{14} + O \rightarrow C_4H_8 + C_2H_4 + CH_2O$	3.620×10^{3}	1.88	7.600×10^{2}	[202, 203]
3.98	$C_7H_{14} + HO_2 \rightarrow C_4H_8 + C_2H_4 + CH_2O + OH$	1.000×10^{9}	0.00	6.000×10^{4}	[202, 203]
3.99	$C_7H_{13} \rightarrow C_2H_4 + C_2H_4 + C_2H_2 + CH_3$	2.000×10^{13}	0.00	1.681×10^{5}	[202, 203]
3.100	$C_7H_{13} + O_2 \rightarrow CH_2CHO + CH_2O + C_4H_8$	1.640×10^{18}	-2.78	1.056×10^{4}	[202, 203]
3.101	$2\,C_5H_{10} \rightarrow 2\,C_4H_9 + C_2H_2$	2.000×10^{13}	0.00	1.000×10^{4}	[202, 203]
3.102	$2\,C_4H_9 \rightarrow 3\,C_2H_4 + 2\,CH_3$	9.504×10^{10}	0.77	1.280×10^{5}	[198]
3.103	$C_4H_8 \rightarrow C_2H_4 + C_2H_4$	1.000×10^{13}	0.00	2.573×10^{5}	[210]

3.3.2 n-Heptane chemical mechanism

An n-heptane sub-mechanism containing 14 chemical species and 44 reactions, shown in Table 3.4, was used within a mechanism containing a total of 65 chemical species and 359 chemical reactions. An identical approach to that used for the iso-octane mechanism was applied here, with the use of the rapid decomposition hypothesis and isomer lumping to reduce the state space required. Rapid decomposition products include C_5H_{10} and C_4H_9 and C_4H_8, which were also used in the iso-octane sub-mechanism. Functionally the structure of the n-heptane sub-mechanism is similar to the iso-octane sub-mechanism discussed in Section 3.2.2, and a comparable discussion is included.

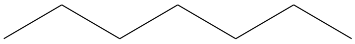

Figure 3.19: n-Heptane (C_7H_{16}).

n-Heptane thermal decomposition: The thermal decomposition pathways for n-heptane include reactions (R3.60–R3.62) and schematics of n-heptane and two heptyl radicals, 1-C_7H_{15} and 2-C_7H_{15}, are shown in Figs. 3.19 and 3.20, respectively. Reactions (R3.60) and (R3.61) are the reversible thermal decomposition of n-heptane and the rates from Mehl et al. [198] were increased by a factor of three. The irreversible rapid decomposition step (R3.62) was adapted from: $C_7H_{16} \rightleftharpoons$ i-C_3H_7 + i-C_4H_9 [198], where i-C_3H_7 is the iso-propyl radical with the rate also increased by a factor of three.

$$C_7H_{16} \rightleftharpoons 1\text{-}C_7H_{15} + H \tag{R3.60}$$

$$C_7H_{16} \rightleftharpoons 2\text{-}C_7H_{15} + H \tag{R3.61}$$

$$C_7H_{16} \longrightarrow CH_3 + C_2H_4 + C_2H_5 \tag{R3.62}$$

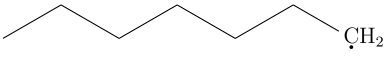

(a) 1-Heptyl radical(1-C_7H_{15}).

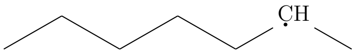

(b) 2-Heptyl radical (2-C_7H_{15}).

Figure 3.20: Heptyl radicals, C_7H_{15}.

n-Heptane hydrogen abstraction reactions: A further twelve fuel hydrogen abstraction reactions, forming both heptyl radicals, were also included with H, O, OH, CH_3, O_2 and HO_2 as the abstractors (R3.63–3.74) with H_2, H_2O, OH, CH_4, HO_2 and H_2O_2 as their respective products.

Heptyl radical consumption: At high temperatures the heptyl radicals subsequently isomerise (R3.79) and thermally decompose to form C_7H_{14} via (R3.77–78) or rapidly decomposed to form an unsaturated hydrocarbon (C_5H_{10}) and the ethyl radical (C_2H_5) (R3.75–76). In addition, reactions with molecular oxygen either resulted in hydrogen abstraction and the formation of C_7H_{14} and HO_2 (R3.80 and R3.81) or oxygen addition and the formation of the alkylperoxy radical, $C_7H_{15}OO$, (R3.82 and R3.83) discussed in more detail below. As for iso-octane, the reaction intermediate C_5H_{10} can be viewed as a place holder for the inclusion of an appropriate sub-mechanism.

Consumption of other C_7 species: Consumption of C_7H_{14} occurs either through hydrogen abstraction with H, O, OH or CH_3 (R3.93–96) forming C_7H_{13} and H_2, OH, H_2O or CH_4, respectively. Additionally, consumption of C_7H_{14} via O or HO_2 (R3.97 and R3.98) is included along with the rapid decomposition of the abstraction product, C_7H_{13} (R3.99 and R3.100) to form a combination of C_4H_8, C_2H_4, C_2H_2, CH_3, CH_2O, OH and CH_2CHO.

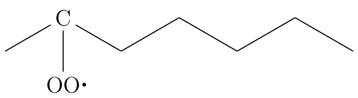

(a) Alkylperoxy radical ($C_7H_{15}OO$).

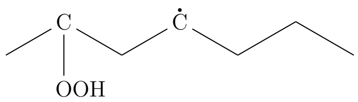

(b) Hydroperoxy-alkyl radical ($C_7H_{14}OOH$).

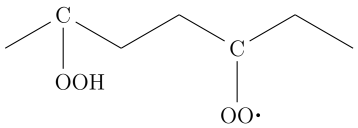

(c) Peroxy-alkyl hydroperoxide radical ($C_7H_{15}O_4$).

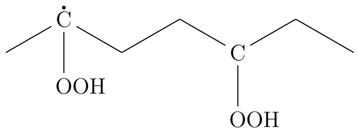

(d) Alkyl dihydroperoxide ($C_7H_{14}O_4H$).

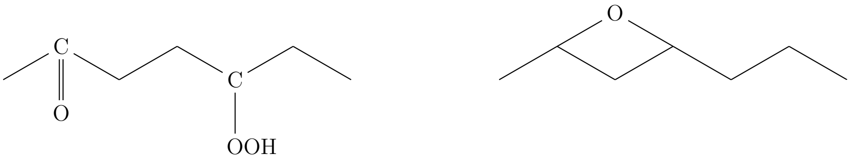

(e) Ketohydroperoxide ($C_7H_{14}O_3H$). (f) Cyclic ether ($C_7H_{14}O$).

Figure 3.21: Example n-heptane low temperature oxidation species, showing the defining functional group in each case.

Low temperature chemistry: The low temperature chemistry for n-heptane follows a similar structure to that of iso-octane and is discussed in Section 3.2.2. This work is based on that of Curran et al. [65] and was reduced and applied by Lindstedt [202, 203]. Twelve reactions, (R3.82–3.92) and (R3.100), were used to capture the low temperature behaviour. This includes reactions with oxygen or the oxygenated heptane products of these reactions with the chemical species $C_7H_{15}OO$, $C_7H_{14}OOH$, $C_7H_{14}O$, $C_7H_{15}O_4$, $C_7H_{14}O_4H$ and $C_7H_{13}O_3H$ included. The alkylperoxy radical formed in (R3.82) and (R3.83) isomerises to form the hydroperoxy-alkyl radical ($C_7H_{14}OOH$) (R3.84). The hydroperoxy-alkyl radical decomposes to form C_7H_{14} (R3.85), a cyclic ether (R3.86) or CH_2CHO, C_4H_8, CH_3 and OH (R3.87). In addition, reactions with molecular oxygen (R3.88) to form the hydroperoxy-alkyl-peroxy radical, $C_7H_{15}O_4$ is possible. The hydroperoxy-alkyl-peroxy radical isomerises to form the peroxy-alkyl hydroperoxide species, $C_7H_{14}O_4H$, in reaction (R3.89). The peroxy-alkyl hydroperoxide species decomposes to form a ketohydroperoxide ($C_7H_{13}O_3H$) and OH (R3.90) with the former then rapidly decomposing (R3.91) to form CH_2CHO, C_2H_4, CH_3 and OH. The cyclic ether formed in (R3.86) rapidly decomposes (R3.92) to form CH_2CHO, C_4H_8 and CH_3.

Rapid decomposition of intermediates: Reactions (R3.102) and (R3.103) match those used in the iso-octane sub-mechanism (see Table 3.1 and Section 3.2.2) with the addition of (R3.101). Reaction (R3.101) describes the rapid thermal decomposition of C_5H_{10} and, with (R3.102) and (R3.103), controls the decay of the fuel and other

C_7 decomposition products into shorter chain C_1 and C_2 hydrocarbons which are then consumed in accordance with the detailed hydrogen and C_1–C_2 sub-mechanism. The product distribution of (R3.101) may require revision, as outlined below.

$$2\,C_5H_{10} \longrightarrow 2\,C_4H_9 + C_2H_2 \tag{R3.101}$$

3.3.3 Computational methods

The computational methods are described further in Section 3.2.3 and 2.2.1 above. The shock tube data sets were computed as outlined previously and the stirred reactor data set was computed as zero-dimensional, homogeneous, isothermal and isobaric using time steps of 40 µs and integrated for twice the experimentally defined residence time of the reactor to ensure steady-state was reached. The laminar burning velocities were modelled in a counterflow flame geometry as before with the rate of strain maintained below 150 s^{-1} with locally refined cells as described for iso-octane. The low pressure flat flames featured imposed experimental temperature profiles and were resolved using local refinement with cell sizes ranging from 40 to 200 µm.

3.3.4 Results and discussion

The computational results for ignition delay times, laminar burning velocities and jet stirred reactor species concentrations as a function of temperature are presented. In addition, the ability of the n-heptane sub-mechanism to predict the low temperature behaviour through the incorporation of a simplified oxygenated heptane sub-mechanism is also presented.

3.3.4.1 Ignition delay times

The ignition delay time is a crucial metric for n-heptane sub-mechanism performance because of its application to devices where autoignition phenomena play a critical role. The ignition delay time predictions for various temperatures and pressures are shown in Figs. 3.22, 3.23 and 3.24 for ϕ = 0.5, 1.0 and 2.0, respectively, and compared with experimental data from Ciezki and Adomeit [230], Shen et al. [232] and Shao et al. [201].

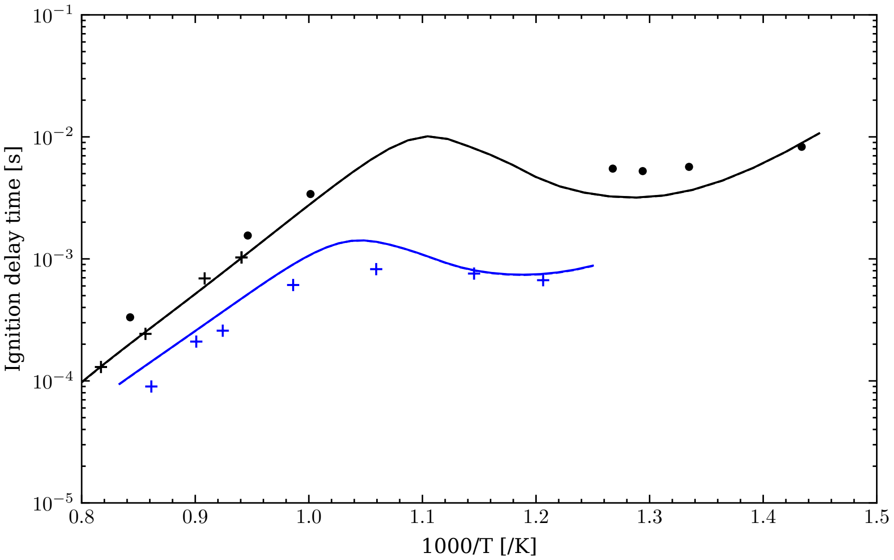

Figure 3.22: Ignition delay times for ϕ = 0.5 n-heptane/air shock tube experiments near 13 atm (black markers and lines) and 45 atm (blue markers and lines). Experimental data from: dots [230]; pluses [232].

The results for the fuel lean ϕ = 0.5 cases in Fig. 3.22 show very good agreement with the experimental data for both 13 and 45 atm, demonstrating an NTC region. Good agreement is also shown for the stoichiometric cases in Fig. 3.23, including for the low temperature behaviour which maintains and even reduces the IDT at temperatures in the range 750 – 900 K. At 1000 K for the fuel lean mixtures, about 80-90% of n-heptane consumption produces a heptyl radical which subsequently decomposes to the ethyl radical and the butyl radical and acetylene through C_5H_{10}. The H radical, responsible for 62 and 44% of OH production in the 13 and 45 atm cases, respectively, is predominantly produced in both cases by the reaction of carbon monoxide with the hydroxyl radical (its major consumption pathway). However, for the stoichiometric cases shown in Fig. 3.23 the major n-heptane consumption

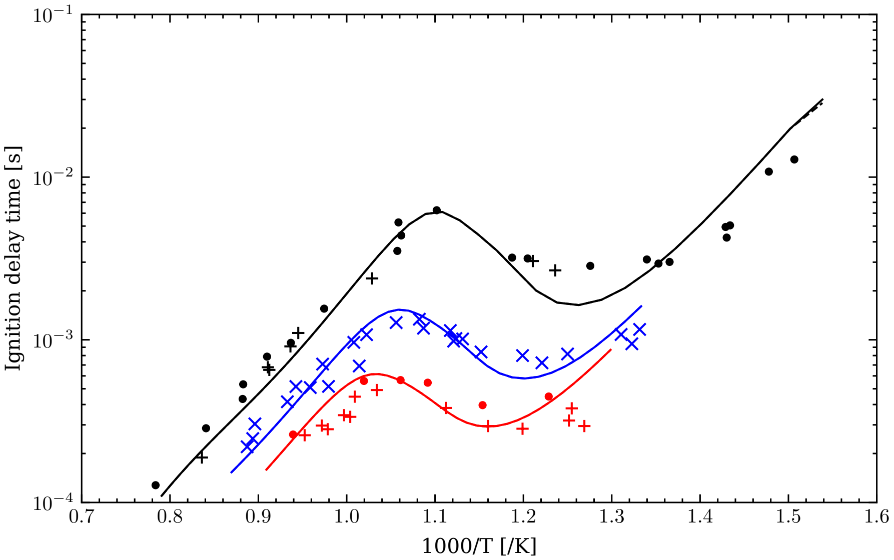

Figure 3.23: Ignition delay times for ϕ = 1.0 n-heptane/air shock tube experiments near 12 atm (black markers and lines), 28 atm (blue markers and lines) and 50 atm (red markers and lines). The key is as defined in Fig. 3.22, with the addition of crosses [201].

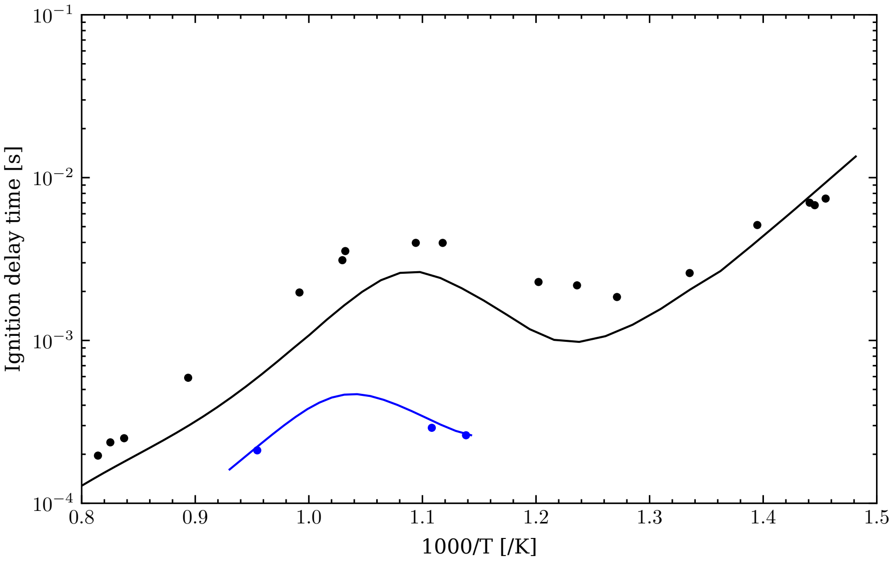

Figure 3.24: Ignition delay times for ϕ = 2.0 n-heptane/air shock tube experiments near 13.5 atm (black markers and lines) and 41 atm (blue markers and lines). Experimental data from: dots [230].

pathway at 1000 K is its rapid thermal decomposition forming the ethyl radical, ethylene and the methyl radical (R3.62), accounting for up to two thirds of fuel consumption for all pressures. The hydrogen and hydroxyl radicals behaviour is similar to the lean case, discussed above. Considering the stoichiometric, 12 atm case in Fig. 3.23, at 650 K the low temperature chemistry with the formation of oxygenated species plays the critical role in fuel decomposition after hydrogen abstraction by the hydroxyl radical to the heptyl radicals (R3.65) and (R3.66). The oxygenated species decay to account for the formation of both the hydroxyl and hydrogen radical, the latter occurring from dissociation of CH_3O which is formed as a result of methyl radical production, another product of oxygenated heptane species decomposition. For the fuel-rich IDTs, shown in Fig. 3.24, limited data is available, as with iso-octane. However, good agreement with the lower pressure, 13.5 atm, data is shown with a slight but consistent underprediction at higher temperatures. For the higher pressure, 41 atm, experimental data are well matched by the computations. As before, reduced weighting can be assigned to these results due to the age and scarcity of fuel-rich n-heptane ignition delay time measurements.

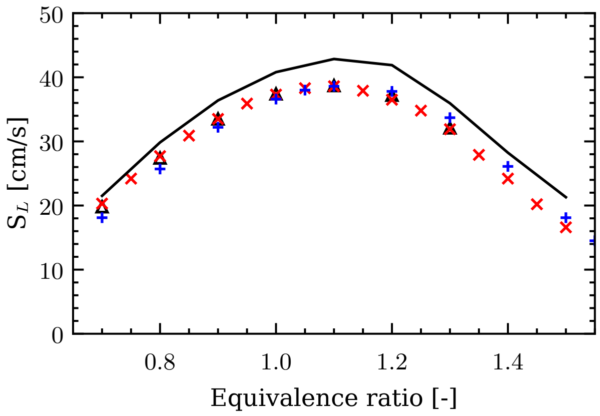

Figure 3.25: Laminar burning velocities of n-heptane at atmospheric pressure and inlet temperature of 298 K for a range of stoichiometries calculated in a counterflow geometry with rate of strain 80–125 s^{-1} compared to experimental data: black triangles [221]; red crosses [220]; blue pluses [222].

3.3.4.2 Laminar burning velocities

The laminar burning velocities of n-heptane for a range of stoichiometries at atmospheric pressure with inlet temperature of 298 and 358 K are shown in Figs. 3.25

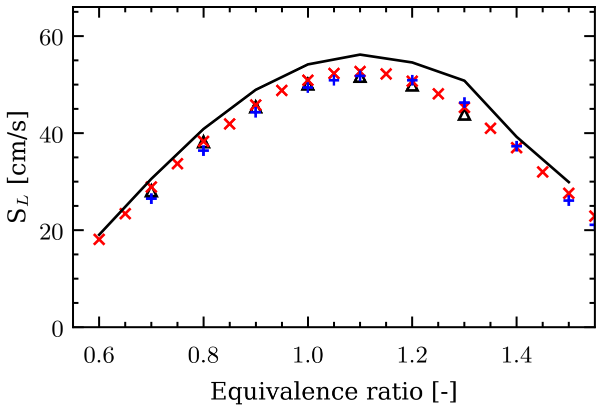

Figure 3.26: Laminar burning velocities of n-heptane at atmospheric pressure and inlet temperature of 358 K for a range of stoichiometries calculated in a counterflow geometry with rate of strain 80–140 s^{-1} compared to experimental data. The key is as defined in Fig. 3.25.

and 3.26, respectively. Good agreement is shown with the experimental data from Dirrenberger et al. [220], Sileghem et al. [221] and Han et al. [222] with only a modest overprediction that is within the uncertainty bounds of the data which ranges from 0.6 – 3.4 cm/s at the stoichiometric flammability limits.

Considering the stoichiometric cases at both inlet temperatures, approximately 97% of n-heptane consumption produces the heptyl radicals (1-C_7H_{15} and 2-C_7H_{15}). Subsequent behaviour at both temperatures is similar, where the heptyl radical primarily decomposes to C_5H_{10} and C_2H_5, with the former rapidly decomposing to C_4H_9 and C_2H_2. A smaller proportion of 1-C_7H_{15} (about 3%) decomposes to C_7H_{13} via C_7H_{14} which about 75% then also subsequently rapidly decomposes to C_2H_4, C_2H_2 and CH_3. For a fuel lean flame, $\phi = 0.7$, with inlet temperature of 298 K all the fuel decomposes to the heptyl radicals and their subsequent decomposition follows the same process as discussed above for the stoichiometric flames.

3.3.4.3 Speciation in a jet stirred reactor

Oxidation of n-heptane at low temperatures was investigated in a jet stirred reactor by Herbinet et al. [234]. Experiments were conducted at 1.06 bar with a residence time of 2 s for stoichiometric mixtures using helium or argon as the diluent. Data was obtained using gas chromatography and novel synchrotron vacuum ultraviolet photoionisation mass spectrometry (SVUV-PIMS) with direct sampling through a molecular jet. This allowed the measurement of a large number of species, including unstable species such as hydroperoxides. The experimental data was modelled using an isothermal stirred reactor and integrated for twice the residence time to ensure steady-state operation.

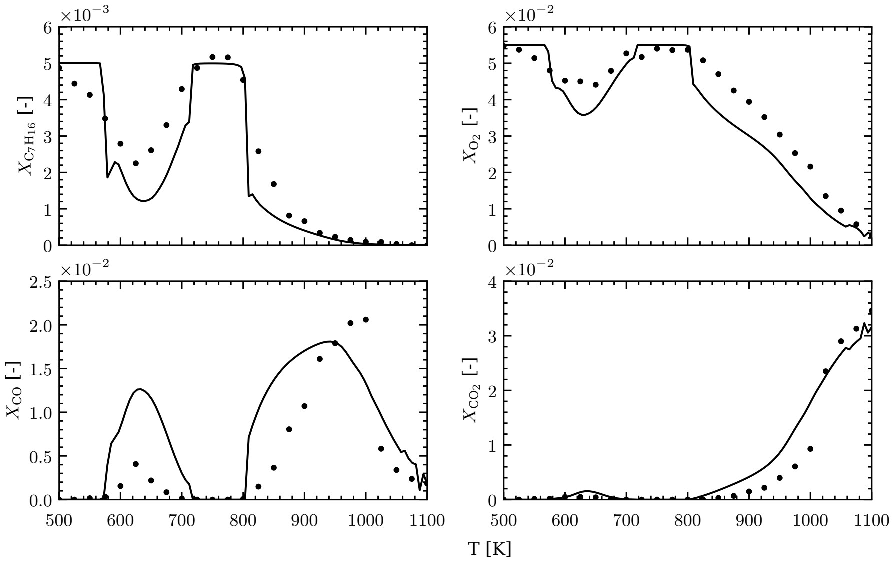

Figure 3.27: Computations of major reactants and product species for a stoichiometric n-heptane/oxygen/argon mixture at 1.06 bar in a jet stirred reactor with a residence time of 2 s. Experimental data from Herbinet et al. [234].

Figures 3.27 and 3.28 show the experimental data [234] and computational predictions for major reactants and products and key shorter chain alkyl products. For the major species C_7H_{16}, O_2, CO and CO_2 shown in Fig. 3.27 the model predictions are very good with a minor overprediction of the first carbon monoxide peak and a slight under prediction of the second peak. The other notable feature is the reformation of n-heptane at about 600 K. This can be attributed to reaction (R3.91), the decomposition of the ketohydroperoxide $C_7H_{13}O_3H$ to form the hydroxyl radical which is the major reactant for fuel consumption through hydrogen abstraction

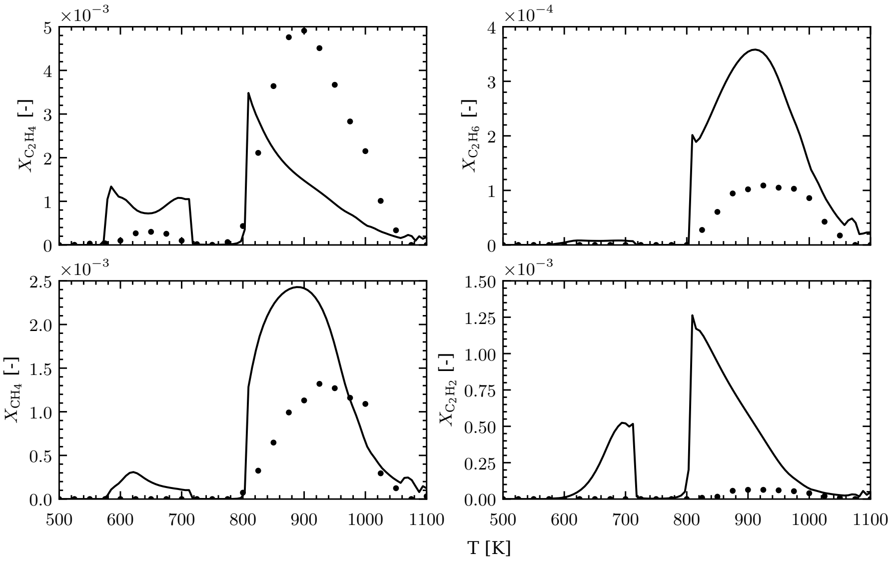

Figure 3.28: As defined in Fig. 3.27 for shorter chain alkyl products.

reactions (R3.65) and (R3.66). The concentration of $C_7H_{13}O_3H$ reduces by a factor of ten from 579 K to 603 K resulting in a 2.5 times reduced OH radical production from (R3.91). The computations for C_2H_4, C_2H_6, CH_4 and C_2H_2 are shown in Fig. 3.28. Excellent agreement with the onset of peaks in the experimental data for all species is seen, with overpredictions of the peak concentration of C_2H_6 and CH_4 by approximately a factor of 3.5 and 1.8 respectively. The overprediction of C_2H_2 is considerably larger. For the overprediction of acetylene the major production pathway (100%) is (R3.101). Furthermore, sharp peaks in the C_2H_4 and C_2H_2 profiles at approximately 810 K were predicted. By conducting a rate analysis at this point and at 900 K the sudden reduction in C_2H_2 can be attributed to the fourfold increase in its consumption by hydrogen abstraction with O ($C_2H_2 + O \rightleftharpoons C_2HO + H$) and a doubling of its reformation with hydrogen radical forming C_2H_3. Similarly for C_2H_4 the primary production pathways at both temperatures is the rapid decomposition of C_4H_9 (R3.102) which reduces at the higher temperature while the consumption of C_2H_4 by reformation to C_2H_5 increases by about 50%. All profile irregularities here can be traced to the use of these species as rapid decomposition products or products of the subsequent decay of rapid decomposition products, for example the production of C_2H_6 can be attributed to $2\,CH_3 \rightleftharpoons C_2H_6$ with the major methyl radical formation path from (R3.102). This is by design a shortcoming of the rapid decomposition hypothesis and would require further tuning in order to achieve a sufficiently slow fuel decomposition to shorter chain alkyl products for oxidation progress without overly favouring specific 'bucket' species.

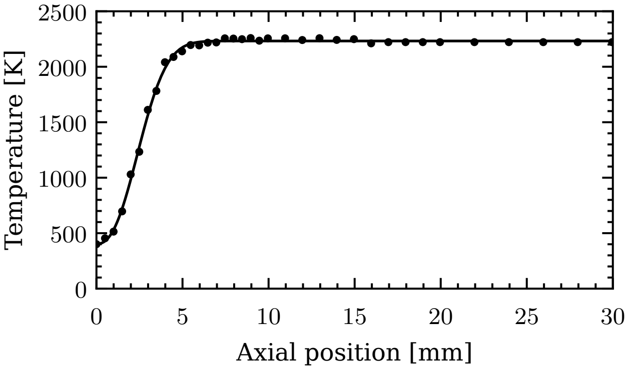

Figure 3.29: Measured temperature for a fuel rich (ϕ = 1.69) premixed $C_7H_{16}/O_2/Ar$ flame at a pressure of 40 mbar with the fitted profile used in computations. Dots are experimental data from [239].

3.3.4.4 Speciation in a low pressure flame

Seidel et al. [239] studied a fuel rich (ϕ = 1.69) n-heptane flame at a pressure of 40 mbar and measured the spatial distribution of species by sampling and a mass spectrometry analysis. The measured temperature profile and fitted profile used in the computations is shown in Fig. 3.29. It assumes an inlet temperature of about 400 K. Full details of the experimental conditions can be found elsewhere [239].

The results for a selection of species profiles are shown in Figs. 3.30 and 3.31. The computational predictions show excellent agreement with the experimental data for all species, including those used in the global rapid decomposition reactions (C_2H_4, C_2H_2, CH_2O) where the maximum discrepancy at the peak is maintained below 50%.

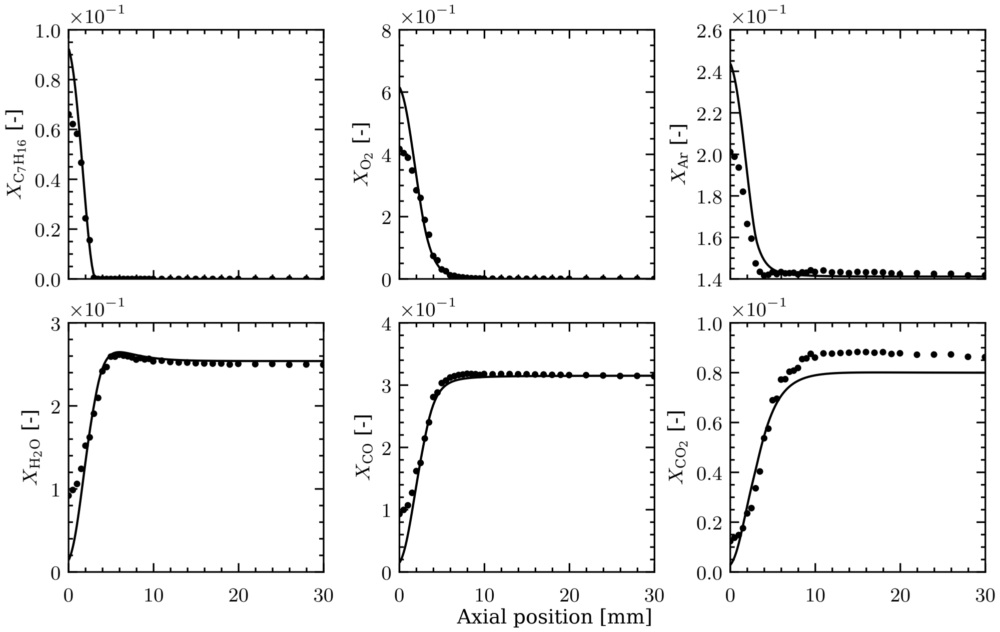

Figure 3.30: Major species profiles for a fuel-rich (ϕ = 1.69) premixed $C_7H_{16}/O_2/Ar$ flame at a pressure of 40 mbar with computational prediction. Dots are experimental data from [239].

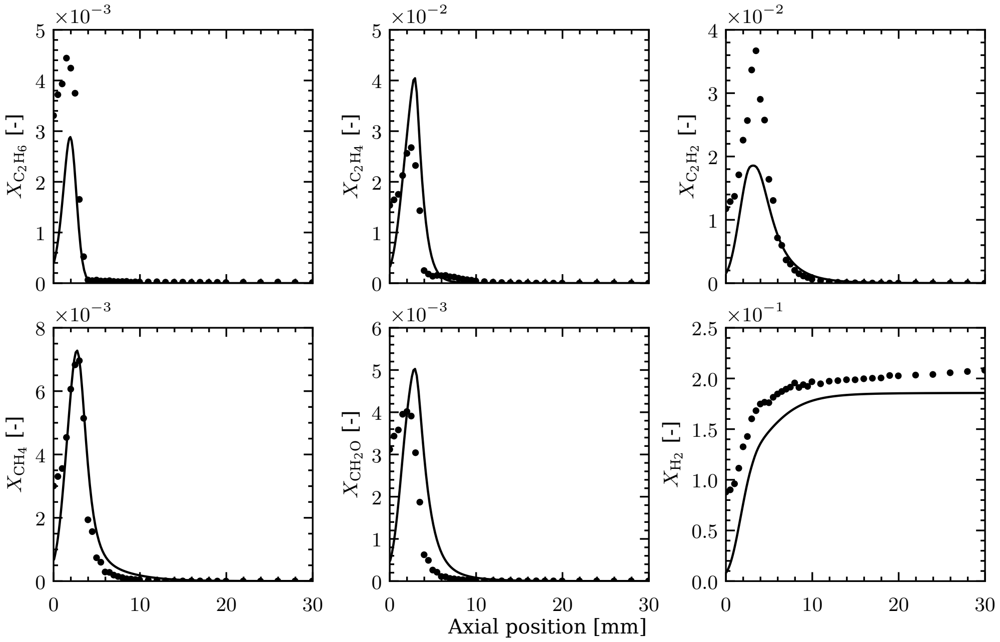

Figure 3.31: Other species profiles for a fuel-rich (ϕ = 1.69) premixed $C_7H_{16}/O_2/Ar$ flame at a pressure of 40 mbar with the legend as described in Fig. 3.30.

3.4 Summary

In this work a reduced iso-octane sub-mechanism has been further refined using recent studies of ignition delay times at lower temperatures and high pressures. The scheme has then been used to calculate laminar burning velocities and time histories in a shock tube. The key kinetic sensitivities have been identified and quantified. The final iso-octane sub-mechanism consists of 57 reactions and 18 species utilised within a scheme containing a total of 383 chemical reactions and 68 chemical species. The reduced size was achieved by using the rapid decomposition hypothesis to remove all C_3 to C_7 chemical species, with the exception of the butyl radical, iso-butene and hexanal which have been retained as place holders for the possible inclusion of further sub-mechanisms. The mechanism provides excellent agreement with the literature data for laminar burning velocities at atmospheric pressure. Additionally, good agreement with the experimental data for ignition delay times for temperatures above 750 K and a range of stoichiometries at elevated pressures was achieved. For temperatures below 750 K, limited experimental data exists but the error has been reduced in line with the data currently available. Deviation from the measured time history of OH has been examined and explained in the context of third body collision efficiencies.

Similarly, a reduced n-heptane sub-mechanism has also been adjusted and validated using experimental data for ignition delay times, laminar burning velocities and speciation data in a jet stirred reactor and a low pressure flame. Predictions of the global properties shows excellent agreement with the literature data for a range of stoichiometries, temperatures and pressures. Good agreement with the high temperature low pressure flame speciation data is shown, however some species used as 'buckets' in the rapid decomposition hypothesis show a significant deviation from the literature data in the low temperature JSR measurements. Future work would aim to further improve the n-heptane speciation predictions at lower temperatures.

Chapter 4 | Fuel additives

In this chapter chemical kinetic mechanisms for ammonia and nitromethane, both of which are fuel additives or fuels in their own right, were updated and further developed. A comprehensive validation was conducted for their oxidation, including highly sensitive and specific conditions such as the SNCR window for nitric oxide reduction by ammonia. The ammonia sub-mechanism was appended to the H sub-mechanism (see Appendix A) and the nitromethane sub-mechanism was further appended. A discussion of the key sensitivities is included. The ammonia section is based on the work presented by Greenblatt et al. [187].

4.1 Background

Additives are used to alter and ultimately enhance the performance of a fuel in a given context. In the most common and obvious application, including a fuel additive can improve the ignition and burning characteristics of the original fuel, to achieve a higher power output. For example, nitromethane has been used in high-performance racing vehicles [240], where maximum power output from the engine is desirable and since the engine is only required to be used for short lengths of time between servicing. On the other hand, an additive can also be used to moderate fuel reactivity, such as in the case of the addition of antiknock agents [241] which increase the octane rating of a fuel. In all cases, environmental and toxicological risks must be assessed in addition to the performance enhancement.

Additionally, additives may also be fuels in their own right, such as ammonia, and are blended with other fuels in order to reduce the environmental impact or for practical and safety reasons [22, 242]. Ammonia contains no carbon and as such when it is combusted emits no carbon emissions. This characteristic is a significant driving factor for interest in ammonia and its ability to displace fossil fuels in power production [243]. Both ammonia and nitromethane are discussed in this chapter and sub-mechanisms for each have been comprehensively validated with key uncertainties and sensitivities highlighted.

4.2 Ammonia

4.2.1 Introduction

The chemistry of ammonia has intermittently attracted interest over the last several decades with the current requirement for decarbonisation of the energy and transportation sectors reigniting interest through its potential use as an energy vector [243]. Elbaz et al. [242] further highlight the potential of direct use of ammonia in practical applications. Despite not producing carbon emissions, ammonia typically produces significant amounts of oxides of nitrogen (NO_x) with associated health and air-quality concerns as outlined by Kobayashi et al. [244] in the context of decarbonisation obligations in Japan and elsewhere. However, the chemistry of ammonia in terms of interactions with oxides of nitrogen is surprisingly complex. Maclean and Wagner [245] conducted the first detailed studies of the structure of ammonia/oxygen flames by measuring the evolution of selected species concentrations at ultra-low pressure. Lyon and co-workers [246, 247] developed the selective non-catalytic reduction (SNCR) method and showed that in a (narrow) temperature window ammonia has the potential to significantly reduce such emissions. Hanson and Salimian [162] acknowledged the harmful impact of emissions of oxides of nitrogen from ammonia combustion and conducted a thorough review of N/H/O chemistry building on the work by Baulch et al. [164].

The seminal work by Miller and Bowman [248] resulted in arguably the first comprehensively validated chemical reaction mechanism for nitrogen under combustion conditions. Many of the key elementary reactions required to capture thermal and prompt NO formation as well as those responsible for the SNCR process were included. The work has had a lasting impact with many of the reaction sequences that were included for the first time remaining in current formulations [249–251]. Lindstedt et al. [180, 214] further studied ammonia oxidation and formulated a comprehensively validated reaction mechanism based on the understanding derived by Miller and Bowman [248] while taking into account updates of the reaction kinetics presented by Cohen and Westberg [157], Baulch et al. [165] and Tsang and Herron [160]. Systematically reduced forms [252] were also derived in order to facilitate the inclusion of ammonia chemistry into calculation methods for turbulent flames. Subsequent reviews by Dean and Bozzelli [163] and Baulch et al. [166] served to refine rate constant recommendations and to highlight uncertainties in key reaction sequences. The latter include reactions in the pivotal reaction pathway passing via NNH which has an important role in determining the evolution of the H radical pool. Klippenstein et al. [249] used accurate coupled-cluster methods at the CCSD(T) and QCISD(T) levels combined with multi-reference electronic structure calculations to study reactions with O and O_2 as well as the $NH_2 + O_2$ and NH + NO reactions. Altinay and Macdonald [253] conducted an experimental study of amidogen (NH_2) and hydrogen radical recombination with temperatures limited to 533 K. Glarborg et al. [250] built on the work by Klippenstein et al. [249], Skreiberg et al. [254] and Glarborg et al. [255] and, with Dean and Bozzelli [163], identified the key role of the aminoxyl radical (H_2NO)[1] in promoting general applicability of models for the SNCR temperature window. The rate constant data was typically based on estimations with the related chemistry of NH_2OH investigated by Klippenstein

---

[1] Following naming convention of Baulch et al. [166]

et al. [256] and the H_2NO + O_2 reaction by Song et al. [257].

Despite the significant efforts outlined above, Kobayashi et al. [244] identified significant discrepancies in the ability of different proposed chemical mechanisms to predict basic (global) properties such as the laminar burning velocity and ignition delay times for fuel mixtures with ammonia. Accordingly, chemical reaction mechanisms have been developed by Okafor et al. [258], Han et al. [251, 259] and Shrestha et al. [260], amongst others, that provide good agreement with global properties. To assess the accuracy of chemical kinetic mechanisms such properties are important, but not sufficient as comprehensive validation against speciation data is essential in order to assess the ability to compute emissions of oxides of nitrogen. Examples of useful data sets include the laminar flame work by McLean and Wagner [245], Bian et al. [261, 262], Vandooren [263] and, recently using non-intrusive diagnostics, Zubairova et al. [264]. Similarly, the ability to reproduce the SNCR temperature window under different conditions can be viewed as an essential requirement given that it provides a potential route towards mitigating emissions of oxides of nitrogen. The reaction mechanism of Glarborg et al. [250] featured updated thermochemistry and was comprehensively validated against speciation and SNCR data. However, its performance for laminar burning velocities (LBVs) and ignition delay times (IDTs) was arguably less satisfactory [242, 251, 265, 266]. Good agreement with LBV data and major species profiles was achieved by Shrestha et al. [260, 267] with more limited consideration of SNCR and IDT data and of the critical balancing of H radical production via NNH and HNO. Stagni et al. [268] presented jet-stirred and flow reactor data and highlighted the importance of the H_2NO and HNO chemistries at low and high temperatures, respectively.

The N/H/O reaction mechanism extracted from the C/H/N/O mechanism of Glarborg et al. [250] features 31 chemical species and 202 elementary chemical reactions and constitutes a reference mechanism following the comprehensive validation performed in the manner of Miller and Bowman [248]. The current study (i) formulates a reduced size mechanism with 22 chemical species and 102 elementary reactions that takes into account recent kinetic data [269–272] and is subjected to (ii) a comprehensive validation process featuring speciation data obtained in laminar flames [261–263], SNCR related data [268, 273–276], ignition delay times [37] and laminar burning velocities [277–283]. (iii) Some outstanding uncertainties in the chemistry are highlighted and the impact discussed.

Table 4.1: Argon diluted ammonia/oxygen flames with nitric oxide and hydrogen addition with their respective reactant velocities (v_0) and operating pressure (absolute) with reactant compositions in mole fractions. For Flame 4A* the diluent is N_2 and the inlet flow velocity was selected to match the flame stabilisation point to the experimental stagnation flow data.

Flame	NH_3	NO	O_2	H_2	Ar / N_2	ϕ	P [kPa]	v_0 [m/s]	Ref.
1A	0.030	-	0.1270	0.2090	0.634	1.00	4.6000	0.654	[262]
1B	0.029	-	0.1040	0.3540	0.513	1.91	4.7500	1.310	[263]
1C	0.034	-	0.7650	0.1350	0.066	0.12	4.6000	0.598	[262]
2A	0.015	0.015	0.1195	0.2315	0.619	1.00	4.6000	0.654	[262]
2B	0.017	0.017	0.7562	0.1605	0.049	0.12	4.6000	0.598	[262]
3D	0.480	-	0.5100	-	0.010	0.71	4.6663	0.608	[261]
4A*	0.200	-	0.1670	-	0.633	0.90	101.33	-	[264]

4.2.2 Validation data sets

A comprehensive selection of validation data covering speciation in laminar flames, ignition delay times and the chemistry of the SNCR window were selected in order to provide a thorough assessment of the ability of the selected and revised reaction mechanisms to reproduce experimentally observed trends. All data sets, as well as the applied kinetic rate parameters, contain uncertainties and it can be viewed as essential to conduct a comprehensive validation of the type performed by Miller and Bowman [248] in order to avoid over-fitting aimed at reproducing more limited data sets. This is particularly important when considering global properties such as laminar burning velocities that do not in isolation significantly constrain the parameter space. The low-pressure laminar flame data sets selected are given in Table 4.1 and stem from the work by Bian et al. [261, 262] and Vandooren [263]. The flames have been used extensively for validation purposes in past work [214, 250] so offer a useful point of comparison and remain important in part due to the diversity of conditions that include mixtures of NH_3 and H_2 as well as the use of NO addition. Furthermore, the peak temperatures range from around 1200 K to well over 2000 K and the conditions are accordingly of relevance to the evaluation of both the SNCR and high temperature chemistry. However, while these experiments were conducted by the same group ensuring similar set-ups and uncertainties between experiments, any systematic errors may be consistent in all datasets. Therefore, data from multiple laboratories helps to minimise the impact of erroneous data and the recent non-intrusive measurements by Zubairova et al. [264], obtained in a stagnation flow geometry, were also considered.

Table 4.2: Shock tube experiments of Mathieu and Petersen [37] at 1.4, 11.0 and 30.0 atm for fuel lean, stoichiometric and rich fuel mixtures diluted with 99% argon.

Pressure [atm]	ϕ -	Temperature range [K]
1.4	0.5, 1.0, 2.0	1900 - 2500
11.0	0.5, 1.0, 2.0	1600 - 2110
30.0	0.5, 1.0, 2.0	1540 - 1910

The ability of chemical mechanisms to reproduce ignition delay times is of particular importance in the context of flame stabilisation through autoignition (e.g. flameless combustion) as considered by Greenblatt et al. [187] in the context of lifted turbulent flames. The accurate reproduction will also influence the amount of local extinction experienced in turbulent flames. The selected validation data sets of Mathieu and Petersen [37] cover a wide range of conditions, as shown in Table 4.2. The ability to reproduce experimental LBV data for ammonia–air flames is subject to additional uncertainties due to the impact of moderate amounts of heat loss [268, 284] and are explored in more detail below by consideration of different heat loss factors.

Given the potential benefits of the SNCR temperature window in reducing emis-

Table 4.3: Experimental SNCR data [273–276] with varied residence times and reactant compositions of NH_3, NO, O_2 and H_2O. The reactant compositions were balanced with N_2.

NH_3 [ppm]	NO [ppm]	O_2 [%]	H_2O [%]	Residence time [s]	Ref.
750	500	2.0	-	525.0/T(K)	[273]
1000	25	40.0	-	48.7/T(K)	[274]
1000	100	40.0	-	48.7/T(K)	[274]
1000	250	40.0	-	48.7/T(K)	[274]
832	507	4.0	-	92.7/T(K)	[275]
832	507	4.0	2.8	92.7/T(K)	[275]
832	507	4.0	10.0	92.7/T(K)	[275]
1000	500	1.0	5.0	88.0/T(K)	[276]
1000	500	10.0	5.0	88.0/T(K)	[276]
1000	500	20.0	5.0	88.0/T(K)	[276]
1000	500	50.0	5.0	88.0/T(K)	[276]

sion of oxides of nitrogen, a wide range of SNCR related data sets is considered as outlined in Table 4.3. The data includes the impact of variations in residual O_2 and H_2O concentrations. The related data set of Stagni et al. [268] that includes some speciation data at higher temperatures is also included.

The N/H/O chemistry extracted from the comprehensive model of Glarborg et al. [250] is here treated as the reference point due to the extensive recent validation. The mechanism of Lindstedt et al. [214] is of similar size (22 chemical species and 95 elementary reactions) to that derived in the current work (22 chemical species and 102 elementary reactions) and provides a further point of comparison.

Table 4.4: Reduced size ammonia mechanism applied in the current work. Forward rate constants as $k_f = AT^n e^{-E_a/RT}$. Units: kg, m, s, kmol, kJ, K. Chaperon efficiencies used to evaluate M set to unity unless otherwise indicated.

No.	Reaction	A	n	E_a	Ref.
4.1	$H + O_2 \rightleftharpoons O + OH$	1.040×10^{11}	0.00	6.396×10^{4}	[285]
4.2	$O + H_2 \rightleftharpoons H + OH$	5.080×10^{1}	2.67	2.633×10^{4}	[286]
4.3	$H_2 + OH \rightleftharpoons H_2O + H$	2.160×10^{5}	1.51	1.433×10^{4}	[286]
4.4	$OH + OH \rightleftharpoons O + H_2O$	3.340×10^{1}	2.42	-8.065×10^{3}	[166]
4.5	$H_2 + M \rightleftharpoons H + H + M$ H_2 = 2.50; H_2O = 12.0; Ar = 0.0	4.577×10^{16}	-1.40	4.367×10^{5}	[286]
4.6	$H_2 + M \rightleftharpoons H + H + M$ Ar = 1.0; otherwise = 0.0	5.840×10^{15}	-1.10	4.367×10^{5}	[286]

Table 4.4 (Continued)

No.	Reaction	A	n	E_a	Ref.
4.7	$O + O + M \rightleftharpoons O_2 + M$	6.165×10^{9}	-0.50	0	[286]
	$H_2 = 2.50$; $H_2O = 12.0$; $Ar = 0.0$				
4.8	$O + O + M \rightleftharpoons O_2 + M$	1.886×10^{7}	0.00	-7.481×10^{3}	[286]
	$Ar = 1.0$; otherwise = 0.0				
4.9	$O + H + M \rightleftharpoons OH + M$	4.714×10^{12}	-1.00	0	[286]
	$H_2 = 2.50$; $H_2O = 12.0$; $Ar = 0.75$				
4.10	$H_2O + M \rightleftharpoons H + OH + M$	6.064×10^{24}	-3.32	5.054×10^{5}	[287]
	$H_2 = 3.0$; $H_2O = 0.0$; $O_2 = 1.5$; $N_2 = 2.0$				
4.11	$H_2O + M \rightleftharpoons H + OH + M$	1.006×10^{23}	-2.44	5.028×10^{5}	[287]
	$H_2O = 1.0$; otherwise = 0.0				
4.12	$H + O_2 \rightleftharpoons HO_2$	4.651×10^{9}	0.44	0	[288]
	k_0	6.366×10^{14}	-1.72	2.196×10^{3}	[286]
	$F_c = 0.5$				
	$H_2 = 2.0$; $H_2O = 14.0$; $O_2 = 0.78$; $Ar = 0.67$				
4.13	$HO_2 + H \rightleftharpoons H_2 + O_2$	2.750×10^{3}	2.09	-6.071×10^{3}	[289]
4.14	$HO_2 + H \rightleftharpoons OH + OH$	7.079×10^{10}	0.00	1.234×10^{3}	[286]
4.15	$HO_2 + O \rightleftharpoons O_2 + OH$	1.750×10^{10}	0.00	-1.660×10^{3}	[158]
4.16	$HO_2 + OH \rightleftharpoons H_2O + O_2$	2.890×10^{10}	0.00	-2.079×10^{3}	[286]
4.17	$HO_2 + HO_2 \rightleftharpoons H_2O_2 + O_2$	4.200×10^{11}	0.00	5.013×10^{4}	[286]
+		1.300×10^{8}	0.00	-6.817×10^{3}	[286]
4.18	$H_2O_2 \rightleftharpoons OH + OH$	2.000×10^{12}	0.90	2.040×10^{5}	[290]
	k_0	2.490×10^{21}	-2.30	2.040×10^{5}	
	$F_c = 0.43$				
	$H_2 = 3.7$; $H_2O = 7.5$; $H_2O_2 = 7.7$; $N_2 = 1.5$; $Ar = 0.65$				
4.19	$H_2O_2 + H \rightleftharpoons H_2O + OH$	2.410×10^{10}	0.00	1.661×10^{4}	[286]
4.20	$H_2O_2 + H \rightleftharpoons HO_2 + H_2$	4.820×10^{10}	0.00	3.326×10^{4}	[286]
4.21	$H_2O_2 + O \rightleftharpoons OH + HO_2$	9.630×10^{3}	2.00	1.661×10^{4}	[286]
4.22	$H_2O_2 + OH \rightleftharpoons HO_2 + H_2O$	4.600×10^{10}	0.00	2.187×10^{4}	[285]
4.23	$NH_3 + M \rightleftharpoons NH_2 + H + M$	2.510×10^{13}	0.00	3.924×10^{5}	[162]
4.24	$NH_3 + H \rightleftharpoons NH_2 + H_2$	6.360×10^{2}	2.39	4.256×10^{4}	[214, 248]
4.25	$NH_3 + OH \rightleftharpoons NH_2 + H_2O$	4.300	2.83	-1.802×10^{3}	[291]
4.26	$NH_3 + O \rightleftharpoons NH_2 + OH$	2.790×10^{-1}	3.29	1.871×10^{4}	[256]
4.27	$NH_2 + H \rightleftharpoons NH + H_2$	5.670×10^{8}	0.59	1.526×10^{4}	[214]
4.28	$NH_2 + OH \rightleftharpoons NH + H_2O$	9.000×10^{4}	1.50	-1.912×10^{3}	[157, 214]
4.29	$NH_2 + O \rightleftharpoons NH + OH$	7.000×10^{9}	0.00	0	[157, 214]
+		3.300×10^{5}	1.50	2.124×10^{4}	[163]
4.30	$NH_2 + O \rightleftharpoons HNO + H$	8.800×10^{11}	-0.50	0	adj. [214]
4.31	$NH_2 + NO \rightleftharpoons N_2 + H_2O$	2.610×10^{16}	-2.37	3.624×10^{3}	[292]
4.32	$NH_2 + NO \rightleftharpoons NNH + OH$	4.290×10^{7}	0.29	-3.640×10^{3}	[292]
4.33	$NH_2 + O_2 \rightleftharpoons HNO + OH$	2.900×10^{-5}	3.76	7.609×10^{4}	[249]
4.34	$NH_2 + HO_2 \rightleftharpoons NH_3 + O_2$	6.040×10^{15}	-1.91	1.280×10^{3}	[271]
+		5.910×10^{4}	1.59	-5.745×10^{3}	[271]

Table 4.4 (Continued)

No.	Reaction	A	n	E_a	Ref.
4.35	$NH_2 + HO_2 \rightleftharpoons HNO + H_2O$	$1.020{\times}10^{9}$	0.17	$-3.925{\times}10^{3}$	[271]
4.36	$NH_2 + NH \rightleftharpoons N_2H_2 + H$	$4.260{\times}10^{11}$	-0.27	$-3.240{\times}10^{2}$	[256]
4.37	$NH_2 + NH \rightleftharpoons NH_3 + N$	9.580	2.48	$4.490{\times}10^{2}$	[256]
4.38	$NH_2 + NH_2 \rightleftharpoons N_2H_2 + H_2$	$1.740{\times}10^{5}$	1.02	$4.931{\times}10^{4}$	[256]
4.39	$NH_2 + NH_2 \rightleftharpoons NH + NH_3$	$5.640{\times}10^{-3}$	3.53	$2.311{\times}10^{3}$	[256]
4.40	$NH + H \rightleftharpoons N + H_2$	$1.000{\times}10^{10}$	0.00	0	[214]
4.41	$NH + O \rightleftharpoons NO + H$	$1.084{\times}10^{11}$	0.00	$2.494{\times}10^{3}$	[166]
4.42	$NH + OH \rightleftharpoons N + H_2O$	$1.590{\times}10^{4}$	1.74	$-2.411{\times}10^{3}$	[256]
4.43	$NH + OH \rightleftharpoons HNO + H$	$3.200{\times}10^{11}$	-0.38	$-1.925{\times}10^{2}$	[256]
4.44	$NH + O_2 \rightleftharpoons NO + OH$	$2.010{\times}10^{13}$	-1.38	$2.373{\times}10^{4}$	[293]
4.45	$NH + O_2 \rightleftharpoons HNO + O$	$4.050{\times}10^{8}$	0.09	$4.465{\times}10^{4}$	[293]
4.46	$NH + N \rightleftharpoons N_2 + H$	$6.410{\times}10^{8}$	0.51	$7.732{\times}10^{1}$	[294]
4.47	$NH + NO \rightleftharpoons N_2O + H$	$2.746{\times}10^{12}$	-0.78	$3.326{\times}10^{2}$	[166]
4.48	$NH + NO \rightleftharpoons N_2 + OH$	$6.865{\times}10^{11}$	-0.78	$3.326{\times}10^{2}$	[166]
4.49	$NH + NH \rightleftharpoons N_2H_2$	$6.260{\times}10^{10}$	-0.04	$-6.730{\times}10^{2}$	[256]
4.50a	$NNH \rightleftharpoons N_2 + H$	$1.000{\times}10^{9}$	0.00	0	[249]
4.50b	$NNH \rightleftharpoons N_2 + H$	$6.500{\times}10^{7}$	0.00	0	[258, 295]
4.50c	$NNH + M \rightleftharpoons N_2 + H + M$	$7.600{\times}10^{9}$	0.00	$2.930{\times}10^{4}$	pw
4.51a	$NNH + O_2 \rightleftharpoons N_2 + HO_2$	$5.600{\times}10^{11}$	-0.39	$-5.439{\times}10^{1}$	[249]
4.51b	$NNH + O_2 \rightleftharpoons N_2 + HO_2$	$2.000{\times}10^{11}$	0.00	0	[258, 295]
4.51c	$NNH + O_2 \rightleftharpoons N_2 + HO_2$	$1.200{\times}10^{9}$	-0.34	$6.236{\times}10^{2}$	[163]
4.51d	$NNH + O_2 \rightleftharpoons N_2 + H + O_2$	$5.0{\times}10^{10}$	0.00	0.00	[258, 296]
4.52	$NNH + O \rightleftharpoons NH + NO$	$5.200{\times}10^{8}$	0.38	$-1.711{\times}10^{3}$	[249]
4.53	$NNH + O \rightleftharpoons N_2 + OH$	$1.200{\times}10^{10}$	0.15	$-9.079{\times}10^{2}$	[249]
4.54	$NNH + O \rightleftharpoons N_2O + H$	$1.900{\times}10^{11}$	-0.27	$-9.205{\times}10^{1}$	[249]
4.55	$NNH + H \rightleftharpoons N_2 + H_2$	$1.000{\times}10^{11}$	0.00	0	[248, 250]
4.56	$NNH + OH \rightleftharpoons N_2 + H_2O$	$2.390{\times}10^{19}$	-2.88	$1.023{\times}10^{4}$	[297]
4.57	$NNH + NH_2 \rightleftharpoons N_2 + NH_3$	$5.000{\times}10^{10}$	0.00	0	[250]
4.58	$N + O_2 \rightleftharpoons NO + O$	$5.841{\times}10^{6}$	1.01	$2.594{\times}10^{4}$	[166]
4.59	$N + OH \rightleftharpoons NO + H$	$1.084{\times}10^{11}$	-0.20	0	[166]
4.60	$N + NO \rightleftharpoons N_2 + O$	$2.108{\times}10^{10}$	0.00	0	[166]
4.61	$N_2H_2 + M \rightleftharpoons NNH + H + M$ $H_2O = 7.0$	$1.900{\times}10^{24}$	-3.05	$2.766{\times}10^{5}$	[254]
4.62	$N_2H_2 + H \rightleftharpoons NNH + H_2$	$8.490{\times}10^{1}$	2.63	$-9.560{\times}10^{2}$	[298]
4.63	$N_2H_2 + OH \rightleftharpoons NNH + H_2O$	$6.000{\times}10^{-2}$	3.40	$-5.704{\times}10^{3}$	[298]
4.64	$N_2H_2 + NH_2 \rightleftharpoons NH_3 + NNH$	$8.800{\times}10^{-5}$	4.05	$-6.735{\times}10^{3}$	[298]
4.65	$N_2O + O \rightleftharpoons NO + NO$	$9.150{\times}10^{10}$	0.00	$1.158{\times}10^{5}$	[299]
4.66	$N_2O + O \rightleftharpoons N_2 + O_2$	$1.660{\times}10^{9}$	0.00	$4.874{\times}10^{4}$	[270]
4.67	$N_2O + H \rightleftharpoons N_2 + OH$	$1.280{\times}10^{5}$	1.84	$5.645{\times}10^{4}$	adj. [249]

Table 4.4 (Continued)

No.	Reaction	A	n	E_a	Ref.
4.68	$N_2O \rightleftharpoons N_2 + O$	9.900×10^{10}	0.00	2.423×10^{5}	[166]
	k_0	6.022×10^{11}	0.00	2.404×10^{5}	
	$F_c = 1.167 - 1.25\times10^{-4}$ T				
4.69	$N_2O + OH \rightleftharpoons N_2 + HO_2$	1.300×10^{-5}	4.72	1.536×10^{5}	[163]
4.70	$NO + H \rightleftharpoons HNO$	1.500×10^{12}	-0.41	0	[160]
	k_0	2.400×10^{8}	0.21	-6.485×10^{3}	[300]
	$F_c = 0.82$				
	$N_2 = 1.6$				
4.71	$HNO + H \rightleftharpoons H_2 + NO$	6.690×10^{7}	0.94	2.070×10^{3}	[301]
4.72	$HNO + O \rightleftharpoons OH + NO$	3.600×10^{10}	0.00	0	[214]
4.73	$HNO + OH \rightleftharpoons H_2O + NO$	4.820×10^{10}	0.00	4.157×10^{3}	[160]
4.74	$HNO + HO_2 \rightleftharpoons HNO_2 + OH$	2.000	2.36	3.757×10^{4}	[250]
4.75	$HNO + HNO \rightleftharpoons H_2O + N_2O$	8.430×10^{5}	0.00	1.297×10^{4}	[160]
4.76	$HNO + NH_2 \rightleftharpoons NH_3 + NO$	0.587	2.95	-1.452×10^{4}	[302]
4.77	$HNO + NO \rightleftharpoons N_2O + OH$	8.510×10^{9}	0.00	1.239×10^{5}	[303]
4.78a	$HNO + O_2 \rightleftharpoons NO + HO_2$	3.160×10^{9}	0.00	1.260×10^{4}	[214, 304]
4.78b	$HNO + O_2 \rightleftharpoons NO + HO_2$	2.000×10^{10}	0.00	6.694×10^{4}	[163, 250]
4.79	$HNO + NO_2 \rightleftharpoons HNO_2 + NO$	6.022×10^{8}	0.00	8.346×10^{3}	[160]
4.80	$NO + HO_2 \rightleftharpoons NO_2 + OH$	2.170×10^{9}	0.00	-2.254×10^{3}	[305]
4.81	$NO + O \rightleftharpoons NO_2$	1.300×10^{12}	-0.75	0	[160]
	k_0	4.714×10^{18}	-2.87	6.493×10^{3}	
	$F_c = 0.95 - 1.0\times10^{-4}$ T				
4.82	$NO + OH \rightleftharpoons HNO_2$	1.990×10^{9}	-0.05	-3.018×10^{3}	[160]
	k_0	5.077×10^{17}	-2.51	-2.830×10^{2}	
	$F_c = 0.62$				
4.83	$NO_2 + H \rightleftharpoons NO + OH$	8.850×10^{10}	0.00	0	[306]
4.84	$NO_2 + O \rightleftharpoons NO + O_2$	3.900×10^{9}	0.00	-1.002×10^{3}	[160]
4.85	$HNO_2 + H \rightleftharpoons H_2 + NO_2$	2.300×10^{1}	2.80	8.368×10^{3}	[269]
4.86	$HNO_2 + H \rightleftharpoons OH + HNO$	3.700×10^{4}	1.80	2.343×10^{4}	[269]
4.87	$HNO_2 + H \rightleftharpoons NO + H_2O$	3.400×10^{6}	1.10	2.343×10^{4}	[269]
4.88	$HNO_2 + OH \rightleftharpoons H_2O + NO_2$	1.510×10^{9}	0.00	-2.170×10^{3}	[305]
4.89	$HNO_2 + O \rightleftharpoons OH + NO_2$	1.200×10^{10}	0.00	2.494×10^{4}	[160]
4.90	$NH_2 + HO_2 \rightleftharpoons H_2NO + OH$	2.190×10^{6}	0.79	-5.975×10^{3}	[271]
4.91	$NH_2 + NO_2 \rightleftharpoons H_2NO + NO$	8.600×10^{8}	0.11	-4.962×10^{3}	[250]
4.92	$NH_2 + O_2 \rightleftharpoons H_2NO + O$	2.600×10^{8}	0.49	1.215×10^{5}	[249]
4.93	$H_2NO + M \rightleftharpoons HNO + H + M$	2.800×10^{21}	-2.83	2.716×10^{5}	[163]
4.94	$H_2NO + H \rightleftharpoons HNO + H_2$	3.000×10^{4}	2.00	8.368×10^{3}	[250]
4.95	$H_2NO + H \rightleftharpoons NH_2 + OH$	5.000×10^{10}	0.00	0	[250]
4.96	$H_2NO + O \rightleftharpoons HNO + OH$	3.000×10^{4}	2.00	8.368×10^{3}	[250]
4.97	$H_2NO + OH \rightleftharpoons HNO + H_2O$	1.080×10^{11}	0.00	0	[250]
4.98	$H_2NO + HO_2 \rightleftharpoons HNO + H_2O_2$	5.410×10^{1}	2.16	-1.505×10^{4}	[272]

Table 4.4 (Continued)

No.	Reaction	A	n	E_a	Ref.
4.99a	$H_2NO + O_2 \rightleftharpoons HNO + HO_2$	1.730×10^{2}	2.19	7.535×10^{4}	[272]
4.99b	$H_2NO + O_2 \rightleftharpoons HNO + HO_2$	0.230	2.99	6.904×10^{4}	[250]
4.100	$H_2NO + NH_2 \rightleftharpoons HNO + NH_3$	9.490×10^{9}	-0.08	-6.879×10^{3}	[272]
4.101	$H_2NO + NO \rightleftharpoons HNO + HNO$	2.000×10^{1}	2.00	5.439×10^{4}	[250]
4.102	$H_2NO + NO_2 \rightleftharpoons HNO_2 + HNO$	7.950×10^{-3}	2.95	-1.378×10^{4}	[272]
4.103*	$N_2O + O_2(b^1\Sigma_g^+)^\dagger \rightleftharpoons$ products	1.584×10^{3}	1.50	-4.906×10^{3}	[307]
4.104*	$N_2O_3 \rightleftharpoons NO + NO_2$	4.800×10^{14}	0.40	4.057×10^{4}	[305]
	k_0 (for T = 225–300 K)	4.070×10^{35}	-8.70	4.057×10^{4}	[305]
4.105*	$N_2O + O_2 \rightleftharpoons NO + NO_2$	2.560×10^{8}	0.00	4.057×10^{4}	pw‡
4.106*	$H_2 + O(^1D)^\dagger \rightleftharpoons H_2O$	1.000×10^{9}	0.50	0	[308]
4.107*	$H + HO_2 \rightleftharpoons H_2O + O(^1D)^\dagger$	4.840×10^{10}	0.00	7.416×10^{3}	[308]
4.108*	$H_2 + O(^1D)^\dagger \rightleftharpoons OH + H$	3.000×10^{10}	0.50	1.413×10^{5}	[308]
4.109*	$N_2O + O(^1D)^\dagger \rightleftharpoons N_2 + O_2$	2.650×10^{10}	0.00	0	[305]
4.110*	$N_2O + O(^1D)^\dagger \rightleftharpoons NO + NO$	4.340×10^{10}	0.00	0	[305]

*See text, impact evaluation only, †electronically excited state, ‡Fitted global step.

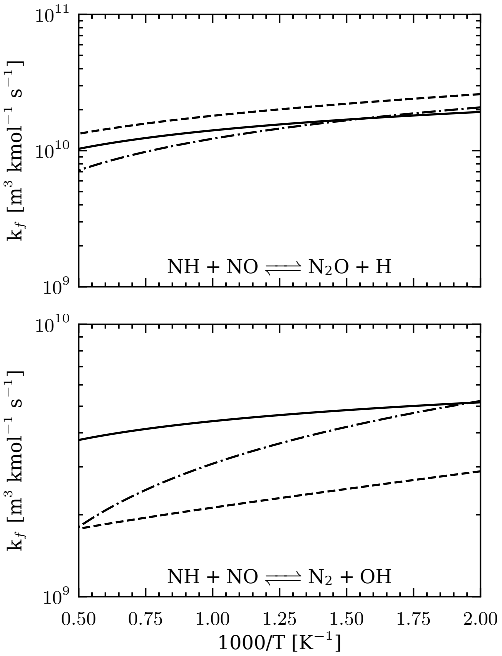

Figure 4.1: Rate comparison plots for NH + NO to (top) N_2O + H and (bottom) N_2 + OH. Solid lines from Miller and Melius [309]; dashed lines from Klippenstein et al. [249]; dot-dashed lines from Glarborg et al. [250] using a fit to the branching ratios of Baulch et al. [166].

4.2.3 Comments on the chemical mechanism

The reaction pathways for ammonia oxidation have been extensively discussed in recent studies as summarised by Klippenstein et al. [249] and Glarborg et al. [250], amongst others, with a few key aspects mentioned below. The N/H/O chemistry extracted from the comprehensive model of Glarborg et al. [250] comprises 31 chemical species and 202 elementary reactions and provides the reference (comparison) point. The species removed from this mechanism following an extensive validation procedure were N_2H_4, N_2H_3, H_2NN, NH_2OH, HNOH, HON, HONO, $HONO_2$ and NO_3 resulting in 22 species and 102 reactions as shown in Table 4.4 with reactions (R4.50a,R4.51a) considered as the "current mechanism". The impact of the simplifications is discussed below through comparisons with the validation data sets and also with the mechanisms of Lindstedt et al. [214] and Okafor et al. [258].

The updated reaction channels (R4.85,R4.86,R4.87) for HNO_2 + H from Fuller and Goldsmith [269] have been incorporated along with the data for $NH_2 + HO_2 \rightleftharpoons H_2NO + OH$ (R4.90) from Klippenstein and Glarborg [271]. The data from Pham et al. [270] for (R4.66) $N_2O + O \rightleftharpoons N_2 + O_2$ has also been used. The importance of the aminoxyl radical (H_2NO) chemistry was identified by Dean and Bozzelli [163] with Glarborg et al. [250] acknowledging that it is not well established. Subsequent studies have further highlighted the importance [268] at low temperatures. The associated reactions (R4.98,R4.99,R4.100,R4.102) have been updated following the recent theoretical study by Stagni and Cavalotti [272] with reaction (R4.99) identified as particularly sensitive for IDTs at low temperature [266].

$$H_2NO + O_2 \rightleftharpoons HNO + HO_2 \qquad \text{(R4.99)}$$

The reverse of the thermal decomposition of ammonia (R4.23) is chain terminating and impacts ignition delay times while (R4.27) leads to further oxidation.

$$\mathrm{NH_3 + M \rightleftharpoons NH_2 + H + M} \tag{R4.23}$$

$$\mathrm{NH_2 + H \rightleftharpoons NH + H_2} \tag{R4.27}$$

Although, it is not uncommon for the (R4.23) to be omitted altogether [248, 259], the reaction contributes to the net loss of NH_2 radicals. Altinay and Macdonald [253] studied the reverse of (R4.23) up to a temperature of 533 K and a low-pressure limit rate expression was determined with a high-pressure limit suggested using analogous CH_3 + H and OH + H recombination reactions. The reaction is important for ignition delay times and the recommendation by Hanson and Salimian [162] applicable to a temperature range of 1740 – 3450 K is preferred here, although both were considered. At all conditions (R4.23) results in the reformation of NH_3 and is therefore chain terminating and delays ignition. For auto-igniting mixtures at 1900 K, (R4.23) accounts for 20% and 77% of NH_3 production at pressures of 1.4 and 30 atm, respectively. This corresponds to 12% of NH_2 consumption at 30 atm with (R4.27) the major (52%) pathway.

The subsequent reaction of imidogen (NH) with nitric oxide (R4.47,R4.48) is of key importance in balancing the formation of N_2O, as discussed below, and a comparison of rate constants is shown in Fig. 4.1.

$$\mathrm{NH + NO \rightleftharpoons N_2O + H} \tag{R4.47}$$

$$\mathrm{NH + NO \rightleftharpoons N_2 + OH} \tag{R4.48}$$

There is good agreement on the overall rate and a reasonable consensus on the branching ratio with the production of N_2O + H favoured. Klippenstein et al. [249] favour the pathway more strongly compared to Miller and Melius [309] and Glarborg et al. [250]. The latter study fitted the branching ratios of Baulch et al. [166] and the same methodology has been applied here. The chemistry of amidogen (NH_2) is crucial in overall reaction progress and the growth of the radical pool. The two pathways in reaction (R4.31,R4.32) are critical in SNCR behaviour with reaction (R4.32) the major pathway for NNH production leading to subsequent H radical production. Furthermore, they are the most significant reactions for the consumption of NH_2 and NO under such conditions and account for over 80% of each. Reaction (R4.31) is, effectively, chain terminating and (R4.32) leads to chain branching via the subsequent decomposition of NNH. Accordingly, there is a high sensitivity of model predictions to the branching fraction $\alpha = k_{f,32}/(k_{f,31} + k_{f,32})$ and for the SNCR process to be self-sustaining this must be greater than 25% [248]. More recent studies have established a branching fraction in the range 30 – 40% for temperatures around the SNCR window [295, 310]. Examples of suggested rates for reactions (R4.31) and (R4.32) from the work of Lindstedt et al. [214], Miller and co-workers [295, 310] and the experimental study by Song et al. [292] are compared in Fig. 4.2. As shown, there is good agreement between different studies with modest uncertainties, particularly for the SNCR temperature window, as discussed by Miller and Klippenstein [310] and Song et al. [292]. The latter rates are used by Glarborg et al. [250] and in the current work. As noted by Klippenstein et al. [249], reactions (R4.31, R4.32) have a high sensitivity but once the branching ratio is fixed the lifetime of NNH becomes critical.

$$\mathrm{NH_2 + NO \rightleftharpoons N_2 + H_2O} \qquad \text{(R4.31)}$$

$$\mathrm{\rightleftharpoons NNH + OH} \qquad \text{(R4.32)}$$

The subsequent NNH dissociation via reaction (R4.50) is of major importance for H radical production under SNCR conditions. A wide range of rates [214, 249, 297, 311] have been proposed as shown in Fig. 4.3 with no consensus as outlined by Klippenstein et al. [249]. The lifetime of NNH has been estimated from a millisecond to well below a nanosecond [249, 255].

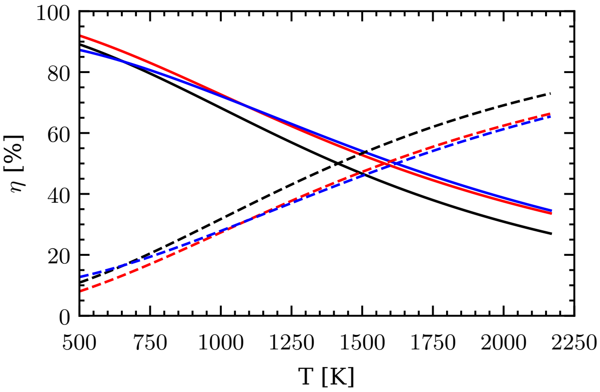

Figure 4.2: Comparison of the branching fractions for (R4.31) (solid line) and (R4.32) (dashed line) for the rates of Lindstedt et al. [214] (black), Miller and co-workers [295, 310] (red) and Song et al. [292] (blue).

$$\mathrm{NNH\,(+M)} \rightleftharpoons \mathrm{N_2 + H\,(+M)} \tag{R4.50}$$

$$\mathrm{NNH + O_2} \rightleftharpoons \mathrm{N_2 + HO_2} \tag{R4.51}$$

Bozzelli and Dean [297] estimated an energy barrier of 7 ± 1 kcal/mol for (R4.50), assuming stabilisation, somewhat below the values (e.g. 10.6 ± 0.2 [312]) discussed by Klippenstein et al. [249]. Vandooren et al. [311] analysed the low-pressure data set of Bian et al. [261] and suggested a third-body reaction scaling and proposed a rate based on a truncated steady-state balance. The short lifetime of NNH suggests that such an analysis is valid. However, the higher estimated energy barrier 16 ± 2 kcal/mol was impacted by uncertainties in the thermochemistry including the heat of formation of NNH. The authors further discussed the measured [261] non-zero amounts of NNH (mass 29) and could not rule out the fragmentation of N_2H_2 or HNNOH as an alternative source. The uni-molecular barrierless rate from Klippenstein et al. [249] of 1×10^9 s^{-1} is typically applied in recent work [250, 259, 268] and is applied here. Klippenstein et al. [249] discuss the large range (3×10^{-11} to 4×10^{-8} s) of predicted ground state lifetimes of NNH and confine the best estimates to the comparatively narrow range 8×10^{-10} to 2×10^{-9} s. A comparison of proposed rates is shown in Fig. 4.3 , where bimolecular rates have been adjusted for comparison purposes by assuming a mixture with air at atmospheric pressure as $[M] \simeq \rho/\overline{M_w} = P/RT$ with $\overline{M_w}$ the mean molecular weight.

The matter is further complicated by the potentially competing reaction NNH + O_2 (R4.51). The rate suggested by Dean and Bozzelli [163] is approximately 300 times slower than that of Klippenstein et al. [249] , as shown in Fig. 4.3. Competition with NNH dissociation suggests that selecting a slower rate for (R4.51) enables a slower (R4.50) to still reproduce the SNCR behaviour through balanced H radical formation. There is, however, an impact on global properties with faster NNH decomposition resulting, for example, in higher laminar burning velocities. A possible alternative pairing using the slower (R4.51c) rate of Dean and Bozzelli [163], with a rate explored in this work (R4.50c) to achieve appropriate balancing was also considered. The formulation of a bimolecular rate for (R4.50c) with an energy barrier of 7 kcal/mol [297] to accompany the slower rate (R4.51c) [163] while maintaining a similar H radical balance over the SNCR temperature window is also discussed. Experimentally, NNH has been inferred to have a lifetime of 0.5 μs [314] but theoretical work has estimated it to be several orders of magnitude slower [249, 312]. An energy diagram from Klippenstein et al. [249], based on the work of Bozkaya et al. [312], is shown in Fig. 4.4. If there is stabilisation of NNH in the well, then the partial equilibrium concentration of NNH would become non-trivial and a rate including the energy barrier and third body collision partners may become relevant. However, given the uncertainties reaction (R4.50c) is used for illustration purposes and constitutes a lower limit as it approaches the value 1×10^7 s^{-1} used by Miller and Glarborg [315] and falls below 2.5×10^7 s^{-1} defined by Klippenstein et al. [249] as the lower limit. The different (R4.50,R4.51) reaction pairs, see Table 4.4, also include (R4.50b,R4.51b) [258, 295] utilised in the mechanism of Okafor et al. [258], as discussed below. The impact of the balancing of (R4.50,R4.51) is discussed below and later in the context of SNCR predictions through the comparison of the

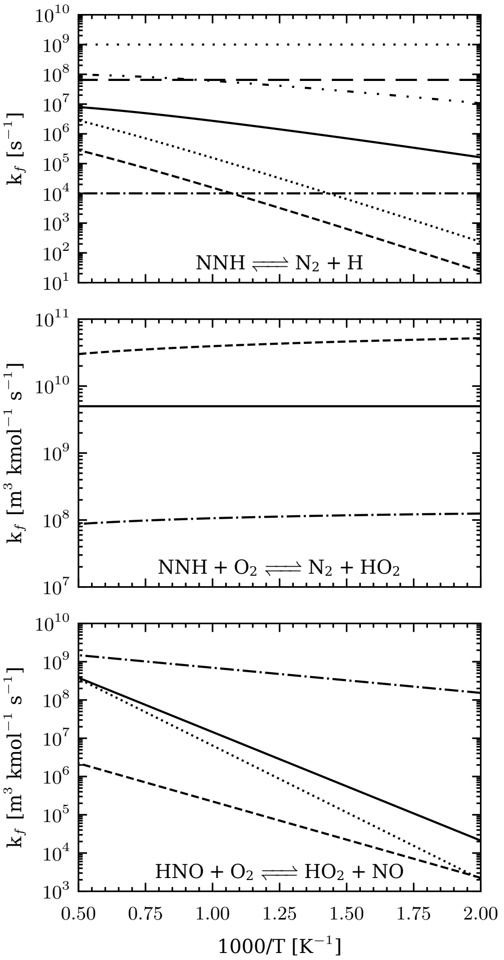

Figure 4.3: Rate comparisons: (top) NNH (+ M) $\rightleftharpoons$ N_2 + H (+ M) Reaction (R4.50b) (solid line), Lindstedt et al. [214] (dashed line), Miller and Bowman [248] (dot-dashed line), Vandooren et al. [311] (dotted line), Bozzelli and Dean [297] (dot-dot-dash line), Miller and Glarborg [295] (long dashed line) and Klippenstein et al. [249] (R4.50a) (sparse dotted line); (middle) NNH + O_2 $\rightleftharpoons$ N_2 + HO_2 with GRI-Mech 3.0 [175] (solid line), Klippenstein et al. [249] (dashed line) and Dean and Bozzelli [163] (dot-dashed line); (bottom) HNO + O_2 $\rightleftharpoons$ HO_2 + NO with GRI-Mech 3.0 [175] (solid line), Bryukov et al. [313] (dashed line), Fujii et al. [304] (dot-dashed line) and Dean and Bozzelli [163] (dotted line).

rate pairing applied in the mechanism of Glarborg et al. [250] (R4.50a,R4.51a), in addition to an alternative rate pairing (R4.50b,R4.51b) [258, 295] used by Okafor et al. [258], as discussed below.

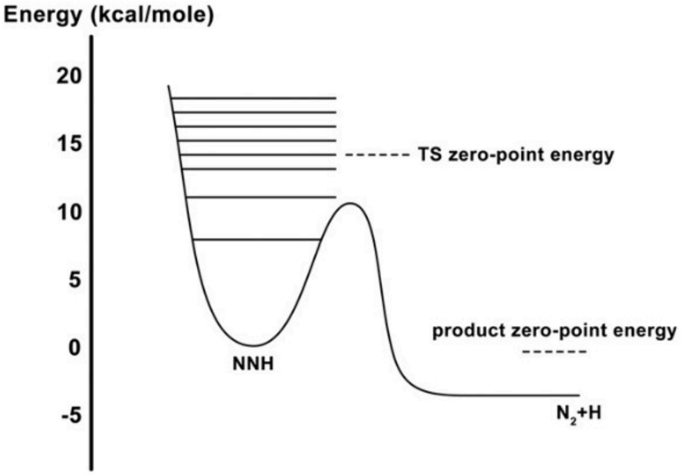

Figure 4.4: Potential energy diagram for NNH dissociation to N_2 + H, including the lowest vibrational energy levels for NNH. From Klippenstein et al. [249] based on the work of Bozkaya et al. [312].

Similar to the NNH chemistry, the balance between HNO decomposition, leading to the H radical via the reverse of (R4.70), and oxidation via (R4.78) becomes important. The CEC recommendation by Baulch et al. [166] for (R4.70) provides good agreement with experimental data for a limited temperature and pressure range. However, the current mechanism combines the high-pressure limit from Tsang and Herron [160] with the low-pressure limit from Riley et al. [300], as suggested by Glarborg et al. [250]. However, significant differences are present for (R4.78) as discussed below. The rate of Dean and Bozzelli [163] was obtained by analogy to other RH + O_2 reactions, while Bryukov et al. [313] use a single experimental data point. The faster rate of Fujii et al. [304] was used by Lindstedt et al. [214] (R4.78a), while Glarborg et al. [250] used the alternative rate proposed by Dean and Bozzelli [163] (R4.78b) which has a substantially higher energy barrier. The impact is discussed below.

$$\mathrm{H + NO + M \rightleftharpoons HNO + M} \tag{R4.70}$$

$$\mathrm{HNO + O_2 \rightleftharpoons NO + HO_2} \tag{R4.78}$$

The mechanism listed in Table 4.4 applied with reactions (R4.50a,R4.51a) is considered as the "current mechanism", with alternative reaction pairs discussed as appropriate.

4.2.4 Computational methods

The calculation methods applied to compute the validation data sets have been described previously (Section 3.2.3) and are discussed only briefly. The shock tube and flow reactor data sets were computed as zero-dimensional, homogeneous, adiabatic and isobaric [217] using time steps in the range 10 to 100 ns. The low pressure flat flames [261–263] featured imposed experimental temperature profiles and were resolved using local refinement according to the derivative of the heat release resulting in cell sizes from 20 to 200 μm. Premixed counterflow flames were used for the laminar burning velocity computations and the stagnation flow geometry of Zubairova et al. [264]. Rates of strain were maintained below 50 s^{-1} to minimise the impact of stretch effects on the computed laminar burning velocities. The stagnation flow geometry of Zubairova et al. [264] used the experimentally applied separation distance of 20 mm between the burner nozzle exit and the stagnation plate. Local grid refinement resulted in a size range of 5 to 750 μm and a maximum temperature difference below 10 K between adjacent cells.

4.2.5 Validation of the ammonia reaction mechanism

The experimental data sets and computational results are compared below with a focus on differences between the current and alternative mechanisms. The thermochemistry of Glarborg et al. [250] is applied in all computations with the exception of the mechanism of Lindstedt et al. [214] where the original data is used.

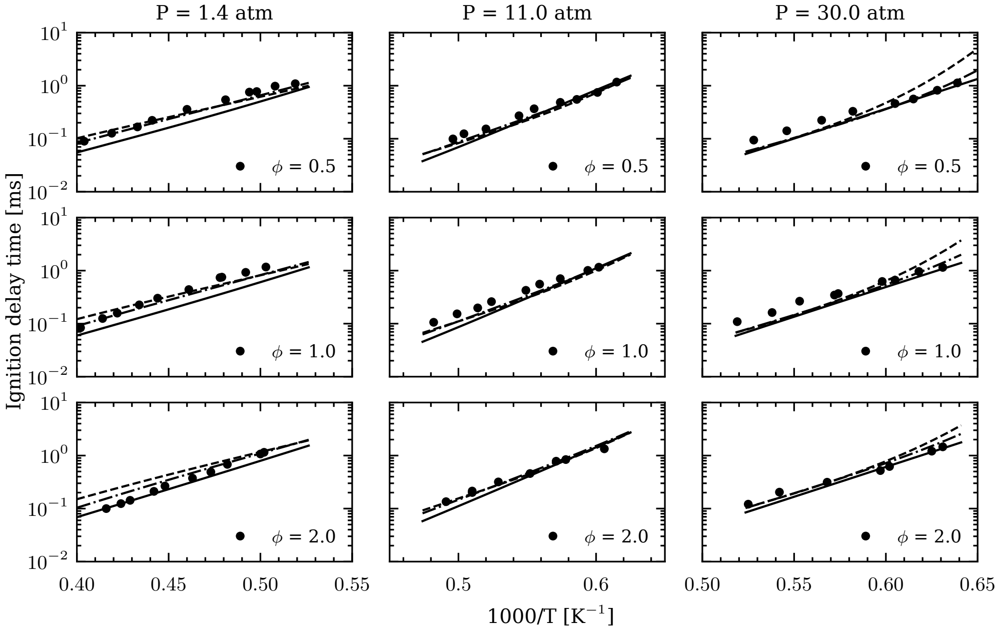

Figure 4.5: Computed ignition delay times at different stoichiometries, ϕ = 0.5, 1.0 and 2.0, comparing the mechanisms from this study (dot-dashed lines), Glarborg et al. [250] (solid lines) and Lindstedt et al. [214] (dashed lines) with the experimental results of Mathieu and Petersen [37] at pressures around 1.4, 11 and 30 atm.

4.2.5.1 Ignition delay time

The ignition delay time (IDT) at a range of pressures and stoichiometries was measured by Mathieu and Petersen [37], as shown in Table 4.2. The results for all cases using the three mechanisms of Glarborg et al. [250], Lindstedt et al. [214] and the current mechanism (see Table 4.4) are shown in Fig. 4.5. The maximum heat release method was used to define the IDT in the shock tube computations. All mechanisms perform well at pressures of 1.4 and 11 atm for lean and stoichiometric mixtures. The mechanism from Glarborg et al. [250] tends to under-predict somewhat, but the discrepancy is reduced for rich mixtures and higher pressures. The current mechanism generally performs well, but tends to under-predict slightly at higher temperatures, above about 1750 K, as the pressure is increased as well as for the fuel lean mixtures. The mechanism of Lindstedt et al. [214] shows a consistent over-prediction of IDTs at lower temperatures for the highest pressure case.

The current work has updated the aminoxyl radical chemistry following the recent work by Stagni et al. [272]. Dai et al. [266] show that the ignition delay times for ammonia at high pressure have principal sensitivities to the critical branching ratio of the NH_2 + NO reaction, which is considered well established, and the $H_2NO + O_2 \rightleftharpoons HNO + HO_2$ reaction (R4.99). The uncertainty in the latter is estimated to around a factor of two with the rates suggested by Glarborg et al. [250] and Stagni et al. [272] shown in Table 4.4. The experimental data analysed by Dai et al. [266] was obtained in a rapid compression machine and the modelling challenges were clearly outlined including the need to apply the measured pressure trace. The work showed that the mechanism by Glarborg et al. [250] matched the experimental data well following the application of a revised computational procedure. The impact of the more recent rate (R4.99a) is assessed here through a simplified computation procedure in which the nominal pressure and temperature following compression [266] is specified as the initial condition. The experimental data is also shown in Fig. 4.6 to provide an impression of the impact of the simplified computational method and, as no attempt was made to account for heat losses, increasing disagreement can be expected at longer ignition delay times. The current mechanism matches that of Glarborg et al. [250] quite well when the same rate (R4.99b) is applied. However, a significant sensitivity to this reaction is also noted, particularly under fuel lean conditions. The kink in the computed curve noted for $\phi = 3.0$ at a temperature around 1170 K with (R4.99b) is due to the onset of increased high-temperature chain branching resulting in a change in the reaction pathways. A similar impact can be noted at around 1210 K with the application of (R4.99a) further emphasising the sensitivity to the reaction step at high pressures.

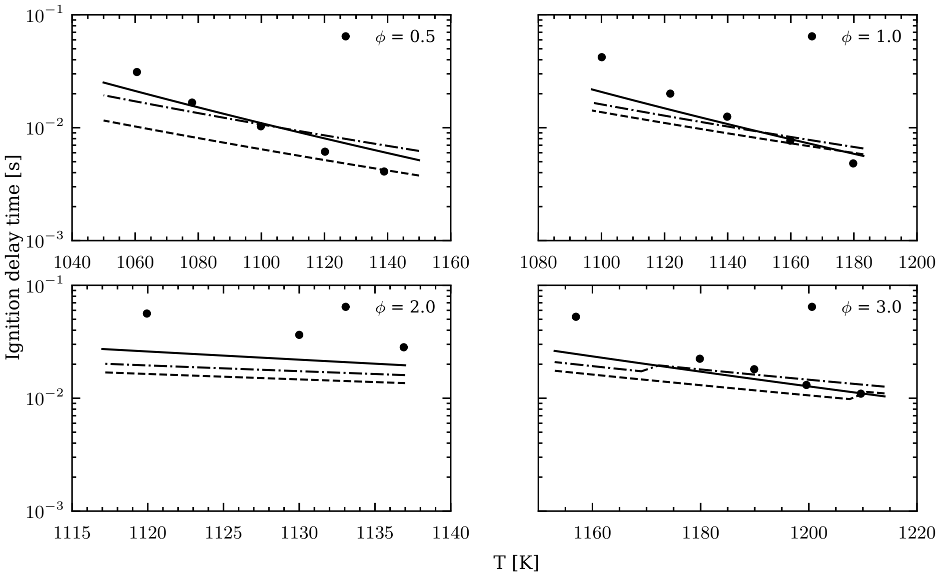

Figure 4.6: Ignition delay times computations for a range of stoichiometries (ϕ = 0.5, 1.0, 2.0 and 3.0) compared to the experimental data of Dai et al. [266]. Top left and right and bottom left are measurements at a pressure of 60 bar and bottom right at 70 bar. Solid lines: Glarborg et al. [250]; dashed lines: current mechanism with R4.99a; dot-dashed lines: current mechanism with R4.99b.

4.2.5.2 Selective Non-Catalytic Reduction

The SNCR temperature window is very narrow and sensitive to the inlet species composition. It is possible to change and widen the active window by altering the latter as outlined by Klippenstein et al. [249]. Following the conversion of NH_3 to NH_2 the subsequent removal of NO proceeds via (R4.31,R4.32) and there is good agreement regarding the branching ratio as outlined above.

In order for reactions to be self-sustaining, a sufficient radical pool must be created through dissociation of NNH, produced by reaction (R4.32), via reaction (R4.50) (NNH (+ M) $\rightleftharpoons$ N_2 + H (+ M)).

The non-chain branching reaction with oxygen (NHH + $O_2 \rightleftharpoons N_2 + HO_2$ (R4.51)) is a potential competitor and must, essentially, not excessively impede H radical production, as discussed further later. The mechanisms of Glarborg et al. [250], Lindstedt et al. [214] and that of the current work were used to compute the SNCR

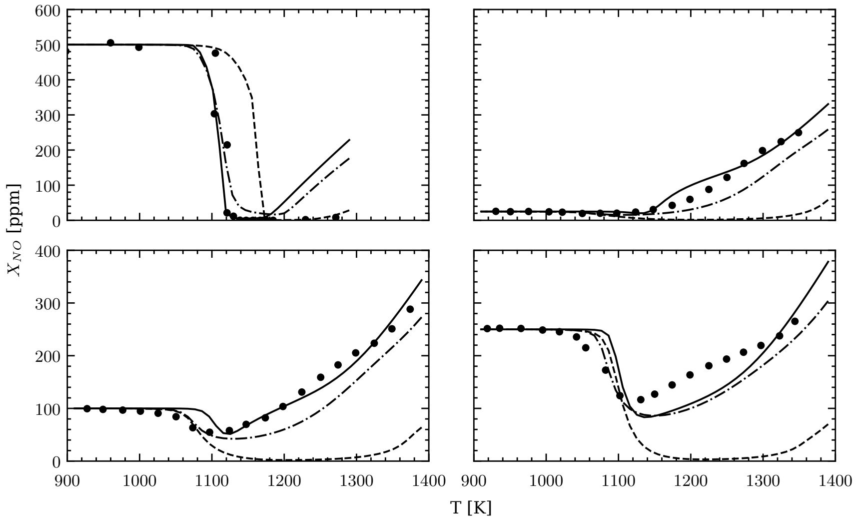

Figure 4.7: SNCR behaviour obtained with the mechanisms from Glarborg et al. [250] (solid lines), Lindstedt et al. [214] (dashed lines) and this study (dash-dotted lines). The top left shows experimental results of Muris [273] with inlet mole fractions: NO = 500 ppm, NH_3 = 750 ppm and O_2 = 2% with residence times (s) = 525/T(K). Other cases: experimental data of Vilas [274] with inlet concentrations: NO = 25, 100 and 500 ppm, NH_3 = 1000 ppm and O_2 = 40% with residence times (s) = 48.7/T(K). Pressure 101 kPa and mole fractions balanced with N_2.

behaviour for a range of flow reactor conditions, with varied inlet concentrations of O_2, H_2O, NH_3 and NO. Figure 4.7 compares computations of NO for conditions with relatively low [273] and very high [274] oxygen concentrations with different amounts of NO. The temperature broadening effect of increased O_2 concentration is well reproduced with the balancing of the dominant NNH reaction pathways. The mechanism of Lindstedt et al. [214] predicts the SNCR onset temperature well with some delay for the Muris [273] case. However, the mechanism fails to capture the reformation of NO for the Vilas and Glarborg [274] cases due, principally, to the absence of a H_2NO mechanism. The Glarborg et al. [250] mechanism captures the reformation of NO with good agreement especially for the 25 and 100 ppm NO inlet conditions, but shows some disagreement for the Muris [273] case leading to too rapid reformation of NO. The latter is also observed with the current mechanism. The relative ratio of NO production to consumption at

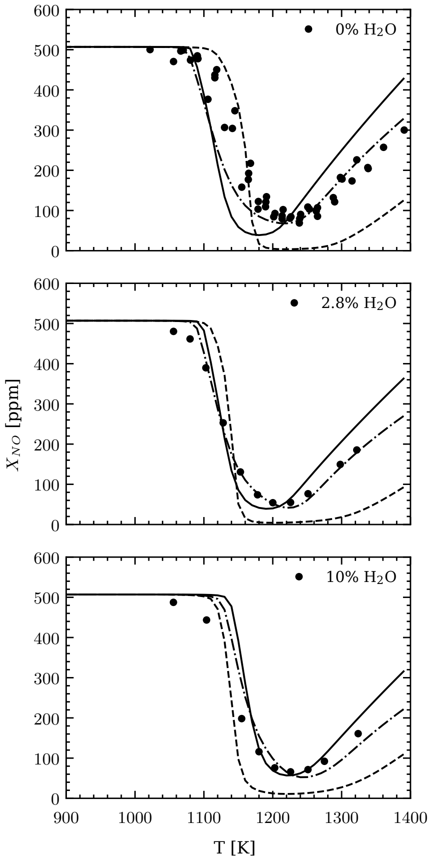

Figure 4.8: Flow reactor calculations comparing the SNCR behaviour as in Fig. 4.7. Experimental data from Duo [275] showing the impact of H_2O on the SNCR behaviour with inlet concentrations: NH_3 = 832 ppm, NO = 507 ppm, O_2 = 4.0%, H_2O = 0, 2.8 and 10% with residence time (s) = 92.7/T(K). Pressure 101 kPa and mole fractions balanced with N_2. Legend as in Fig. 4.7.

the highest temperatures (around 1300 K) is almost identical for the current and Glarborg et al. [250] mechanisms. However, the latter leads to a 50% increase of NO in absolute terms via (R4.84) $NO_2 + O \rightleftharpoons NO + O_2$ caused by increased formation of NO_2 via $NO + O \rightleftharpoons NO_2$ (R4.81). The same rates [160] are used in both mechanisms, but with different broadening factors (F_c) applied in the Troe expression.

The above results suggest that the aminoxyl radical chemistry is essential for capturing reformation of NO under SNCR conditions and is essentially responsible for the improvement of predictions compared to previous work e.g. Lindstedt et

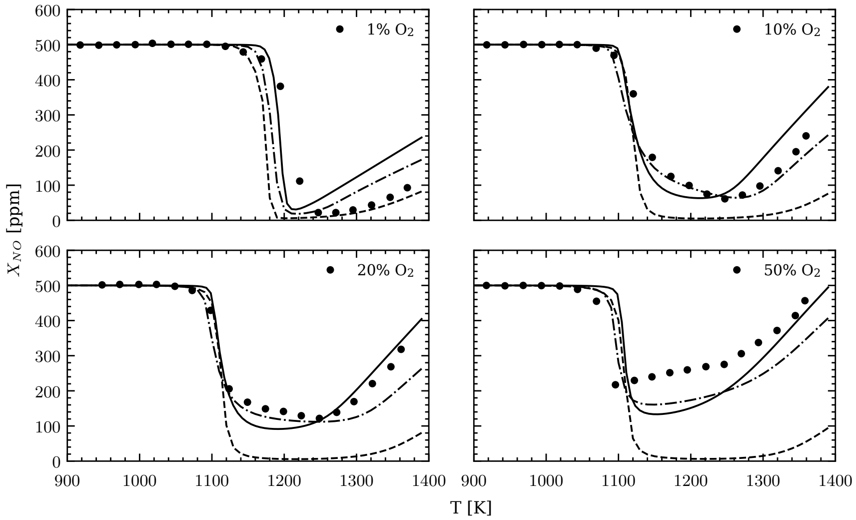

Figure 4.9: Flow reactor calculations comparing the SNCR behaviour as in Fig. 4.7. Experimental data from Kasuya et al. [276] showing the impact of O_2 on the SNCR behaviour with inlet concentrations: NH_3 = 1000 ppm, NO = 500 ppm, O_2 = 0, 1, 10 and 50%, H_2O = 5% with residence time (s) = 88.0/T(K). Pressure 101 kPa and mole fractions balanced with N_2. Legend as in Fig. 4.7.

al. [214]. Further examples of the impact of other species on the SNCR behaviour are shown in Figs. 4.8 and 4.9 for addition of H_2O and O_2, respectively. The addition of H_2O has a modest impact on the SNCR temperature window and arguably excellent agreement with experimental data is obtained by the current and Glarborg et al. [250] mechanisms for all temperatures and with various H_2O inlet concentrations. The impact of O_2 on the SNCR behaviour is more acute, with increased concentrations resulting in earlier onset of NH_3 oxidation and incomplete reduction of NO prior to its reformation. The ability to reproduce the SNCR temperature window under conditions with excess molecular oxygen concentrations is essential in the context of the prediction of autoignition stabilised turbulent flames [187] where mixing with preheated (vitiated) air determines the overall behaviour. The current mechanism predicts the reduction onset temperature very well for all concentrations, but arguably over-predicts NO reformation at the lowest O_2 concentrations and under-predicts at the highest concentrations. The mechanism of Glarborg et al. [250] predicts a similar behaviour albeit with somewhat faster NO reformation. The absence of H_2NO

chemistry [214] again results in excessive NO reduction. An analysis of the above SNCR behaviour with 10% O_2 at a temperature of 1200 K (cf. Fig. 4.9) for the current mechanism suggests that only the decomposition (R4.50) and oxidation (R4.51) reactions are important for NNH removal with a heavy bias towards decomposition at 96% compared to 4%. The NNH decomposition is thus crucial for maintaining the radical pool and accounts for about 93% of H radical production. For the Glarborg et al. [250] mechanism, NNH is 96% consumed by decomposition (R4.50a) and 4% by its reaction with molecular oxygen. This leads to 86% of hydrogen radical production coming from NNH decomposition and 2% from HNO decomposition. Production of NO is via (R4.78) HNO + O_2 (49%) and (R4.91) NH_2 + NO_2 (45%). For the current mechanism (R4.78a) accounts for $\approx$ 100% of HNO removal compared to 97% with the slower rate of Dean and Bozzelli [163] used by Glarborg et al. [250] (R4.78b). Both rate suggestions (R4.78a,R4.78b) are compatible with the SNCR temperature window.

The dominant NNH reactions (R4.50) and (R4.51) are subject to uncertainties and the impact of these are discussed below with particular reference to the required balancing of the two channels in the context of the SNCR temperature window. The rates used in the current mechanism (R4.50a,R4.51a) and that of Glarborg et al. [250] stem from the work of Klippenstein et al. [249] and, as shown above, result in good agreement over the SNCR temperature window.

Okafor et al. [258] apply the older data (R4.50b) and (R4.51b) that stem from Miller et al. [295]. The mechanism also includes a further reaction (R4.51d) from Miller and Glarborg [296] that leads to some degree of H radical production. The reaction step is omitted in the more recent work [250]. The rates for NNH $\rightleftharpoons$ N_2 + H that lead to chain branching differ by approximately a factor of 15 (R4.50a) and (R4.50b). Furthermore, the rates for the effectively chain terminating reaction NNH + $O_2 \rightleftharpoons N_2$ + HO_2 (R4.51a,R4.51b) differ by a factor around 6 in the SNCR temperature window, while (R4.51c) from Dean and Bozzelli [163] differs by over three orders of magnitude from the upper limit of Miller and Glarborg [295] (R4.51b). For illustration purposes, (R4.51c) can be balanced by a slower thermal decomposition step (R4.50c), developed in this work and shown in Table 4.4, that includes a barrier of 7 kcal/mol, consistent with the work by Bozzelli and Dean [297], as discussed in Section 4.2.3. The sensitivity to the different rate parameters for the above reaction steps is discussed below. However, it is apparent that as long as a sufficient radical pool is generated through the relative rates of (R4.50) and (R4.51), the SNCR temperature window can be reproduced.

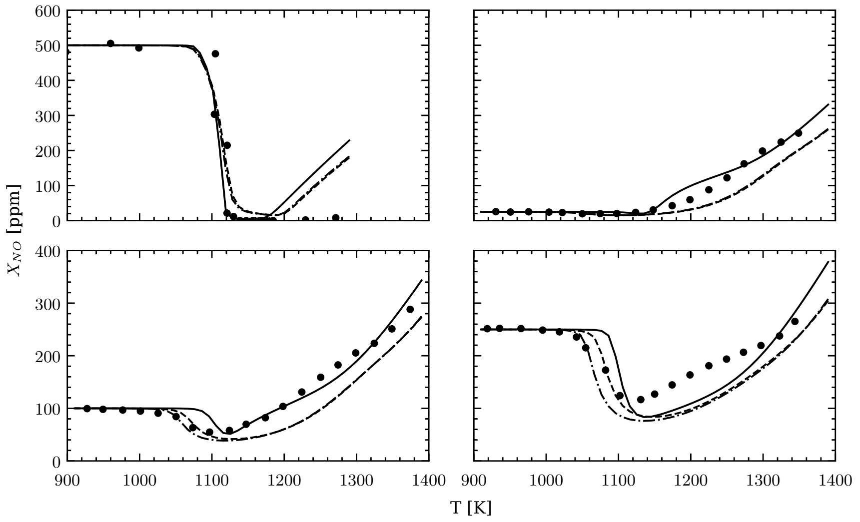

Figure 4.10: Flow reactor calculations comparing the SNCR behaviour for the mechanisms from Glarborg et al. [250] (solid lines), the current mechanism using the slower NNH consumption pairing (R4.50c, R4.51c) (dashed lines) and the current study using fast NNH decomposition and slow oxidation (R4.50a, R4.51c) (dot-dashed lines). The figure layout, experimental data and conditions is as defined in Fig. 4.7.

As shown in Figs. 4.10 to 4.12, the inclusion of the slower NNH consumption pairing (R4.50c,R4.51c) in the current mechanism reproduces the selected SNCR data reasonably well (see Fig. 4.11). The combination of a fast NNH decomposition (R4.50a) and the slower oxidation step (R4.51c) results in similar agreement. Accordingly, as long as a sufficient radical pool is generated through the relative rates of (R4.50) and (R4.51), the SNCR temperature window can be reproduced. By contrast, a combination of a slower NNH decomposition rate and a fast oxidation

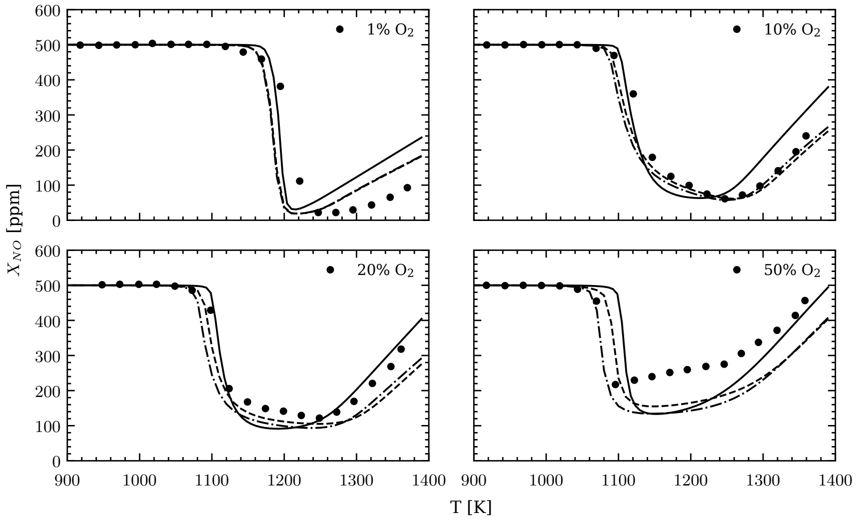

Figure 4.11: Flow reactor calculations comparing the SNCR behaviour as in Fig. 4.10. Experimental data and condition is as defined in Fig. 4.9.

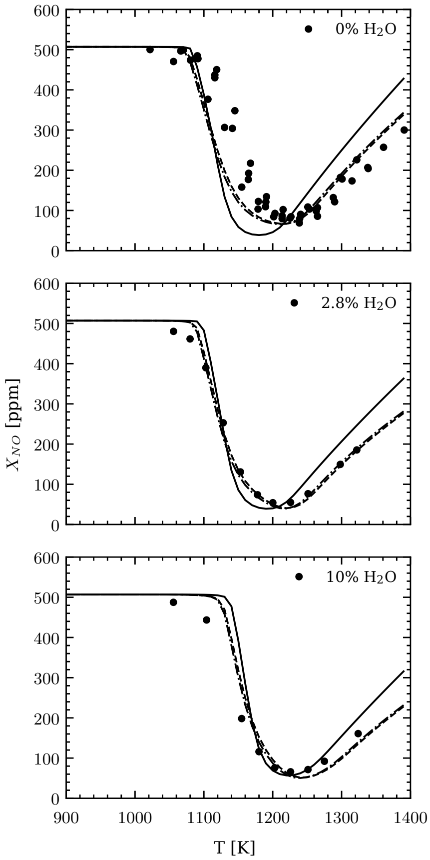

Figure 4.12: Flow reactor calculations comparing the SNCR behaviour as in Fig. 4.10. Experimental data and condition is as defined in Fig. 4.8.

rate fails to reproduce the SNCR data due to insufficient H radical generation. This is highlighted by the reaction pairing used in the mechanism of Okafor et al. [258] (R4.50b,R4.51b). As shown later, the mechanism of Okafor et al. [258] provides excellent agreement with experimental laminar burning velocity data without the need to consider heat losses. However, it does so in part by using a slow NNH decomposition rate (R4.50b) and a fast (upper limit) NNH oxidation rate (R4.51b) that is approximately two times faster than the rate from Klippenstein et al. [249] (R4.51a). This combination produces about a third less H radical for a premixed stoichiometric flame when compared to the current mechanism. Furthermore, application of the same NNH decomposition-oxidation pairing in the current mechanism also results in burning velocity predictions that are in line with the experimental data without the need to consider the impact of heat losses. In short, it is essential that, in relative terms, the thermal decomposition pathway (R4.50) remains sufficiently fast.

The mechanism of Okafor et al. [258] was therefore applied under SNCR conditions with results shown in Figs. 4.13 to 4.15. It is clear that insufficient levels of the H radical are produced at lower temperatures with discrepancies particularly pronounced for elevated residual O_2 concentrations. This results in a delayed onset of NO removal by SNCR consistent with the above discussion. Reaction (R4.51d) is in effect a third body reaction $NNH + M \rightleftharpoons N_2 + H + M$ with $M = O_2$ and a unity chaperon efficiency. The reaction only contributes around 1% to NNH consumption in the Okafor et al. [258] mechanism for a stoichiometric ammonia-air flame and was excluded by Glarborg et al. [250].

The H_2O_2 + OH reaction (R3.22) was explored. The bi-exponential form presented in the work by Hong et al. [285] approximates the low temperature behaviour to the rate of Atkinson et al. [305] and the high temperature behaviour to the rate presented in their work. However, only the high temperature rate, which is relevant to temperatures around and including the SNCR window and combustion regimes,

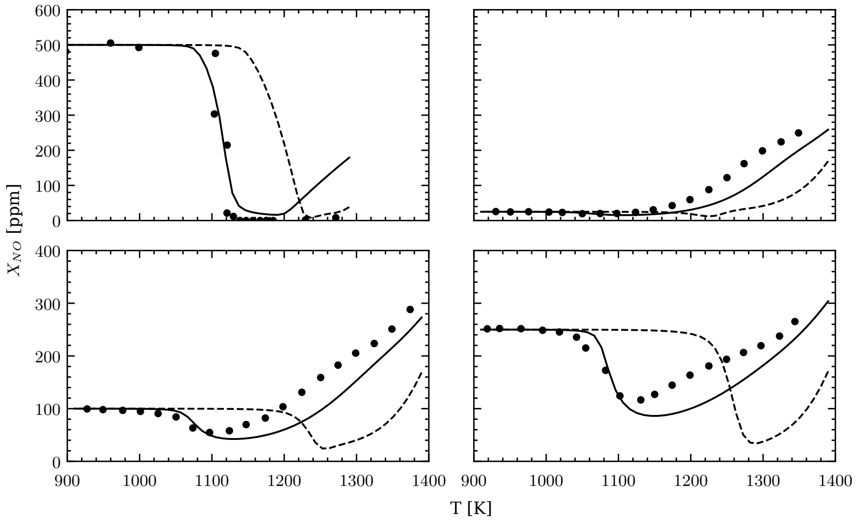

Figure 4.13: Flow reactor calculations comparing the SNCR behaviour for the current mechanism (solid lines) and the mechanism of Okafor et al. [258] (dashed lines). The figure layout, experimental data and conditions is as defined in Fig. 4.7.

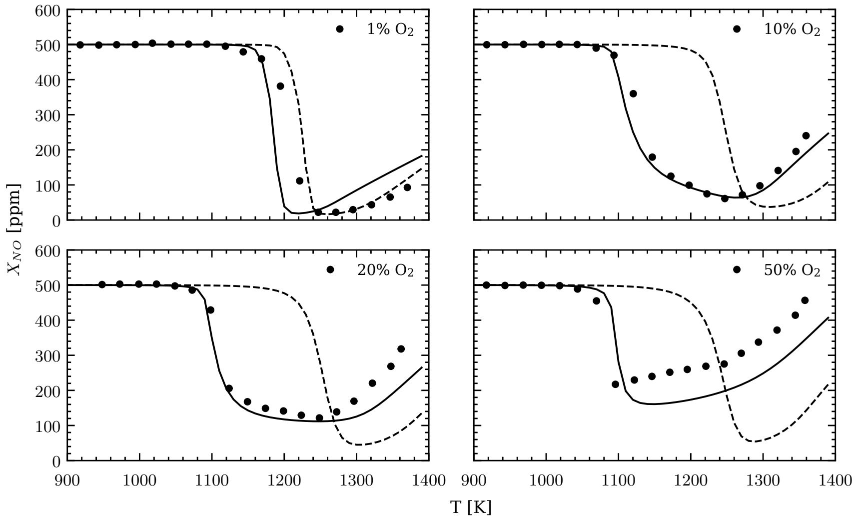

Figure 4.14: Flow reactor calculations comparing the SNCR behaviour as in Fig. 4.13. Experimental data and condition is as defined in Fig. 4.9.

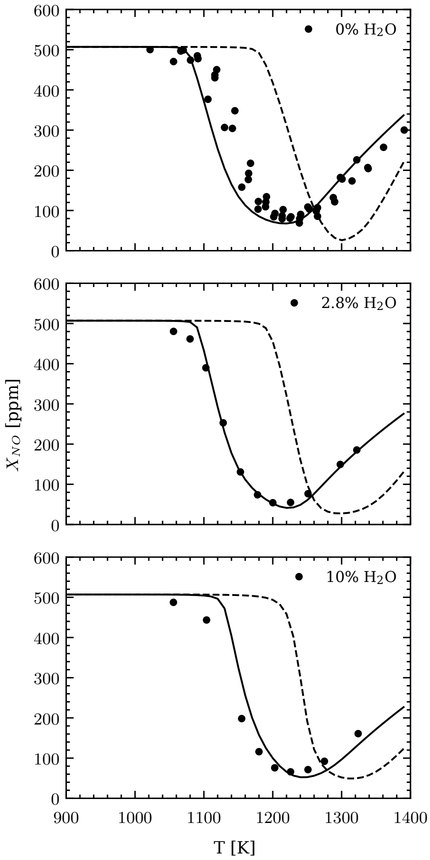

Figure 4.15: Flow reactor calculations comparing the SNCR behaviour as in Fig. 4.13. Experimental data and condition is as defined in Fig. 4.8.

has been included in the hydrogen sub-mechanism used in this work.

Stagni et al. [268] studied speciation in a flow reactor at higher temperatures as shown in Fig. 4.16. All mechanisms provide similar agreement with experimental data and an over-prediction of the peak NO value. At 1600 K the primary pathway to NO is via (R4.83) NO_2 + H (72%) with NO_2 essentially produced by (R4.81) NO + O (90%) suggesting a potential inaccuracy in the rate of formation. The onset of conversion is predicted in a similar manner for all mechanisms, while the kinetic model of Stagni et al. [268] shows a reduced overprediction, < 25% at 2000 K. Stagni et al. [268] recommended an alternative rate, using the PLOG approach, for HNO thermal decomposition via the reverse of (R4.70). The suggestion merits testing in future work.

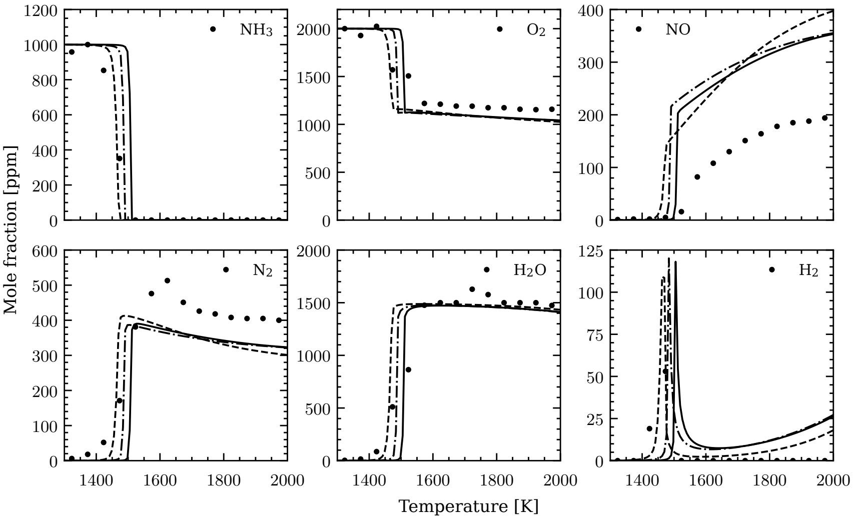

Figure 4.16: Oxidation of 1000 ppm NH_3 with 2000 ppm O_2 in a flow reactor at 1.25 atm with an average residence time of 50 ms [268]. The computations using the mechanisms from Glarborg et al. [250] (solid lines), Lindstedt et al. [214] (dashed lines) and the current study (dot-dashed lines) are shown.

In summary, the current mechanism and that of Glarborg et al. [250] treat NNH and HNO consumption in a similar manner in the SNCR window and the low sensitivity to the rate of NNH decomposition stems from its dominance in the reaction path.

4.2.5.3 Laminar burning velocities

Kobayashi et al. [244] cover global laminar flame properties such as laminar burning velocities (LBVs) and extinction strain rates as part of their comprehensive review. Both types of data are subject to experimental and modelling uncertainties. Burrell et al. [316] discussed the large differences, up to a factor of two, in measurements of extinction rates of strain caused by non-uniform inlet velocity profiles and Kobayashi et al. [244] showed, using ten different reaction mechanisms, that typically large differences between experimental data and computed LBVs are obtained for ammonia-air flames. The reaction mechanism of Okafor et al. [258] is an exception and provides excellent agreement. Nakamura and Shindo [284]

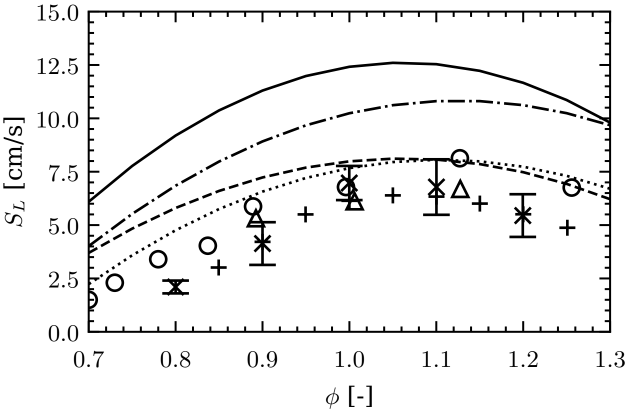

Figure 4.17: Laminar burning velocities obtained with the mechanisms of Glarborg et al. [250] (solid line), Okafor et al. [258] (dashed line), the current study (dot-dashed line) and the current study with 7% heat loss (dotted line). The experimental results: (+) [277]; (×) [281]; (○) [282]; (△) [283] for conditions at standard temperature and pressure.

explored the impact of radiative heat losses on ammonia flames using a detailed reaction mechanism [317] and an influence was observed across a broad range of stoichiometries, unlike methane flames where a strong impact is only observed near the flammability limits. Close to stoichiometric conditions the flame temperature was reduced by up to 80 K with larger discrepancies at the flammability limits. The observation partly accounts for some of the discrepancies noted by Kobayashi et al. [244]. Stagni et al. [268] included an optically-thin model to account for radiation effects and showed good agreement with experimental data. Han et al. [277] further note potential inaccuracies in experimental data where stretch effects have not been taken into account.

Extensive sensitivity analyses have been performed by Shrestha et al. [260] and Han et al. [251, 259] and only key reactions for stoichiometric flames are discussed. Reaction (R4.25) $NH_3 + OH \rightleftharpoons NH_2 + H_2O$ is the most important ammonia consumption path. However, the sensitivity to the rate constant is modest. By contrast, the dissociation reactions of NNH and HNO show a comparatively high sensitivity with perturbations by a factor of 5 causing changes in LBVs up to 15%. The dissociation of NNH via (R4.50) is one of the most significant contributors to H radical production and accounts for around 21% for the current mechanism with the dissociation of HNO contributing about 2%. The reaction NH + OH $\rightleftharpoons$ HNO + H (R4.43) contributes about 50% to HNO and 5% to H radical production then leading to further H formation via HNO dissociation. The mechanism of Lindstedt et al. [214] used a rate twice that of Cohen and Westberg [157]. The recommendation of Klippenstein et al. [256] is slower for temperatures above 325 K, but faster than the original Cohen and Westberg [157] rate for all temperatures. The current mechanism includes the rate of Klippenstein et al. [256]. Alternative determinations are within a factor of 2 to 3 with some studies proposing increased branching to H_2O + N [256]. The reaction NH_2 + NH $\rightleftharpoons$ N_2H_2 + H (R4.36) is a significant contributor to H radical production at 17% and 13% for the current and Glarborg et al. [250] mechanisms, respectively. Reaction (R4.78a) contributes 28% to HNO consumption for the current mechanism and (R4.78b) contributes 7% for that of Glarborg et al. [250].

Computations were performed using a counterflow configuration at a low rate of strain ($\leq 50\,\mathrm{s}^{-1}$).[2] All mechanisms predict the overall trend well with the mechanism of Glarborg et al. [250] resulting in values 4 to 6 cm/s too high as shown in Fig. 4.17. The current reaction mechanism reduces the overpredictions to around 3 cm/s. The application of a 7% heat loss, introduced via a heat loss factor [214], provides agreement across the stoichiometric range. The mechanism of Okafor et al. [258] matches the experimental data well without consideration of heat losses. However, this is achieved by a NNH decomposition-oxidation pairing (R4.50b,R4.51b) from Miller and Glarborg [295] with the oxidation pathway dominating in a manner that is incompatible with more recent data [249, 250]. The application of (R4.50b,R4.51b) in the current mechanism also results in good agreement without heat losses. However, the reaction pairing delays the onset of the SNCR behaviour substantially, particularly for mixtures with higher O_2 concentrations, as discussed in the Section 4.2.5.2.

---

[2] Laminar burning velocities determined using reaction rate integrals.

4.2.5.4 Speciation in laminar flames

Computed results for flames in Table 4.1 are discussed below with argon diluted stoichiometric, rich and lean ammonia/hydrogen/oxygen flames (Flames 1A, 1B and 1C) shown in Figs. 4.18 to 4.20. For the stoichiometric (Flame 1A) and fuel lean (Flame 1C) flames, the computed NO values show similar agreement with a scatter of less than 20%. Computed values for nitrous oxide show differences for Flame 1A with the mechanism of Lindstedt et al. [214] providing the best agreement and the current mechanism an overprediction. However, for the (ultra-) lean flame (Flame 1C) the N_2O levels show a consistent and significant deviation from the experimental post flame value with all mechanisms predicting peak values up to 2.5 times larger. While the mechanism of Lindstedt et al. [214] shows somewhat better agreement, the discrepancies suggest a mechanistic uncertainty under such conditions as the trend is not consistent for other data sets. The production of N_2O is ($\approx$ 100%) via (R4.47) ($NH + NO \rightleftharpoons N_2O + H$) [166, 250] with the major consumption paths for Flame 1C via (R4.66) 14% and (R4.67) 86%. The rate of (R4.67) $N_2O + H \rightleftharpoons N_2 + OH$ was increased by a factor of two to approximate the sum of the four pathways identified by Bozzelli et al. [318] for temperatures greater than 1000 K and the recommendation from Tsang and Herron [160] below this temperature. Reactions (R4.47) $NH + NO \rightleftharpoons N_2O + H$ and (R4.48) $NH + NO \rightleftharpoons N_2 + OH$ have a temperature independent branching ratio (4:1) in favour of (R4.47) [166]. However, while there is a large change in the chemical environment between Flames 1A and 1C, the temperature differences are moderate due to differences in argon dilution.

Computations provide similar agreement with experimental data for the fuel rich Flame 1B including ammonia consumption and the principal fragments of amidogen (NH_2) and imidogen (NH) as shown in Fig. 4.19. However, for NH the mechanism of Glarborg et al. [250] shows substantially reduced concentrations due to reduced production from $NH_2 + H \rightleftharpoons NH + H_2$ (R4.27). The other mechanisms use the faster rate of Lindstedt et al. [214]. Figure 4.20 shows that the different

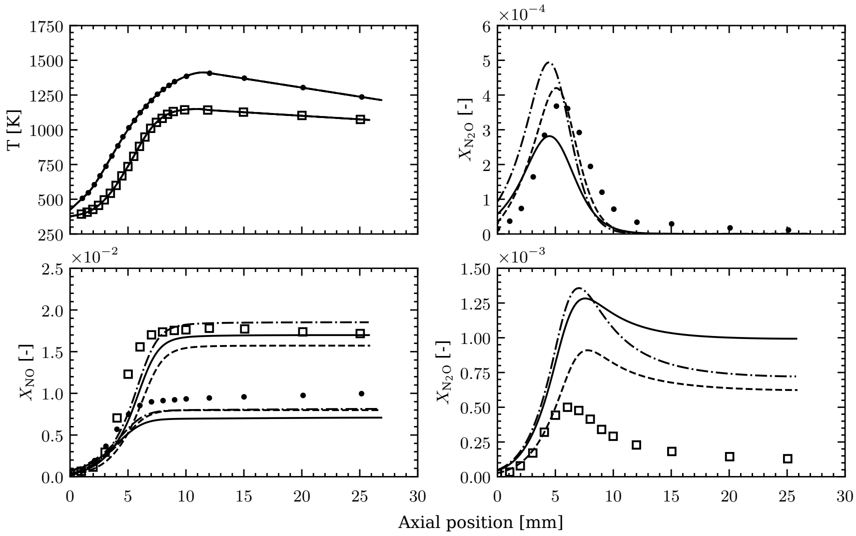

Figure 4.18: Flames 1A and 1C. The experimental data for Flame 1A (dots) and Flame 1C (squares) and the computations using the mechanisms from Glarborg et al. [250] (solid lines), Lindstedt et al. [214] (dashed lines) and the current study (dash-dotted lines).

mechanisms provide similar agreement for the H and O radicals as well as for NO. The formation of N_2O appears to be underpredicted in contrast to Flame 1A, further suggesting a potential mechanistic omission of relevance to ultra-lean conditions.

Figure 4.21 shows stoichiometric (Flame 2A) and (ultra-) lean (Flame 2B at $\phi = 0.12$) ammonia/hydrogen flames with nitric oxide doping. For the stoichiometric flame, the mechanism of Glarborg et al. [250] reproduces the N_2O experimental data most closely, with all mechanisms able to capture the early consumption of NO prior to its production with a small under-prediction of the experimental equilibrium value. The overprediction of N_2O obtained by the current mechanism can again be traced to (R4.47). Despite using the same rate expression [166, 250], the reaction rate integral is over two times greater than that obtained with the mechanism of Glarborg et al. [250] due to the increased net production of NH as indicated by Fig. 4.19. As for Flame 1C, problematic N_2O post flame values are obtained for the ultra-lean flames. The matter is further discussed below where the potential influence of excited state oxygen chemistry is explored.

Results for the a fuel lean ($\phi = 0.71$) ammonia/oxygen Flame 3D are shown in

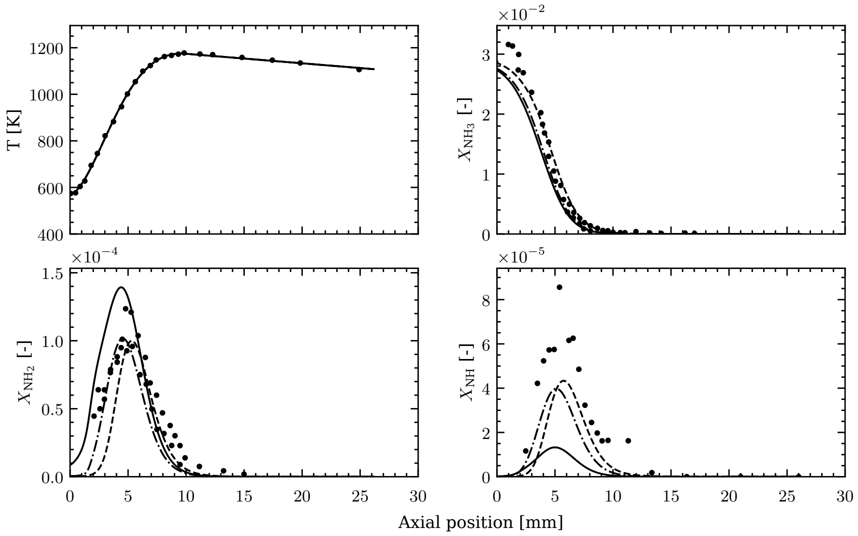

Figure 4.19: Flame 1B. The key is as defined in Fig. 4.18.

Fig. 4.22. For this flame, the temperature profile is estimated close to the burner and hence subject to significant uncertainties. All mechanisms provide similar values for the principal ammonia fragments (NH_2 and NH). Both NNH and HNO contribute to the growth of the H radical pool and for the current and Glarborg et al. [250] mechanisms the thermal decomposition of NNH accounts for 19% of the H radical production and that of HNO for 2%. The NNH concentration measurements are subject to uncertainties associated with the origin of mass 29 [311]. The mechanism of Lindstedt et al. [214] over-predicts the NNH concentration by about a factor of five due to the slower NNH decomposition. By contrast, the mechanism of Glarborg et al. [250] and the current mechanism predict negligible concentrations of NNH. The lower rate limit reaction pairing (R4.50c,R4.51c) brings the peak value more in line with that measured but at a different physical location. While it is not possible to draw a firm conclusion, it would appear inappropriate to attach significant weight to this aspect of the data set given the experimental uncertainties associated with the origin of mass 29 [311], as discussed above.

The data for HNO stems from an indirect determination using a differential technique [261] and some caution is accordingly required. As shown in Fig 4.23,

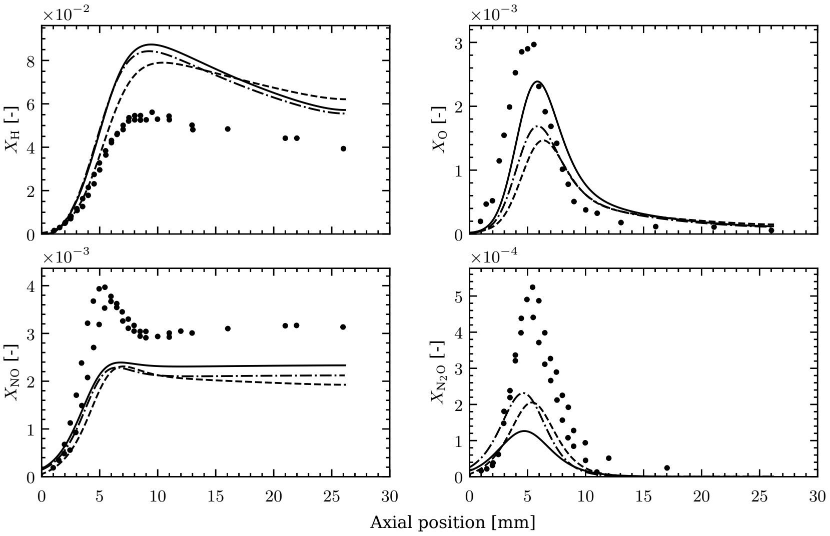

Figure 4.20: Flame 1B. The key is as defined in Fig. 4.18.

the mechanism of Glarborg et al. [250] provides an overprediction of the HNO radical by about a factor of six. This reduces to a factor around two for the other mechanisms. The difference can essentially be traced to the current faster rate of HNO + $O_2 \rightleftharpoons$ NO + HO_2 (R4.78). The rate for (R4.78a) stems from Fujii et al. [304] and is around one order of magnitude faster at 1500 K (factor of four at 2000 K) than that of Dean and Bozzelli [163] applied by Glarborg et al. [250] (R4.78b). The latter rate was derived by analogy with other RH + O_2 reactions due to the very limited experimental data available [313]. The difference between (R4.78a) and (R4.78b) becomes further pronounced at lower temperatures. The faster rate selection, (R4.78a), remains in excess of an order of magnitude slower than the corresponding rate for NNH + O_2 determined by Klippenstein et al. [249], and a more accurate determination for (R4.78) remains highly desirable.

Both NNH and HNO decomposition contribute to the growth of the H radical pool and in the mechanism of Glarborg et al. [250] the decomposition of NNH accounts for 19% of the H radical production and that of HNO for 2%. The current mechanism results in an identical relative balance of the H radical production. The experimental data for HNO is not subject to the same uncertainties as outlined above

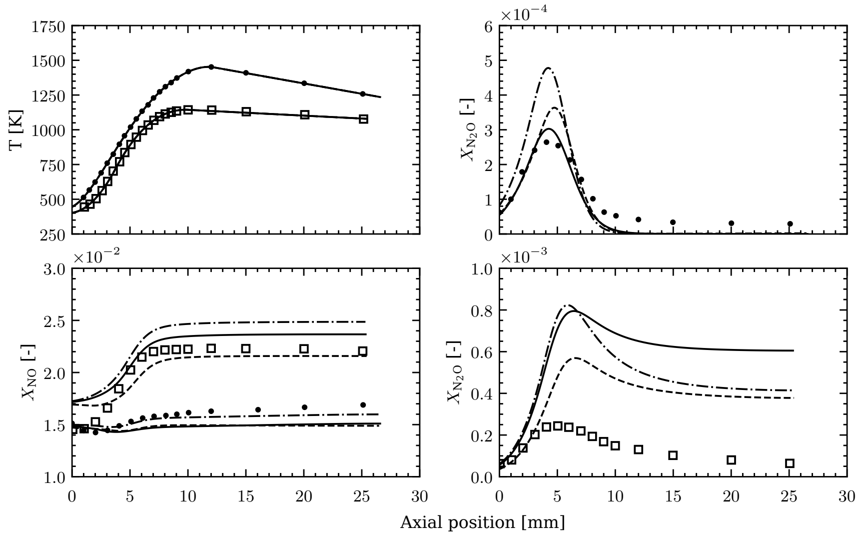

Figure 4.21: Flames 2A and 2B. Experimental data for Flame 2A (dots) and Flame 2B (squares) presented with the key as defined in Fig. 4.18.

for NNH. However, some caution is required as a differential technique was used to determine concentrations as discussed in detail by Bian et al. [261].

Significant discrepancies were noted for N_2O in the post flame region of the ultra-fuel lean ($\phi = 0.12$) low-temperature Flames 1C and 2B as shown above. The discrepancies can not be explained by reasonable temperature variations, e.g. ± 100 K in the post-flame zone for Flame 1C. The main reaction sequence for the latter flame appears simple with formation of N_2O exclusively ($\approx$ 100%) via NH + NO $\rightleftharpoons$ N_2O + H (R4.47) and the dominant (86%) destruction via N_2O + H $\rightleftharpoons$ N_2 + OH (R4.67). The uncertainties in the rates of reaction are modest with the channel NH + NO $\rightleftharpoons$ N_2 + OH (R4.48) considered the minor route. The potential impact of excited state oxygen chemistry is discussed below.

Kistiakowsky and Kydd [319] postulated the existence of NO + NO_2 $\rightleftharpoons$ N_2O + O_2 as a result of flash photolysis studies yielding "hot" NO. The forward part of the above reaction without excited states is well established in atmospheric chemistry as NO + NO_2 $\rightleftharpoons$ N_2O_3. Atkinson et al. [305] also evaluated the reverse decomposition N_2O_3 (+ M) $\rightleftharpoons$ NO + NO_2 (+ M) and provided low- and high-pressure rate

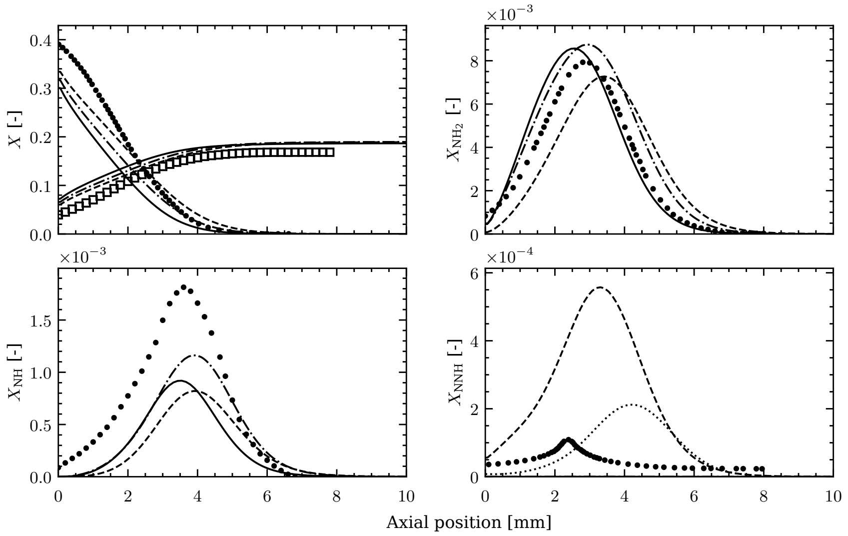

Figure 4.22: Flame 3D. Top left: dots for NH_3 and squares for N_2 mole fractions. The reaction pair (R4.50c,R4.51c) is indicated by the dotted line. The key is otherwise as defined in Fig. 4.18.

recommendations for a narrow temperature range (225 – 300 K). An energy barrier of 40.57 kJ/mol was allocated, consistent with the difference in the heat of formation. However, pathways leading from N_2O_3 to $N_2O + O_2$ are not established. Two recent studies [307, 320] obtained rates (R4.103) for $N_2O + O_2(b^1\Sigma_g^+) \rightleftharpoons$ Products covering a temperature range up to 806 K. The formation of $O_2(b^1\Sigma_g^+)$ can result from reactions of HO_2 with O, H, OH and HO_2 with yields less than 10^{-2}, 8×10^{-3}, 10^{-3} and 3×10^{-2} at 300 K as outlined by Keyser et al. [321]. Monge-Palacios and Sarathy [322] suggest that the yield for the lowest singlet form $O_2(^1\Delta_g)$ from OH + HO_2 is strongly temperature dependent and reaches a modest value of 1.43×10^{-2} at 2000 K.

The influence of excited molecules on combustion is well-established [323], particularly for fuel lean mixtures. However, evidence supporting the importance of the above pathway is slender. The required rate for a global step $N_2O + O_2 \rightleftharpoons NO + NO_2$ (R4.105) to alleviate the lack of post flame conversion of N_2O can be estimated by assuming that it proceeds via N_2O_3 with the decomposition step rate limiting. The required rate constant is about 125 times slower at 806 K compared

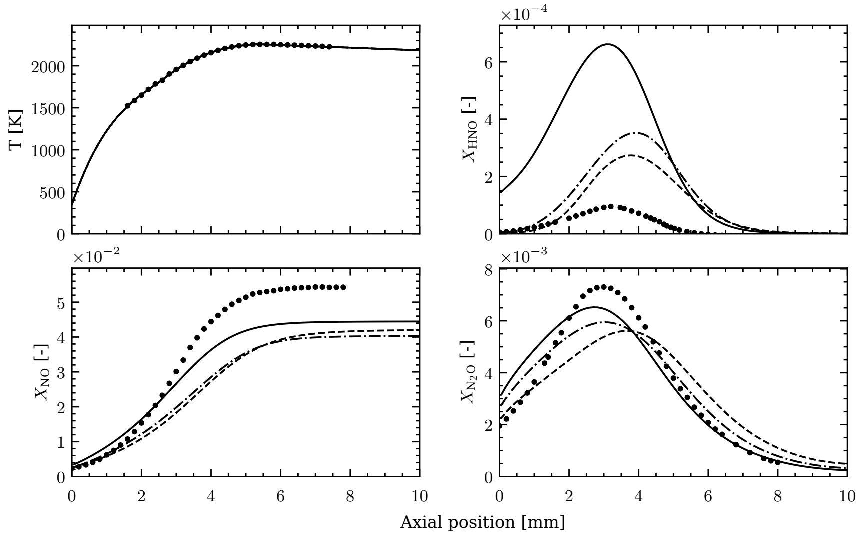

Figure 4.23: Flame 3D. The key is as defined in Fig. 4.18.

to the measured rate (R4.103) featuring $O_2(b^1\Sigma_g^+)$ [307] and 33 times slower at the maximum temperature around 1100 K in Flame 1C. However, it must also be noted that the derived rate is only marginally slower at $\approx 2/3$ of the quenching rate for the reaction N_2O + $O_2(^1\Delta_g)$ at 298 K measured by Findlay and Snelling [324]. Alternatively, the corresponding amounts of $O_2(b^1\Sigma_g^+)$ would have to be formed *in situ* e.g. via reactions featuring HO_2. The potential impact on N_2O consumption is shown in Fig. 4.24 and only ultra-lean flames (Flames 1C and 2B) show a sensitivity. The impact of a reaction sequence featuring singlet oxygen ($O(^1D)$) proceeding via a skeleton mechanism (R4.106) to (R4.110) [305, 308] is also shown. Again, additional formation and quenching pathways for $O(^1D)$ are required and the formulation of a comprehensive excited state reaction mechanism is beyond the current work. Hence, reactions (R4.105) and (R4.106) to (R4.110) have only been introduced for the purpose of exploring the potential impact and do not constitute rate suggestions. However, the link to atmospheric chemistry is interesting and given the environmental impact of N_2O further investigation may be merited.

Zubairova et al. [264] applied quantitative Raman spectroscopy to provide measurements of major reactants, products and temperature for Flame 4A in a stagnation

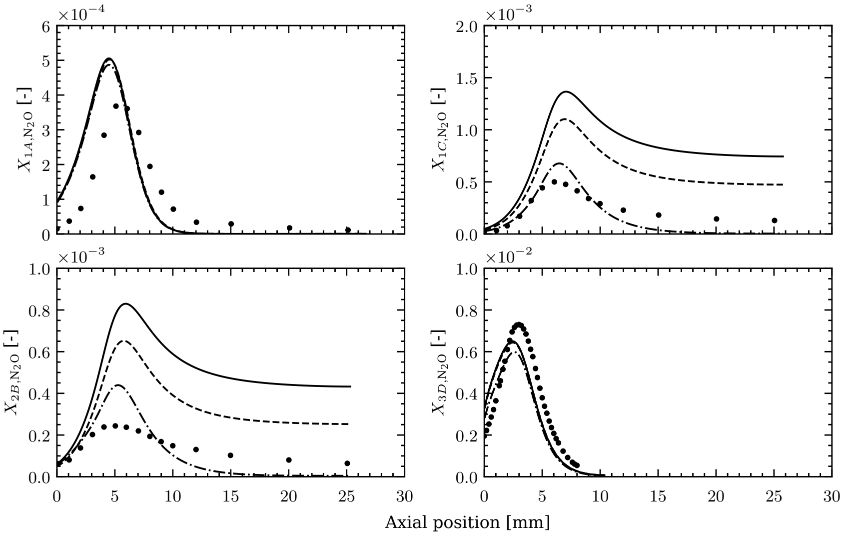

Figure 4.24: Flames 1A (top right), 1C (top left), 2B (bottom left) and 3D (bottom right). The sensitivity to fitted rate (R4.113) for $N_2O + O_2 \rightleftharpoons NO + NO_2$; (solid lines) base case mechanism of Table 4.4; (dashed lines) with singlet oxygen, $O(^1D)$, chemistry included (R4.106-R4.110); (dot-dashed lines) with (R4.105) the global one-step reaction.

flow configuration as shown in Fig. 4.25. Measurement uncertainties were quantified. The flame was slightly lifted from the burner exit and flow variations [264] are indicated by NH_3 and O_2 measurements in this region. Some deviations from the nominal reactant concentrations (see Table 4.1) are observed and can be attributed to experimental uncertainties. The current results were obtained using inflow velocities that mirror the LBV computations in Fig. 4.17 with 10 cm/s required for the current mechanism, 12.8 cm/s for that of Glarborg et al. [250] and 8.3 cm/s for Okafor et al. [258]. A positional uncertainty in the flame front location of 1.5 to 2 mm was observed between the recording of different data sets. No adjustment was done in the presentation of the current results. Accounting for the positional uncertainty, computed values are within the experimental variability apart from close to the burner and the stagnation plate. The latter has a negligible impact elsewhere. Some differences in flame dynamics are observed with the mechanism of Okafor et al. [258] consuming reactants more slowly than that of Glarborg et al. [250] with the current mechanism in-between. Measured NO levels reach a plateau of 3720 ± 120 ppm with

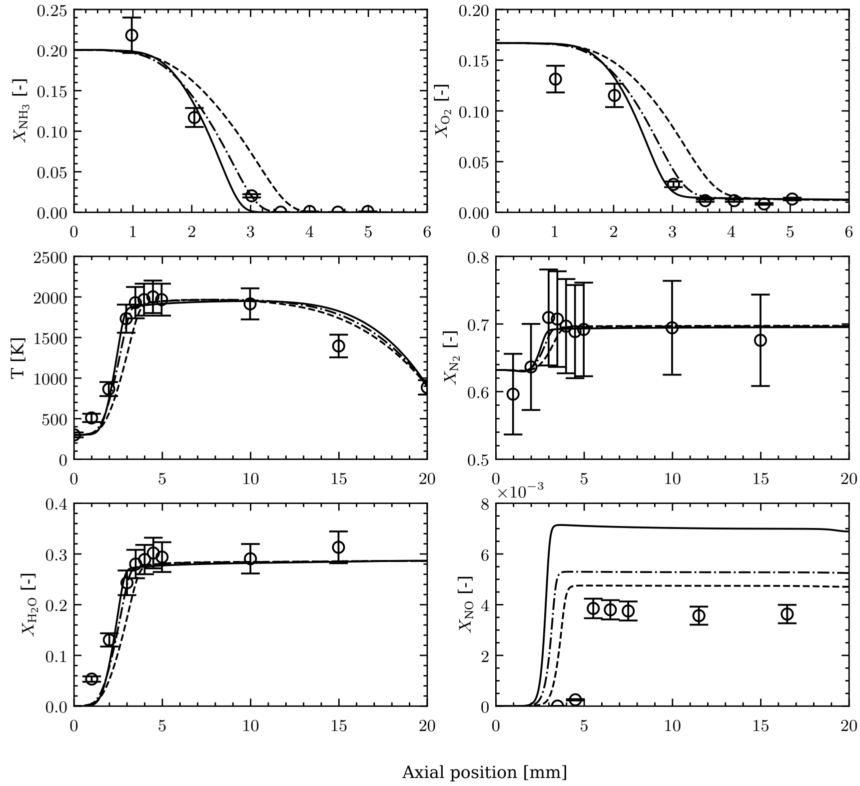

Figure 4.25: Flame 4A. Comparison of the mechanism of Glarborg et al. [250] (solid lines), Okafor et al. [258] (dashed lines) and the current mechanism (dot-dashed lines). Experimental data (circles) obtained using quantitative Raman spectroscopy by Zubairova et al. [264].

computations resulting in overpredictions to varying degrees. Zubairova et al. [264] applied an inflow velocity of 7.0 cm/s and obtained NO levels within experimental uncertainties using the mechanism of Okafor et al. [258]. Computed NO values are sensitive to the absolute rate for NH + OH $\rightleftharpoons$ HNO + H and the branching to H_2O + N. Computed NO results are also very sensitive to modest deviations in NH_3 concentrations close to the burner and to temperature. For example, NO levels are underpredicted for Flame 3D where temperature uncertainties are much greater. Overall, the exceptional sensitivity of NO to experimental conditions is evident and further characterisation close to the burner as well as measurements of the H and HNO radicals would be of exceptional value.

4.3 Nitromethane

4.3.1 Introduction

The study of alternative fuel options to be used directly and in fuel blends has increased in recent decades in order to meet the new more stringent regulations on pollution and CO_2 emissions. Nitromethane, CH_3NO_2, has a history of use in high-performance vehicles, particularly in blends with methanol for drag racing, as well as in explosives [240]. Assessment of the impact of nitromethane on engine performance when used as an additive began in the 1950s with Starkman [325] who showed that the engine power increased with nitromethane addition. More recently, studies of the laminar burning velocity of nitromethane/air spherical flames were conducted by Brequigny et al. [326] for an initial temperature of 423 K and a pressure range of 0.5-3 bar. A mechanism was developed containing 88 species and 701 reactions building on the prior work of Zhang et al. [327]. Nauclér et al. [328] extended this study by measuring laminar flame speeds for flat flames at atmospheric pressure and three initial temperatures in the range 338-358 K and compared the kinetic mechanisms of Zhang et al. [327] and Brequigny et al. [326]. It was found that the burning velocity was under predicted by both mechanisms and high uncertainties were encountered. Subsequently, Brackmann et al. [329] conducted further burning velocity experiments for nitromethane/air flames and compared the mechanisms of Brequigny et al. [326] and Mathieu et al. [330] for both burning velocity and ignition delay time calculations. Brackmann et al. [329] concluded that neither mechanism sufficiently predicted the combustion of nitromethane, failing to adequately predict both burning velocities and ignition delay times across a range of pressures, temperatures and dilution ratios and made recommendations for the consideration of the work of Annesley et al. [331] and Matsugi and Shiina [332] on nitromethane decomposition reaction pathways.

More recently, Gao et al. [333] studied the ignition delay time in shock tubes of

CH_3NO_2/Ar mixtures in the temperature range 1200-2000 K at 2 and 10 atm. They developed a kinetic model and compared it with that of Mathieu et al. [330] producing comparable results, with slight improvement of the prediction of experimental data from other literature. Shrestha et al. [334] conducted studies on the pyrolysis and oxidation of nitromethane in a plug flow and jet stirred reactor. Species profiles were measured and a model developed; they reported the model to provide satisfactory agreement with experimental results, but required improvement for predicting intermediate species for pyrolysis. The reaction $CH_3 + NO_2 \rightleftharpoons CH_3O + NO$ was highlighted to be the most important reaction for all conditions studied. In addition, the mechanism of Shrestha et al. [334] was used to calculate burning velocities and compared to the experimental data of Brequigny et al. [326] for spherical flames. The model matched the trend well across equivalence ratios and temperatures, but over-predicted the burning velocity for very rich mixtures. Whereas, when compared with the experimental data of Nauclér et al. [328], there was an under-prediction of flame speed, most prevalent at the maximum of around $\phi = 1.2$ (according to R4b, below).

In this work, a nitromethane sub-mechanism, primarily based on the work from Dean and Bozzelli [163], Miller and Bowman [248], Brequigny et al. [326], Mathieu et al. [330], Juchmann et al. [335] and Gao et al. [333] is appended to the ammonia sub-mechanism presented in Section 4.2 and both global and detailed properties are computed and compared to experimental data.

Table 4.5: Nitromethane sub-mechanism applied in the current work. Forward rate constants as $k_f = AT^n e^{-E_a/RT}$. Units: kg, m, s, kmol, kJ, K.

No.	Reaction	A	n	E_a	Ref.
4.111	$NO + C_1 \rightleftharpoons N + CO$	2.800×10^{10}	0.00	0	[336]
4.112	$NO + C_1 \rightleftharpoons CN + O$	2.000×10^{10}	0.00	0	[336]
4.113	$NO + CH \rightleftharpoons HCN + O$	4.800×10^{10}	0.00	0	[335]
4.114	$NO + CH \rightleftharpoons CO + NH$	5.000×10^{9}	0.00	0	[335]
4.115	$NO + CH \rightleftharpoons NCO + H$	1.800×10^{10}	0.00	0	[335]
4.116	$NO + CH \rightleftharpoons CHO + N$	2.600×10^{10}	0.00	0	[335]

Table 4.5 (Continued)

No.	Reaction	A	n	E_a	Ref.
4.117	$NO + CH_2t \rightleftharpoons HCNO + H$	2.500×10^{9}	0.00	2.510×10^{4}	[335]
4.118	$NO + CH_2t \rightleftharpoons HCN + OH$	5.012×10^{8}	0.00	1.205×10^{4}	[335]
4.119	$NO + CH_2s \rightleftharpoons HCN + OH$	3.300×10^{9}	0.00	0	[335]
4.120	$NO + CH_2s \rightleftharpoons HCNO + H$	6.600×10^{9}	0.00	0	[335]
4.121	$NO + CH_3 \rightleftharpoons HCN + H_2O$	1.200×10^{11}	0.00	1.218×10^{5}	[337]
4.122	$NO + CHO \rightleftharpoons HNO + CO$	1.085×10^{9}	0.10	-2.010×10^{3}	[338]
4.123	$NO + CH_2O \rightleftharpoons HNO + CHO$	1.023×10^{10}	0.00	1.714×10^{5}	[160]
4.124	$NO + CH_3O \rightleftharpoons CH_2O + HNO$	1.300×10^{11}	-0.70	0	[339]
4.125	$NO + C_2HO \rightleftharpoons HCN + CO_2$	1.630×10^{12}	-0.74	4.356×10^{3}	[185]
4.126	$NO + C_2HO \rightleftharpoons HCNO + CO$	5.652×10^{10}	0.00	3.553×10^{3}	[185]
4.127	$NO + C_2H \rightleftharpoons HCN + CO$	6.000×10^{10}	0.00	2.395×10^{3}	[340]
4.128	$NO_2 + CH \rightleftharpoons CHO + NO$	1.010×10^{11}	0.00	0	[341]
4.129	$NO_2 + CH_3 \rightleftharpoons CH_3O + NO$	1.300×10^{10}	0.00	0	[342]
4.130	$NO_2 + CH_4 \rightleftharpoons CH_3 + HNO_2$	1.200×10^{10}	0.00	1.260×10^{5}	[343]
4.131	$NO_2 + CHO \rightleftharpoons HNO_2 + CO$	1.700×10^{10}	0.00	0	[160]
4.132	$NO_2 + CO \rightleftharpoons NO + CO_2$	9.033×10^{10}	0.00	1.419×10^{5}	[160]
4.133	$N_2O + C_1 \rightleftharpoons CN + NO$	1.000×10^{10}	0.00	0	[344]
4.134	$N_2O + CO \rightleftharpoons N_2 + CO_2$	3.200×10^{8}	0.00	8.532×10^{4}	[345]
4.135	$N_2 + CH \rightleftharpoons HCN + N$	3.680×10^{4}	1.42	8.704×10^{4}	[346]
4.136	$N_2 + CH_2t \rightleftharpoons HCN + NH$	1.000×10^{9}	0.00	3.102×10^{5}	[163]
4.137	$N + CH \rightleftharpoons CN + H$	1.300×10^{10}	0.00	0	[347]
4.138	$N + CH_2t \rightleftharpoons HCN + H$	5.000×10^{10}	0.00	0	[248]
4.139	$N + CH_3 \rightleftharpoons HCN + H_2$	7.000×10^{9}	0.00	0	[348]
4.140	$N + CH_4 \rightleftharpoons NH + CH_3$	1.000×10^{10}	0.00	1.008×10^{5}	[344]
4.141	$NH + CH \rightleftharpoons HCN + H$	5.000×10^{10}	0.00	0	[344]
4.142	$NH + CH_2t \rightleftharpoons H_2CN + H$	3.000×10^{10}	0.00	0	[344]
4.143	$HCN + O \rightleftharpoons CN + OH$	4.200×10^{7}	0.40	8.683×10^{4}	[163]
4.144	$HCN + O \rightleftharpoons NH + CO$	5.400×10^{5}	1.21	3.146×10^{4}	[163]
4.145	$HCN + O \rightleftharpoons NCO + H$	2.000×10^{5}	1.47	3.188×10^{4}	[163]
4.146	$HCN + OH \rightleftharpoons CN + H_2O$	3.900×10^{3}	1.83	4.322×10^{4}	[163]
4.147	$HCN + OH \rightleftharpoons HNCO + H$	4.800×10^{8}	0.00	4.620×10^{4}	[344]
4.148	$HCN + OH \rightleftharpoons HOCN + H$	9.200×10^{9}	0.00	6.300×10^{4}	[344]
4.149	$HCN + OH \rightleftharpoons NH_2 + CO$	7.830×10^{-7}	4.00	1.680×10^{4}	[344]
4.150	$CN + O \rightleftharpoons CO + N$	7.700×10^{10}	0.00	0	[163]
4.151	$CN + H_2 \rightleftharpoons HCN + H$	3.000×10^{2}	2.45	9.396×10^{3}	[349]
4.152	$CN + OH \rightleftharpoons NCO + H$	6.000×10^{10}	0.00	0	[165]
4.153	$CN + O_2 \rightleftharpoons NCO + O$	6.620×10^{9}	0.00	-1.707×10^{3}	[165]
4.154	$CN + NO_2 \rightleftharpoons NCO + NO$	3.000×10^{10}	0.00	0	[248]
4.155	$CN + N_2O \rightleftharpoons NCO + N_2$	1.000×10^{10}	0.00	0	[248]

Table 4.5 (Continued)

No.	Reaction	A	n	E_a	Ref.
4.156	$CN + CH_4 \rightleftharpoons HCN + CH_3$	2.170×10^{10}	0.00	5.137×10^{3}	[248]
4.157	$CN + N \rightleftharpoons C_1 + N_2$	1.040×10^{12}	-0.50	0	[248]
4.158	$CN + NO \rightleftharpoons N_2 + CO$	1.080×10^{11}	0.00	3.372×10^{4}	[350]
4.159	$CN + NO \rightleftharpoons N + NCO$	9.640×10^{10}	0.00	1.769×10^{5}	[351]
4.160	$NCO + M \rightleftharpoons N + CO + M$	1.020×10^{12}	0.00	1.961×10^{5}	[165]
4.161	$NCO + H \rightleftharpoons NH + CO$	5.000×10^{10}	0.00	0	[352]
4.162	$NCO + O \rightleftharpoons NO + CO$	5.600×10^{10}	0.00	0	[353]
4.163	$NCO + OH \rightleftharpoons NO + CHO$	5.000×10^{9}	0.00	6.304×10^{4}	[354]
4.164	$NCO + NO \rightleftharpoons N_2O + CO$	6.200×10^{14}	-1.73	3.207×10^{3}	[355]
4.165	$NCO + NO \rightleftharpoons N_2 + CO_2$	7.800×10^{14}	-1.73	3.207×10^{3}	[355]
4.166	$NCO + N \rightleftharpoons N_2 + CO$	2.000×10^{10}	0.00	0	[352]
4.167	$NCO + HNO \rightleftharpoons HNCO + NO$	1.800×10^{10}	0.00	0	[356]
4.168	$NCO + NCO \rightleftharpoons N_2 + CO + CO$	1.800×10^{10}	0.00	0	[356]
4.169	$NCO + O_2 \rightleftharpoons NO + CO_2$	2.000×10^{9}	0.00	8.406×10^{4}	[354]
4.170	$HNCO + M \rightleftharpoons NCO + H + M$	5.000×10^{12}	0.00	5.007×10^{5}	[357]
4.171	$HNCO + H \rightleftharpoons NCO + H_2$	5.500×10^{11}	0.00	1.143×10^{5}	[358]
4.172	$HNCO + H \rightleftharpoons NH_2 + CO$	2.089×10^{11}	0.00	7.094×10^{4}	[358]
4.173	$HNCO + O \rightleftharpoons NCO + OH$	2.230×10^{3}	2.11	4.799×10^{4}	[359]
4.174	$HNCO + O \rightleftharpoons NH + CO_2$	9.600×10^{4}	1.41	3.581×10^{4}	[359]
4.175	$HNCO + O \rightleftharpoons HNO + CO$	1.500×10^{5}	1.57	1.850×10^{5}	[360]
4.176	$HNCO + OH \rightleftharpoons NCO + H_2O$	3.450×10^{4}	1.50	1.510×10^{4}	[361]
4.177	$HNCO + OH \rightleftharpoons NH_2 + CO_2$	3.630×10^{3}	1.50	1.510×10^{4}	[361]
4.178	$HNCO + CN \rightleftharpoons HCN + NCO$	1.500×10^{10}	0.00	0	[359]
4.179	$HNCO + NH \rightleftharpoons NH_2 + NCO$	2.000×10^{10}	0.00	5.006×10^{4}	[362]
4.180	$HOCN + M \rightleftharpoons HNCO + M$	3.100×10^{5}	0.84	8.054×10^{3}	[163]
4.181	$HOCN + H \rightleftharpoons NH_2 + CO$	1.200×10^{5}	0.61	8.721×10^{3}	[163]
4.182	$HOCN + H \rightleftharpoons NCO + H_2$	2.400×10^{5}	1.50	2.779×10^{4}	[163]
4.183	$HOCN + O \rightleftharpoons NCO + OH$	1.700×10^{5}	1.50	1.736×10^{4}	[163]
4.184	$HOCN + OH \rightleftharpoons NCO + H_2O$	1.200×10^{3}	2.00	-1.043×10^{3}	[163]
4.185	$HCNO + M \rightleftharpoons HNCO + M$	2.100×10^{12}	-0.69	1.198×10^{4}	[163]
4.186	$HCNO + M \rightleftharpoons HOCN + M$	1.400×10^{8}	-0.19	1.043×10^{4}	[163]
4.187	$HCNO + H \rightleftharpoons HCN + OH$	2.700×10^{8}	0.18	8.888×10^{3}	[163]
4.188	$HCNO + H \rightleftharpoons NH_2 + CO$	1.700×10^{11}	-0.75	1.214×10^{4}	[163]
4.189	$HCNO + O \rightleftharpoons CHO + NO$	7.000×10^{10}	0.00	0	[163]
4.190	$HCNO + OH \rightleftharpoons CH_2O + NO$	4.000×10^{10}	0.00	0	[163]
4.191	$N + CH_3 \rightleftharpoons H_2CN + H$	7.100×10^{10}	0.00	0	[348]
4.192	$NO + CH_3 \rightleftharpoons H_2CN + OH$	5.200×10^{9}	0.00	1.018×10^{5}	[337]
4.193	$NH + CH_3 \rightleftharpoons H_2CN + H_2$	7.100×10^{10}	0.00	0	[348]
4.194	$H_2CN + H \rightleftharpoons HCN + H_2$	1.000×10^{10}	0.00	0	[357]

Table 4.5 (Continued)

No.	Reaction	A	n	E_a	Ref.
4.195	$H_2CN + OH \rightleftharpoons HCN + H_2O$	1.000×10^{10}	0.00	0	[357]
4.196	$H_2CN + M \rightleftharpoons HCN + H + M$	3.000×10^{11}	0.00	9.240×10^{4}	[248]
4.197	$H_2CN + N \rightleftharpoons CH_2t + N_2$	2.000×10^{10}	0.00	0	[248]
4.198	$HCN + M \rightleftharpoons HNC + M$	1.600×10^{23}	-3.23	2.082×10^{5}	[163]
4.199	$HNC + O \rightleftharpoons NH + CO$	4.600×10^{9}	0.00	9.180×10^{3}	[163]
4.200	$HNC + OH \rightleftharpoons HNCO + H$	2.800×10^{10}	0.00	1.552×10^{4}	[163]
4.201	$CH_3NO_2 \rightleftharpoons CH_3 + NO_2$			See Table 4.6	
4.202	$CH_3NO_2 \rightleftharpoons CH_3O + NO$			See Table 4.6	
4.203	$CH_3NO_2 + H \rightleftharpoons HNO_2 + CH_3$	3.300×10^{9}	0.00	1.561×10^{4}	[330]
4.204	$CH_2NO_2 + CH_3 \rightleftharpoons C_2H_5 + NO_2$	5.000×10^{10}	0.00	0	[330]
4.205	$CH_3NO_2 + O \rightleftharpoons CH_2NO_2 + OH$	1.510×10^{10}	0.00	2.239×10^{0}	[330]
4.206	$CH_3NO_2 + OH \rightleftharpoons CH_2NO_2 + H_2O$	5.000×10^{2}	2.00	4.184×10^{3}	[330]
4.207	$CH_3NO_2 + OH \rightleftharpoons CH_3OH + NO_2$	2.000×10^{7}	0.00	-4.184×10^{3}	[326]
4.208	$CH_3NO_2 + O_2 \rightleftharpoons CH_2NO_2 + HO_2$	2.000×10^{10}	0.00	2.385×10^{5}	[326]
4.209	$CH_3NO_2 + CH_2t \rightleftharpoons CH_2NO_2 + CH_3$	6.500×10^{9}	0.00	3.305×10^{4}	[326]
4.210	$CH_3NO_2 + H \rightleftharpoons CH_2NO_2 + H_2$	7.500×10^{9}	0.00	4.184×10^{4}	[330]
4.211	$CH_3NO_2 + CH_3 \rightleftharpoons CH_2NO_2 + CH_4$	7.080×10^{8}	0.00	4.661×10^{4}	[330]
4.212	$CH_3NO_2 + CH_3O \rightleftharpoons CH_2NO_2 + CH_3OH$	3.000×10^{8}	0.00	2.929×10^{4}	[330]
4.213	$CH_3NO_2 + C_2H_5 \rightleftharpoons CH_2NO_2 + C_2H_6$	3.000×10^{8}	0.00	4.896×10^{4}	[330]
4.214	$CH_3NO_2 + HO_2 \rightleftharpoons CH_2NO_2 + H_2O_2$	1.500×10^{8}	0.00	6.276×10^{4}	[330]
4.215	$CH_2NO_2 \rightleftharpoons CH_2O + NO$	1.000×10^{13}	0.00	1.506×10^{5}	[330]
4.216	$CH_2NO_2 + H \rightleftharpoons CH_3 + NO_2$	5.000×10^{10}	0.00	0	[326]
4.217	$CH_2NO_2 + O \rightleftharpoons CH_2O + NO_2$	5.000×10^{10}	0.00	0	[326]
4.218	$CH_2NO_2 + OH \rightleftharpoons CH_2OH + NO_2$	1.000×10^{10}	0.00	0	[326]
4.219	$CH_2O + NO_2 \rightleftharpoons HNO_2 + CHO$	1.770×10^{3}	3.10	7.691×10^{5}	[333]
4.220	$C_2H_4 + NO_2 \rightleftharpoons CH_3CHO + NO$	4.340×10^{56}	-14.2	2.173×10^{5}	[333]
4.221	$C_2H_4 + NO_2 \rightleftharpoons C_2H_4O + NO$	6.610×10^{45}	-11.3	1.582×10^{5}	[333]
4.222	$C_2H_4 + NO_2 \rightleftharpoons C_2H_3 + HNO_2$	4.300	3.90	1.263×10^{5}	[333]

4.3.2 Nitromethane sub-mechanism

The nitromethane sub-mechanism shown in Table 4.5 was appended to the ammonia sub-mechanism in Table 4.4 along with the detailed H/C_1–C_2 base mechanism used with the iso-octane and n-heptane sub-mechanisms in Chapter 3. This added an additional 11 chemical species and 112 elementary reactions. A reduced C_1 –

C_2 base mechanism was also explored with ethanol, DME and their associated decomposition products removed for computational efficiency and only a minor impact was noted.

The stoichiometry for nitromethane oxidation can be defined in different ways according to the assumed major products, namely the inclusion of NO instead of N_2. Both balancing equations coexist in the literature and therefore, clearly defining the approach used is required. The two stoichiometric equations are shown below:

$$\mathrm{CH_3NO_2} + 0.75\,\mathrm{O_2} \rightarrow \mathrm{CO_2} + 1.5\,\mathrm{H_2O} + 0.5\,\mathrm{N_2} \tag{R4a}$$

$$\mathrm{CH_3NO_2} + 1.25\,\mathrm{O_2} \rightarrow \mathrm{CO_2} + 1.5\,\mathrm{H_2O} + \mathrm{NO} \tag{R4b}$$

Reactions (R4.201) to (R4.222) show the nitromethane sub-mechanism and the focus of this work. Nitromethane thermal decomposition was approximated by reactions (R4.201) and (R4.202) taken from the work by Annesley et al. [331] and producing the methyl radical and nitrogen dioxide or methoxide (CH_3O) and nitric oxide. Hydrogen abstraction reactions with H, CH_3, O, OH, CH_2, CH_3O, C_2H_5 and HO_2 (R4.203 – R4.214) were also included, producing CH_2NO_2 and the corresponding chemical species. Further thermal decomposition or hydrogen abstraction with O, OH and H was included to consume CH_2NO_2 (R4.215 – R4.218) with the products subsequently consumed by reactions in the base mechanism or other H/N reactions included in (R4.111 – R4.200).

In addition, different rate constants were used for the thermal decomposition reactions (R4.201) and (R4.202), depending on the pressure. The various rate constants according to Annesley et al. [331] are shown in Table 4.6. The rate constants for the closest pressure were used, for the 2 atm cases the 3 atm rate constants were favoured. However, little difference in ignition delay times was observed.

$$\mathrm{CH_3NO_2} \rightleftharpoons \mathrm{CH_3} + \mathrm{NO_2} \tag{R4.201}$$

$$\mathrm{CH_3NO_2} \rightleftharpoons \mathrm{CH_3O} + \mathrm{NO} \tag{R4.202}$$

Table 4.6: The rate constants for the nitromethane thermal decomposition reactions used at different pressures (in atm) [331]. Forward rate constants as $k_f = AT^n e^{-E_a/RT}$. Units: kg, m, s, kmol, kJ, K.

No.	Reaction	Pressure	A	n	E_a
4.201	$CH_3NO_2 \rightleftharpoons CH_3 + NO_2$	10	6.070×10^{51}	-11.0	3.031×10^{5}
		3	1.200×10^{53}	-11.5	3.022×10^{5}
		1	4.150×10^{53}	-11.8	3.003×10^{5}
4.202	$CH_3NO_2 \rightleftharpoons CH_3O + NO$	10	2.370×10^{50}	-11.0	2.965×10^{5}
		3	8.640×10^{51}	-11.6	2.969×10^{5}
		1	6.730×10^{52}	-12.0	2.963×10^{5}

A high sensitivity to the reaction (R4.78) $HNO + O_2 \rightleftharpoons NO + HO_2$ is observed, and the rate used in the mechanism of Glarborg et al. [250] (R4.78b) was used here: $k_f = 2.00 \times 10^{10} e^{(-6.694\times10^4/RT)}$ $\mathrm{m^3\ kmol^{-1}s^{-1}}$ [163]. The selection of (R4.78b) had negligible impact on the SNCR predictions presented in Section 4.2 using (R4.78a), and can be seen as an important issue when incorporating the nitromethane chemistry in addition to the ammonia chemistry. The sensitivity to (R4.78) is discussed further below.

4.3.3 Computational methods

The computational procedure has been described previously (Sections 3.2.3, 3.3.3 and 4.2.4) and an identical methodology is applied here. In some cases the ignition delay time was defined using a fixed temperature rise threshold from the initial temperature and is compared with the conventional hydroxyl radical method and discussed in more detail below. A conversion between stoichiometries defined using R4a and R4b is possible, with the former converted to the latter by reduction by a factor of 0.6.

4.3.4 Results and discussion

4.3.4.1 Ignition delay times

The shock tube nitromethane ignition delay time conditions computed are shown in Table 4.7. The ignition delay time for nitromethane is difficult to measure experimentally due to the explosive nature of the chemical. As such, experimental definitions have focused on the second stage ignition since the first ignition occurred within the order of 10^{-5} s and was therefore within experimental uncertainty [333]. The second stage ignition delay time was identified using the time derivative of the OH radical mole fraction trace. Gao et al. [333] identified the second-stage ignition from the OH radical emission using the method of Stranic et al. [363] to find the total ignition delay time, through an extrapolation of the maximum slope of the second-stage ignition OH radical emission signal to the baseline as shown in Fig. 4.26. This method was also adopted in this computational work, however it was found to be temperamental. The first-stage ignition within a few microseconds was reliably found, but the second-stage peak was not readily deduced. Therefore, an alternative approach was adopted for the 1% nitromethane mixtures which considered the overall temperature rise. Three threshold temperature rises were used for each stoichiometry: lean mixtures 97 K, stoichiometric mixtures 60 K and rich mixtures 35 K. The thresholds were modest due to the weak nature of nitromethane flames.

Two nitromethane mixture percentages were analysed pressures of 2 and 10 atm across a temperature range of 900 – 1810 K for 1% nitromethane mixtures at $\phi = 0.5$, 1.0 and 2.0 (according R4a). The results were compared to experimental data for similar conditions from Gao et al. [333] and Mathieu et al. [330] and are shown in Fig. 4.27. The computations show generally excellent agreement with the experimental data with the same temperature rise threshold applied to both

Table 4.7: Ignition delay time conditions computed.

$X_{CH_3NO_2}$	ϕ	Diluent	Pressure [atm]	Temperature range [K]
1%	0.5	Ar	10	1190 – 1540
1%	1.0	Ar	10	1250 – 1600
1%	2.0	Ar	10	1410 – 1810
1%	0.5	Ar	2	1130 – 1660
1%	1.0	Ar	2	1250 – 1660
1%	2.0	Ar	2	1390 – 1810
4%	0.5	N_2	15	1000– 1430
4%	1.0	N_2	8	900 – 1250

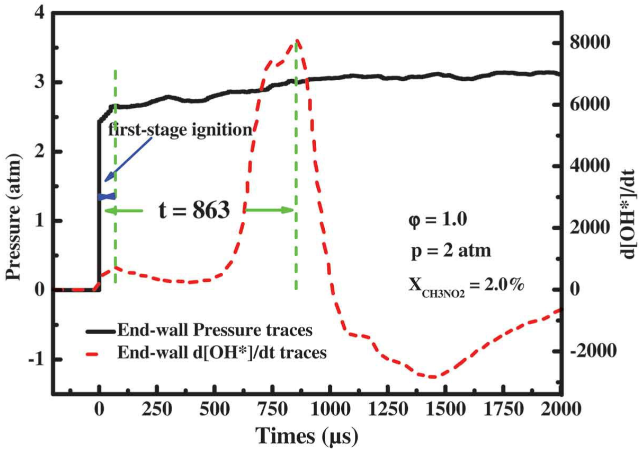

Figure 4.26: An example OH radical time derivative trace used for identifying the total ignition delay time using the second-stage ignition peak. From [333].

pressures. It is clear that the impact of mixture stoichiometry is larger than that of pressure. The results for two further conditions with 4% nitromethane/N_2 mixtures are shown in Fig. 4.28 comparing two IDT identification methods, temperature rise and the second-stage OH peak time derivative methodology. For the temperature rise method, since the 4% nitromethane mixtures produced stronger flames the thresholds were higher, 500 K for both stoichiometries. The results are in good agreement with the experimental data with the stoichiometric mixture IDTs slightly under-predicted. The OH peak method provided similar agreement for the stoichiometric mixture. However, for the fuel lean mixture at around 1000 K there appears to be a change in the ignition behaviour. Hydroxyl radical production from (R4.80) and (R4.83) reduces by about a factor of 20 from 992 K to 1002 K.

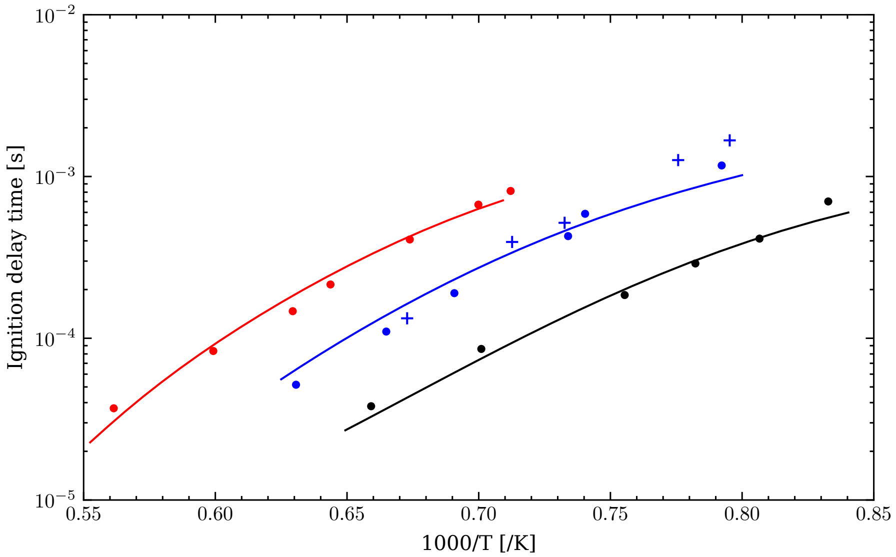

(a) Ignition delay times at 10 atm.

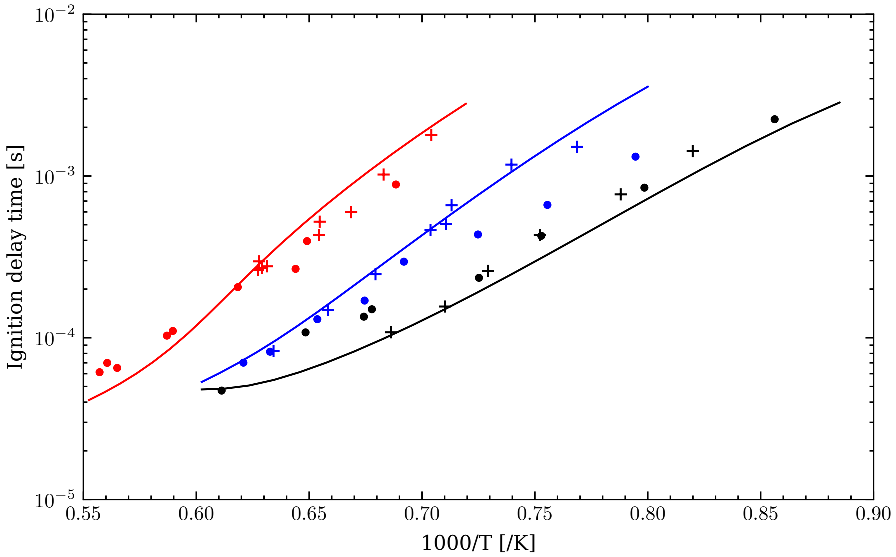

(b) Ignition delay times at 2 atm.

Figure 4.27: The ignition delay time computations for $\phi = 0.5$, 1.0 and 2.0 with 1% nitromethane/Ar mixtures at 10 and 2 atm. Experimental data from: dots [333]; pluses [330]. The colour key is: black: $\phi = 0.5$; blue: $\phi = 1.0$; red: $\phi = 2.0$.

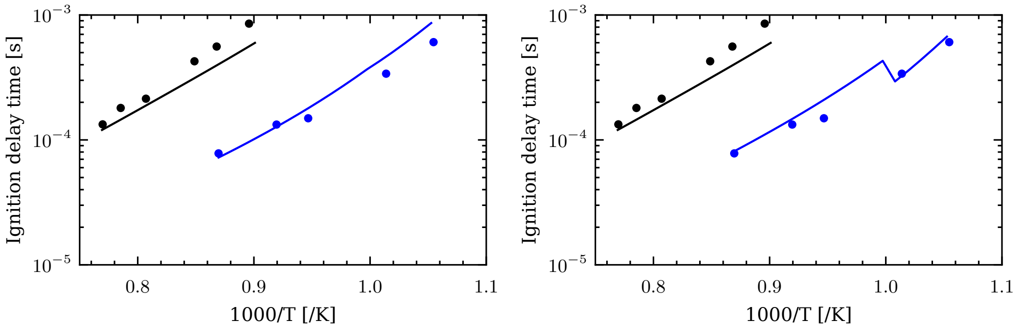

(a) Ignition delay times identified using temperature rise.
(b) Ignition delay times identified using the second-stage ignition OH peak time derivative.

Figure 4.28: The ignition delay time computations for ϕ = 0.5 and 1.0 with 4% nitromethane/N_2 mixtures at 15 and 8 atm. Experimental data from: dots [364]. The colour key is: black: ϕ = 1.0, 8 atm; blue: ϕ = 0.5, 15 atm.

4.3.4.2 Laminar burning velocities

The laminar burning velocities at atmospheric pressure and two different inlet temperatures were calculated and compared with the corresponding experimental data. The results for 348 K inlet temperature are compared with the flat flame data of Nauclér et al. [328] and shown in Fig. 4.29a. The predictions show good agreement with the fuel rich stoichiometries with an increasing discrepancy with the measurements for the leaner mixture, up to about 5.5 cm/s for ϕ = 0.8.

The same trend prediction is seen when compared with the experimental data for the spherical flames of Brequigny et al. [326], but with a maximum overprediction of about 12 cm/s for ϕ = 0.5. However, Nauclér et al. [328] further concluded that discrepancies between models and the spherical flame dataset was likely due to inconsistencies with the measurements. The experimental dataset of Brequigny et al. [326] used a non-linear extrapolation to the unstretched case based on the expansion ratio (ratio of burnt and unburnt gas densities). The spherical flame set-up meant that, particularly at richer conditions, which exhibit a two stage heat release [365], the mixture was not yet completely burnt at the measurement location. Since the expansion ratio used by Brequigny et al. [326] assumed complete combustion and

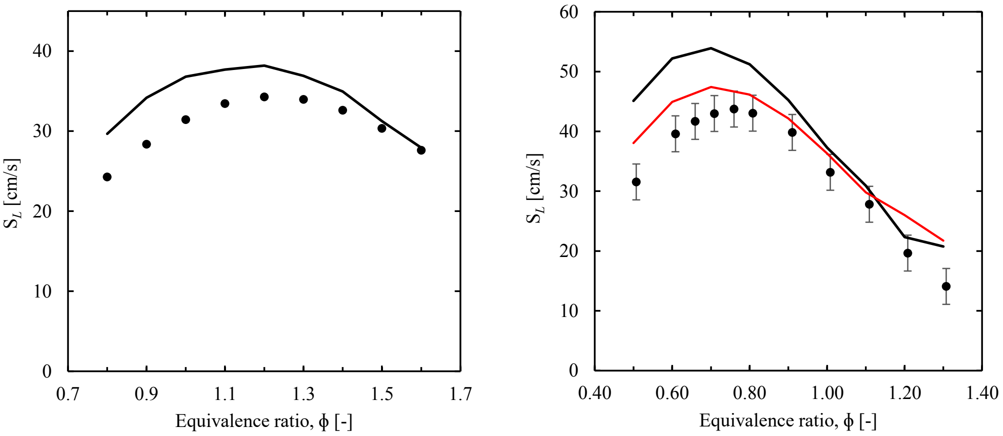

(a) T = 348 K. Experimental data: [328].

(b) T = 423 K. Experimental data: [326]. Red line for current mechanism with the rates of the CH_3NO_2 thermal decomposition reactions (R4.201,R4.202) reduced by a factor of ten.

Figure 4.29: Laminar burning velocities for nitromethane/air flames at 1 atm for a range of equivalence ratios. The stoichiometry is defined by R4b for Fig. 4.29a and R4a for Fig. 4.29b.

used an equilibrium calculation to find the density, it would result in using inappropriate expansion ratios. This was further discussed in the context of methane flames by Brequigny et al. [133]. Therefore, Nauclér et al. [328] suggested corrected expansion ratios using the mixture density at either 6.5 or 20 mm compared to the unburnt mixture density ($\epsilon_{6.5}$ and ϵ_{20}, respectively). These are shown in Fig. 4.30 (edited from Nauclér et al. [328]) along with other extrapolation conducted by Nauclér et al. [328] using their experimental data and the results from this study overlaid.

When considering the updated burning velocities, occupying the greyed region in Fig. 4.30, the discrepancy for both experimental datasets is around 6 cm/s. Furthermore, similar model agreement is achieved in this work for the corrected velocities of Brequigny et al. [326] and the lower temperature results from Nauclér et al. [328], with good agreement with the fuel rich mixtures and an overprediction of the leaner mixtures. The model of Shrestha et al. [334] predicts the burning velocities well for the original data from Brequigny et al. [326], showing an overprediction for richer mixtures, but does so for the unadjusted values presented by Nauclér et al. [328] and

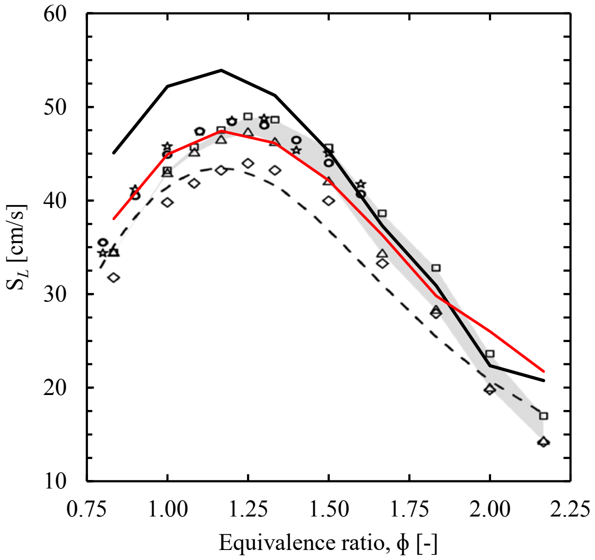

Figure 4.30: Comparison of original experimental data (diamonds) and model prediction of [326] (dashed line), with expected velocities (stars and circles for set one and two, respectively, using extrapolation by Nauclér et al. [328]), recalculated values using updated expansion ratios $\epsilon_{6.5}$ and ϵ_{20} (squares and triangles, respectively), the current work prediction overlaid (solid black line) and with the reduced fuel thermal decomposition rates as in Fig. 4.29b (solid red line). Adapted from [328].

in Fig. 4.30. The key reactions are the fuel thermal decomposition (R4.201,R4.202), with (R4.201) accounting for about 82% of nitromethane consumption and being the most active reaction in the computation for ϕ = 0.7 in Fig. 4.29b. Considering the results presented in Fig. 4.29b, reducing the thermal decomposition reactions by a factor of ten has a more significant impact on the fuel-lean mixtures. The burning velocity is reduced by about 7 cm/s for ϕ = 0.5 and 0.7, which brings the prediction within uncertainty bounds, while having a negligible impact on the fuel-rich mixture (less than 0.5 cm/s for ϕ = 1.1) as shown in Figs. 4.29b and 4.30. This alteration brings the computational prediction broadly in line with the experimental data, certainly when accounting for possible extrapolation errors. Although the recent rate suggestions from Annesley et al. [331] have been used, the uncertainties and in-particular the lack of a high and low pressure limit may restrict the accuracy of the mechanism and its validity across a wide range of conditions. Annesley et al.

[331] also acknowledge the need for further experimental and theoretical studies on these fundamental reactions. The mechanism of Glarborg et al. [250] uses the high pressure rate expression from Glaenzer and Troe [342] with the low pressure limit from Glarborg et al. [366] for (R4.201) and omitted (R4.202) from their mechanism. Future work should test the mechanism with this alternative implementation.

4.3.4.3 Speciation in a jet stirred reactor

The calculated species profiles for the isothermal oxidation of nitromethane in a jet stirred reactor were compared with the experimental results from Weng et al. [367]. A 1% $CH_3NO_2/O_2/Ar$ mixture with ϕ = 2.0 (according to R4b) at 1 atm and with a residence time, τ, of 2.0 s was studied in a temperature range of 600 – 900 K. The results with the rate for reaction (R4.78) from Dean and Bozzelli [163], also used in the mechanism of Glarborg et al. [250], and the faster rate from Fujii et al. [304], shown in Table 4.4, as discussed earlier, are shown in Figs. 4.31 and 4.32, respectively. Both cases show a slightly early onset of ignition, by about 20 K, which can be seen from the depletion of nitromethane and oxygen and the production of water leading the experimental results. As discussed by Shrestha et al. [334], in the device the set temperature only exists within a narrow physical range of the device and therefore the isothermal assumption is likely to break down, especially for cases with increased heat release.

When using the rate from Fujii et al. [304] for (R4.78) oxygen is over-consumed and reaches zero while the experimental data suggests a value nearer to 0.2% at 900 K. It can be seen from Figs. 4.31 and 4.32 that the nitromethane consumption in this temperature range is quite separate from the oxygen consumption. This is due to the thermal decomposition steps, reactions (R4.201) and (R4.202), dominating nitromethane consumption (>50%) at all temperatures and especially at temperatures above 850 K (>80%). This balance is impacted by the size of the radical pool, for example the hydroxyl radical mole fraction at 800 K is almost double when the

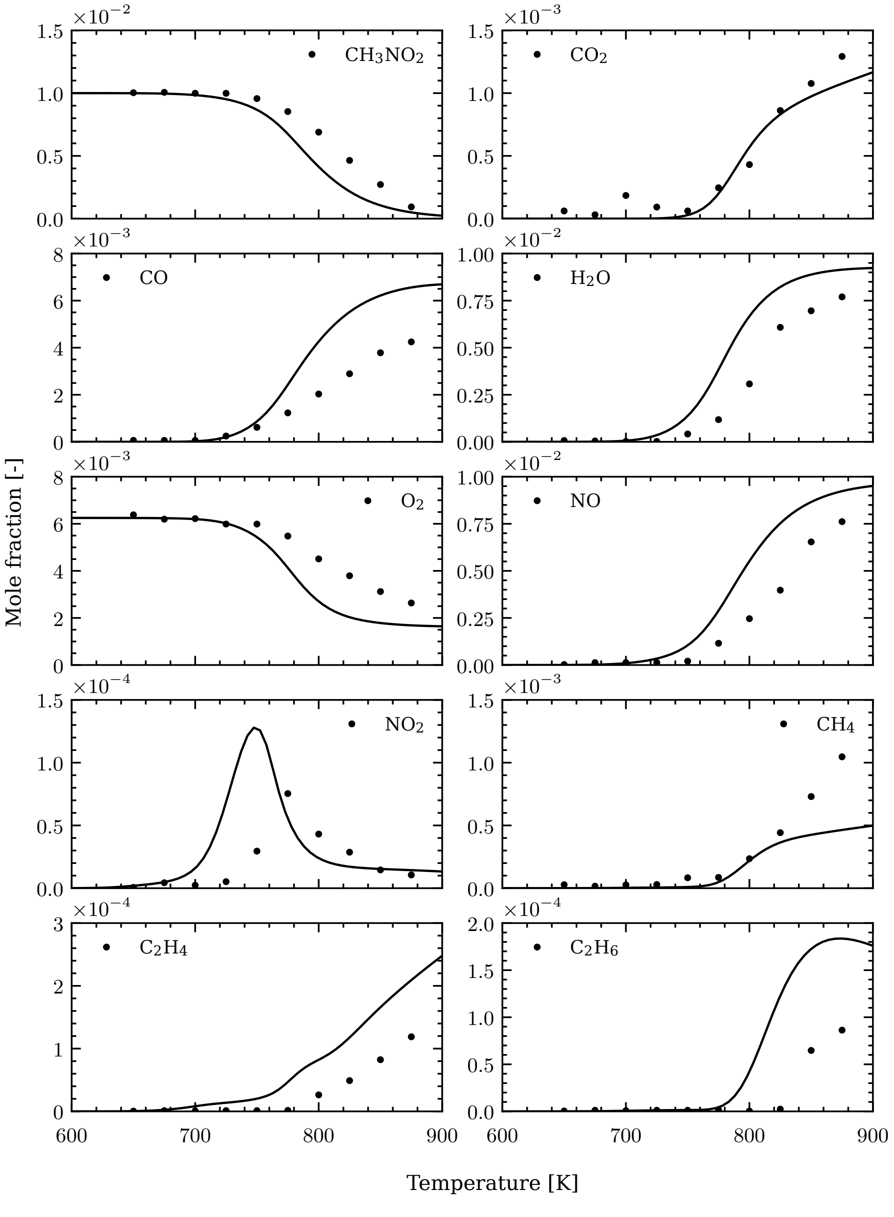

Figure 4.31: Computed species profiles for a ϕ = 2.0, 1% CH_3NO_2 with Ar as the diluent in a jet stirred reactor with residence time of 2.0 s at atmospheric pressure. The rate expression from Dean and Bozzelli [163] was used for (R4.78). Experimental data from [367].

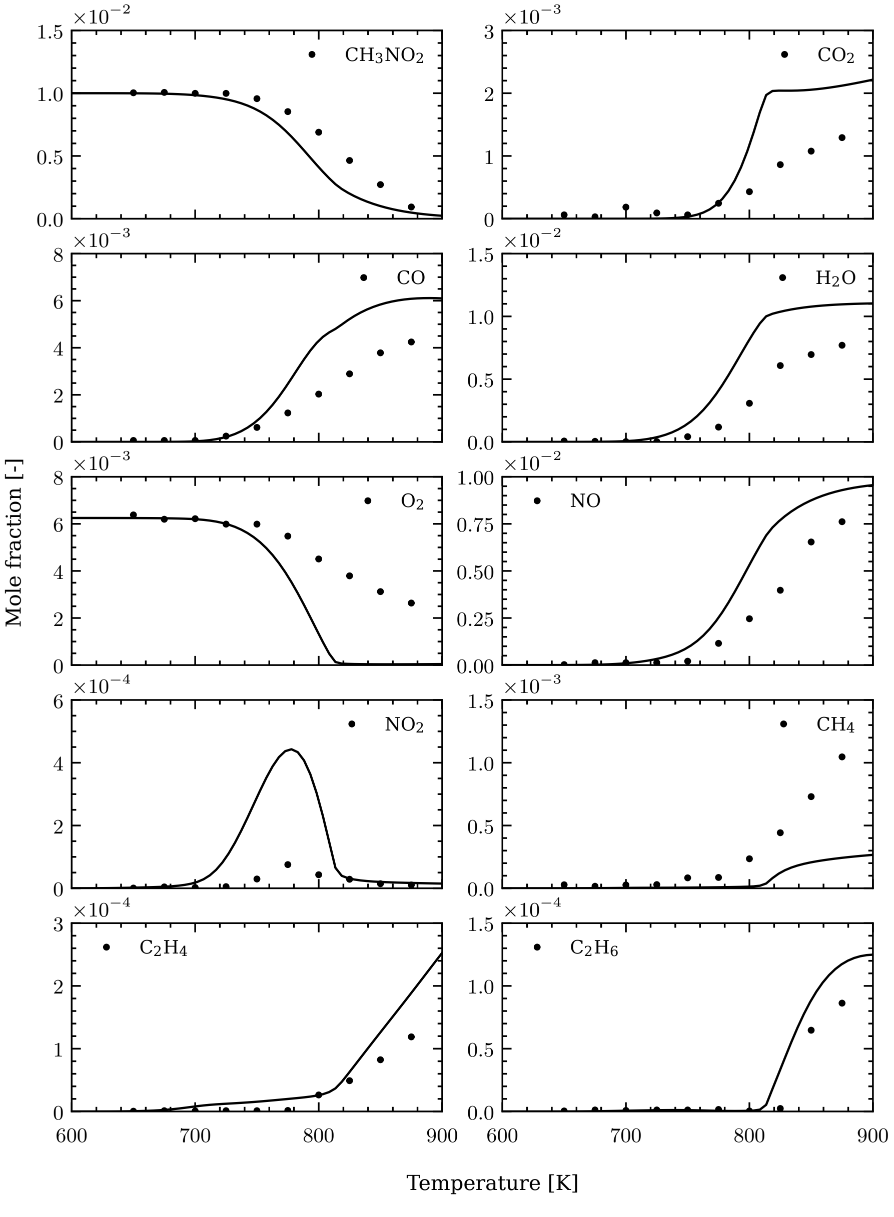

Figure 4.32: As in Fig. 4.31 with the rate expression from Fujii et al. [304] used for (R4.78), as described in Table 4.4.

faster Fujii et al. [304] rate is used for (R4.78). The NO_2 peak is overpredicted by a factor of four when the faster (R4.78) rate is used and a more modest 1.5 when the slower rate is used. Considering the reaction rates at this peak, about 750 K and 780 K for Figs. 4.31 and 4.32 respectively, the balance is similar in both cases but due to the higher temperature in the latter case the contribution from (R4.201) is almost double. Additionally, (R4.80) account for about 50% of NO_2 production in both cases but due to 50 times greater production of NO and O_2 from (R4.78) when the rate of Fujii et al. [304] is used, resulting in a three times greater concentration of NO and about a third less O_2 at the corresponding temperature to the peak NO_2.

4.3.4.4 Speciation in low pressure flames

Zhang et al. [327] studied premixed nitromethane/oxygen/argon flames at low pressure (4.655 kPa) and measured species profiles using a sampling and mass spectrometry analysis technique. The measured temperature profile for a stoichiometric mixture is shown in Fig. 4.33, for ϕ = 1.5 in Fig. 4.36 and for ϕ = 2.0 in Fig. 4.39, in addition to the fitted profile applied in the computational modelling of these flames. It adopts the approach of the modelling conducted by Zhang et al. [327], which assumes an inlet temperature of 800 K for the stoichiometric mixture and 600 K for both fuel-rich mixtures.

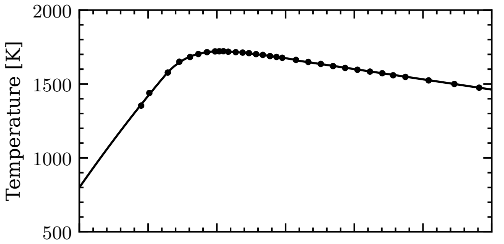

Figure 4.33: Measured and fitted temperature profile for a premixed, ϕ = 1.0 $CH_3NO_2/O_2/Ar$ flame at a pressure of 4.655 kPa. The dots are the experimental measurements by Zhang et al. [327].

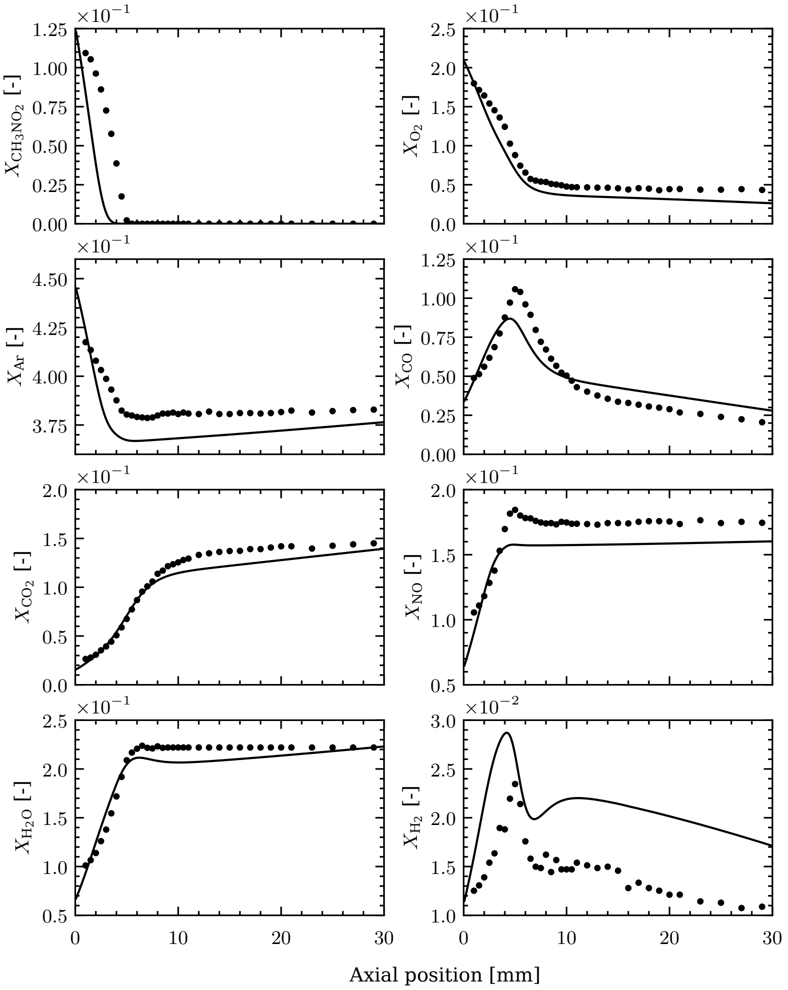

Figure 4.34: Major species profiles for a premixed stoichiometric $CH_3NO_2/O_2/Ar$ flame at a pressure of 4.655 kPa. Experimental data from [327] (dots) with the temperature profile in Fig. 4.33 applied.

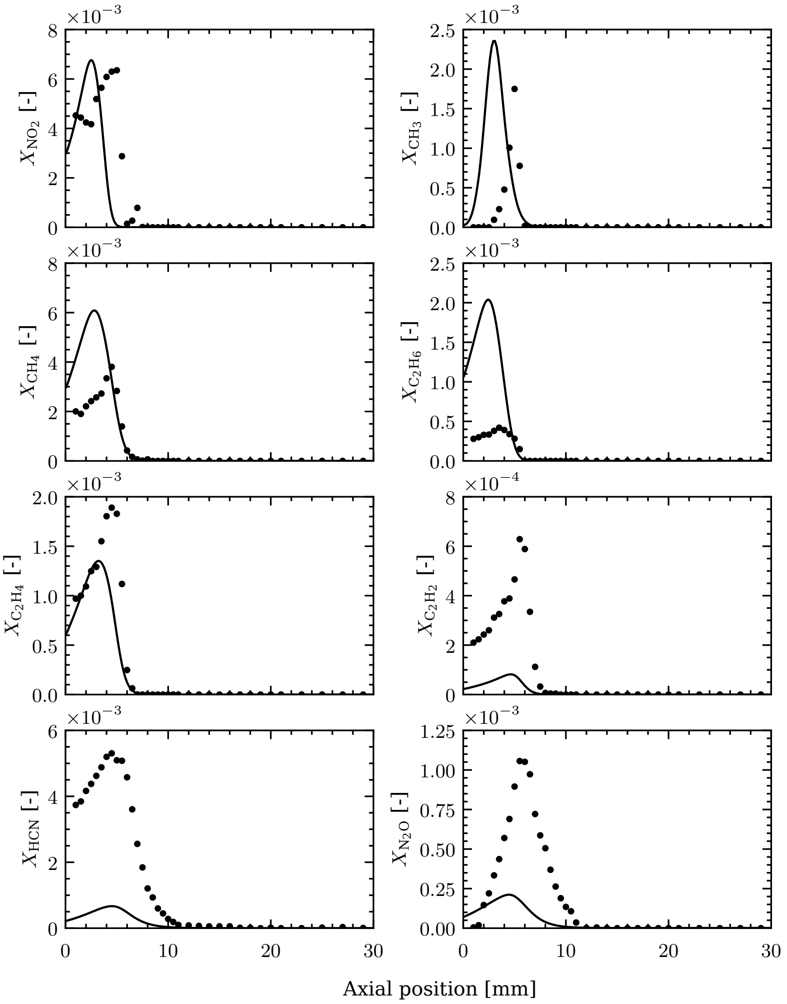

Figure 4.35: As in Fig. 4.34 for minor species profiles.

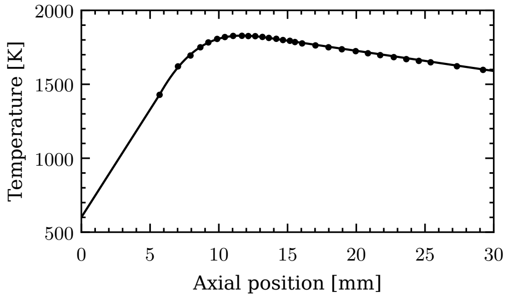

Figure 4.36: Measured and fitted temperature profile for a premixed, $\phi = 1.5$ $CH_3NO_2/O_2/Ar$ flame at a pressure of 4.655 kPa. The dots are the experimental measurements by Zhang et al. [327].

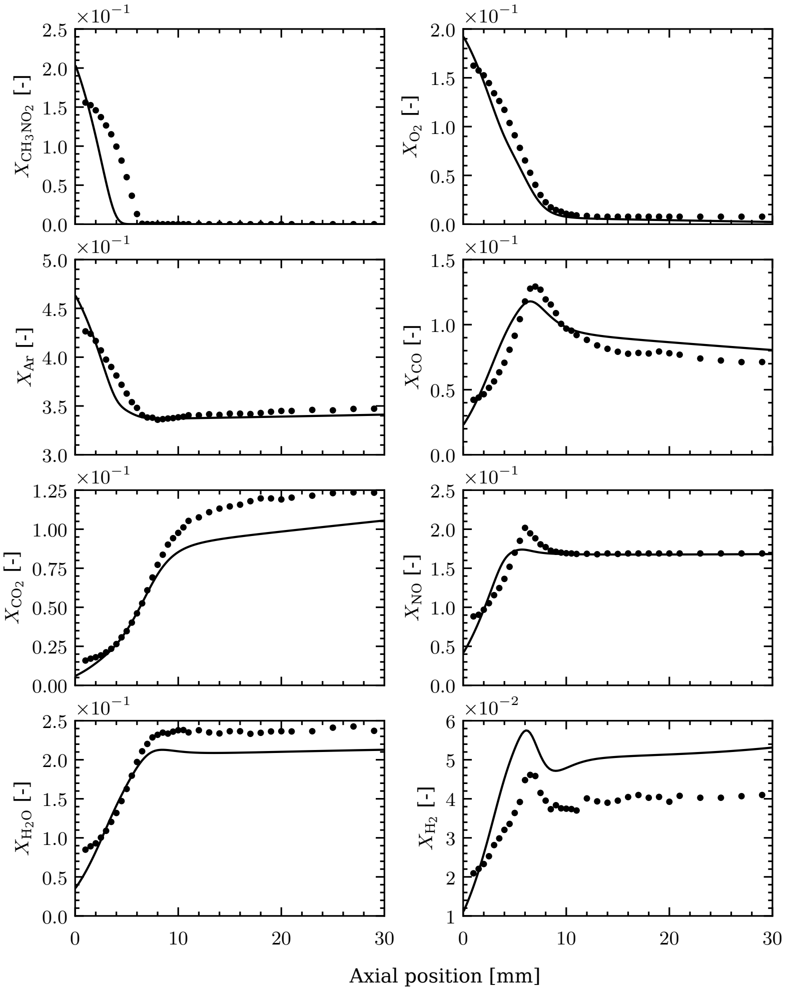

Figure 4.37: Major species profiles for a premixed, ϕ = 1.5 $CH_3NO_2/O_2/Ar$ flame at a pressure of 4.655 kPa. Experimental data from [327] (dots) with the temperature profile in Fig. 4.36 applied.

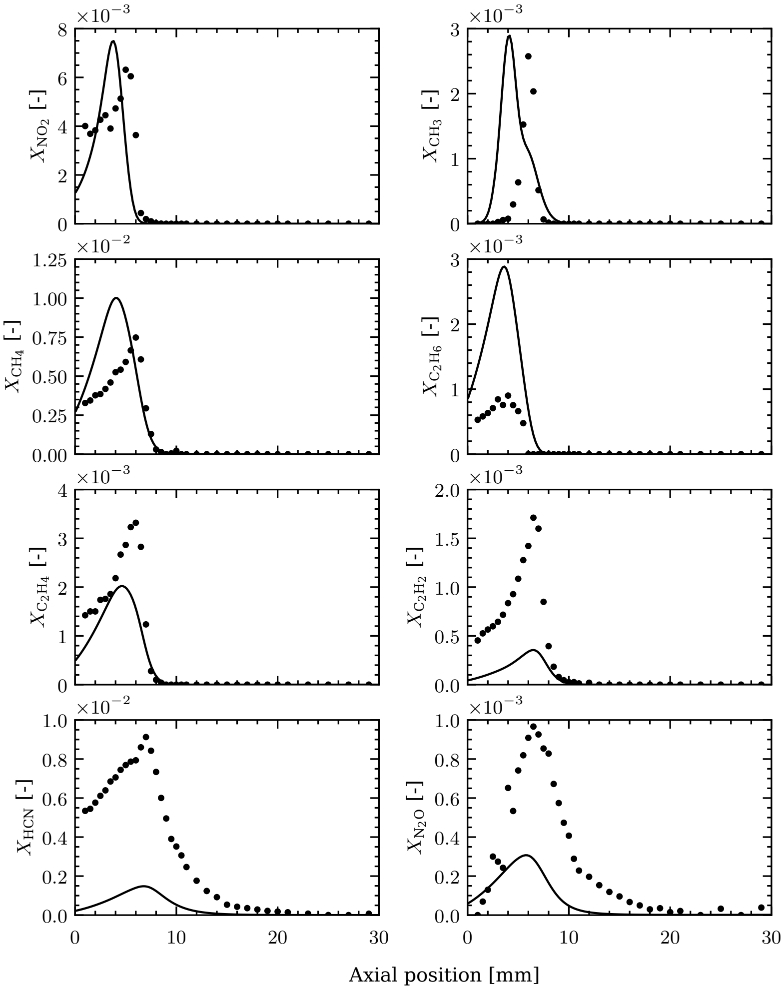

Figure 4.38: As in Fig. 4.37 for minor species profiles.

The computed species profiles are compared with the experimental measurements for both major and minor species. Good agreement is shown with all major species, apart from H_2, in Figs. 4.34, 4.37 and 4.40, with a slightly fast consumption of nitromethane not impacting prediction for O_2 consumption or H_2O and CO_2 production, with the latter slightly underpredicted in the ϕ = 2.0 flame. The predicted steady state value of NO is about 10% below the measured value for the stoichiometric flame and about 10% above the measured value for the ϕ = 2.0 flame, which is within experimental uncertainties. An interesting trough in the H_2 profile is predicted at the same point as a cluster of fluctuating experimental data points with its prominence reducing as the mixture becomes more fuel-rich. The final H_2 value is about 70% higher than the experimental data for the stoichiometric flame and reduces to closer to 20% for the fuel-rich flames. In the stoichiometric flame, about 35% of total H_2 production can be attributed to (R4.71), a further 32% to $CH_2O + H \rightleftharpoons CHO + H_2$ (RA.92) and 12% to $CHO + H \rightleftharpoons CO + H_2$ (RA.85). In addition, a dual peak is predicted for the CH_3 profile in the ϕ = 2.0 flame, shown in Fig. 4.41. The formation of CH_3 for the first peak can be attributed to the fuel thermal decomposition (R4.201) and the trough primarily due to the reduction in this rate, with approximately 71% of CH_3 consumed by (R4.129). The second peak is created by a more distributed reaction pathway including CH_4 hydrogen abstraction reactions and thermal decomposition of DME, indirectly produced by CH_3 itself. This analysis further suggests that the fuel thermal decomposition rate is too fast.

The prediction for the minor species included in Figs. 4.35, 4.38 and 4.41 show more variation than for the major species. Good agreement of the peak location is shown, however for C_2H_6, C_2H_2, HCN and N_2O differences of up to a factor of six are seen between measured and computed peak predictions for all stoichiometries. Some of these discrepancies, such as for HCN are consistent with the predictions in the literature, such as those included in the work of Zhang et al. [327]. Furthermore, the uncertainty for intermediate species was quoted as

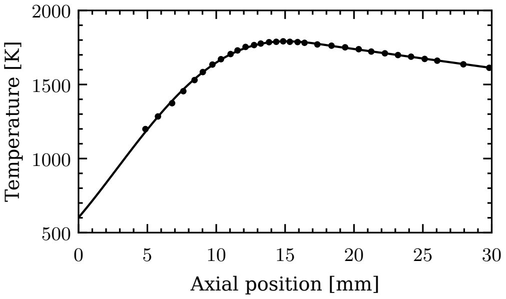

Figure 4.39: Measured and fitted temperature profile for a premixed, $\phi = 2.0$ $CH_3NO_2/O_2/Ar$ flame at a pressure of 4.655 kPa. The dots are the experimental measurements by Zhang et al. [327].

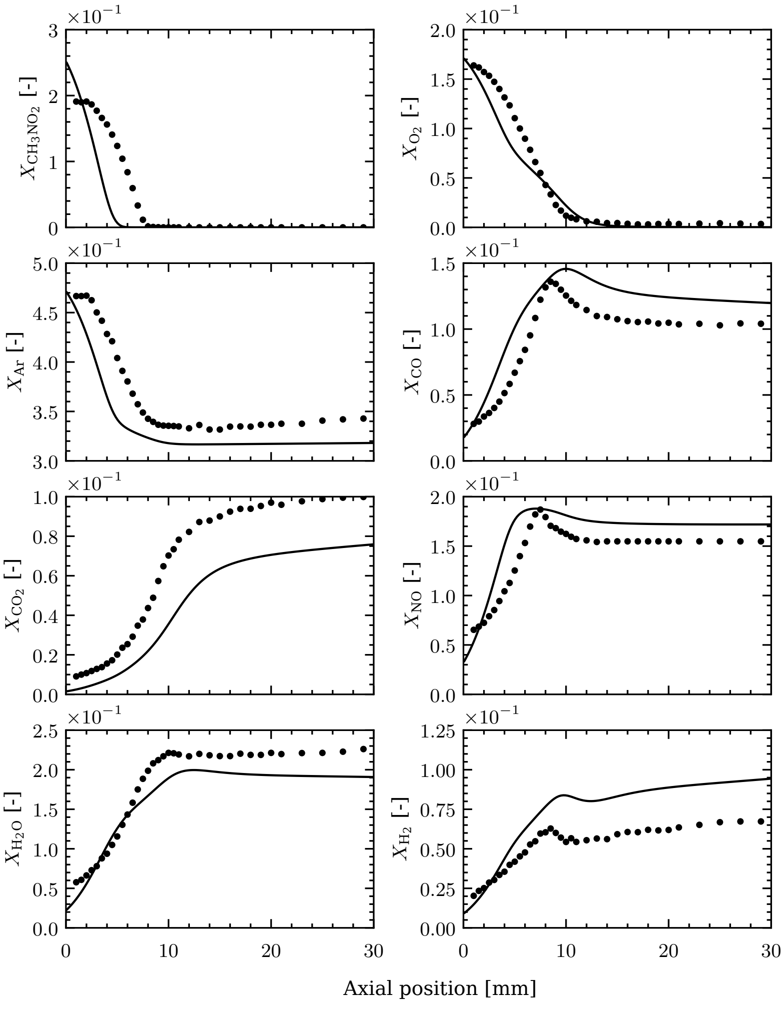

Figure 4.40: Major species profiles for a premixed, $\phi = 2.0$ $CH_3NO_2/O_2/Ar$ flame at a pressure of 4.655 kPa. Experimental data from [327] (dots) with the temperature profile in Fig. 4.39 applied.

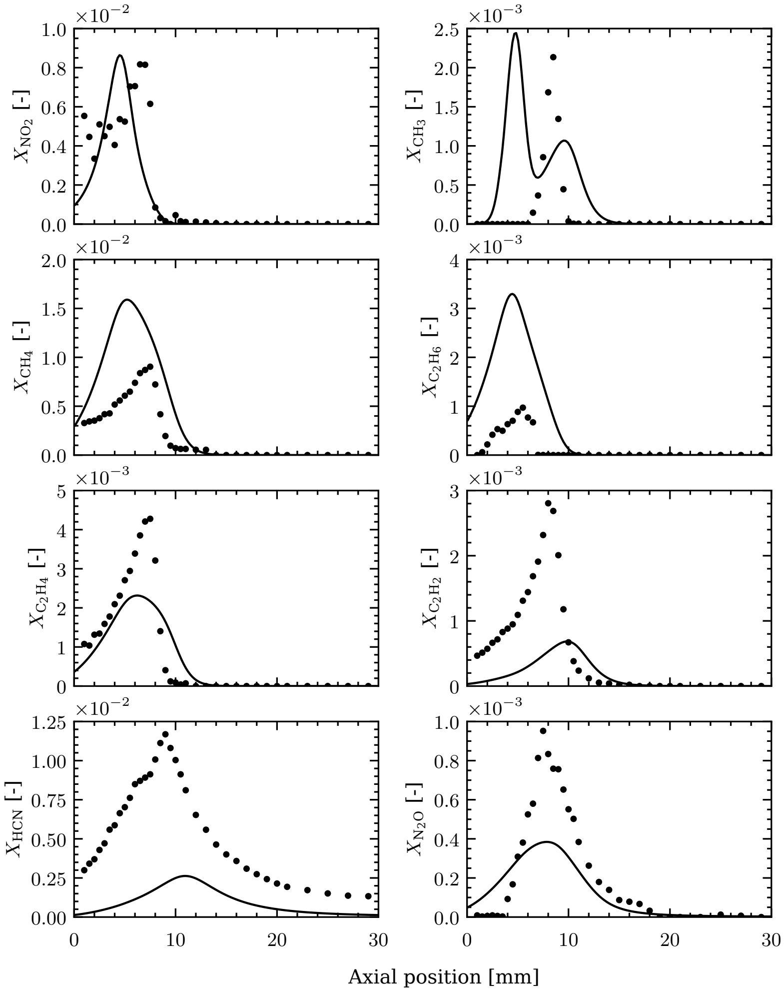

Figure 4.41: As in Fig. 4.40 for minor species profiles.

25% and larger than a factor of two for radical species due to quenching on the probe surface. Additionally, the temperature profile was recalibrated to account for radiation losses and perturbation effects of the thermocouple with errors estimated to ± 100 K. Therefore, the computed results arguably show adequate agreement with the available flame data.

4.4 Summary

A compact N/H/O reaction mechanism that enables more efficient application to turbulent flame computations via JPDF methods, as shown in [187], has been derived and shown to offer similar agreement over a wide range of data sets when compared to the reference mechanism of Glarborg et al. [250]. The current mechanism also includes recently updated chemical kinetics data. The study highlights the exceptional sensitivity to the H radical chemistry, particularly in the context of the balancing of thermal decomposition and molecular oxygen reactions for NNH and HNO. It has been confirmed that the choice made for the NNH + O_2 reaction essentially constrains the rate for the NNH thermal decomposition such that the SNCR temperature window can only be reproduced when NNH $\rightleftharpoons$ N_2 + H remains dominant. The balancing also impacts global properties, such as the laminar burning velocity, and it is suggested that close agreement for ammonia/air mixtures without consideration of moderate heat losses may be misleading. The study by Klippenstein et al. [249] resolves, at least in part, some of the issues with the chemistry of NNH. However, it is suggested that the corresponding H + NO $\rightleftharpoons$ HNO and HNO + O_2 $\rightleftharpoons$ NO + HO_2 reactions require more accurate determinations. A sensitivity to the NH + OH reaction has also been noted. Experimental data for NNH and HNO concentrations in laminar flames are exceptionally rare and subject to conjecture (NNH) or indirect determinations (HNO) [261]. Accordingly, non-intrusive flame measurements that provide uncertainty quantified temperature data and H radical concentrations would be exceptionally helpful. The same applies to measurements of the HNO radical. It has been shown that for ultra-lean ammonia flames a reaction path leading to the removal of N_2O appears absent or that current rate determinations are significantly in error. Given the high greenhouse gas potential of N_2O and long atmospheric lifetime [368], studies that extend atmospheric chemistry to ultra-lean combustion conditions are arguably essential and may require consideration of excited state oxygen chemistry e.g. arising from reactions featuring the HO_2 radical.

The nitromethane sub-mechanism has been validated against ignition delay times, laminar burning velocities and speciation in a jet stirred reactor and low pressure premixed flames. Due to the explosive nature of nitromethane the first stage ignition occurs within experimental precision and therefore the second stage ignition is used to define the IDT. This definition makes computationally defining the IDT non-trivial and a fixed temperature rise threshold, which differs for each stoichiometry, has been used to define the IDT. Using these definitions, IDTs show good agreement with the experimental data. Furthermore, different definitions for the stoichiometric equation of nitromethane oxidation necessitates clearly defining which methodology has been applied. Laminar burning velocity predictions showed deviation from the experimental data, particularly for fuel lean mixtures. Heat losses, as with ammonia, could be of relevance in this context and difficulties with experimental extrapolations could make literature data misleading. Given the possible breakdown of the isothermal assumption, reasonably good agreement is obtained when selecting the slower rate expression [163] for $HNO + O_2 \rightleftharpoons NO + HO_2$ and when the uncertainties with experimental speciation data is considered. This further emphasises the need for accurate determinations of HNO reaction pathways. Finally, speciation in a premixed flame show excellent agreement with the experimental data. It is clear that great care must be taken when studying nitromethane, both experimentally and computationally, due to its explosive nature and the multiple definitions used for its stoichiometry.

Chapter 5 | Applications

The development and validation of chemical kinetic models, as discussed in depth over the past couple of chapters, is with a view to applying the kinetic models to conditions of relevance to practical, real-world, applications. This is especially important for industry critical applications, such as in gas turbines for both aviation and power generation. The validated kinetic models allow insight into the behaviour of a given fuel at conditions that cannot be probed experimentally in a simple or cost effective manner. Such conditions may have elevated reactant temperatures, pressures, external enthalpy support, exist near the flammability limit of a fuel or any combination of these at the same time. In this section some such instances are explored.

5.1 Introduction

The ultimate goal of chemical kinetic model development and validation is their subsequent application to real world conditions for both further understanding of the underlying mechanisms and interactions occurring as well as producing reliable and actionable metrics for the engineer to use when developing and refining practical devices [369]. The chemical kinetic models discussed thus far have been validated, with shortcomings and key sensitivities outlined in their respective chapters, and some are here applied at application relevant conditions or to further explore trends that have practical implications.

In real world devices more extreme conditions are realised, with elevated temperatures, e.g. through the use of exhaust gas recirculation [370], and pressures a key parameter in ensuring complete combustion and high thermal efficiencies. Novel conversion modes, such as MILD combustion [28], involve high inlet mixture preheat and low combustion temperature due to high levels of dilution. The absence of distinct flame fronts and often the need for thermal support to sustain oxidation are characteristic of these modes aiming to greatly reduce pollutant emissions [371]. Additionally, with increased turbulence levels and the chemical timescales occurring in these devices make the accurate modelling of the combustion chemistry crucial. Further, well constrained experiments, with the aid of computational modelling, will allow for a better understanding of the flow-chemistry interactions occurring.

In this section the nature of combustion is studied at a variety of inlet temperatures, velocities and pressures with and without external enthalpy support for iso-octane flames. Mixtures of iso-octane and n-heptane are studied in shock tubes and the impact on the IDT considered. Finally, the impact of hydrogen co-firing with ammonia is briefly revisited by modelling counterflow flames with different ammonia–hydrogen fuel blends.

5.2 Methodology

In order for experiments to be of the greatest use and applicability matching the flame structure and characteristics of the desired real world device is necessary. Through exploring the burning velocity and flame thickness, defined as the 5-95% fuel consumption layer in this work, the characteristic timescale of a flame can be elicited according to:

$$t_c = \frac{l_F}{S_L} \tag{5.1}$$

where t_c is the characteristic timescale, l_F is the flame thickness and S_L is the laminar burning velocity.

There exists four parameters that can be adjusted: (i) mixture stoichiometry (ii) inlet temperature (iii) external enthalpy support and its temperature (iv) rate of strain through associated inlet velocity modulation. By calculating the characteristic timescale at elevated temperatures and pressures, experiments can be designed, through the control of the four parameters listed above, which may allow for timescale matching without having to achieve high pressures. The use of the rate of strain, fuel preheating and support on hot combustion products all allow for manipulation of the flame structure and combustion characteristics.

The computational methodology is identical to that described in previous chapters (see Section 4.3.3). In the Back-to-Burnt computations with flames supported on hot combustion products one of the boundary conditions was altered. A stoichiometric hydrogen flame with nitrogen dilution to achieve the desired temperature was calculated to steady-state as a freely propagating flame with the final composition used as an input at the 'Burnt' boundary. A hydrogen flame was selected to be consistent with previous experimental work [116] since, due to its high burning velocity, the products would be at or close to thermochemical equilibrium by the nozzle exit.

5.3 Results and discussion

5.3.1 TME conditions

The laminar burning velocity at and around the the Toyota Motor Europe (TME) conditions, which were $\phi = 0.6$, P = 700 kPa and T = 650 K and $\phi = 0.6$, P = 304 kPa and T = 450 K, were assessed. These are of relevance to in-cylinder conditions for novel combustion modes aimed at improving fuel economy and reducing emissions.

The results for three temperatures at 700 kPa are shown in Table 5.1. The TME provided[1] computed value for the first conditions was 30.2 cm/s, whereas in this

---

[1] The source of the applied mechanism is not clear.

study a value of 36.1 cm/s was found when averaging the minimum and reaction rate integral velocities for iso-octane. This is a moderate discrepancy of about 6 cm/s. However, as the temperature is reduced to 600 K the discrepancy reduced to within 1 cm/s. As shown previously, the low temperature chemistry is active at temperatures below 700 K and additionally the model tended to over-predict ignition delay times for these conditions as discussed in Section 3.2. However, as noted previously, accurate measurements of IDT are difficult for longer ignition delay times due to, amongst other issues, heat transfer to the shock tube itself. At 650 K and 700 kPa, by using the OH trace, the first stage ignition was detected at approximately 60 μs and the second stage ignition at about 6 ms. Due to the nature of the twin flame set-up, residence times can exceed tens of milliseconds and these conditions may be prone to autoignition which may produce spurious burning velocity predictions.

The laminar burning velocity for the second TME condition at a pressure of 304 kPa and inlet temperature of 450 K was calculated as 14.9 cm/s. This demonstrates the significant impact of temperature on laminar burning velocity, which acts to increase. Furthermore, the laminar flame thickness was greatly reduced by the increased pressure, with the 700 kPa flames thickness in the range of 50 – 60 μm (reducing with increasing temperature from 600 K to 650 K) and at about 160 μm for the lower 304 kPa pressure flame.

Table 5.1: Laminar burning velocities of iso-octane/air flames near the TME conditions of ϕ = 0.6, P = 700 kPa and preheat temperature of 650 K comparing differing temperatures where autoignition of the mixture becomes relevant.

Equivalence ratio, ϕ	Laminar burning velocity [cm/s]			
	TME value (650 K)	600 K	625 K	650 K
0.6	30.2	29.5	32.2	36.1

Table 5.2: The inlet conditions for the hot combustion products at about 1300, 1500 and 1700 K including the major species mole fractions.

T [K]	N_2	H_2O	H_2	O_2	OH	H	O
1314	0.857	0.142	4.53×10^{-4}	2.27×10^{-4}	5.98×10^{-5}	1.14×10^{-5}	1.21×10^{-6}
1505	0.819	0.179	9.93×10^{-4}	3.68×10^{-4}	1.78×10^{-4}	2.88×10^{-5}	3.84×10^{-6}
1699	0.765	0.233	1.93×10^{-3}	2.86×10^{-4}	2.46×10^{-4}	3.98×10^{-5}	4.09×10^{-6}

5.3.2 External enthalpy

The use of external enthalpy, supplied from a hot combustion product (HCP) stream from the lower nozzle of a counterflow burner, offers support for flames that would extinguish in a Back-to-Back configuration. Prior work [40, 116] has used an external enthalpy support to study premixed JP-10 and DME flames using the heat generated from flames of mixtures of H_2 and CH_4.

In this work the impact of stoichiometry, reactant inlet temperature and external enthalpy support temperature was explored. The composition of the hot combustion product stream at three temperatures are shown in Table 5.2. These compositions were calculated from the steady state composition of a stoichiometric hydrogen/air flame with nitrogen dilution to achieve temperatures of approximately 1300, 1500 and 1700 K. The results for three stoichiometries, ϕ = 0.7, 1.0 and 1.3, three fuel/air inlet temperatures, T_{in} = 300, 400 and 500 K, and three external enthalpy temperatures, T_{HCP} = 1300, 1500 and 1700 K, are shown in Table 5.3 for iso-octane and in Table 5.4 for n-heptane. This limited dataset allows the state space to be coarsely described and overarching trends elicited. The characteristic timescales for iso-octane/air and n-heptane/air mixtures are shown in Figs. 5.1 and 5.2, respectively, as a function of two of the variables with the third variable kept constant. Two trends are clear for both fuels, at low rates of strain the temperature of the hot combustion products has little impact on the chemical timescale and only the mixture stoichiometry and inlet temperature have an impact. Secondly, the longest timescales are seen for the fuel lean mixtures, with the shortest timescales at stoichiometric with a more gradual impact of further increases in stoichiometry to fuel-rich conditions. Furthermore, increasing the inlet temperature from 300 K to 500 K is sufficient to reduce even the longest timescales by about up to a factor of five. When comparing the different fuels, the general trends are identical, however, the timescale for the n-heptane mixtures were shorter by up to about a factor of two and were less strongly impacted by mixture stoichiometry.

Table 5.3: Results for varied stoichiometry, reactant inlet temperature and external enthalpy temperature for premixed iso-octane/air flames at atmospheric pressure and low rates of strain.

Equivalence ratio [-]	T_{HCP} [K]	T_{in} [K]	Strain rate [s^{-1}]	v_{RI} [m/s]	Thickness [μm]	Timescale [ms]
0.7	1300	300	93	0.14	339	2.47
		400	118	0.29	254	0.88
		500	117	0.48	207	0.43
	1500	300	93	0.14	339	2.45
		400	108	0.28	254	0.89
		500	105	0.47	207	0.44
	1700	300	101	0.14	339	2.44
		400	106	0.28	253	0.91
		500	112	0.47	206	0.43
1.0	1300	300	131	0.34	173	0.52
		400	121	0.51	151	0.30
		500	132	0.78	137	0.18
	1500	300	111	0.31	172	0.55
		400	120	0.51	152	0.30
		500	143	0.81	137	0.17
	1700	300	103	0.30	172	0.57
		400	111	0.49	152	0.31
		500	140	0.80	136	0.17
1.3	1300	300	122	0.28	207	0.73
		400	105	0.42	175	0.41
		500	136	0.72	152	0.21
	1500	300	124	0.28	206	0.73
		400	105	0.42	175	0.41
		500	114	0.66	151	0.23
	1700	300	127	0.28	205	0.72
		400	115	0.44	175	0.40
		500	129	0.69	152	0.22

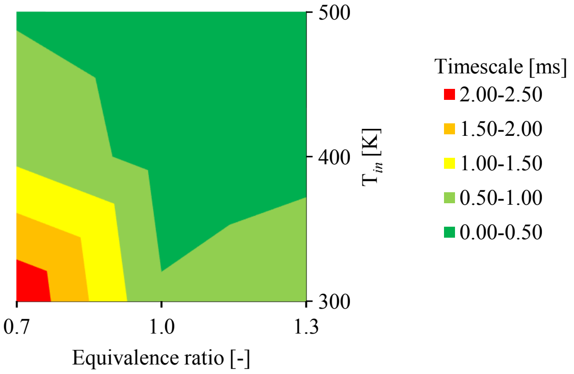

(a) Flame timescale as a function of stoichiometry and inlet temperature, with T_{HCP} = 1500 K.

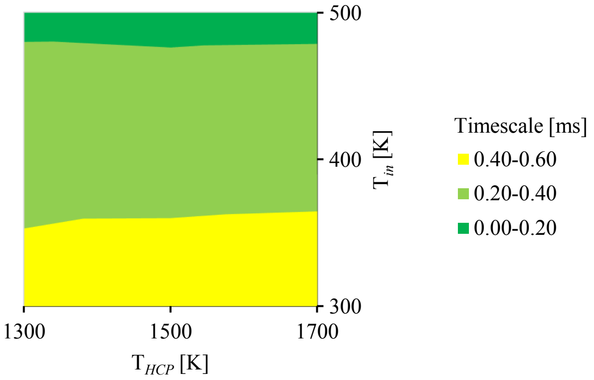

(b) Flame timescale as a function of external enthalpy temperature and inlet temperature, with ϕ = 1.0.

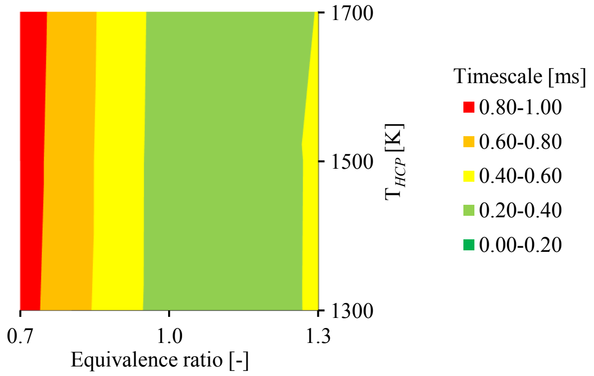

(c) Flame timescale as a function of stoichiometry and external enthalpy temperature, with T_{in} = 400 K.

Figure 5.1: Premixed iso-octane/air flames at atmospheric pressure with stoichiometry (ϕ = 0.7, 1.0 and 1.3), inlet temperature (T_{in} = 300, 400 and 500 K) and external enthalpy temperature (T_{HCP} = 1300, 1500 and 1700 K) varied.

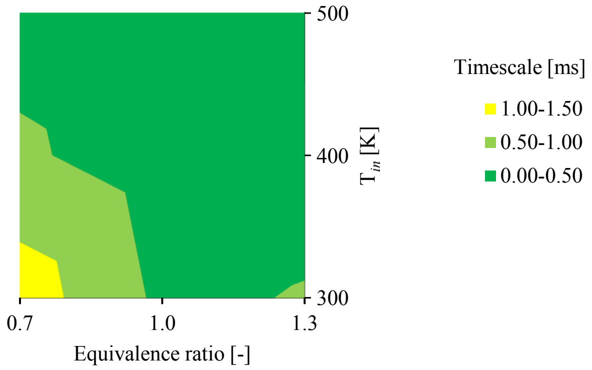

(a) Flame timescale as a function of stoichiometry and inlet temperature, with T_{HCP} = 1500 K.

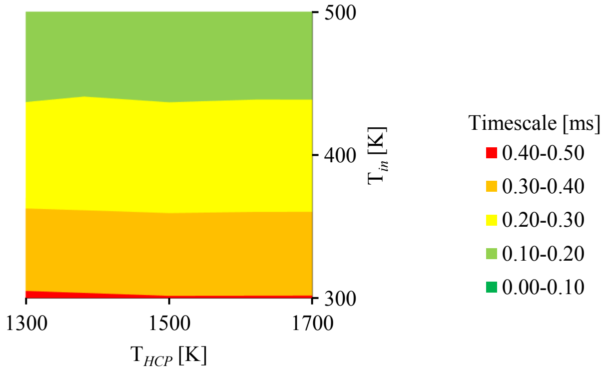

(b) Flame timescale as a function of external enthalpy temperature and inlet temperature, with ϕ = 1.0.

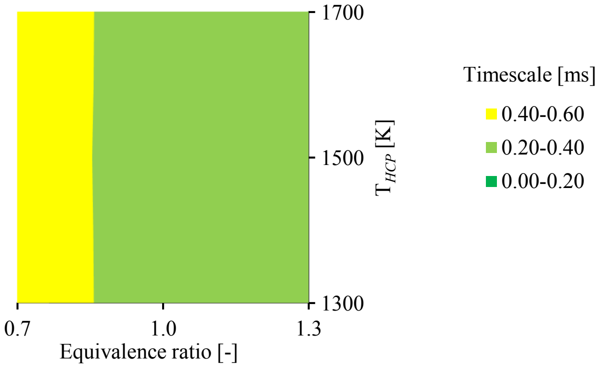

(c) Flame timescale as a function of stoichiometry and external enthalpy temperature, with T_{in} = 400 K.

Figure 5.2: Premixed n-heptane/air flames at atmospheric pressure with stoichiometry (ϕ = 0.7, 1.0 and 1.3), inlet temperature (T_{in} = 300, 400 and 500 K) and external enthalpy temperature (T_{HCP} = 1300, 1500 and 1700 K) varied.

Table 5.4: Results for varied stoichiometry, reactant inlet temperature and external enthalpy temperature for premixed n-heptane/air flames at atmospheric pressure and low rates of strain.

Equivalence ratio [-]	T_{HCP} [K]	T_{in} [K]	Strain rate [s^{-1}]	v_{RI} [m/s]	Thickness [μm]	Timescale [ms]
0.7	1300	300	105	0.20	250	1.23
		400	93	0.36	207	0.58
		500	102	0.57	179	0.31
	1500	300	93	0.20	250	1.27
		400	94	0.36	206	0.58
		500	112	0.58	180	0.31
	1700	300	82	0.20	249	1.27
		400	89	0.35	207	0.59
		500	112	0.59	181	0.31
1.0	1300	300	100	0.38	154	0.41
		400	118	0.61	142	0.23
		500	161	0.96	135	0.14
	1500	300	112	0.38	155	0.40
		400	134	0.63	144	0.23
		500	129	0.90	134	0.15
	1700	300	109	0.39	155	0.40
		400	129	0.62	143	0.23
		500	131	0.90	134	0.15
1.3	1300	300	107	0.33	184	0.56
		400	143	0.58	166	0.28
		500	125	0.80	150	0.19
	1500	300	126	0.35	187	0.53
		400	110	0.53	165	0.31
		500	134	0.82	150	0.18
	1700	300	126	0.36	187	0.52
		400	118	0.54	165	0.31
		500	136	0.82	150	0.18

This analysis has direct application to the conditions used in the Imperial College fractal grid based burner used for studying combustion mode transitions [372] and low Da number [41] turbulent premixed flames where HCP support (up to 1700 K) was used to sustain combustion beyond the flammability limit and for studying the transition to distributed combustion modes. Such modes, as discussed above, tend to be characterised by lower peak temperatures and, for example, lower pollutant emissions of oxides of nitrogen. This makes further understanding of such modes critical in meeting stringent pollutant emission requirements. Conducting the above analysis on atmospheric flames may be used for further comparisons, through the use of the flame timescale, to the flames with high preheat and at high pressures existing in real-world devices.

5.3.2.1 Strain rate dependency

The strain rate dependency of atmospheric iso-octane/air and n-heptane/air flames with fuel inlet temperature of 400 K and hot combustion temperature of 1500 K in a back-to-burnt configuration was explored by increasing the fuel-side inlet velocity (which also results in a momentum matched increased inlet velocity of the hot combustion products). The results for the burning velocity, flame thickness and characteristic timescale are shown in Fig. 5.3 for both fuels. It is seen that the linear approximation to zero strain, by taking the average of the fuel reaction rate integral and minimum velocities, is appropriate for both fuels and only a modest impact of the rate of strain is noted on this value. Furthermore, for the iso-octane/air flames at strain rates above about 800 s^{-1} begin to extinguish, while the n-heptane/air flames remain self-sustaining. Counter-intuitively, the flame thickness (as defined by the 5-95% fuel consumption) tends to increase as the flames become more strained. The effect is modest in both cases, but more present for the iso-octane/air flames, especially as they begin to extinguish from 800 s^{-1}. The same trend is repeated in the flame timescales.

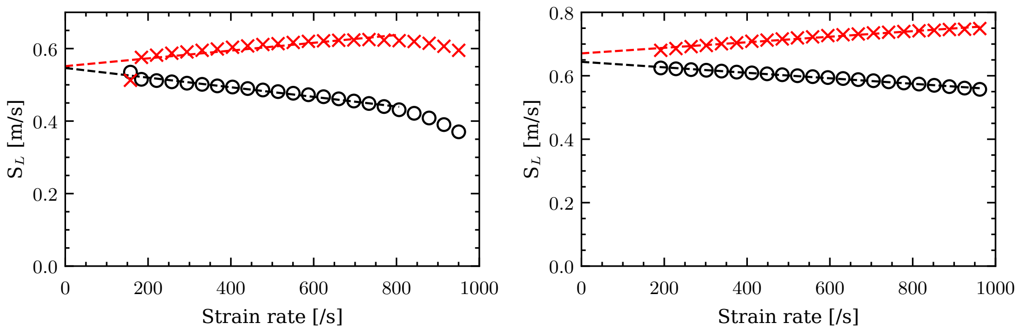

(a) Burning velocities of iso-octane/air flames. Reaction rate integral (black) and minimum velocity (red) with linear extrapolation to zero strain.

(b) Burning velocities of n-heptane/air flames. Key as described in Fig. 5.3a.

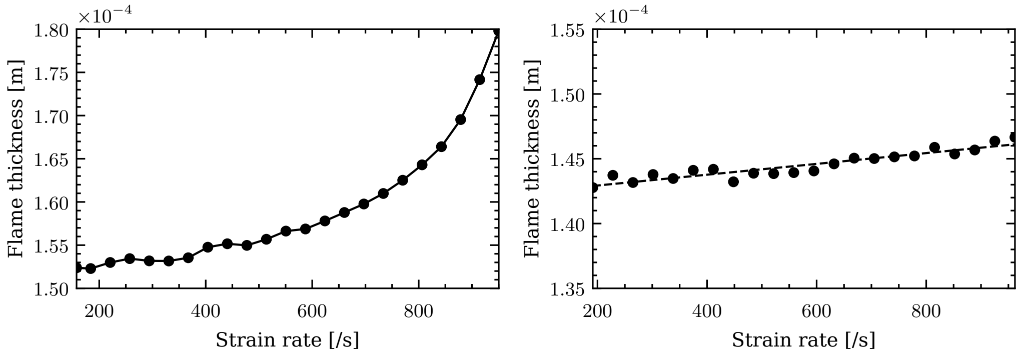

(c) Flame thickness for C_8H_{18}.

(d) Flame thickness for C_7H_{16}.

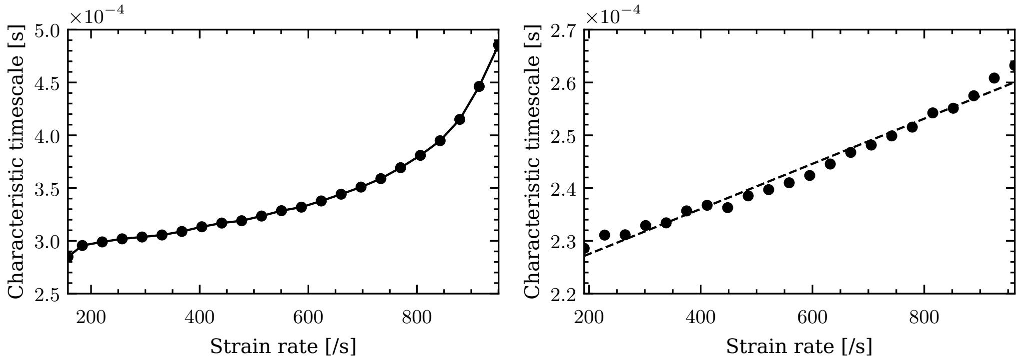

(e) Characteristic flame timescale for C_8H_{18}.

(f) Characteristic flame timescale for C_7H_{16}.

Figure 5.3: Premixed stoichiometric iso-octane/air and n-heptane/air flames at atmospheric pressure with inlet temperature of 400 K and external enthalpy temperature of 1500 K for varied strain rates.

Considering the temperature and species profiles shown in Fig. 5.4 for a low rate of strain (< 200 s^{-1}) and a high rate of strain ($\simeq 950$ s^{-1}), it is clear that the hot combustion products, at a temperature of 1500 K, have a quenching effect on the flame. This effect is highlighted by a reduced peak temperature in the more highly strained flames by up to 25%. This resembles a conclusion made by Hampp et al. [41], where self-sustaining turbulent flames would detach from the stagnation plane and, when supported by hot combustion products cooler than the adiabatic flame temperature, were partly quenched by the HCPs and began a transition towards a distributed reaction mode. Using a definition of flame thickness based on the OH profile, from 10% to 10% of the peak value, the expected trend with the rate of strain is reproduced with the flame thickness for an iso-octane/air flame reducing from 11.5 mm at 158 s^{-1} to 1.8 mm at 950 s^{-1}. Hence, care has to be taken in tailoring the definition of flame parameters to be compatible with the feature investigated.

Therefore, the impact of increasing the rate of strain on a fuel-lean mixture was explored. Figure 5.5 shows the strain rate dependency for a $\phi = 0.6$ iso-octane/air flame with reactant inlet temperature of 400 K and hot combustion temperature of 1500 K. After approximately 150 s^{-1} the flame extinguishes and becomes fully supported by the HCPs. This is shown in Fig. 5.6 where the temperature profile for the flame with a rate of strain of 224 s^{-1}, that is above the extinction limit, demonstrates complete fuel consumption but without a temperature rise above the HCP temperature. Complete combustion has occurred as once all the fuel is depleted, at about 16 mm for the flame with the higher rate of strain, the major components of the mixture are H_2O, CO_2 and CO in similar proportions to the self-sustaining low rate of strain flame. This transition of flame mode, demonstrated by the reduced OH peak, to a broadened reaction zone is paired with reduced pollutant emissions seen by the lower peak value of CO and CO_2 for the higher rate of strain flame.

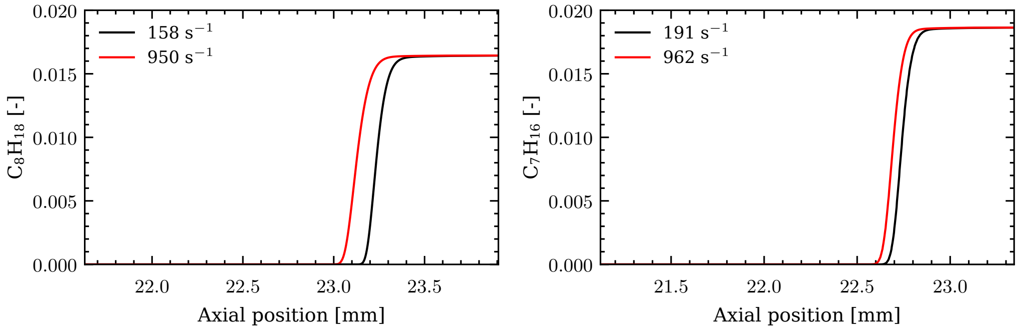

(a) C_8H_{18} (shifted to align OH peaks). (b) C_7H_{16} (shifted to align OH peaks).

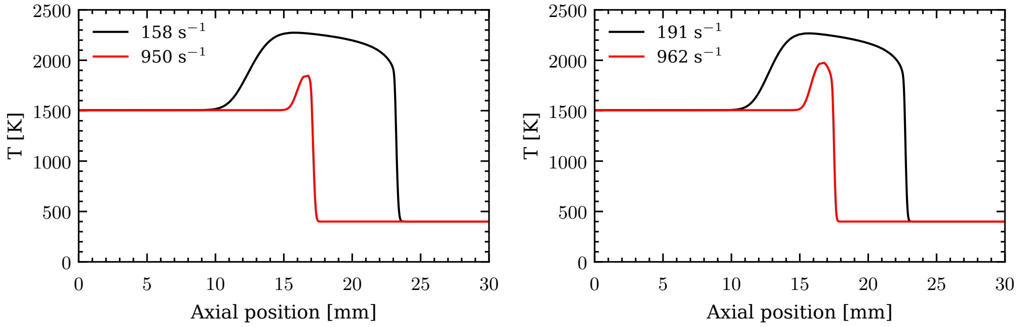

(c) Temperature (C_8H_{18}). (d) Temperature (C_7H_{16}).

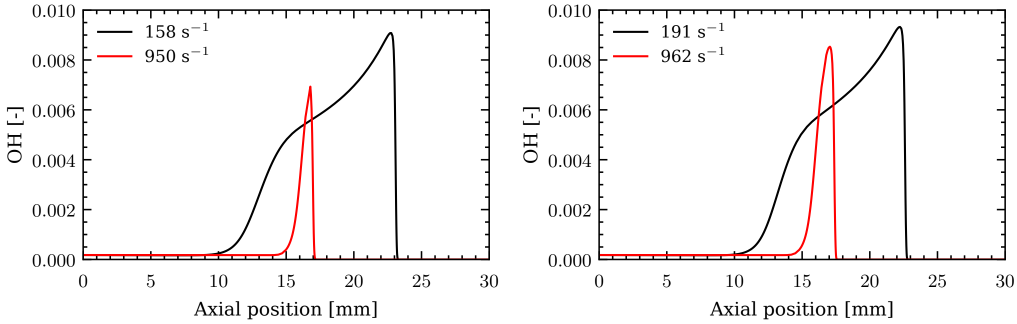

(e) OH (C_8H_{18}). (f) OH (C_7H_{16}).

Figure 5.4: Species and temperature profiles for flames as described in Fig. 5.3.

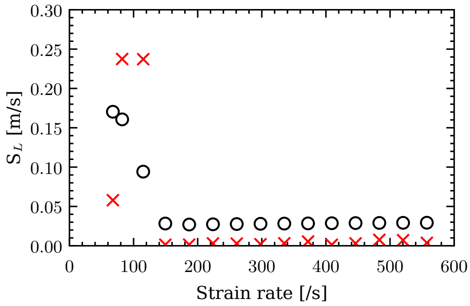

(a) Burning velocities. Reaction rate integral (black) and minimum velocity (red).

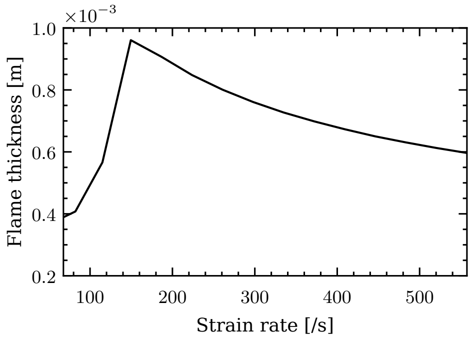

(b) Flame thickness.

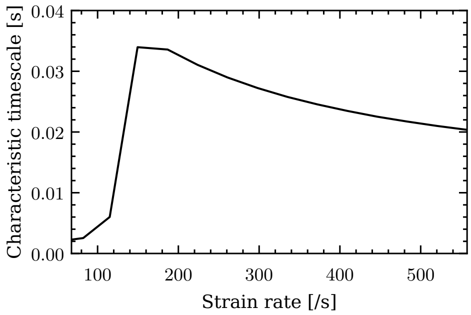

(c) Characteristic flame timescale.

Figure 5.5: Premixed ϕ = 0.6 iso-octane/air flames at atmospheric pressure with inlet temperature of 400 K and external enthalpy temperature of 1500 K for varied strain rates.

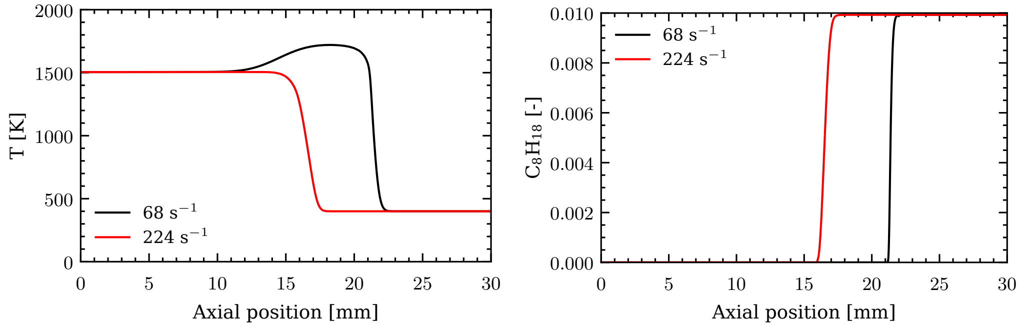

(a) Temperature. (b) C_8H_{18}.

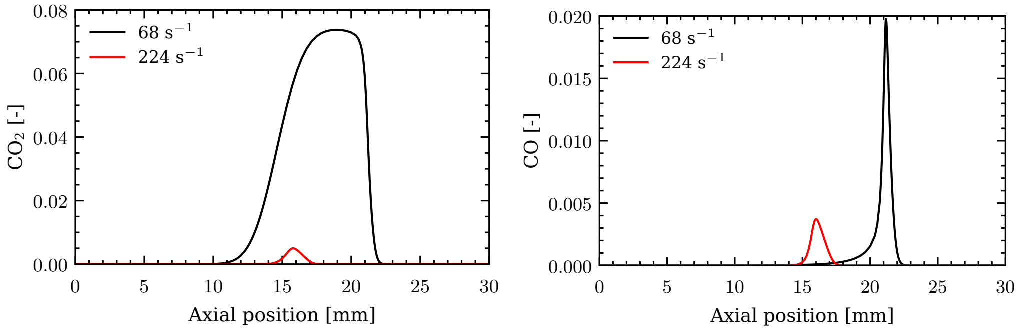

(c) CO_2. (d) CO.

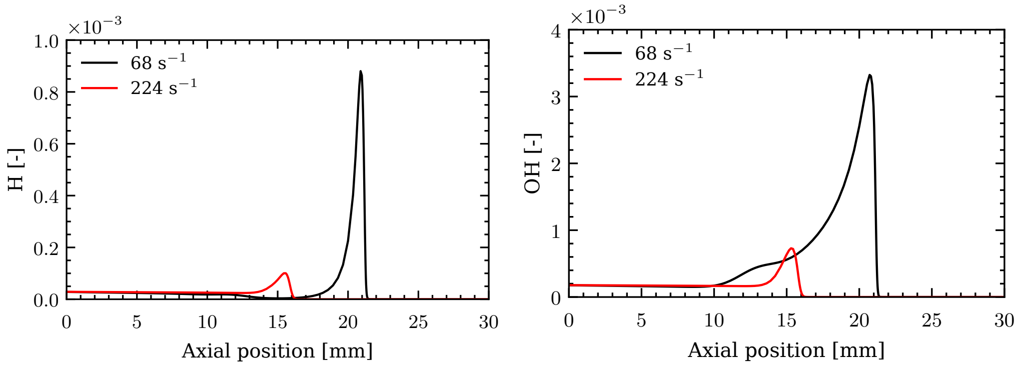

(e) H. (f) OH.

Figure 5.6: Species and temperature profiles for flames as described in Fig. 5.5.

5.3.3 PRF flames at elevated pressures and temperatures

Pressures far in excess of atmospheric pressure are reached in practical combustors. Furthermore, the use of technologies such as exhaust gas recirculation result in far higher in-cylinder temperatures. These elevated temperatures and pressures have a significant impact on the flame structure and properties.

Stoichiometric iso-octane/air and n-heptane/air flames were explored at three pressures, 13, 28 and 50 atm (matching the IDT computations in Section 3.2) and a range of inlet temperatures, 500 to 800 K. The latter is treated as a likely upper limit of preheating of the fuel containing reactant stream. The laminar flame thickness provides a description of the spatial distribution of the reaction zone and therefore the gradients of flame scalars. Since at elevated pressures the reaction zone becomes extremely narrow, the domain size was reduced to 10 mm for computational expediency and computational cells in the range of 50 to 200 nm were used to resolve the reaction zone. The flame thickness was calculated using the 5-95% fuel consumption layer with linear interpolation. The impact of inlet temperature on the flame thickness is shown in Fig. 5.7. Two trends are clear, with one exception, increased pressure results in a thinner flame for all temperatures and as the temperature is increased, the mixture becomes more reactive and the flame also becomes thinner. The n-heptane/air flames are thinner than the iso-octane/air flames when compared at the same pressure, however this reduction becomes less pronounced at the higher pressures. One important exception is for the n-heptane/air flames with inlet temperature of 800 K and at 50 atm. At these conditions, flame broadening is observed when using the fuel 5-95% consumption flame thickness definition. When using the maximum temperature gradient thickness (defined in Section 2.4.4), the expected trend is recovered. This result is due to the immediate activation of the low temperature chemistry. Figure 5.8 shows the temperature and species profiles for the 50 atm n-heptane/air flames with reactant inlet temperature of 500 and 800 K around the reaction zone and with the 800 K profiles shifted to align the hydroxyl peaks. The double peak in the HO_2 profile is indicative of low temperature chemistry. The rate of production of HO_2 is almost double in the flame with inlet temperature of 800 K compared with 500 K, this is a result of the increased proportion of fuel consumption into the alkyl-peroxy radical and subsequently into the methyl and hydrogen radicals. Furthermore, despite the earlier reduction in fuel consumption, the temperature rise in the 800 K inlet flame lags that of the 500 K flame due to the endothermic nature of the initial low temperature oxidation reactions.

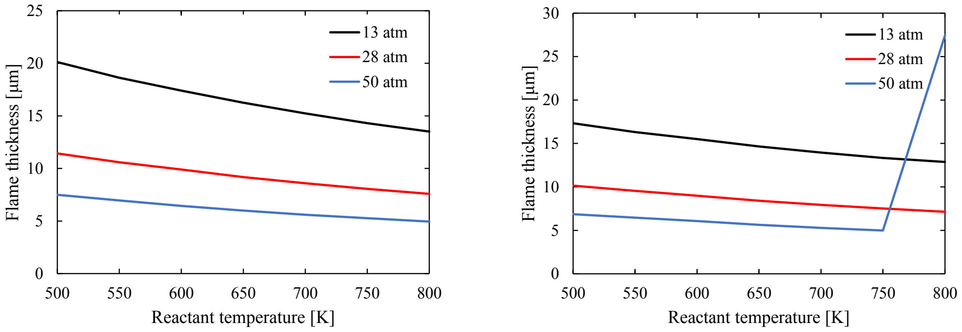

(a) Iso-octane/air.

(b) n-Heptane/air.

Figure 5.7: Stoichiometric iso-octane/air and n-heptane/air flame thicknesses calculated using 5-95% fuel consumption for 13, 28 and 50 atm.

The laminar burning velocity according to the reaction rate integral for iso-octane is shown in Fig. 5.9. The burning velocity is reduced by increased pressure and increases with increased temperature. Across all pressures the burning velocity with a reactant temperature of 800 K is about three times faster than at 500 K. The impact of temperature on the characteristic timescale is shown in Fig. 5.10. As before, the two trends are apparent. Increased pressure results in thinner flames and a shorter timescale, despite reduced burning velocity at higher pressures. In addition, as the temperature is increased the flame thickness and characteristic timescale reduces and this effect is more pronounced at the lower pressures. This asymptotic behaviour suggests a minimal possible flame thickness before autoignition occurs or the influence of low temperature chemistry and flame broadening effects if the inlet

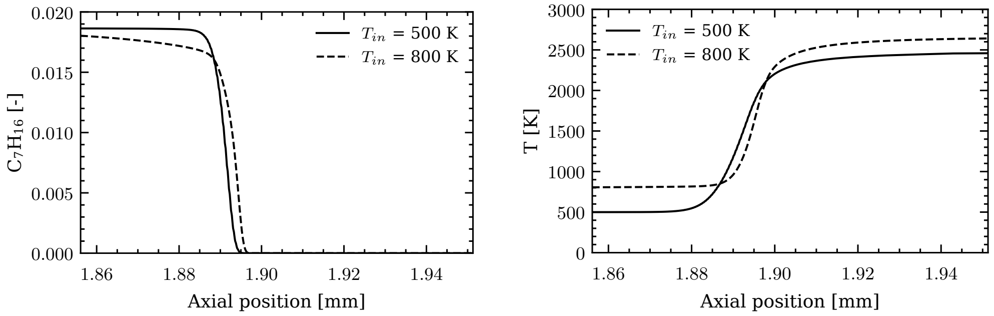

(a) C_7H_{16}. (b) Temperature.

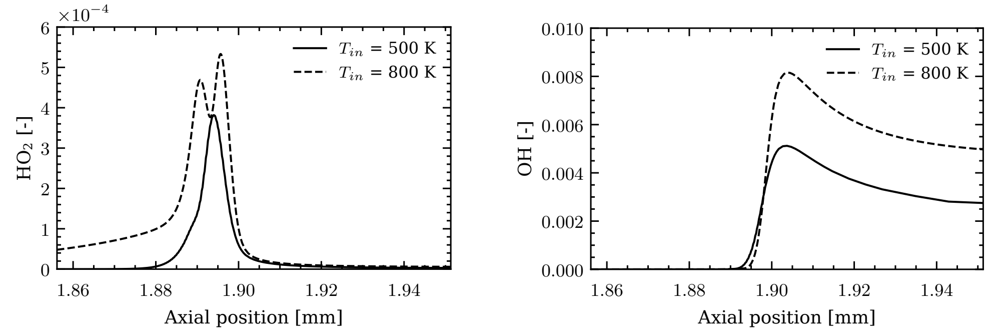

(c) HO_2. (d) OH.

Figure 5.8: Species and temperature profile around the reaction zone, with the 800 K profiles shifted to align the OH peaks, for stoichiometric n-heptane/air flame at 50 atm and with inlet temperature of 500 and 800 K.

temperature becomes sufficient, as it did for the 800 K inlet n-heptane/air flame.

Additionally, as the inlet temperature was increased, the applied rate of strain was also increased across all pressures and temperatures and varied from 250 – 750 s^{-1}. This range is primarily due to the increased burning velocity and earlier onset of ignition as the inlet temperature of the reactants is increased, but also at the highest temperatures above 750 K, the inlet velocity was increased by up to 50% to prevent flashback. In essence, it appears that reactant mixtures containing n-heptane and, probably, similar n-alkanes will show autoignition behaviour at temperatures above 750 K for pressures above 50 atm.

The impact of stoichiometry for fuel lean conditions of ϕ = 0.5 – 1.0 was also studied at 50 atm and with an inlet temperature of 600 K. The results for the global properties as a function of stoichiometry are shown in Fig. 5.11. As the

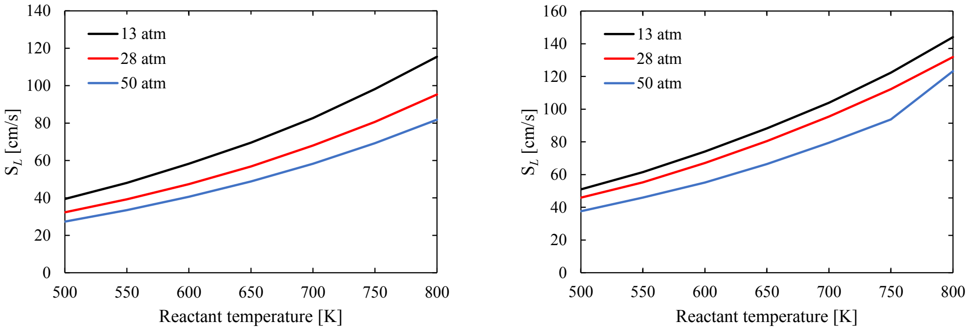

(a) Iso-octane/air.

(b) n-Heptane/air.

Figure 5.9: Stoichiometric iso-octane/air and n-heptane/air laminar burning velocities according to the fuel reaction rate integral for 13, 28 and 50 atm.

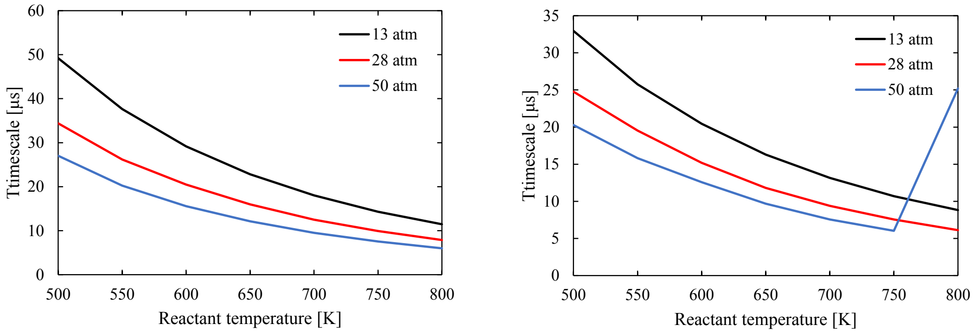

(a) Iso-octane/air.

(b) n-Heptane/air.

Figure 5.10: Stoichiometric iso-octane/air and n-heptane/air characteristic flame timescales for 13, 28 and 50 atm.

stoichiometry is increased from a very fuel-lean to a stoichiometric mixture the flame thickness reduces and the burning velocity increases, with both beginning to plateau from approximately $\phi = 0.9$. Therefore, it can be seen that the timescale reduces significantly from $\phi = 0.5$ to $\phi = 0.6$, by around a factor of four with the minimum timescale in the range seen at stoichiometric at about 12 – 16 µs. The systems at each end of the range differ in a fundamental nature with the major pathway for the leanest flame, $\phi = 0.5$, being the formation of HO_2 while for the stoichiometric flame it is the formation of O and OH. In addition, the thermal decomposition of fuel accounts for about a quarter of fuel consumption in the stoichiometric flame but below 10% in the lean flame. For the iso-octane/air flames, a non-negligible proportion of the iso-octyl radicals go on to form the alkylperoxy radicals which predominantly decay, via a hydroperoxy-alkyl radical, to form C_2H_4 and OH. This increases the radical pool size sufficiently to sustain combustion. The n-heptane/air flames are consistently faster burning and thinner than the iso-octane/air flames at all stoichiometries.

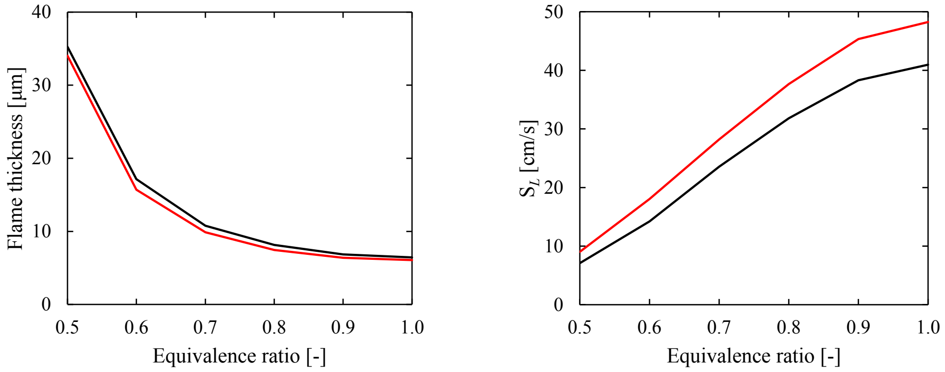

(a) Fuel 5–95% consumption flame thickness.

(b) Laminar burning velocity according to fuel reaction rate integral.

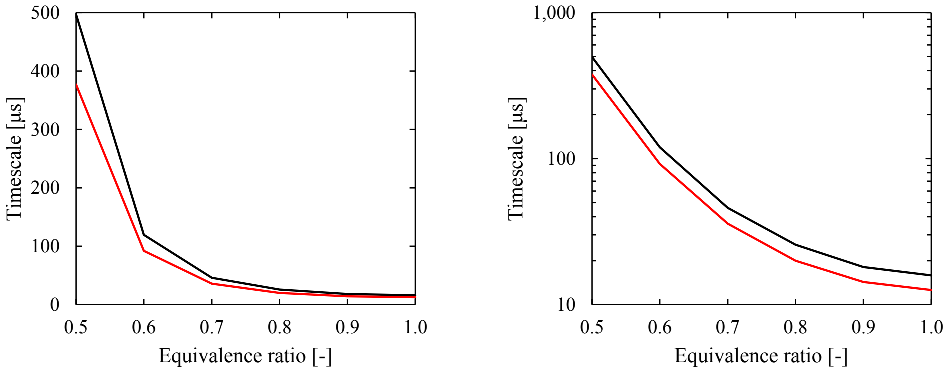

(c) Characteristic flame timescale.

(d) Characteristic flame timescale.

Figure 5.11: Global properties of premixed iso-octane/air (black) and n-heptane/air (red) flames at 50 atm with 600 K inlet temperature for a range of stoichiometries, $\phi = 0.5 - 1.0$.

Figures 5.12 and 5.13 show a comparison of the flame timescales for a variation in stoichiometry at 50 and 13 atm, respectively, with the corresponding ignition delay times. Isotherms are included to show the impact of stoichiometry at a fixed initial temperature on the IDT. The impact of pressure on the ignition delay time is more acute than on the flame timescale and it can be seen that all flame timescales sit within the range of ignition delay times for initial temperature of 1000 – 1600 K. Generally, it is shown that for a stoichiometric mixture with a mixture temperature of about 1400 K the flame timescale and ignition delay time under the corresponding conditions becomes comparable. This reduces to an initial temperature of 1000 – 1100 K for the ultra-lean mixtures at 50 atm and 1100 – 1200 K for 13 atm. Accordingly, autoignition based combustion appears to become competitive under practical conditions.

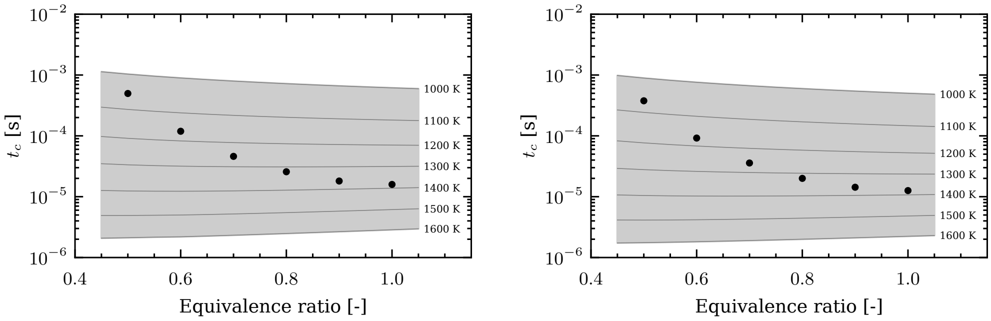

(a) Iso-octane. (b) n-Heptane.

Figure 5.12: Comparison of IDTs (lines) and flame timescales (dots) of PRF/air flames at 50 atm with inlet temperature of 600 K for a range of stoichiometries, ϕ = 0.5 – 1.0.

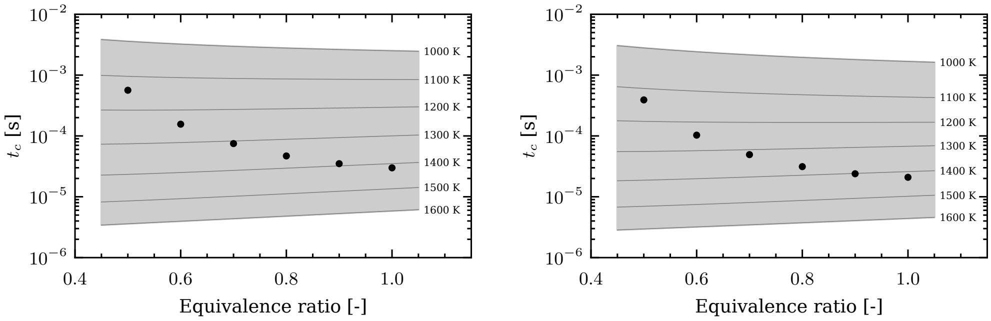

(a) Iso-octane. (b) n-Heptane.

Figure 5.13: Comparison of IDTs (lines) and flame timescales (dots) of PRF/air flames at 13 atm with inlet temperature of 600 K for a range of stoichiometries, ϕ = 0.5 – 1.0.

5.3.3.1 Strain rate dependency

The impact of increased rate of strain for high pressure iso-octane flames was explored by increasing the inlet velocity to vary the rate of strain from 250 to 600 s^{-1} at 13 and 50 atm. An additional, higher rate of strain close to 1100 s^{-1} was also computed for a pressure of 13 atm. The results for global flame properties at both pressures are shown in Fig. 5.14. Generally, a low sensitivity to an increased rate of strain is demonstrated and flame thickness variations remain below 1 µm. Additionally, the burning velocity is relatively insensitive to the rate of strain and therefore using the reaction rate integral at a low rate of strain, the approach taken above, is appropriate.

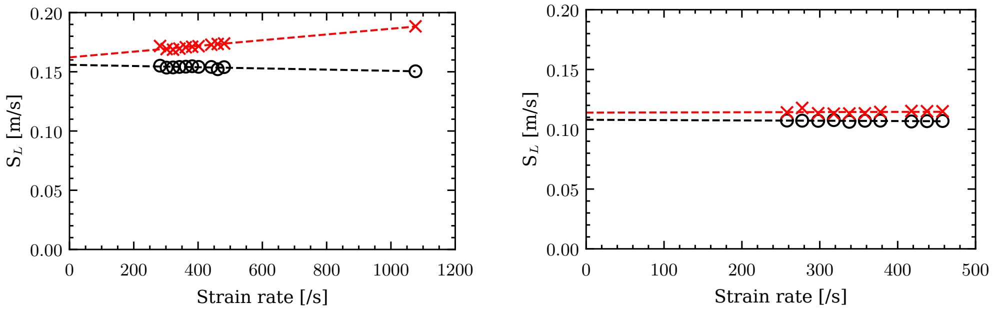

(a) Burning velocities at 13 atm. Reaction rate integral (black) and minimum velocity (red).

(b) Burning velocities as described in Fig. 5.14a at 50 atm.

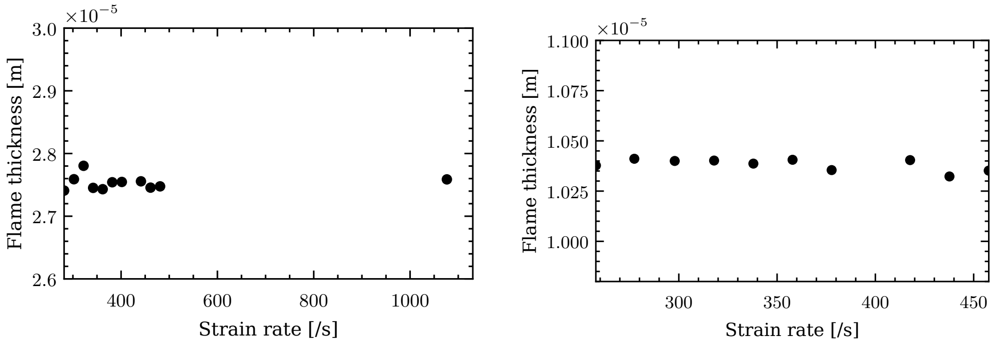

(c) Flame thickness at 13 atm.

(d) Flame thickness at 50 atm.

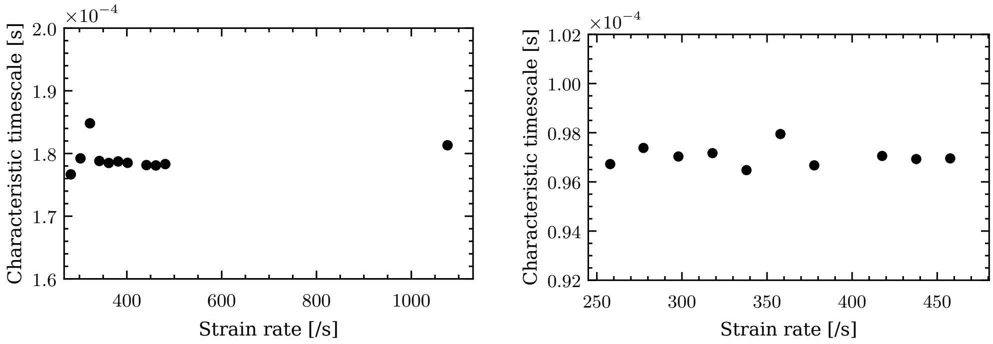

(e) Characteristic flame timescale at 13 atm.

(f) Characteristic flame timescale at 50 atm.

Figure 5.14: Premixed stoichiometric iso-octane/air flames at 13 and 50 atm with inlet temperature of 300 K for varied strain rates.

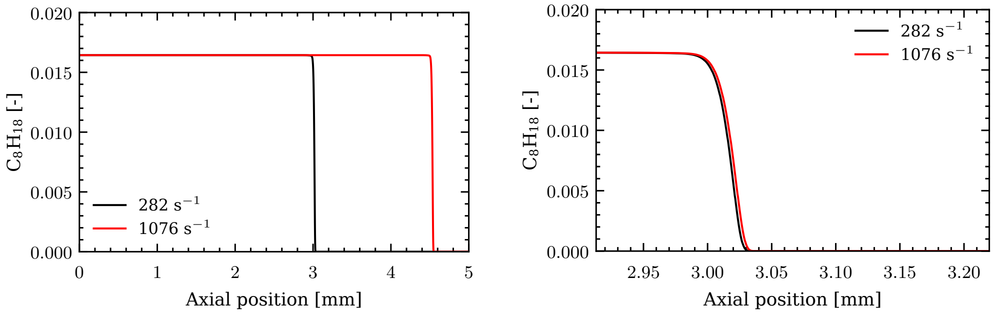

(a) C_8H_{18}.

(b) C_8H_{18}.

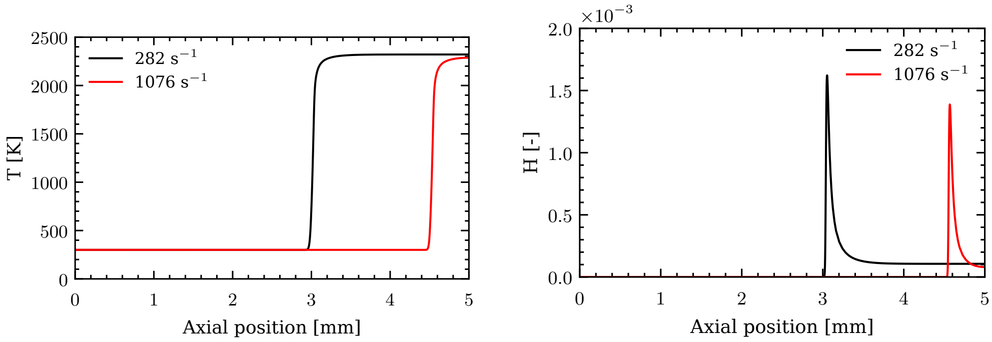

(c) Temperature

(d) H.

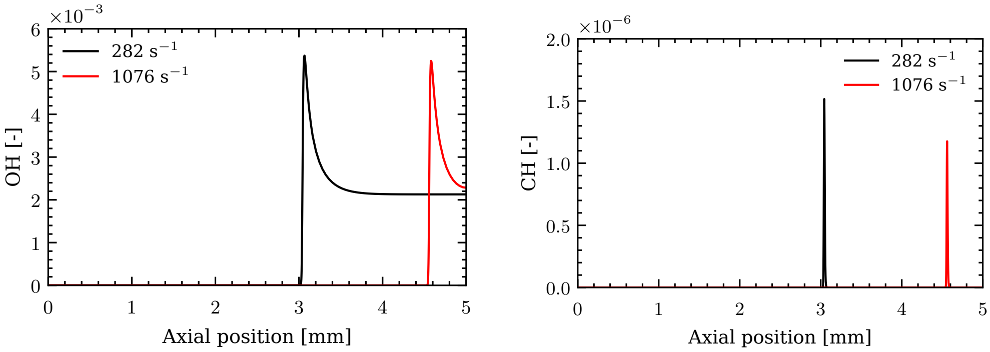

(e) OH

(f) CH.

Figure 5.15: Temperature and species profiles for a premixed stoichiometric iso-octane/air flames at 13 atm with inlet temperature of 300 K at different strain rates.

The temperature and species profiles for a low and high rate of strain at 13 atm are shown in Fig. 5.15. For the higher rate of strain the flame has been forced further into the domain by about 1.5 mm. However, when aligning the profiles by the position of the OH peak, the fuel consumption profile is almost identical even at a rate of strain almost a factor of four larger, as shown in Fig. 5.15a. Peak values for H, OH and CH remain broadly similar with a reduction of up to 20% for the higher rate of strain. This suggests a lower limit on the flame thickness at a specific pressure and, as in Section 5.3.2, the unexpected minor influence of the rate of strain on the flame structure for self-sustained flames.

5.3.4 Transient boundary condition

Fluctuations in mixture conditions can lead to significant oscillations in fuel stoichiometry and are known to occur in practical combustors [373]. They can be the result of acoustics and/or fluid dynamics [374], or simply through error in instrumentations which may enhance the prior physical effects. Examples of studies include the work by De Zilwa et al. [375] that was concerned with large amplitude oscillations in sudden-expansion flows and active control of these fluctuations which can be achieved by applied out-of-phase (closed-loop) or different frequency (open-loop) oscillations on the pressure field or heat release. Malik and Lindstedt [376] explored the impact of pressure and equivalence ratio fluctuations on premixed hydrogen/air flames propagating through inhomogeneous fuel distributions and later expanded this approach to methane/air flames [377]. Increased flame stretch was shown to reduce the relaxation time (time for the flame to return to equilibrium conditions) to 4.0 ms for spherical methane/air flames [377].

The current work considers the impact of periodic fluctuations of the equivalence ratio at timescales relevant to combustion in a flamelet mode. Fuel boundary stoichiometry fluctuations of $\phi = 0.6 - 1.4$ were explored for an initially stoichiometric premixed iso-octane/air flame at atmospheric pressure with an inlet temperature of 500 K and supported by hot combustion products from a hydrogen/air flame at approximately 1500 K, as described above. The fuel stoichiometry was varied by a sinusoid with a period of 3.8 ms, comparable with the integral timescale of turbulence in the Imperial College laboratory burner [116]. Global flame properties were determined, including the 5–95% fuel consumption flame thickness, laminar burning velocity and characteristic timescale found from the quotient of the prior two quantities. Since the fuel boundary value was varied, the 100% fuel value used to compute the flame thickness was taken as the fuel concentration at the onset of oxidation, defined here by a minimum of a 2 K temperature rise. Other approaches may result in different flame thickness approximations, an alternative method found the flame front from the minimum velocity and used the fuel concentration at that point as '100%' which produced similar results to the former method. The results for four complete stoichiometry waves are shown in Fig. 5.16 and a low-pass filter, applied in both the forward and backward direction to produce zero phase shift, was used for the global properties in order to illustrate the impact of the underlying oscillations.

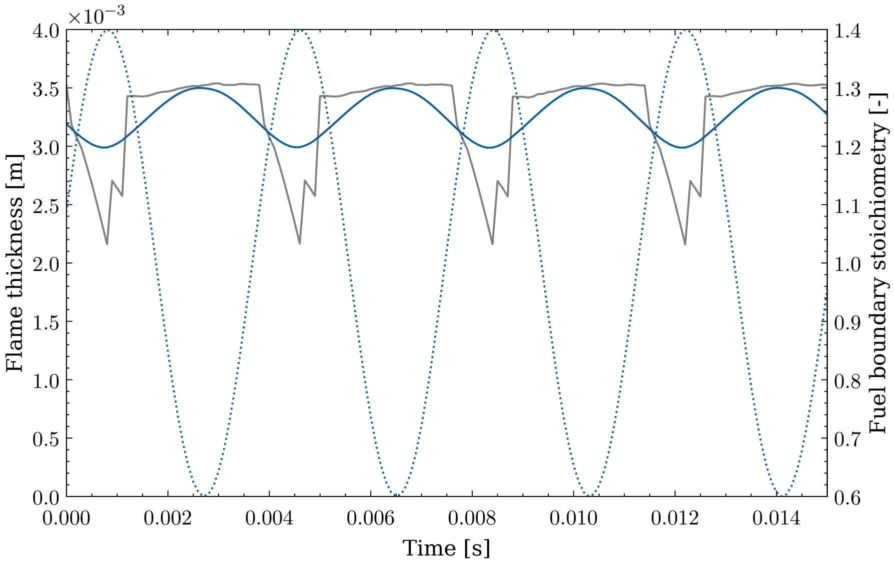

(a) Fuel 5–95% consumption flame thickness with the underlying stoichiometry fluctuations shown.

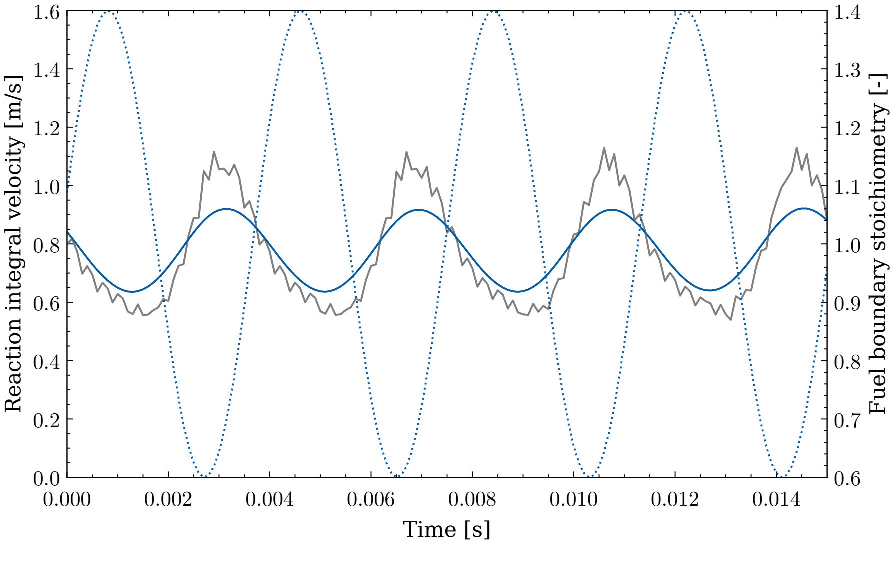

(b) Laminar burning velocity according to reaction rate integral for iso-octane, with the underlying stoichiometry fluctuations shown.

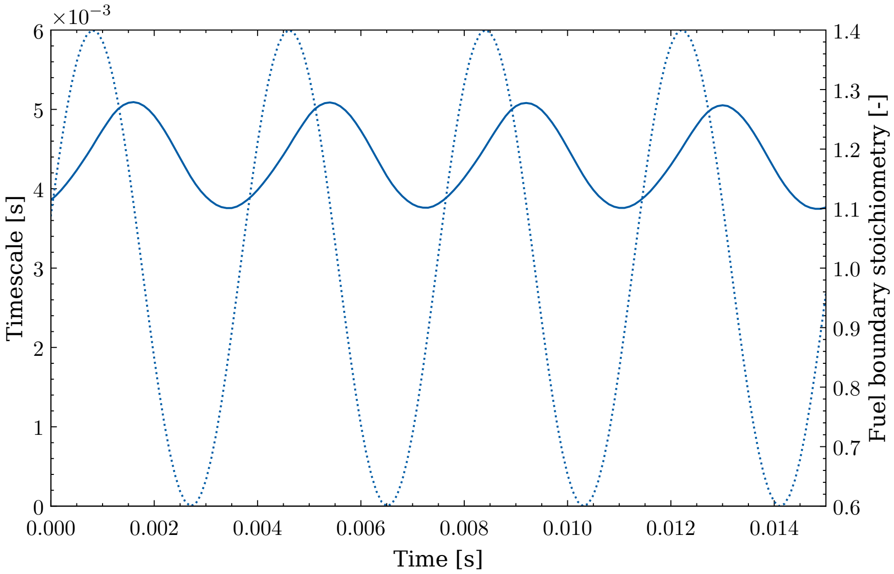

(c) Characteristic flame timescale with the underlying stoichiometry fluctuations shown.

Figure 5.16: Global properties of a stoichiometric laminar premixed iso-octane/air flame at atmospheric pressure perturbed by a 3.8 ms period sinusoidal stoichiometric variation from ϕ = 0.6 – 1.4. Fuel inlet temperature at 500 K, supported by hot combustion products from a hydrogen/air flame at approximately 1500 K.

The flame thickens swiftly from an initial value of approximately 0.125 mm at the onset of the perturbations and then stabilises to fluctuate between 3.0–3.5 mm with the thinnest flames corresponding with the fuel-rich boundary value and therefore lagging the fuel-lean and stoichiometric value propagating into the flame. Different flame thickness definitions may produce differing results. The fuel reaction rate integral burning velocity fluctuates between 0.6–1.0 m/s with maximum velocities corresponding with fuel-lean conditions, which suggests a phase lag of about 2 ms, since maximum burning velocities are expected at around ϕ = 1.1. The flame timescale, after an initial ramp up from about 0.4 ms, due to the flame thickness increase, oscillates between about 4–5 ms. This represents an increase of about an order of magnitude from the initial unperturbed flame with a stoichiometric fuel/air mixture.

The species profiles for the fuel, OH, H and CO are shown in Fig. 5.17 at four times corresponding with inlet mixture stoichiometry of ϕ = 1.0, 1.4, 1.0

and 0.6, respectively. Figure 5.17 demonstrates the negligible impact of boundary perturbation on the position of the flame front, implying a ’memory’ of the flame. However, the peak values are affected by the inlet composition with the H radical peak value range from about 0.006 to 0.01. The broadening effect is shown most strongly by the CO profile with fluctuations continuing for over 10 mm (a third of the domain) after the initial peak. Furthermore, the importance of the flame thickness definition selected is shown clearly by the fuel profile, where the consumption appears to be almost coincident at all times, but the the inlet composition impacts the preceding concentration of fuel and thus what is considered the ’100%’ fuel value.

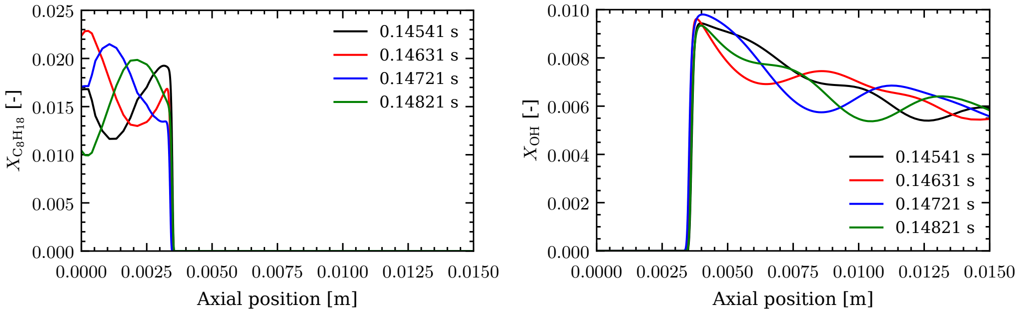

(a) C_8H_{18}.

(b) OH.

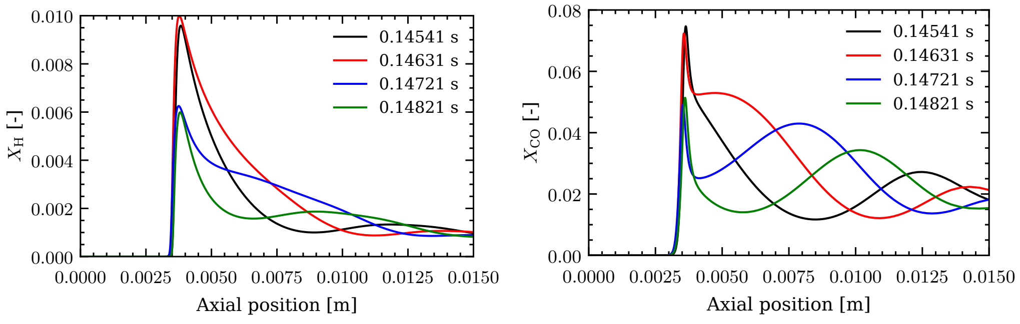

(c) H.

(d) CO.

Figure 5.17: Species profiles at four times corresponding with inlet mixture stoichiometry of ϕ = 1.0, 1.4, 1.0 and 0.6. The flame is as described in Fig. 5.16.

5.3.5 Cool flames

The low temperature n-heptane oxidation results of Callahan et al. [233] in a pressurised flow reactor with a residence time of 1.8 s were modelled in a shock tube and integrated to this residence time. The results for the heat release are shown in Fig. 5.18. The H/C_1-C_2 chemistry in Appendix A and the n-heptane sub-mechanism presented in Chapter 3 predicts a three stage ignition profile, as seen in Fig. 5.18. The first stage ignition is slightly delayed and the heat release overpredicted by about 20 K, which remains constant for initial temperatures above about 600 K. The second stage ignition point is well predicted and a more gradual third ignition event at about 850 K is shown. The impact of including the iso-octane sub-mechanism was also explored with no significant impact. The partial decoupling of the pure n-heptane behaviour from the influence of the iso-octane sub-mechanism and its behaviour is essential for predictions of surrogate fuels requiring PRF blends. The data of Callahan et al. [233] showed no low temperature heat release from iso-octane and therefore only n-heptane has been considered here. Furthermore, longer n-alkanes are of greater interest in the context of aviation fuels.

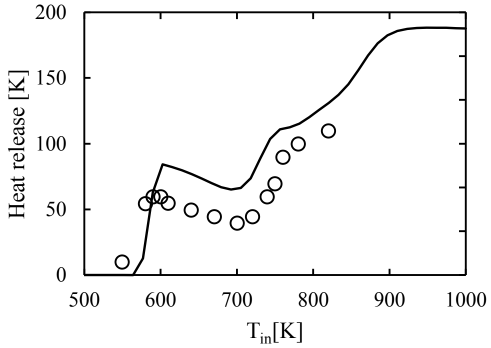

Figure 5.18: Heat release data in the cool flame region for the oxidation of 0.14% stoichiometric n-heptane mixture obtained in a pressurised flow reactor and modelled in a shock tube at 12.5 atm with a residence time of 1.8 s. Experimental data from [233] with the model prediction (solid line).

5.3.6 Iso-octane and n-heptane blends

The impact of blending n-heptane, of interest in studies of autoignition phenomena [231], and iso-octane, a fuel surrogate suitable for spark ignition engines due to its autoignition resistance, on ignition delay times was studied at 40 atm in a shock tube. Experimental results from shock tube studies conducted at 40 atm by AlAbbad et al. [378] for iso-octane/n-heptane blends with similar ratios to those studied here are included in Fig. 5.19. A scatter in the experimental data is evident, with seemingly no clear correlation between increased n-heptane concentration and a reduction in IDT.

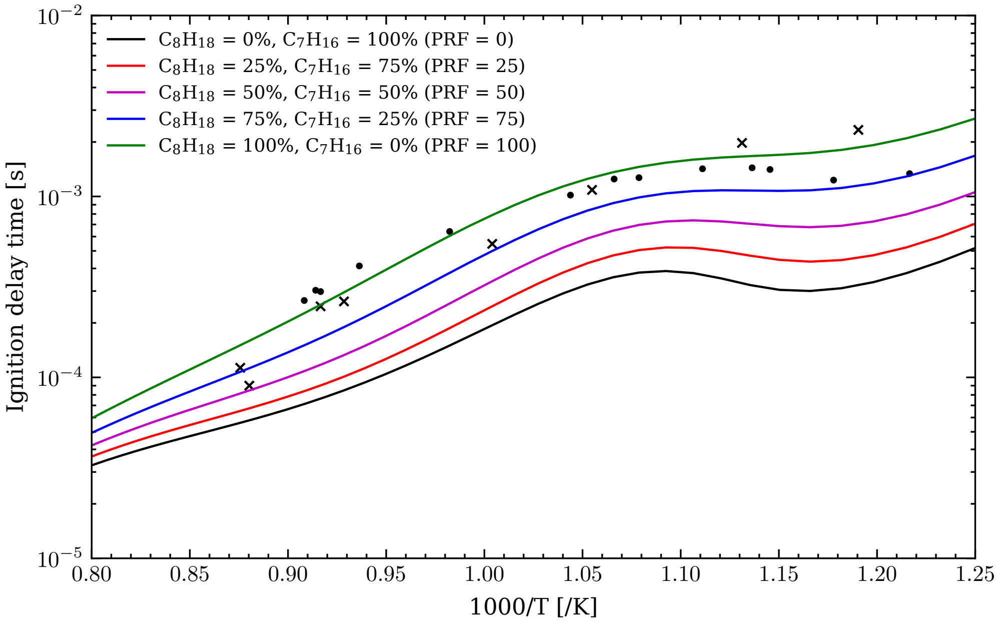

Figure 5.19: Ignition delay times at 40 atm for stoichiometric iso-octane/n-heptane blends for a temperature range of 800 – 1250 K. Experimental data from [378] is included: dots = PRF 70; crosses = PRF 80.

Contrary to the experimental data, the computed results shown in Fig. 5.19 show that increased iso-octane concentration increases the ignition delay time as expected. Furthermore, the impact is larger at lower temperature and the impact at one temperature across the all the blends is not linear. For example, at 1000 K the IDT for PRF 0 is 0.19 ms increasing to 0.79 ms for PRF 100. However, for PRF 50 the IDT is 0.34 ms which shows the stronger impact of the addition of n-heptane than iso-octane.

5.3.7 Ammonia and hydrogen blends

The hydrogen radical was identified as a crucial species in the oxidation of ammonia and in its relation to the balancing of NNH oxidation and decomposition in Section 4.2. In order to further explore this, and since hydrogen and ammonia blending in practical applications, such as gas turbines for power production, is of clear real-world relevance [379, 380], blends of hydrogen and ammonia were explored in a counterflow flame.

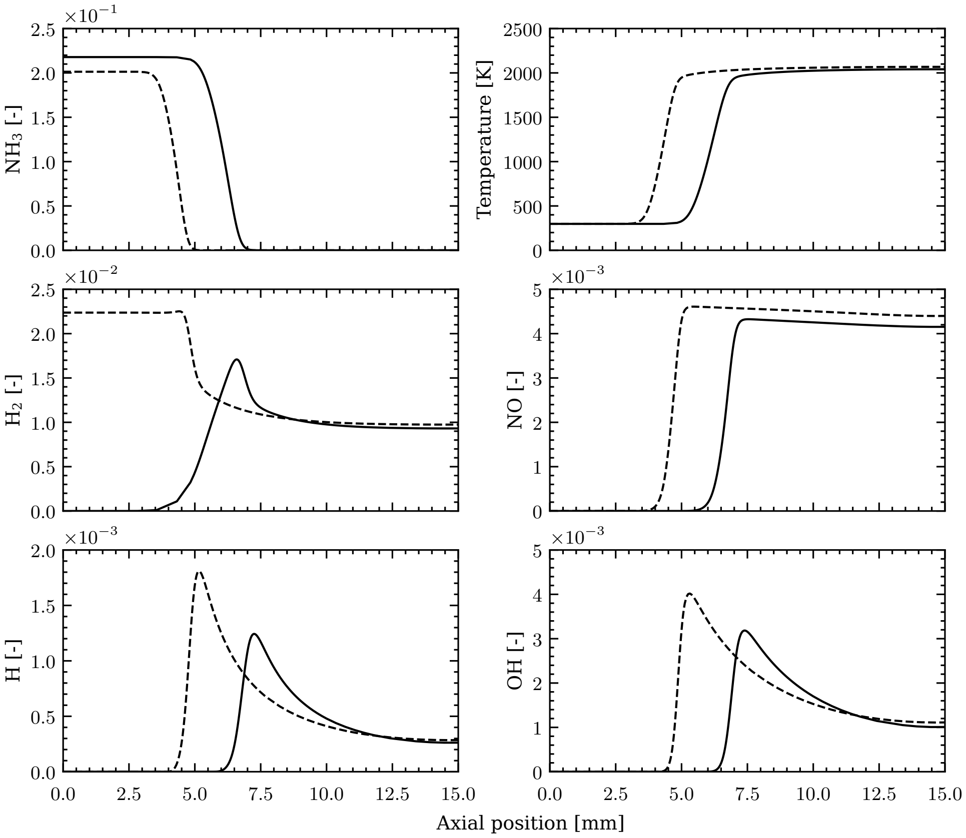

Figure 5.20: Species profiles up to the symmetry point in a stoichiometric NH_3/H_2/air counterflow flame with a strain rate of about 40 s^{-1}. The solid line is for a pure ammonia fuel blend and the dashed line for a fuel blend with 10% hydrogen and 90% ammonia.

Figure 5.20 shows the temperature profile and species profiles for NH_3, H_2, H, NO and OH for a stoichiometric counterflow flame at atmospheric pressure and with inlet temperature of 300 K with pure ammonia and 10% hydrogen substituted with at a rate of strain of about 40 s^{-1} up to the symmetry point at 15 mm. It is clear that the blend with hydrogen burns faster than with pure ammonia, by about 3 cm/s, showing earlier onset product formation. In addition, the hydrogen radical trace shows an earlier onset and higher peak value by about a factor of 1.5 for the blend containing hydrogen. Most interesting is the relationship to the molecular hydrogen species profile. In the blend with hydrogen, fuel consumption begins at about 3.5 mm and the hydrogen radical concentration begins to increase from 4 mm. By contrast, in the pure ammonia flame the ammonia concentration begins to decrease at about 5 mm and the H radical to increase from 6 mm. The temperature trace sheds light on the matter. The onset of H radical formation corresponds with a temperature in excess of about 800 K. Thus, it is clear that a sufficiently high temperature must be reached before the hydrogen radical is formed, the importance of which was discussed in Section 4.2. With 10% hydrogen blended the faster temperature rise results in rapid hydrogen radical formation and subsequent formation of molecular hydrogen, shown by the slight peak at about 4.5 mm. A slightly higher steady state NO concentration is noted in the hydrogen blended flame due to the higher peak temperature, otherwise both blends still reach almost identical steady state values of both molecular hydrogen and the hydrogen radical, as well as the other species shown in Fig. 5.20. However, the flame dynamics are very different.

5.4 Summary

In this chapter, iso-octane and n-heptane combustion was studied over a wide variety of conditions. The burning velocity and flame thickness were used to define a characteristic flame timescale in order to compare different flame structures created through altering the reactant inlet temperature, fuel stoichiometry, pressure and external enthalpy support temperature in counterflow flames. In addition, the inlet velocity and therefore rate of strain were altered and the impact on the laminar burning velocity, as calculated using the minimum velocity in the flame front and the reaction rate integral, was studied. It was shown that increased pressure tended to reduce the characteristic timescale as did increased reactant inlet temperature. The relationship with stoichiometry was related to the burning velocity trend, with the smallest timescales around stoichiometric conditions and fuel lean mixtures tending to increase the timescale most rapidly. Furthermore, for flames that are not highly strained the temperature of the hot combustion products does not impact the characteristic timescale. For the most highly strained self-sustaining flames, the hot combustion products, if below the adiabatic flame temperature, tended to quench the flames and reduce the peak temperatures. However, for flames at rates of strain above the extinction strain rate the HCPs support allowed for complete oxidation of the fuel and resulted in reduced peak concentrations of pollutants, such as CO and CO_2. Additionally, for high pressure flames the impact of the rate of strain was shown to be less influential on flame properties than pressure, inlet temperature or stoichiometry. The impact of the latter on the flame timescale was compared with IDTs computed with initial temperatures from 1000 – 1600 K. It was shown that for stoichiometric PRF flames, temperatures in excess of 1400 K would result in comparable flame timescales and IDTs for pressures above 13 atm. Additionally, for an n-heptane/air flame at 50 atm and with reactant inlet temperatures above 750 K the low temperature chemistry was shown to be immediately active resulting in flame broadening.

A novel transient boundary stoichiometry condition was applied to an iso-octane/air flame and the impact on the characteristic timescale was studied. It was shown that the flame in effect has a 'memory' and that the amplitude of flame timescale oscillations is non-negligible (of the order of 1 ms) in comparison to the stoichiometry fluctuation which varied from ϕ = 0.6 to ϕ = 1.4 with a period of oscillation of 3.8 ms. In addition, the cool flame behaviour of n-heptane was studied, demonstrating a three stage ignition behaviour, along with the impact of blending n-heptane and iso-octane. It was shown that n-heptane has a strong impact in the reduction of the ignition delay time. Finally, the impact of hydrogen substitution of ammonia was studied in a counterflow flame. A temperature greater than about 800 K was necessary for H radical formation with the NH_3/H_2 flame burning more rapidly. Despite different flame dynamics, the steady state values remained almost identical for both blends. This clearly illustrates that any conclusions regarding the use of ammonia blends based on a chemical equilibrium analysis are likely to be invalid.

Chapter 6 | Conclusion and recommendations for future work

6.1 Conclusion

In this thesis chemical kinetic models for primary reference fuels, crucial in combustion research for modelling real world fuels, and emerging fuels and additives have been further developed. Subsequently, a comprehensive validation of these mechanisms using recent and critical experimental data has been conducted and key sensitivities and model uncertainties have been highlighted. The validation conducted has considered both global properties, e.g. laminar burning velocities and ignition delay times, and detailed speciation at low and high temperatures. All mechanisms developed have been kept compact, limiting the number of chemical species included, in order for their viable and economical implementation in modelling highly dynamic systems. Chapter 3 deals with the chemical kinetic models for the primary reference fuels, iso-octane and n-heptane and Chapter 4 with fuel additives, ammonia (a fuel in its own right) and nitromethane.

The iso-octane sub-mechanism discussed in Chapter 3 provides excellent agreement with atmospheric laminar burning velocity predicting a maximum value of approximately 35 cm/s at ϕ = 1.1 and STP. In addition, the ignition delay time for temperatures above about 750 K is well reproduced for a range of elevated pressures. While the sub-mechanism is not able to reproduce the hydroxyl radical time history prior to second stage ignition, it has been shown that this has a high sensitivity to the chaperon efficiency assigned to argon for reaction (RA.84) that is amplified by the significant concentration (>99%) of argon in the mixture studied. Similarly, the n-heptane sub-mechanism performs excellently for IDT and laminar burning velocity predictions for a range of stoichiometries and inlet conditions. Major species predictions show good agreement with experimental data for stirred reactors. Some rapid decomposition product species are over-predicted but speciation in low pressure flames shows excellent agreement with literature data.

The comprehensive validation of an updated ammonia sub-mechanism, including highly sensitive SNCR conditions, is presented in Chapter 4. The key sensitivities are outlined, in particular the critical balancing of NNH consumption through decomposition and its reaction with molecular oxygen in reproducing the SNCR onset temperature and its impact on global properties like the laminar burning velocity. Additionally, uncertainties are highlighted in the consumption of HNO and the need for accurate rate determinations. Furthermore, the need for more experimental data, particularly in relation to these species and their impact on the concentration of the hydrogen radical, is noted. A comprehensive validation of nitromethane is also conducted, highlighting the sensitivity to the reaction of HNO with molecular oxygen, as introduced in the ammonia study. In addition, the non-standardised approach to nitromethane stoichiometry categorisation and experimentation makes the role of the kinetic modeller more challenging. Ignition delay times were well reproduced but required an alternative heat-release-based definition for low nitromethane concentration compositions. The laminar burning velocity was reasonably well reproduced, considering experimental uncertainties, with fuel lean mixtures more over-predicted. A high sensitivity to the fuel thermal decomposition reactions was shown and the need to test a high/low-pressure limit rate pairing was emphasised. The impact of heat loss was noted, as discussed in the context of the over-prediction of laminar burning velocities with the ammonia sub-mechanism. Speciation predictions, particularly in a low pressure flame, showed good agreement with the experimental data with some discrepancies related to the fuel thermal decomposition rates.

In Chapter 5 the developed mechanisms for PRFs were applied to conditions of practical relevance considering technological trends. These conditions include high preheat temperatures and pressures, ultimately resulting in reduced combustion timescales. When turbulence is factored in, the chemical and flow timescales may become comparable and an understanding of the chemistry is critical. The impact of hot combustion products support was studied on self-sustaining flames at low and high pressure, in addition to extinguished fuel-lean flames at high rates of strain. It was shown that for self-sustaining flames the HCPs did not influence flame timescale. However, for increased rates of strain they could have a quenching effect if the support temperature was below the adiabatic flame temperature. Increased pressure and increased reactant inlet temperature reduced the flame timescale at all conditions, with the exception of stoichiometric n-heptane/air flames at 50 atm with inlet temperature of 800 K where the low temperature chemistry was immediately active resulting in a flame broadening effect when defined using the 5–95% fuel consumption thickness. Furthermore, by comparing ignition delay times with initial conditions of 1000 – 1600 K with the flame timescales of high pressure PRF flames, it was shown that for a stoichiometric mixture the IDT and flame timescale become comparable from about 1400 K and therefore, autoignition based combustion could become competitive under practical conditions. In addition, the impact of fuel inlet stoichiometry oscillations has also been studied and it has been demonstrated that the flame can have a 'memory' resulting in a minor impact of large stoichiometry variations on the position of the flame front but with oscillations in downstream species profiles present. A three stage heat release is predicted in cool n-heptane flames. Additionally, the impact of n-heptane on reactivity when blended with iso-octane was studied by computing the ignition delay time for different fuel blend ratios. The strong influence of n-heptane was demonstrated with about a factor of four reduction from PRF 100 to PRF 0 at 1000 K. Finally, the importance of a sufficient temperature rise in the formation of the hydrogen radical and subsequent combustion in slow ammonia flames was demonstrated by comparing a pure ammonia and ammonia/hydrogen fuel blend in a counterflow flame.

6.2 Future work

Further improvements to the chemical kinetic models are always possible and while experimental uncertainties can lead to misleading conclusions, new experimental data and kinetic determinations should be considered.

Opportunities for further refinement and improvement for the kinetic models presented in this thesis include:

- Further analysis of low temperature iso-octane oxidation, with aim to improving time history speciation predictions and the IDT predictions below 750 K at higher pressures. Furthermore, additional data at these low temperature conditions would be useful for verification, for example for stoichiometric iso-octane/air mixtures near 50 atm.

- The low temperature prediction of the rapid decomposition products with the n-heptane mechanism could be improved, as demonstrated in the stirred reactor results in Section 3.3.4.3.

- Additional clarification on the impact of the H radical on ammonia oxidation, with a focus on the NNH and HNO consumption reactions. Both computational rate determinations, in particular for HNO thermal decomposition, and species evolution measurements for both NNH and HNO in low pressure flames, such as in the work of Bian et al. [261], with well defined uncertainty bounds would be very useful. Furthermore, uncertainty quantified H radical measurements under the same conditions may circumvent the need for NNH and HNO measurements due to the importance of the H radical in governing the laminar burning velocity and SNCR process, and would provide critical information.

- Expand the study on the uncertainties in N_2O formation/destruction in ultra-lean ammonia flames, including excited state oxygen chemistry.
- Further sensitivity analyses of nitromethane thermal decomposition reactions, particularly at higher temperatures, which could help inform experimentation, for example in the measurement of laminar burning velocities where quantification of the impact of heat losses would aid with kinetic model evaluation based on this property.
- Seeking new data for nitromethane oxidation with well defined experimental conditions, including complete temperature profiles and uncertainties. Examples of such experiments would include the work of Zhang et al. [327], but with full domain temperature measurements including close to the burner exit. A good example of this is the low pressure n-heptane flame work by Seidel et al. [239]. Furthermore, the inclusion of and clarity with measurement uncertainties, particularly for intermediate and radical species like HCN, H and OH, would be of great value.

Additional transient flame computations with other fuels and fuel blends, as well as studying the impact of different inlet conditions including elevated pressures, would provide further information about the effect of stoichiometry oscillations at conditions of practical relevance. Furthermore, the parametric analysis should be extended to further refine the regions of interest in relation to possible timescale matching between atmospheric, laboratory capable conditions and real-world conditions. Through understanding the impact of altering the inlet conditions on the flame characteristic timescale, future experiments could be designed to match the timescales occurring in real-world applications but at atmospheric conditions in the laboratory. These comparative analyses would open up the possibility to use data obtained in flames at atmospheric pressure to approximate combustion at the extreme conditions present in the highest performing devices in order to improve their performance while reducing pollutant emissions.

References

[1] M. Allen, H. de Coninck, O. Dube, O. Hoegh-Guldberg, D. Jacob, K. Jiang, et al. Technical Summary: Global warming of 1.5°C. An IPCC Special Report on the impacts of global warming of 1.5°C above pre-industrial levels and related global greenhouse gas emission pathways, in the context of strengthening the global response to the threat of climate change, sustainable development, and efforts to eradicate poverty. Technical report (2018). URL: https://www.ipcc.ch/site/assets/uploads/sites/2/2022/06/SR15_Technical_Summary.pdf. [Accessed 22 August 2023].

[2] Climate Action Tracker (n.d.). URL: https://climateactiontracker.org/. [Accessed 22 August 2023].

[3] M. Hulme. 1.5 °C and climate research after the Paris Agreement (2016).

[4] GOV.UK. Transport and environment statistics 2022 (2022). URL: https://www.gov.uk/government/statistics/transport-and-environment-statistics-2022/transport-and-environment-statistics-2022. [Accessed 22 August 2023].

[5] BP. Statistical Review of World Energy 2022. Technical report (2022). URL: https://www.bp.com/content/dam/bp/business-sites/en/global/corporate/pdfs/energy-economics/statistical-review/bp-stats-review-2022-full-report.pdf. [Accessed 22 August 2023].

[6] BP. BP Energy Outlook 2022. Technical report (2022).

[7] IPCC. Climate Change 2023: Synthesis Report. Contribution of Working Groups I, II and III to the Sixth Assessment Report of the Intergovernmental Panel on Climate Change. Technical report, IPCC, Geneva, Switzerland (2023). URL: https://www.ipcc.ch/report/ar6/syr/downloads/report/IPCC_AR6_SYR_FullVolume.pdf. [Accessed 23 August 2023].

[8] K. Riahi, R. Schaeffer, J. Arango, K. Calvin, C. Guivarch, T. Hasegawa, et al. Mitigation pathways compatible with long-term goals. In *Mitigation of Climate Change. Contribution of Working Group III to the Sixth Assessment Report of the Intergovernmental Panel on Climate Change*, Chapter 3, pages 295–408 (2022). URL: https://www.ipcc.ch/report/ar6/wg3/downloads/report/IPCC_AR6_WGIII_Chapter03.pdf. [Accessed 23 August 2023].

[9] IEA. World Energy Outlook 2022. Technical report, IEA, Paris (2022). URL: https://www.iea.org/reports/world-energy-outlook-2022. [Accessed 23 August 2023].

[10] T. Cooper, I. Reagan, C. Porter, K. Green, and C. Franzoni. Global Fleet and MRO Market Forecast 2020-2030. Technical report, Oliver Wyman (2020). URL: https://www.oliverwyman.com/content/dam/oliver-wyman/global/en/images/insights/energy/2020/Fleet_and_MRO_forecast_commentary_2020_2030.pdf. [Accessed 22 August 2023].

[11] Japan Aircraft Development Corporation. Worldwide Market Forecast 2022-2041. Technical report, JADC (2022).

[12] D. Forsberg. Aircraft Retirement and Storage Trends: Economic Life Analysis Reprised and Expanded. Technical report, Avolon (2015). URL: https://aviation.report/Resources/Whitepapers/c7ca1e8f-fd11-4a96-9500-85609082abf7_whitepaper1.pdf.

[13] Federal Aviation Administration. Airworthiness Certification (n.d.). URL: https://www.faa.gov/aircraft/air_cert/airworthiness_certification. [Accessed 22 August 2023].

[14] L. Barelli, G. Bidini, P. A. Ottaviano, F. Gallorini, and D. Pelosi (2022). Coupling Hybrid Energy Storage System to Regenerative Actuators in a More Electric Aircraft: Dynamic Performance Analysis and CO2 Emissions Assessment concerning the Italian Regional Aviation Scenario. *J. Energy Storage*, 45:103776.

[15] Rolls-Royce. Sustainability in Civil Aerospace (n.d.). URL: https://www.rolls-royce.com/products-and-services/civil-aerospace/sustainability.aspx{#}/.

[16] Air BP. What is sustainable aviation fuel (SAF)? (2022). URL: https://www.bp.com/en/global/air-bp/news-and-views/views/what-is-sustainable-aviation-fuel-saf-and-why-is-it-important.html.

[17] Fulcrum BioEnergy. Our Fuel Process (n.d.). URL: https://www.fulcrum-bioenergy.com/our-fuel-process.

[18] S. Blakey, L. Rye, and C. W. Wilson (2011). Aviation gas turbine alternative fuels: A review. *Proc. Combust. Inst.*, 33(2):2863–2885.

[19] J. M. Bergthorson and M. J. Thomson (2015). A review of the combustion and emissions properties of advanced transportation biofuels and their impact on existing and future engines. *Renew. Sustain. Energy Rev.*, 42:1393–1417.

[20] G. T. Kalghatgi. Is it really the end of internal combustion engines and petroleum in transport? (2018).

[21] D. R. MacFarlane, P. V. Cherepanov, J. Choi, B. H. Suryanto, R. Y. Hodgetts, J. M. Bakker, et al. (2020). A Roadmap to the Ammonia Economy. *Joule*, 4(6):1186–1205.

[22] A. Valera-Medina, F. Amer-Hatem, A. K. Azad, I. C. Dedoussi, M. De Joannon, R. X. Fernandes, et al. (2021). Review on ammonia as a potential fuel: From synthesis to economics. *Energy and Fuels*, 35(9):6964–7029.

[23] Y. Fujimura. International Cooperation for Implementation of Green Ammonia. In *NH3 Fuel Conf.*, Pittsburg (2018). URL: https://www.ammoniaenergy.org/wp-content/uploads/2021/02/AEA-Imp-Con-01Nov18-Yasushi-Fujimura-Session-6.pdf. Presentation.

[24] T. Seljak, M. Buffi, A. Valera-Medina, C. T. Chong, D. Chiaramonti, and T. Katrašnik (2020). Bioliquids and their use in power generation – A technology review. *Renew. Sustain. Energy Rev.*, 129:109930.

[25] O. W. Awe, Y. Zhao, A. Nzihou, D. P. Minh, and N. Lyczko (2017). A Review of Biogas Utilisation, Purification and Upgrading Technologies. *Waste and Biomass Valorization*, 8(2): 267–283.

[26] P. Sabia, G. Sorrentino, G. B. Ariemma, M. V. Manna, R. Ragucci, and M. de Joannon (2021). MILD Combustion and Biofuels: A Minireview. *Energy and Fuels*, 35(24):19901–19919.

[27] A. K. Agarwal (2007). Biofuels (alcohols and biodiesel) applications as fuels for internal combustion engines. *Prog. Energy Combust. Sci.*, 33(3):233–271.

[28] A. Cavaliere and M. de Joannon (2004). Mild Combustion. *Prog. Energy Combust. Sci.*, 30 (4):329–366.

[29] J. Wünning (1997). Flameless oxidation to reduce thermal no-formation. *Prog. Energy Combust. Sci.*, 23(1):81–94.

[30] F. Martin and P. Dederick (1977). NOx from fuel nitrogen in two-stage combustion. *Proc. Combust. Inst.*, 16(1):191–198.

[31] M. Katsuki and T. Hasegawa (1998). The science and technology of combustion in highly preheated air. *Proc. Combust. Inst.*, 27(2):3135–3146.

[32] F. L. Dryer (2015). Chemical kinetic and combustion characteristics of transportation fuels. *Proc. Combust. Inst.*, 35(1):117–144.

[33] R. Cook, D. Davidson, and R. Hanson. Measurements of ignition delay times and OH species concentrations in DME/O_2/Ar mixtures. In *Shock Waves*, pages 763–767. Springer, Berlin, Heidelberg (2009).

[34] M. Baigmohammadi, V. Patel, S. Nagaraja, A. Ramalingam, S. Martinez, S. Panigrahy, et al. (2020). Comprehensive Experimental and Simulation Study of the Ignition Delay Time Characteristics of Binary Blended Methane, Ethane, and Ethylene over a Wide Range of Temperature, Pressure, Equivalence Ratio, and Dilution. *Energy and Fuels*, 34(7):8808–8823.

[35] O. Herbinet and G. Dayma. Jet-Stirred Reactors. In F. Battin-Leclerc, J. M. Simmie, and E. Blurock, editors, *Clean. Combust. Dev. Detail. Chem. Kinet. Model.*, pages 183–210. Springer London, London (2013).

[36] D. L. Baulch, J. F. Griffiths, A. J. Pappin, and A. F. Sykes (1988). Stationary-state and oscillatory combustion of hydrogen in a well-stirred flow reactor. *Combust. Flame*, 73(2): 163–185.

[37] O. Mathieu and E. L. Petersen (2015). Experimental and modeling study on the high-temperature oxidation of Ammonia and related NO_x chemistry. *Combust. Flame*, 162(3): 554–570.

[38] D. F. Davidson, J. K. Shao, R. Choudhary, M. Mehl, N. Obrecht, and R. K. Hanson (2019). Ignition delay time measurements and modeling for gasoline at very high pressures. *Proc. Combust. Inst.*, 37(4):4885–4892.

[39] Hanson Research Group. Shock Tubes (n.d.). URL: https://hanson.stanford.edu/our-approaches/shock-tubes.

[40] K. Goh, P. Geipel, F. Hampp, and R. Lindstedt (2013). Regime transition from premixed to flameless oxidation in turbulent JP-10 flames. *Proc. Combust. Inst.*, 34(2):3311–3318.

[41] F. Hampp, S. Shariatmadar, and R. Lindstedt (2019). Quantification of low Damköhler number turbulent premixed flames. *Proc. Combust. Inst.*, 37(2):2373–2381.

[42] H. Shariatmadar, P. G. Aleiferis, and R. P. Lindstedt (2022). Particle size distributions in turbulent premixed ethylene flames crossing the soot inception limit. *Combust. Flame*, 243: 111978.

[43] A. Movaghar, R. Lawson, and F. N. Egolfopoulos (2021). Radiation effects in confined spherically expanding flames: Application to C_5–C_{10} flames at engine-relevant conditions. *Proc. Combust. Inst.*, 38(2):2195–2203.

[44] R. R. Burrell, D. J. Lee, and F. N. Egolfopoulos (2018). Propagation and extinction of subatmospheric counterflow methane flames. *Combust. Flame*, 195:117–127.

[45] P. Dirrenberger, H. Le Gall, R. Bounaceur, P. A. Glaude, and F. Battin-Leclerc (2015). Measurements of laminar burning velocities above atmospheric pressure using the heat flux method-application to the case of n- pentane. *Energy and Fuels*, 29(1):398–404.

[46] S. Wang, Z. Wang, C. Chen, A. M. Elbaz, Z. Sun, and W. L. Roberts (2022). Applying heat flux method to laminar burning velocity measurements of NH_3/CH_4/air at elevated pressures and kinetic modeling study. *Combust. Flame*, 236:111788.

[47] J. O. Hirschfelder, C. F. Curtiss, and D. E. Campbell (1953). The theory of flame propagation. IV. *J. Phys. Chem.*, 57(4):403–414.

[48] D. B. Spalding (1957). A theory of inflammability limits and flame-quenching. *Proc. R. Soc. London. Ser. A. Math. Phys. Sci.*, 240(1220):83–100.

[49] G. Dixon-Lewis (1967). Flame structure and flame reaction kinetics I. Solution of conservation equations and application to rich hydrogen-oxygen flames. *Proc. R. Soc. London. Ser. A. Math. Phys. Sci.*, 298(1455):495–513.

[50] D. B. Spalding (1956). The Theory of Flame Phenomena with a Chain Reaction. *Philos. Trans. R. Soc. London. Ser. A, Math. Phys. Sci.*, 249(957):1–25.

[51] D. B. Spalding, P. L. Stephenson, and R. G. Taylor (1971). A calculation procedure for the prediction of laminar flame speeds. *Combust. Flame*, 17(1):55–64.

[52] S. V. Patankar and D. B. Spalding (1967). A finite-difference procedure for solving the equations of the two-dimensional boundary layer. *Int. J. Heat Mass Transf.*, 10(10):1389–1411.

[53] G. Tsatsaronis (1978). Prediction of propagating laminar flames in methane, oxygen, nitrogen mixtures. *Combust. Flame*, 33(C):217–239.

[54] K. C. Lück and G. Tsatsaronis (1979). A study of flat methane-air flames at various equivalence ratios. *Acta Astronaut.*, 6(3-4):467–475.

[55] M. D. Smooke (1982). Solution of burner-stabilized premixed laminar flames by boundary value methods. *J. Comput. Phys.*, 48(1):72–105.

[56] W. P. Jones and R. P. Lindstedt (1988). Global reaction schemes for hydrocarbon combustion. *Combust. Flame*, 73(3):233–249.

[57] R. P. Lindstedt and V. Sakthitharan. Parallel Processing and Direct Simulation of Transient Premixed Laminar Flames with Detailed Chemical Kinetics. In *High-Performance Computing*, pages 417–428. Springer US, Boston, MA (1999).

[58] M. P. Meyer and R. P. Lindstedt. Evaluation of Hazard Correlations for Hydrogen-Rich Fuels Using Stretched Transient Flames. In *Green Energy and Technology*, pages 197–222. Springer Science and Business Media Deutschland GmbH (2022).

[59] F. A. Lindemann, S. Arrhenius, I. Langmuir, N. R. Dhar, J. Perrin, and W. C. McC. Lewis (1922). Discussion on “the radiation theory of chemical action”. *Trans. Faraday Soc.*, 17(0):598–606.

[60] R. G. Gilbert, K. Luther, and J. Troe (1983). Theory of Thermal Unimolecular Reactions in the Fall-off Range. II. Weak Collision Rate Constants. *Berichte der Bunsengesellschaft/Physical Chem. Chem. Phys.*, 87(2):169–177.

[61] Reaction Design, CHEMKIN Tutorials Manual CHEMKIN ® Software. Technical Report December (2011).

[62] T. Lu and C. K. Law (2009). Toward accommodating realistic fuel chemistry in large-scale computations. *Prog. Energy Combust. Sci.*, 35(2):192–215.

[63] H. J. Curran (2019). Developing detailed chemical kinetic mechanisms for fuel combustion. *Proc. Combust. Inst.*, 37(1):57–81.

[64] R. P. Lindstedt and L. Q. Maurice (1995). Detailed Kinetic Modelling Of n-Heptane Combustion. *Combust. Sci. Technol.*, 107(4-6):317–353.

[65] H. J. Curran, P. Gaffuri, W. J. Pitz, and C. K. Westbrook (1998). A comprehensive modeling study of n-heptane oxidation. *Combust. Flame*, 114(1-2):149–177.

[66] K. Zhang, C. Banyon, J. Bugler, H. J. Curran, A. Rodriguez, O. Herbinet, et al. (2016). An updated experimental and kinetic modeling study of n-heptane oxidation. *Combust. Flame*, 172:116–135.

[67] H. J. Curran, P. Gaffuri, W. J. Pitz, and C. K. Westbrook (2002). A comprehensive modeling study of iso-octane oxidation. *Combust. Flame*, 129(3):253–280.

[68] N. Atef, G. Kukkadapu, S. Y. Mohamed, M. A. Rashidi, C. Banyon, M. Mehl, et al. (2017). A comprehensive iso-octane combustion model with improved thermochemistry and chemical kinetics. *Combust. Flame*, 178:111–134.

[69] R. Lindstedt. Systematically reduced kinetic models: A European perspective. In *33rd Jt. Propuls. Conf. Exhib.*, pages 1–7. American Institute of Aeronautics and Astronautics Inc, AIAA (1997).

[70] U. Maas and S. B. Pope (1992). Simplifying chemical kinetics: Intrinsic low-dimensional manifolds in composition space. *Combust. Flame*, 88(3-4):239–264.

[71] S. H. Lam. Singular Perturbation for Stiff Equations Using Numerical Methods. In C. Casci and C. Bruno, editors, *Recent Adv Aerosp Sci*, pages 3–19. Springer US, Boston, MA (1985).

[72] F. C. Christo, A. R. Masri, E. M. Nebot, and S. B. Pope (1996). An integrated PDF/neural network approach for simulating turbulent reacting systems. *Proc. Combust. Inst.*, 26(1): 43–48.

[73] J. Warnatz (1981). The structure of laminar alkane-, alkene-, and acetylene flames. *Proc. Combust. Inst.*, 18(1):369–384.

[74] J. Warnatz (1985). Chemistry of high temperature combustion of alkanes up to octane. *Proc. Combust. Inst.*, 20(1):845–856.

[75] B. Varatharajan, M. Petrova, F. A. Williams, and V. Tangirala (2005). Two-step chemical-kinetic descriptions for hydrocarbon-oxygen-diluent ignition and detonation applications. *Proc. Combust. Inst.*, 30(2):1869–1877.

[76] S. C. Li, B. Varatharajan, and F. A. Williams (2001). Chemistry of JP-10 ignition. *AIAA J.*, 39(12):2351–2356.

[77] H. Wang, R. Xu, K. Wang, C. T. Bowman, R. K. Hanson, D. F. Davidson, et al. (2018). A physics-based approach to modeling real-fuel combustion chemistry - I. Evidence from experiments, and thermodynamic, chemical kinetic and statistical considerations. *Combust. Flame*, 193:502–519.

[78] R. Xu, K. Wang, S. Banerjee, J. Shao, T. Parise, Y. Zhu, et al. (2018). A physics-based approach to modeling real-fuel combustion chemistry – II. Reaction kinetic models of jet and rocket fuels. *Combust. Flame*, 193:520–537.

[79] K. Wang, R. Xu, T. Parise, J. Shao, A. Movaghar, D. J. Lee, et al. (2018). A physics-based approach to modeling real-fuel combustion chemistry – IV. HyChem modeling of combustion kinetics of a bio-derived jet fuel and its blends with a conventional Jet A. *Combust. Flame*, 198:477–489.

[80] Y. Tao, R. Xu, K. Wang, J. Shao, S. E. Johnson, A. Movaghar, et al. (2018). A Physics-based approach to modeling real-fuel combustion chemistry – III. Reaction kinetic model of JP10. *Combust. Flame*, 198:466–476.

[81] E. Ranzi, M. Dente, S. Pleruccl, and G. Blardl (1983). Initial Product Distributions from Pyrolysis of Normal and Branched Paraffins. *Ind. Eng. Chem. Fundam.*, 22(1):132–139.

[82] E. Ranzi, T. Faravelli, P. Gaffuri, and A. Sogaro (1995). Low-temperature combustion: Automatic generation of primary oxidation reactions and lumping procedures. *Combust. Flame*, 102(1-2):179–192.

[83] E. Ranzi, M. Dente, A. Goldaniga, G. Bozzano, and T. Faravelli (2001). Lumping procedures in detailed kinetic modeling of gasification, pyrolysis, partial oxidation and combustion of hydrocarbon mixtures. *Prog. Energy Combust. Sci.*, 27(1):99–139.

[84] E. Ranzi, A. Frassoldati, A. Stagni, M. Pelucchi, A. Cuoci, and T. Faravelli (2014). Reduced kinetic schemes of complex reaction systems: Fossil and biomass-derived transportation fuels. *Int. J. Chem. Kinet.*, 46(9):512–542.

[85] E. Ranzi, A. Frassoldati, S. Granata, and T. Faravelli (2005). Wide-range kinetic modeling study of the pyrolysis, partial oxidation, and combustion of heavy n-alkanes. *Ind. Eng. Chem. Res.*, 44(14):5170–5183.

[86] A. Stagni, A. Cuoci, A. Frassoldati, T. Faravelli, and E. Ranzi (2014). Lumping and reduction of detailed kinetic schemes: An effective coupling. *Ind. Eng. Chem. Res.*, 53(22):9004–9016.

[87] A. Frassoldati, G. D'Errico, T. Lucchini, A. Stagni, A. Cuoci, T. Faravelli, et al. (2015). Reduced kinetic mechanisms of diesel fuel surrogate for engine CFD simulations. *Combust. Flame*, 162(10):3991–4007.

[88] M. Bodenstein (1913). Eine Theorie der photochemischen Reaktionsgeschwindigkeiten. *Zeitschrift für Phys. Chemie*, 85U(1):329–397.

[89] D. L. Chapman and L. K. Underhill (1913). LV. - The interaction of chlorine and hydrogen. the influence of mass. *J. Chem. Soc. Trans.*, 103(0):496–508.

[90] M. Bodenstein and H. Lütkemeyer (1924). Die photochemische Bildung von Bromwasserstoff und die Bildungsgeschwindigkeit der Brommolekel aus den Atomen. *Zeitschrift für Phys. Chemie*, 114U(1):208–236.

[91] N. N. Semenov (1939). On the Kinetics of Complex Reactions. *J. Chem. Phys.*, 7(8):683.

[92] N. N. Semenov (1943). *Acta Physicochim. USSR*, 18:433.

[93] N. N. Semenov (1943). *Zh. Fiz. Him.*, 17:187.

[94] T. Turányi, A. S. Tomlin, and M. J. Pilling (1993). On the error of the quasi-steady-state approximation. *J. Phys. Chem.*, 97(1):163–172.

[95] N. Peters. Numerical and asymptotic analysis of systematically reduced reaction schemes for hydrocarbon flames. In *Numer. Simul. Combust. Phenom.*, pages 90–109. Springer, Berlin, Heidelberg (1985).

[96] N. Peters and B. Rogg. *Lecture Notes in Physics-Reduced Kinetic Mechanisms for Applications in Combustion Systems*, volume 15 of *Lecture Notes in Physics Monographs*. Springer Berlin Heidelberg, Berlin, Heidelberg (1993).

[97] F. Mauss, N. Peters, B. Rogg, and F. A. Williams. Reduced Kinetic Mechanisms for Premixed Hydrogen Flames. pages 29–43. Springer, Berlin, Heidelberg (1993).

[98] G. Paczko, P. M. Lefdal, and N. Peters (1988). Reduced reaction schemes for methane, methanol and propane flames. *Proc. Combust. Inst.*, 21(1):739–748.

[99] P. Glarborg, N. I. Lilleheie, S. Byggstøyl, B. F. Magnussen, P. Kilpinen, and M. Hupa (1992). A reduced mechanism for nitrogen chemistry in methane combustion. *Proc. Combust. Inst.*, 24(1):889–898.

[100] R. P. Lindstedt and S. A. Louloudi (2002). Joint scalar transported probability density function modeling of turbulent methanol jet diffusion flames. *Proc. Combust. Inst.*, 29(2):2147–2154.

[101] S. H. Lam (1993). Using CSP to Understand Complex Chemical Kinetics. *Combust. Sci. Technol.*, 89(5-6):375–404.

[102] A. Massias, D. Diamantis, E. Mastorakos, and D. A. Goussis (1999). An algorithm for the construction of global reduced mechanisms with CSP data. *Combust. Flame*, 117(4):685–708.

[103] S. B. Pope (1997). Computationally efficient implementation of combustion chemistry using in situ adaptive tabulation. *Combust. Theory Model.*, 1(1):41–63.

[104] T. Lu and C. K. Law (2005). A directed relation graph method for mechanism reduction. *Proc. Combust. Inst.*, 30(1):1333–1341.

[105] T. F. Lu and C. K. Law (2008). Strategies for mechanism reduction for large hydrocarbons: n-heptane. *Combust. Flame*, 154(1-2):153–163.

[106] L. L. Franke, A. K. Chatzopoulos, and S. Rigopoulos (2017). Tabulation of combustion chemistry via Artificial Neural Networks (ANNs): Methodology and application to LES-PDF simulation of Sydney flame L. *Combust. Flame*, 185:245–260.

[107] T. Readshaw, T. Ding, S. Rigopoulos, and W. P. Jones (2021). Modeling of turbulent flames with the large eddy simulation-probability density function (LES-PDF) approach, stochastic fields, and artificial neural networks. *Phys. Fluids*, 33(3):035154.

[108] R. S. Cant and E. Mastorakos. *An introduction to turbulent reacting flows*. Imperial College Press (2007).

[109] F. A. Williams (1970). An approach to turbulent flame theory. *J. Fluid Mech.*, 40(2):401–421.

[110] F. Williams (1976). Criteria for existence of wrinkled laminar flame structure of turbulent premixed flames. *Combust. Flame*, 26:269–270.

[111] R. Borghi (1988). Turbulent combustion modelling. *Prog. Energy Combust. Sci.*, 14(4): 245–292.

[112] N. Peters (1988). Laminar flamelet concepts in turbulent combustion. *Proc. Combust. Inst.*

[113] N. Peters (1999). The turbulent burning velocity for large-scale and small-scale turbulence. *J. Fluid Mech.*, 384:107–132.

[114] N. Peters. Premixed turbulent combustion. In *Turbul. Combust.*, pages 66–169. Cambridge University Press, Cambridge (2000).

[115] K. N. C. C. Bray, P. A. Libby, and J. B. Moss (1985). Unified modeling approach for premixed turbulent combustion-Part I: General formulation. *Combust. Flame*, 61(1):87–102.

[116] F. Hampp and R. Lindstedt (2017). Quantification of combustion regime transitions in premixed turbulent DME flames. *Combust. Flame*, 182:248–268.

[117] F. Hampp and R. P. Lindstedt (2017). Strain distribution on material surfaces during combustion regime transitions. *Proc. Combust. Inst.*, 36(2):1911–1918.

[118] D. Bradley, P. H. Gaskell, and X. J. Gu (1996). Burning velocities, Markstein lengths, and flame quenching for spherical methane-air flames: A computational study. *Combust. Flame*, 104(1-2):176–198.

[119] C. K. Law. *Combustion Physics*. Cambridge University Press (2006).

[120] A. A. Konnov, A. Mohammad, V. R. Kishore, N. I. Kim, C. Prathap, and S. Kumar (2018). A comprehensive review of measurements and data analysis of laminar burning velocities for various fuel+air mixtures. *Prog. Energy Combust. Sci.*, 68:197–267.

[121] F. N. Egolfopoulos, N. Hansen, Y. Ju, K. Kohse-Höinghaus, C. K. Law, and F. Qi (2014). Advances and challenges in laminar flame experiments and implications for combustion chemistry. *Prog. Energy Combust. Sci.*, 43:36–67.

[122] B. Lewis and G. Von Elbe (1934). Determination of the speed of flames and the temperature distribution in a spherical bomb from time-pressure explosion records. *J. Chem. Phys.*, 2(5): 283–290.

[123] C. Xiouris, T. Ye, J. Jayachandran, and F. N. Egolfopoulos (2016). Laminar flame speeds under engine-relevant conditions: Uncertainty quantification and minimization in spherically expanding flame experiments. *Combust. Flame*, 163:270–283.

[124] G. K. Giannakopoulos, A. Gatzoulis, C. E. Frouzakis, M. Matalon, and A. G. Tomboulides (2015). Consistent definitions of "Flame Displacement Speed" and "Markstein Length" for premixed flame propagation. *Combust. Flame*, 162(4):1249–1264.

[125] C. K. Wu and C. K. Law (1985). On the determination of laminar flame speeds from stretched flames. *Proc. Combust. Inst.*, 20(1):1941–1949.

[126] L. P. de Goey, A. van Maaren, and R. M. Ouax (1993). Stabilization of Adiabatic Premixed Laminar Flames on a Flat Flame Burner. *Combust. Sci. Technol.*, 92(1-3):201–207.

[127] A. van Maaren and L. P. H. de Goey (1994). Stretch and the adiabatic burning velocity of methane- and propane-air flames. *Combust. Sci. Technol.*, 102(1-6):309–314.

[128] V. Mittal, H. Pitsch, and F. Egolfopoulos (2012). Assessment of counterflow to measure laminar burning velocities using direct numerical simulations. *Combust. Theory Model.*, 16 (3):419–433.

[129] W. Liang, F. Wu, and C. K. Law (2017). Extrapolation of laminar flame speeds from stretched flames: Role of finite flame thickness. *Proc. Combust. Inst.*, 36(1):1137–1143.

[130] X. J. Gu, M. Z. Haq, M. Lawes, and R. Woolley (2000). Laminar burning velocity and Markstein lengths of methane-air mixtures. *Combust. Flame*, 121(1-2):41–58.

[131] J. H. Tien and M. Matalon (1991). On the burning velocity of stretched flames. *Combust. Flame*, 84(3-4):238–248.

[132] C. K. Law. A Compilation of Experimental Data on Laminar Burning Velocities. Lecture Notes in Physics Monographs. In N. Peters and B. Rogg, editors, *Reduc. Kinet. Mech. Appl. Combust. Syst.*, volume 15, pages 15–26. Springer Berlin Heidelberg, Berlin, Heidelberg (1993).

[133] P. Brequigny, H. Uesaka, Z. Sliti, D. Segawa, F. Foucher, G. Dayma, and C. Mounaïm-Rousselle. Uncertainty in measuring laminar burning velocity from expanding methane-air flames at low pressures. In *11th Mediterranean Combust. Symp.* (2019).

[134] P. D. Ronney and G. I. Sivashinsky (1989). A Theoretical Study of Propagation and Extinction of Nonsteady Spherical Flame Fronts. *SIAM J. Appl. Math.*, 49(4):1029–1046.

[135] A. P. Kelley and C. K. Law (2009). Nonlinear effects in the extraction of laminar flame speeds from expanding spherical flames. *Combust. Flame*, 156(9):1844–1851.

[136] M. L. Frankel and G. I. Sivashinskyt (1983). On effects due to thermal expansion and lewis number in spherical flame propagation. *Combust. Sci. Technol.*, 31(3-4):131–138.

[137] F. Wu, W. Liang, Z. Chen, Y. Ju, and C. K. Law (2015). Uncertainty in stretch extrapolation of laminar flame speed from expanding spherical flames. *Proc. Combust. Inst.*, 35(1):663–670.

[138] G. Kalghatgi (2018). Knock onset, knock intensity, superknock and preignition in spark ignition engines. *Int. J. Engine Res.*, 19(1):7–20.

[139] K. Fieweger, R. Blumenthal, and G. Adomeit (1997). Self-ignition of S.I. engine model fuels: A shock tube investigation at high pressure. *Combust. Flame*, 109(4):599–619.

[140] B. M. Gauthier, D. F. Davidson, and R. K. Hanson (2004). Shock tube determination of ignition delay times in full-blend and surrogate fuel mixtures. *Combust. Flame*, 139(4): 300–311.

[141] D. Bradley and R. A. Head (2006). Engine autoignition: The relationship between octane numbers and autoignition delay times. *Combust. Flame*, 147(3):171–184.

[142] G. Kalghatgi, R. Head, J. Chang, Y. Viollet, H. Babiker, and A. Amer (2014). An Alternative Method Based on Toluene/n-Heptane Surrogate Fuels for Rating the Anti-Knock Quality of Practical Gasolines. *SAE Int. J. Fuels Lubr.*, 7(3):663–672.

[143] G. Kalghatgi, H. Babiker, and J. Badra (2015). A Simple Method to Predict Knock Using Toluene, N-Heptane and Iso-Octane Blends (TPRF) as Gasoline Surrogates. *SAE Int. J. Engines*, 8(2):505–519.

[144] N. Naser, S. Y. Yang, G. Kalghatgi, and S. H. Chung (2017). Relating the octane numbers of fuels to ignition delay times measured in an ignition quality tester (IQT). *Fuel*, 187:117–127.

[145] T. Poinsot and D. Veynante. *Theoretical and Numerical Combustion*. Edwards (2005).

[146] N. Peters (2010). Combustion theory. *RWTH Aachen Univ. (CEFRC Summer Sch.).*

[147] T. A. Milne and F. T. Greene. Molecular Beams in High Temperature Chemistry. In L. Eyring, editor, *Adv. High Temp. Chem.*, volume 2, pages 107–150 (1969).

[148] A. Kantrowitz and J. Grey (1951). A high intensity source for the molecular beam. Part I. Theoretical. *Rev. Sci. Instrum.*, 22(5):328–332.

[149] W. J. McLean and R. F. Sawyer (1974). Molecular beam sampling from high-pressure sources. *Acta Astronaut.*, 1(3-4):523–540.

[150] H. Shariatmadar, F. Hampp, and R. P. Lindstedt (2021). Quantification of PAH concentrations in premixed turbulent flames crossing the soot inception limit. 38(1):1163–1172.

[151] K. G. Sulzmann, F. Bien, and S. S. Penner (1967). Intensity and collision half-width measurements using a laser source-II. Continuum and line absorption of Br2 at 6328 A. *J. Quant. Spectrosc. Radiat. Transf.*, 7(6):969–977.

[152] W. J. Tango, J. K. Link, and R. N. Zake (1968). Spectroscopy of K2 using laser-induced fluorescence. *J. Chem. Phys.*, 49(10):4264–4268.

[153] J. W. Daily (1997). Laser induced fluorescence spectroscopy in flames. *Prog. Energy Combust. Sci.*, 23(2):133–199.

[154] R. K. Hanson (2011). Applications of quantitative laser sensors to kinetics, propulsion and practical energy systems. *Proc. Combust. Inst.*, 33(1):1–40.

[155] R. Hanson, J. Monat, and C. Kruger (1976). Absorption of CO laser radiation by NO. *J. Quant. Spectrosc. Radiat. Transf.*, 16(8):705–713.

[156] N. Cohen and K. R. Westberg (1983). Chemical Kinetic Data Sheets for High Temperature Chemical Reactions. *J. Phys. Chem. Ref. Data*, 12(3):531–590.

[157] N. Cohen and K. R. Westberg (1991). Chemical Kinetic Data Sheets for High-Temperature Reactions. Part II. *J. Phys. Chem. Ref. Data*, 20(6):1211–1311.

[158] W. Tsang and R. F. Hampson (1986). Chemical Kinetic Data Base for Combustion Chemistry. Part I. Methane and Related Compounds. *J. Phys. Chem. Ref. Data*, 15(3):1087–1279.

[159] W. Tsang (1990). Chemical Kinetic Data Base for Combustion Chemistry Part 4. Isobutane. *J. Phys. Chem. Ref. Data*, 19(1):1–68.

[160] W. Tsang and J. T. Herron (1991). Chemical Kinetic Data Base for Propellant Combustion I. Reactions Involving NO, NO_2, HNO, HNO_2, HCN and N_2O. *J. Phys. Chem. Ref. Data*, 20 (4):609–663.

[161] W. Tsang. Heats of Formation of Organic Free Radicals by Kinetic Methods. In J. A. Martinho Simões, A. Greenberg, and J. F. Liebman, editors, *Energ. Org. Free Radicals*, pages 22–58. Springer Netherlands, Dordrecht (1996).

[162] R. K. Hanson and S. Salimian. Survey of Rate Constants in the N/H/O System. In *Combust. Chem.*, pages 361–421. Springer, New York, NY (1984).

[163] A. M. Dean and J. W. Bozzelli. Combustion Chemistry of Nitrogen. In *Gas-Phase Combust. Chem.*, pages 125–341. Springer, New York, NY (2000).

[164] D. L. Baulch. *Evaluated kinetic data for high temperature reactions, Volume 1*. Butterworths (1972).

[165] D. L. Baulch, C. J. Cobos, R. A. Cox, C. Esser, P. Frank, T. Just, et al. (1992). Evaluated Kinetic Data for Combustion Modelling. *J. Phys. Chem. Ref. Data*, 21(3):411–734.

[166] D. L. Baulch, C. T. Bowman, C. J. Cobos, R. A. Cox, T. Just, J. A. Kerr, et al. (2005). Evaluated kinetic data for combustion modeling: Supplement II. *J. Phys. Chem. Ref. Data*, 34(3):757–1397.

[167] J. Prager, H. N. Najm, K. Sargsyan, C. Safta, and W. J. Pitz (2013). Uncertainty quantification of reaction mechanisms accounting for correlations introduced by rate rules and fitted Arrhenius parameters. *Combust. Flame*, 160(9):1583–1593.

[168] H. Wang and D. A. Sheen (2015). Combustion kinetic model uncertainty quantification, propagation and minimization. *Prog. Energy Combust. Sci.*, 47:1–31.

[169] S. J. Klippenstein (2017). From theoretical reaction dynamics to chemical modeling of combustion. *Proc. Combust. Inst.*, 36(1):77–111.

[170] A. Burcat and B. Ruscic. Third millenium ideal gas and condensed phase thermochemical database for combustion (with update from active thermochemical tables). Technical Report ANL-05/20 TAE 960, Argonne National Lab., Argonne, IL (United States) (2005).

[171] N. J. Brown, L. A. Bastien, and P. N. Price (2011). Transport properties for combustion modeling. *Prog. Energy Combust. Sci.*, 37(5):565–582.

[172] T. Turányi (1990). Sensitivity analysis of complex kinetic systems. Tools and applications. *J. Math. Chem.*, 5(3):203–248.

[173] W. E. Stewart and J. P. Sørensen. Sensitivity and regression of multicomponent reactor models. In *Dechema 4th Int. Eur. Symp. Chem. React. Eng.*, page 12 (1976).

[174] R. Feeley, P. Seiler, A. Packard, and M. Frenklach (2004). Consistency of a reaction dataset. *J. Phys. Chem. A*, 108(44):9573–9583.

[175] M. Frenklach, H. Wang, M. Goldenberg, G. Smith, D. Golden, C. Bowman, et al. GRI-Mech. 3.0. An Optimized Detailed Chemical Reaction Mechanism for Methane Combustion. Technical report, Berkeley (2000). URL: http://combustion.berkeley.edu/gri-mech/. [Accessed 22 August 2023].

[176] M. Frenklach (1984). Systematic optimization of a detailed kinetic model using a methane ignition example. *Combust. Flame*, 58(1):69–72.

[177] M. Frenklach, H. Wang, and M. J. Rabinowitz (1992). Optimization and analysis of large chemical kinetic mechanisms using the solution mapping method-combustion of methane. *Prog. Energy Combust. Sci.*, 18(1):47–73.

[178] P. A. Berg, G. P. Smith, J. B. Jeffries, and D. R. Crosley (1998). Nitric oxide formation and reburn in low-pressure methane flames. *Proc. Combust. Inst.*, 27(1):1377–1384.

[179] R. P. Lindstedt and L. Q. Maurice (1996). Detailed Kinetic Modelling of Toluene Combustion. *Combust. Sci. Technol.*, 120(1-6):119–167.

[180] R. P. Lindstedt, F. C. Lockwood, and M. A. Selim (1995). A Detailed Kinetic Study of Ammonia Oxidation. *Combust. Sci. Technol.*, 108(4-6):231–254.

[181] V. Sick, F. Hildenbrand, and P. Lindstedt (1998). Quantitative laser-based measurements and detailed chemical kinetic modeling of nitric oxide concentrations in methane-air counterflow diffusion flames. 27(1):1401–1409.

[182] P. Lindstedt, L. Maurice, and M. Meyer (2001). Thermodynamic and kinetic issues in the formation and oxidation of aromatic species. *Faraday Discuss.*, 119(1):409–432.

[183] R. Lindstedt and M. Meyer (2002). A dimensionally reduced reaction mechanism for methanol oxidation. *Proc. Combust. Inst.*, 29(1):1395–1402.

[184] R. P. Lindstedt, S. A. Louloudi, J. J. Driscoll, and V. Sick (2004). Finite Rate Chemistry Effects in Turbulent Reacting Flows. *Flow, Turbul. Combust.*, 72(2):407–426.

[185] C. Gibaud, J. A. Snyder, V. Sick, and R. P. Lindstedt (2005). Laser-induced fluorescence measurements and modeling of absolute CH concentrations in strained laminar methane/air diffusion flames. *Proc. Combust. Inst.*, 30(1):455–463.

[186] J. J. Driscoll, V. Sick, R. L. Farrow, P. E. Schrader, K.-A. Rizos, and R. P. Lindstedt (2005). NO Reburn and Formation Chemistry in Methane Diffusion Flames. *Zeitschrift für Phys. Chemie*, 219(5):679–698.

[187] D. Greenblatt, L. Tian, and R. P. Lindstedt. The impact of hydrogen substitution by ammonia on low- and high-temperature combustion. (Submitted) (2023).

[188] W. J. Pitz, N. P. Cernansky, F. L. Dryer, F. N. Egolfopoulos, J. T. Farrell, D. G. Friend, and H. Pitsch. Development of an experimental database and chemical kinetic models for surrogate gasoline fuels. In *SAE Tech. Pap.* SAE International (2007).

[189] W. J. Pitz, N. P. Cernansky, F. L. Dryer, F. N. Egolfopoulos, J. T. Farrell, D. G. Friend, and H. Pitsch. Development of an Experimental Database and Chemical Kinetic Models for Surrogate Gasoline Fuels. In *SAE Tech. Pap.* (2007). URL: https://www.sae.org/content/2007-01-0175/.

[190] J. Yanowitz, E. M. A. Ratcliff, R. L. Mccormick, J. D. Taylor, and M. J. Murphy Battelle. Compendium of Experimental Cetane Numbers. Technical report, National Renewable Energy Laboratory (2017).

[191] V. S. Bhavani Shankar, M. Sajid, K. Al-Qurashi, N. Atef, I. Alkhesho, A. Ahmed, et al. Primary Reference Fuels (PRFs) as Surrogates for Low Sensitivity Gasoline Fuels. In *SAE Tech. Pap.* SAE International (2016).

[192] Z. Wang, H. Liu, T. Song, Y. Qi, X. He, S. Shuai, and J. Wang (2015). Relationship between super-knock and pre-ignition. *Int. J. Engine Res.*, 16(2):166–180.

[193] J. Willand, M. Daniel, E. Montefrancesco, B. Geringer, P. Hofmann, and M. Kieberger (2009). Limits on downsizing in spark ignition engines due to pre-ignition. *MTZ Worldw.*, 70 (5):56–61.

[194] J. L. Lumley. *Engines: An Introduction*. Cambridge University Press (1999).

[195] K. Epping, S. Aceves, R. Bechtold, and J. Dec. The potential of HCCI combustion for high efficiency and low emissions. In *SAE Tech. Pap.* SAE International (2002).

[196] G. Kalghatgi and B. Johansson (2018). Gasoline compression ignition approach to efficient, clean and affordable future engines. *Proc. Inst. Mech. Eng. Part D J. Automob. Eng.*, 232(1): 118–138.

[197] R. P. Lindstedt, V. D. Milosavljevic, and M. Persson (2011). Turbulent burning velocity predictions using transported PDF methods. *Proc. Combust. Inst.*, 33(1):1277–1284.

[198] M. Mehl, W. J. Pitz, C. K. Westbrook, and H. J. Curran (2011). Kinetic modeling of gasoline surrogate components and mixtures under engine conditions. *Proc. Combust. Inst.*, 33(1): 193–200.

[199] S. G. Davis and C. K. Law (1998). Laminar flame speeds and oxidation kinetics of iso-octane-air and n-heptane-air flames. 27(1):521–527.

[200] Y. Ra and R. D. Reitz (2008). A reduced chemical kinetic model for IC engine combustion simulations with primary reference fuels. *Combust. Flame*, 155(4):713–738.

[201] J. Shao, R. Choudhary, Y. Peng, D. F. Davidson, and R. K. Hanson (2019). A shock tube study of n-heptane, iso-octane, n-dodecane and iso-octane/n-dodecane blends oxidation at elevated pressures and intermediate temperatures. *Fuel*, 243:541–553.

[202] R. P. Lindstedt. Auto-ignition modelling of higher alkane fuels for internal combustion engine applications (2005). Report prepared for Toyota Motor Europe.

[203] R. P. Lindstedt. Comparison of ignition mechanisms with diesel and gtl fuels (2007). Report prepared for Toyota Motor Europe.

[204] D. Pimentel de Lamo and R. P. Lindstedt. Towards a virtual iqt fuel tester (2013). Presentation prepared for BP.

[205] A. P. Kelley, W. Liu, Y. X. Xin, A. J. Smallbone, and C. K. Law (2011). Laminar flame speeds, non-premixed stagnation ignition, and reduced mechanisms in the oxidation of iso-octane. *Proc. Combust. Inst.*, 33(1):501–508.

[206] H. J. Curran, W. J. Pitz, C. K. Westbrook, C. V. Callahan, and F. L. Dryer. Oxidation of automotive primary reference fuels at elevated pressures. In *Proc. Combust. Inst.*, volume 27, pages 379–387 (1998).

[207] A. Lifshitz and H. Ben-Hamou (1983). Thermal reactions of cyclic ethers at high temperatures. 1. Pyrolysis of ethylene oxide behind reflected shocks. *J. Phys. Chem.*, 87(10):1782–1787.

[208] K. Hoyermann, S. Maarfeld, F. Nacke, J. Nothdurft, M. Olzmann, J. Wehmeyer, et al. (2010). Rate coefficients for cycloalkyl + O reactions and product branching in the decomposition of chemically activated cycloalkoxy radicals: An experimental and theoretical study. *Phys. Chem. Chem. Phys.*, 12(31).

[209] H. J. Curran (2006). Rate constant estimation for C1 to C4 alkyl and alkoxyl radical decomposition. *Int. J. Chem. Kinet.*, 38(4):250–275.

[210] W. A. Bryce and P. Kebarle (1958). The thermal decomposition of 1-butene and 1-butene-4-d3. *Trans. Faraday Soc.*, 54.

[211] E. Prosen, F. Maron, and F. Rossini (1951). Heats of combustion, formation, and insomerization of ten C4 hydrocarbons. *Journal of Research of the National Bureau of Standards*, 46(2): 106.

[212] J. Warnatz (1983). The Mechanism of High Temperature Combustion of Propane and Butane. *Combust. Sci. Technol.*, 34(1-6):177–200.

[213] C. K. Westbrook and W. J. Pitz (1984). A Comprehensive Chemical Kinetic Reaction Mechanism for Oxidation and Pyrolysis of Propane and Propene. *Combust. Sci. Technol.*, 37(3-4): 117–152.

[214] R. P. Lindstedt, F. C. Lockwood, and M. A. Selim (1994). Detailed kinetic modelling of chemistry and temperature effects on ammonia oxidation. *Combust. Sci. Technol.*, 99(4-6): 253–276.

[215] J. J. Driscoll, V. Sick, R. L. Farrow, P. E. Schrader, K. A. Rizos, and R. P. Lindstedt (2005). NO reburn and formation chemistry in methane diffusion flames. *Zeitschrift fur Phys. Chemie*, 219(5):679–698.

[216] W. P. Jones and R. P. Lindstedt (1988). The Calculation of the Structure of Laminar Counterflow Diffusion Flames Using a Global Reaction Mechanism. *Combust. Sci. Technol.*, 61(1-3): 31–49.

[217] J. L. Emdee, K. Brezinsky, and I. Glassman (1992). A kinetic model for the oxidation of toluene near 1200 K. *J. Phys. Chem.*, 96(5):2151–2161.

[218] Y. H. Liao and W. L. Roberts (2016). Laminar Flame Speeds of Gasoline Surrogates Measured with the Flat Flame Method. *Energy and Fuels*, 30(2):1317–1324.

[219] K. Kumar, J. E. Freeh, C. J. Sung, and Y. Huang (2007). Laminar Flame Speeds of Preheated iso-Octane/O_2/N_2 and n-Heptane/O_2/N_2 Mixtures. *J. Propuls. Power*, 23(2):428–436.

[220] P. Dirrenberger, P. A. Glaude, R. Bounaceur, H. Le Gall, A. P. Da Cruz, A. A. Konnov, and F. Battin-Leclerc (2014). Laminar burning velocity of gasolines with addition of ethanol. *Fuel*, 115:162–169.

[221] L. Sileghem, V. A. Alekseev, J. Vancoillie, K. M. Van Geem, E. J. Nilsson, S. Verhelst, and A. A. Konnov (2013). Laminar burning velocity of gasoline and the gasoline surrogate components iso-octane, n-heptane and toluene. *Fuel*, 112:355–365.

[222] X. Han, Z. Wang, Y. He, S. Wang, Y. Liu, and A. A. Konnov (2020). Temperature dependence of the laminar burning velocity for n-heptane and iso-octane/air flames. *Fuel*, 276:118007.

[223] D. F. Davidson, B. M. Gauthier, and R. K. Hanson (2005). Shock tube ignition measurements of iso-octane/air and toluene/air at high pressures. *Proc. Combust. Inst.*, 30(1):1175–1182.

[224] H. P. S. Shen, J. Vanderover, and M. A. Oehlschlaeger (2008). A shock tube study of iso-octane ignition at elevated pressures: The influence of diluent gases. *Combust. Flame*, 155 (4):739–755.

[225] K. Fieweger, R. Blumenthal, and G. Adomeit (1994). Shock-tube investigations on the self-ignition of hydrocarbon-air mixtures at high pressures. *Proc. Combust. Inst.*, 25(1):1579–1585.

[226] A. Lifshitz. Ignition Delay Times. In G. Ben-Dor, O. Igra, and T. Elperin, editors, *Handbook of Shock Waves: Volume 3*, Chapter 16.5, pages 211–256 (2001).

[227] A. Danna, R. Mercogliano, R. Barbella, and A. Ciajolo (1992). Low temperature oxidation chemistry of iso-octane under high pressure conditions. *Combust. Sci. Technol.*, 83(4-6): 217–232.

[228] D. F. Davidson, M. A. Oehlschlaeger, J. T. Herbon, and R. K. Hanson (2002). Shock tube measurements of iso-octane ignition times and OH concentration time histories. *Proc. Combust. Inst.*, 29(1):1295–1301.

[229] D. F. Davidson, M. A. Oehlschlaeger, and R. K. Hanson (2007). Methyl concentration time-histories during iso-octane and n-heptane oxidation and pyrolysis. *Proc. Combust. Inst.*, 31 I (1):321–328.

[230] H. K. Ciezki and G. Adomeit (1993). Shock-tube investigation of self-ignition of n-heptane-air mixtures under engine relevant conditions. *Combust. Flame*, 93(4):421–433.

[231] D. C. Horning, D. F. Davidson, and R. K. Hanson (2002). Study of the high-temperature autoignition of n-alkane/O_2/Ar mixtures. *J. Propuls. Power*, 18(2):363–371.

[232] H. P. S. Shen, J. Steinberg, J. Vanderover, and M. A. Oehlschlaeger (2009). A Shock tube study of the ignition of n-heptane, n-decane, n-dodecane, and n-tetradecane at elevated pressures. *Energy and Fuels*, 23(5):2482–2489.

[233] C. V. Callahan, T. J. Held, F. L. Dryer, R. Minetti, M. Ribaucour, L. R. Sochet, et al. (1996). Experimental data and kinetic modeling of primary reference fuel mixtures. *Proc. Combust. Inst.*, 26(1):739–746.

[234] O. Herbinet, B. Husson, Z. Serinyel, M. Cord, V. Warth, R. Fournet, et al. (2012). Experimental and modeling investigation of the low-temperature oxidation of n-heptane. *Combust. Flame*, 159(12):3455–3471.

[235] C. K. Westbrook, J. Warnatz, and W. J. Pitz (1989). A detailed chemical kinetic reaction mechanism for the oxidation of iso-octane and n-heptane over an extended temperature range and its application to analysis of engine knock. *Proc. Combust. Inst.*, 22(1):893–901.

[236] E. Ranzi, P. Gaffuri, T. Faravelli, and P. Dagaut (1995). A wide-range modeling study of n-heptane oxidation. *Combust. Flame*, 103(1-2):91–106.

[237] N. Cohen and K. R. Westberg (1986). The use of transition-state theory to extrapolate rate coefficients for reactions of O atoms with alkanes. *Int. J. Chem. Kinet.*, 18(1):99–140.

[238] A. Chakir, M. Bellimam, J. C. Boettner, and M. Cathonnet (1992). Kinetic study of n-heptane oxidation. *Int. J. Chem. Kinet.*, 24(4):385–410.

[239] L. Seidel, K. Moshammer, X. Wang, T. Zeuch, K. Kohse-Höinghaus, and F. Mauss (2015). Comprehensive kinetic modeling and experimental study of a fuel-rich, premixed n-heptane flame. *Combust. Flame*, 162(5):2045–2058.

[240] S. B. Markofsky. Nitro Compounds, Aliphatic. In *Ullmann's Encycl. Ind. Chem.* Wiley-VCH Verlag GmbH & Co. KGaA, Weinheim, Germany (2011).

[241] A. Viayna, O. Ghashghaei, D. Vílchez, C. Estarellas, M. López, J. Gómez-Catalán, et al. (2021). Holistic approach to anti-knock agents: A high-throughput screening of aniline-like compounds. *Fuel*, 305:121518.

[242] A. M. Elbaz, S. Wang, T. F. Guiberti, and W. L. Roberts (2022). Review on the recent advances on ammonia combustion from the fundamentals to the applications. *Fuel Commun.*, 10:100053.

[243] A. Valera-Medina, H. Xiao, M. Owen-Jones, W. David, and P. Bowen (2018). Ammonia for power. *Prog. Energy Combust. Sci.*, 69:63–102.

[244] H. Kobayashi, A. Hayakawa, K. D. A. Somarathne, and E. C. Okafor (2019). Science and technology of ammonia combustion. *Proc. Combust. Inst.*, 37(1):109–133.

[245] D. I. Maclean and H. G. Wagner (1967). The structure of the reaction zones of ammonia-oxygen and hydrazine-decomposition flames. *Proc. Combust. Inst.*, 11(1):871–878.

[246] R. K. Lyon. US3900554A - Method for the reduction of the concentration of NO in combustion effluence using ammonia (1973). URL: https://patents.google.com/patent/US3900554A/en.

[247] R. K. Lyon and J. E. Hardy (1986). Discovery and Development of the Thermal Denox Process. *Ind. Eng. Chem. Fundam.*, 25(1):19–24.

[248] J. A. Miller and C. T. Bowman (1989). Mechanism and modeling of nitrogen chemistry in combustion. *Prog. Energy Combust. Sci.*, 15(4):287–338.

[249] S. J. Klippenstein, L. B. Harding, P. Glarborg, and J. A. Miller (2011). The role of NNH in NO formation and control. *Combust. Flame*, 158(4):774–789.

[250] P. Glarborg, J. A. Miller, B. Ruscic, and S. J. Klippenstein (2018). Modeling nitrogen chemistry in combustion. *Prog. Energy Combust. Sci.*, 67:31–68.

[251] X. Han, L. Lavadera, and A. A. Konnov (2021). An experimental and kinetic modeling study on the laminar burning velocity of NH_3 + N_2O + air flames. *Combust. Flame*, 228:13–28.

[252] R. P. Lindstedt and M. A. Selim (1994). Reduced reaction mechanisms for ammonia oxidation in premixed laminar flames. *Combust. Sci. Technol.*, 99(4-6):277–298.

[253] G. Altinay and R. G. Macdonald (2015). Determination of the rate constants for the $NH_2(X^2B_1)$ + $NH_2(X^2B_1)$ and $NH_2(X^2B_1)$ + H recombination reactions in N_2 as a function of temperature and pressure. *J. Phys. Chem. A*, 119(28):7593–7610.

[254] Ø. Skreiberg, P. Kilpinen, and P. Glarborg (2004). Ammonia chemistry below 1400 K under fuel-rich conditions in a flow reactor. *Combust. Flame*, 136(4):501–518.

[255] P. Glarborg, K. Dam-Johansen, and J. A. Miller (1995). The reaction of ammonia with nitrogen dioxide in a flow reactor: Implications for the NH_2 + NO_2 reaction. *Int. J. Chem. Kinet.*, 27 (12):1207–1220.

[256] S. J. Klippenstein, L. B. Harding, B. Ruscic, R. Sivaramakrishnan, N. K. Srinivasan, M. C. Su, and J. V. Michael (2009). Thermal decomposition of NH_2OH and subsequent reactions: Ab initiotransition state theory and reflected shock tube experiments. *J. Phys. Chem. A*, 113 (38):10241–10259.

[257] Y. Song, H. Hashemi, J. M. Christensen, C. Zou, P. Marshall, and P. Glarborg (2016). Ammonia oxidation at high pressure and intermediate temperatures. *Fuel*, 181:358–365.

[258] E. C. Okafor, Y. Naito, S. Colson, A. Ichikawa, T. Kudo, A. Hayakawa, and H. Kobayashi (2018). Experimental and numerical study of the laminar burning velocity of CH_4–NH_3–air premixed flames. *Combust. Flame*, 187:185–198.

[259] X. Han, Z. Wang, Y. He, Y. Zhu, and K. Cen (2020). Experimental and kinetic modeling study of laminar burning velocities of NH_3/syngas/air premixed flames. *Combust. Flame*, 213:1–13.

[260] K. P. Shrestha, C. Lhuillier, A. A. Barbosa, P. Brequigny, F. Contino, C. Mounaïm-Rousselle, et al. (2021). An experimental and modeling study of ammonia with enriched oxygen content and ammonia/hydrogen laminar flame speed at elevated pressure and temperature. *Proc. Combust. Inst.*, 38(2):2163–2174.

[261] J. Bian, J. Vandooren, and P. J. Van Tiggelen (1988). Experimental study of the structure of an ammonia-oxygen flame. *Proc. Combust. Inst.*, 21(1):953–963.

[262] J. Bian, J. Vandooren, and P. J. Van Tiggelen (1991). Experimental study of the formation of nitrous and nitric oxides in H_2-O_2-Ar flames seeded with NO and/or NH_3. *Proc. Combust. Inst.*, 23(1):379–386.

[263] J. Vandooren (1992). Comparison of the Experimental Structure of an Ammonia Seeded Rich-Hydrogen-Oxygen-Argon Flame with the Calculated Ones Along Several Reaction Mechanisms. *Combust. Sci. Technol.*, 84(1-6):335–344.

[264] A. Zubairova, H. Kim, M. Aldén, and C. Brackmann (2022). Fluorescence-free quantitative measurements of nitric oxide and major species in an ammonia/air flame with Raman spectroscopy. *Proc. Combust. Inst.*

[265] X. He, B. Shu, D. Nascimento, K. Moshammer, M. Costa, and R. X. Fernandes (2019). Autoignition kinetics of ammonia and ammonia/hydrogen mixtures at intermediate temperatures and high pressures. *Combust. Flame*, 206:189–200.

[266] L. Dai, S. Gersen, P. Glarborg, H. Levinsky, and A. Mokhov (2020). Experimental and numerical analysis of the autoignition behavior of NH_3 and NH_3/H_2 mixtures at high pressure. *Combust. Flame*, 215:134–144.

[267] K. P. Shrestha, L. Seidel, T. Zeuch, and F. Mauss (2018). Detailed Kinetic Mechanism for the Oxidation of Ammonia Including the Formation and Reduction of Nitrogen Oxides. *Energy and Fuels*, 32(10):10202–10217.

[268] A. Stagni, C. Cavallotti, S. Arunthanayothin, Y. Song, O. Herbinet, F. Battin-Leclerc, and T. Faravelli (2020). An experimental, theoretical and kinetic-modeling study of the gas-phase oxidation of ammonia. *React. Chem. Eng.*, 5(4):696–711.

[269] M. E. Fuller and C. F. Goldsmith (2019). On the relative importance of HONO versus HNO_2 in low-temperature combustion. *Proc. Combust. Inst.*, 37(1):695–702.

[270] T. V. Pham, T. J. Tsay, and M. C. Lin (2020). Thermal decomposition of N_2O near 900 K studied by FTIR spectrometry: Comparison of experimental and theoretical $O(^3P)$ formation kinetics. *Int. J. Chem. Kinet.*, 52(10):632–644.

[271] S. J. Klippenstein and P. Glarborg (2022). Theoretical kinetics predictions for NH_2 + HO2. *Combust. Flame*, 236:111787.

[272] A. Stagni and C. Cavallotti (2022). H-abstractions by O_2, NO_2, NH_2, and HO_2 from H_2NO: Theoretical study and implications for ammonia low-temperature kinetics. *Proc. Combust. Inst.*, 39:(Accepted, in press).

[273] S. Muris. PhD thesis, Ruprecht Karls Universitaet, Heidelberg, Germany (1993).

[274] E. Vilas and P. Glarborg. The selective non-catalytic reduction of NO with ammonia at high oxygen concentration. In *CHEC Rep. R0410*. Lyngby, Denmark (2004).

[275] W. Duo. *Kinetic studies of the reactions involved in selective non-catalytic reduction of nitric oxide*. PhD thesis (1990). URL: https://www.osti.gov/etdeweb/biblio/5328556.

[276] F. Kasuya, P. Glarborg, J. E. Johnsson, and K. Dam-Johansen (1995). The thermal DeNOx process: Influence of partial pressures and temperature. *Chem. Eng. Sci.*, 50(9):1455–1466.

[277] X. Han, Z. Wang, M. Costa, Z. Sun, Y. He, and K. Cen (2019). Experimental and kinetic modeling study of laminar burning velocities of NH_3/air, NH_3/H_2/air, NH_3/CO/air and NH_3/CH_4/air premixed flames. *Combust. Flame*, 206:214–226.

[278] K. Takizawa, A. Takahashi, K. Tokuhashi, S. Kondo, and A. Sekiya (2008). Burning velocity measurements of nitrogen-containing compounds. *J. Hazard. Mater.*, 155(1-2):144–152.

[279] A. Ichikawa, A. Hayakawa, Y. Kitagawa, K. D. Kunkuma Amila Somarathne, T. Kudo, and H. Kobayashi (2015). Laminar burning velocity and Markstein length of ammonia/hydrogen/air premixed flames at elevated pressures. *Int. J. Hydrogen Energy*, 40(30): 9570–9578.

[280] T. Jabbour, D. F. Clodic, J. Terry, and S. Kondo. Burning velocity and refrigerant flammability classification. In *ASHRAE Trans.*, volume 110 PART I, pages 522–533 (2004).

[281] A. Hayakawa, T. Goto, R. Mimoto, Y. Arakawa, T. Kudo, and H. Kobayashi (2015). Laminar burning velocity and Markstein length of ammonia/air premixed flames at various pressures. *Fuel*, 159:98–106.

[282] P. D. Ronney (1988). Effect of Chemistry and Transport Properties on Near-Limit Flames at Microgravity. *Combust. Sci. Technol.*, 59(1-3):123–141.

[283] U. J. Pfahl, M. C. Ross, J. E. Shepherd, K. O. Pasamehmetoglu, and C. Unal (2000). Flammability limits, ignition energy, and flame speeds in H_2-CH_4-NH_3- N_2O-O_2-N_2 mixtures. *Combust. Flame*, 123(1-2):140–158.

[284] H. Nakamura and M. Shindo (2019). Effects of radiation heat loss on laminar premixed ammonia/air flames. *Proc. Combust. Inst.*, 37(2):1741–1748.

[285] Z. Hong, R. D. Cook, D. F. Davidson, and R. K. Hanson (2010). A shock tube study of OH + $H_2O_2 \rightarrow H_2O + HO_2$ and $H_2O_2 + M \rightarrow 2\,OH + M$ using laser absorption of H_2O and OH. *J. Phys. Chem. A*, 114(18):5718–5727.

[286] K. Gkagkas and R. P. Lindstedt (2009). The impact of reduced chemistry on auto-ignition of H_2 in turbulent flows. *Combust. Theory Model.*, 13(4):607–643.

[287] N. K. Srinivasan and J. V. Michael (2006). The thermal decomposition of water. *Int. J. Chem. Kinet.*, 38(3):211–219.

[288] J. Troe (2000). Detailed modeling of the temperature and pressure dependence of the reaction $H + O_2\ (+M) \rightarrow HO_2\ (+M)$. *Proc. Combust. Inst.*, 28(2):1463–1469.

[289] J. V. Michael, J. W. Sutherland, L. B. Harding, and A. F. Wagner (2000). Initiation in H_2/O_2: Rate constants for $H_2 + O_2 \rightarrow H + HO_2$ at high temperature. *Proc. Combust. Inst.*, 28(2): 1471–1478.

[290] J. Troe (2011). The thermal dissociation/recombination reaction of hydrogen peroxide $H_2O_2\ (+M) \rightleftharpoons OH + OH\ (+M)$ III. Analysis and representation of the temperature and pressure dependence over wide ranges. *Combust. Flame*, 158(4):594–601.

[291] T. L. Nguyen and J. F. Stanton (2017). High-level theoretical study of the reaction between hydroxyl and ammonia: Accurate rate constants from 200 to 2500 K. *J. Chem. Phys.*, 147 (15):152704.

[292] S. Song, R. K. Hanson, C. T. Bowman, and D. M. Golden (2001). Shock tube determination of the overall rate of $NH_2 + NO \longrightarrow$ products in the thermal De-NOx temperature window. *Int. J. Chem. Kinet.*, 33(11):715–721.

[293] M. R. Talipov, S. L. Khursan, and R. L. Saflullin (2009). RRKM and Ab initio investigation of the NH (X) oxidation by dioxygen. *J. Phys. Chem. A*, 113(23):6468–6476.

[294] P. J. Caridade, S. P. Rodrigues, F. Sousa, and A. J. Varandas (2005). Unimolecular and bimolecular calculations for HN2. *J. Phys. Chem. A*, 109(10):2356–2363.

[295] J. A. Miller and P. Glarborg (1999). Modeling the thermal De-NOx process: Closing in on a final solution. *Int. J. Chem. Kinet.*, 31(11):757–765.

[296] J. A. Miller (1996). Theory and modeling in combustion chemistry. *Proc. Combust. Inst.*, 26 (1):461–480.

[297] J. W. Bozzelli and A. M. Dean (1995). O + NNH: A possible new route for NO_x formation in flames. *Int. J. Chem. Kinet.*, 27(11):1097–1109.

[298] D. P. Linder, X. Duan, and M. Page (1996). Thermal rate constants for $R + N_2H_2 \rightarrow RH + N_2H$ (R=H, OH, NH_2) determined from multireference configuration interaction and variational transition state theory calculations. *J. Chem. Phys.*, 104(16):6298–6307.

[299] N. E. Meagher and W. R. Anderson (2000). Kinetics of the $O(^3P)$ + N_2O reaction. 2. Interpretation and recommended rate coefficients. *J. Phys. Chem. A*, 104(25):6013–6031.

[300] P. S. Riley, B. Cosic, and A. Fontijn (2003). The H + NO recombination reaction over a wide temperature range. *Int. J. Chem. Kinet.*, 35(8):374–380.

[301] H. M. T. Nguyen, S. Zhang, J. Peeters, T. N. Truong, and M. T. Nguyen (2004). Direct ab initio dynamics studies of the reactions of HNO with H and OH radicals. *Chem. Phys. Lett.*, 388(1-3):94–99.

[302] Shucheng Xu and M. C. Lin (2009). Ab initio chemical kinetics for the NH_2 + HNO_x reactions, Part I: Kinetics and mechanism for NH_2 + HNO. *Int. J. Chem. Kinet.*, 41(11):667–677.

[303] E. W. Diau, M. J. Halbgewachs, A. R. Smith, and M. C. Lin (1995). Thermal reduction of NO by H_2: Kinetic measurement and computer modeling of the HNO + NO reaction. *Int. J. Chem. Kinet.*, 27(9):867–881.

[304] N. Fujii, H. Miyama, M. Koshi, and T. Asaba (1981). Kinetics of ammonia oxidation in shock waves. *Proc. Combust. Inst.*, 18(1):873–883.

[305] R. Atkinson, D. L. Baulch, R. A. Cox, J. N. Crowley, R. F. Hampson, R. G. Hynes, et al. (2004). Evaluated kinetic and photochemical data for atmospheric chemistry: Volume I - gas phase reactions of O_x, HO_x, NO_x and SO_x species. *Atmos. Chem. Phys.*, 4(6):1461–1738.

[306] M. C. Su, S. S. Kumaran, K. P. Lim, J. V. Michael, A. F. Wagner, L. B. Harding, and D. C. Fang (2002). Rate constants, $1100 \leq T \leq 2000$ K, for H + NO_2 → OH + NO using two shock tube techniques: Comparison of theory to experiment. *J. Phys. Chem. A*, 106(36):8261–8270.

[307] M. V. Zagidullin, N. A. Khvatov, G. I. Tolstov, I. A. Medvedkov, A. M. Mebel, M. C. Heaven, and V. N. Azyazov (2018). $O_2(b^1\Sigma_g{}^+)$ Removal by H_2, CO, N_2O, CH_4, and C_2H_4 in the 300-800 K Temperature Range. *J. Phys. Chem. A*, 122(24):5283–5288.

[308] O. V. Skrebkov (2014). Vibrational Nonequilibrium in the Hydrogen-Oxygen Reaction at Different Temperatures. *J. Mod. Phys.*, 5(16):1806–1829.

[309] J. A. Miller and C. F. Melius (1992). The reactions of imidogen with nitric oxide and molecular oxygen. *Proc. Combust. Inst.*, 24(1):719–726.

[310] J. A. Miller and S. J. Klippenstein (2000). Theoretical considerations in the NH_2 + NO reaction. *J. Phys. Chem. A*, 104(10):2061 – 2069.

[311] J. Vandooren, O. M. Sarkisov, V. P. Balakhnin, and P. J. Van Tiggelen (1991). Discussion on the formation and removal of NO_x in ammonia flames. *Chem. Phys. Lett.*, 184(4):294–300.

[312] U. Bozkaya, J. M. Turney, Y. Yamaguchi, and H. F. Schaefer (2010). The barrier height, unimolecular rate constant, and lifetime for the dissociation of HN_2. *J. Chem. Phys.*, 132(6): 064308.

[313] M. G. Bryukov, A. A. Kachanov, R. Timonnen, J. Seetula, J. Vandoren, and O. M. Sarkisov (1993). Kinetics of HNO reactions with O_2 and HNO. *Chem. Phys. Lett.*, 208(5-6):392–398.

[314] S. F. Selgren, P. W. McLoughlin, and G. I. Gellene (1989). Observation of dissociative and radiative states of N2H by neutralized ion beam techniques. *J. Chem. Phys.*, 90(3):1624–1629.

[315] J. A. Miller and P. Glarborg (1996). Modelling the formation of N_2O and NO_2 in the thermal De-NOx process. *Springer Ser. Chem. Phys.*, 61:318–333.

[316] R. R. Burrell, R. Zhao, D. J. Lee, H. Burbano, and F. N. Egolfopoulos (2017). Two-dimensional effects in counterflow methane flames. *Proc. Combust. Inst.*, 36(1):1387–1394.

[317] H. Nakamura, S. Hasegawa, and T. Tezuka (2017). Kinetic modeling of ammonia/air weak flames in a micro flow reactor with a controlled temperature profile. *Combust. Flame*, 185: 16–27.

[318] J. W. Bozzelli, A. Y. Chang, and A. M. Dean (1994). Analysis of the reactions H + N_2O and NH + NO: Pathways and rate constants over a wide range of temperature and pressure. *Proc. Combust. Inst.*, 25(1):965–974.

[319] G. B. Kistiakowsky and P. H. Kydd (1957). A Mass Spectrometric Study of Flash Photochemical Reactions. I. *J. Am. Chem. Soc.*, 79(18):4825–4830.

[320] E. J. Dunlea, R. K. Talukdar, and A. R. Ravishankara (2010). Kinetics and products of the reaction $O_2(^1\Sigma_g{}^+)$ with N_2O. *Zeitschrift fur Phys. Chemie*, 224(7-8):989–1007.

[321] L. F. Keyser, K. Y. Choo, and M. T. Leu (1985). Yields of $O_2(b^1\Sigma_g{}^+)$ from reactions of HO2. *Int. J. Chem. Kinet.*, 17(11):1169–1185.

[322] M. Monge-Palacios and S. M. Sarathy (2018). *Ab initio* and transition state theory study of the OH + $HO_2 \rightarrow H_2O + O_2(^3\Sigma_g^-)/O_2(^1\Delta_g)$: Yield and role of $O_2(^1\Delta_g)$ in H_2O_2 deomposition and in combustion of H_2. *Phys. Chem. Chem. Phys.*, 20(6):4478–4489.

[323] A. M. Starik, B. I. Loukhovitski, A. S. Sharipov, and N. S. Titova (2015). Physics and chemistry of the influence of excited molecules on combustion enhancement. *Philos. Trans. R. Soc. A Math. Phys. Eng. Sci.*, 373(2048).

[324] F. D. Findlay and D. R. Snelling (1971). Collisional deactivation of $O_2(^1\Delta g)$. *J. Chem. Phys.*, 55(2):545–551.

[325] E. S. Starkman (1959). Nitroparaffins as Potential Engine Fuel. *Ind. Eng. Chem.*, 51(12): 1477–1480.

[326] P. Brequigny, G. Dayma, F. Halter, C. Mounaïm-Rousselle, T. Dubois, and P. Dagaut (2015). Laminar burning velocities of premixed nitromethane/air flames: An experimental and kinetic modeling study. *Proc. Combust. Inst.*, 35(1):703–710.

[327] K. Zhang, Y. Li, T. Yuan, J. Cai, P. Glarborg, and F. Qi (2011). An experimental and kinetic modeling study of premixed nitromethane flames at low pressure. *Proc. Combust. Inst.*, 33 (1):407–414.

[328] J. D. Nauclér, E. J. Nilsson, and A. A. Konnov (2015). Laminar burning velocity of nitromethane + air flames: A comparison of flat and spherical flames. *Combust. Flame*, 162 (10):3803–3809.

[329] C. Brackmann, J. D. Nauclér, S. El-Busaidy, A. Hosseinnia, P.-E. Bengtsson, A. A. Konnov, and E. J. Nilsson (2018). Experimental studies of nitromethane flames and evaluation of kinetic mechanisms. *Combust. Flame*, 190:327–336.

[330] O. Mathieu, B. Giri, A. R. Agard, T. N. Adams, J. D. Mertens, and E. L. Petersen (2016). Nitromethane ignition behind reflected shock waves: Experimental and numerical study. *Fuel*, 182:597–612.

[331] C. J. Annesley, J. B. Randazzo, S. J. Klippenstein, L. B. Harding, A. W. Jasper, Y. Georgievskii, et al. (2015). Thermal Dissociation and Roaming Isomerization of Nitromethane: Experiment and Theory. *J. Phys. Chem. A*, 119(28):7872–7893.

[332] A. Matsugi and H. Shiina (2017). Thermal Decomposition of Nitromethane and Reaction between CH_3 and NO_2. *J. Phys. Chem. A*, 121(22):4218–4224.

[333] Z. Gao, M. Yang, C. Tang, F. Yang, K. Yang, F. Deng, and Z. Huang (2020). Measurements of the High Temperature Ignition Delay Times and Kinetic Modeling Study on Oxidation of Nitromethane. *Combust. Sci. Technol.*, 192(2):313–334.

[334] K. P. Shrestha, N. Vin, O. Herbinet, L. Seidel, F. Battin-Leclerc, T. Zeuch, and F. Mauss (2020). Insights into nitromethane combustion from detailed kinetic modeling – Pyrolysis experiments in jet-stirred and flow reactors. *Fuel*, 261:116349.

[335] W. Juchmann, H. Latzel, D. I. Shin, G. Peiter, T. Dreier, H. R. Volpp, et al. (1998). Absolute radical concentration measurements and modeling of low-pressure CH_4/O_2/NO flames. 27 (1):469–476.

[336] A. J. Dean, R. K. Hanson, and C. T. Bowman (1991). A shock tube study of reactions of C atoms and CH with NO including product channel measurements. *J. Phys. Chem.*, 95(8): 3180–3189.

[337] G. Hennig and H. G. Wagner (1994). Investigation of the CH_3 + NO reaction in shock waves. *Berichte der Bunsengesellschaft/Physical Chem. Chem. Phys.*, 98(5):749–753.

[338] Z. F. Xu, C. H. Hsu, and M. C. Lin (2005). Ab initio kinetics of the reaction of HCO with NO: Abstraction versus association/elimination mechanism. *J. Chem. Phys.*, 122(23):234308.

[339] R. Atkinson, D. L. Baulch, R. A. Cox, R. F. Hampson, J. A. Kerr, and J. Troe (1992). Evaluated Kinetic and Photochemical Data for Atmospheric Chemistry: Supplement IV. IUPAC Subcommittee on Gas Kinetic Data Evaluation for Atmospheric Chemistry. *J. Phys. Chem. Ref. Data*, 21(6):1125–1568.

[340] M. P. Meyer. *The Application of Detailed and Systematically Reduced Chemistry to Transient Laminar Flames*. PhD thesis, Imperial College London (2001).

[341] S. S. Wagal, T. Carrington, S. V. Filseth, and C. M. Sadowski (1982). Absolute rate constants for the reactions of CH(X^2II) with NO, N_2O, NO_2 and N2 at room temperature. *Chem. Phys.*, 69(1-2):61–70.

[342] K. Glaenzer and J. Troe (1974). Reactions of alkyl radicals in the shock wave-induced pyrolysis of nitroalkanes. *Berichte der Bunsengeselschaft fur Phys. Chemie*, 78(2):182–184.

[343] M. W. Slack and A. R. Grillo (1981). Shock tube investigation of methane-oxygen ignition sensitized by NO_2. *Combust. Flame*, 40(C):155–172.

[344] M. C. Drake and R. J. Blint (1991). Calculations of NO_x formation pathways in propagating laminar, high pressure premixed CH_4/air flames. *Combust. Sci. Technol.*, 75(4-6):261–285.

[345] N. Fujii, T. Kakuda, T. Sugiyama, and H. Miyama (1985). Direct determination of the rate constant for the reaction $CO + N_2O \rightarrow CO_2 + N_2$. *Chem. Phys. Lett.*, 122(5):489–492.

[346] J. A. Miller and S. P. Walch (1997). Prompt NO: Theoretical prediction of the high-temperature rate coefficient for $CH + N_2 \rightarrow HCN + N$. *Int. J. Chem. Kinet.*, 29(4):253–259.

[347] I. Messing, S. V. Filseth, C. M. Sadowski, and T. Carrington (1981). Absolute rate constants for the reactions of CH with O and N atoms. *J. Chem. Phys.*, 74(7):3874–3881.

[348] G. Marston, F. L. Nesbitt, and L. J. Stief (1989). Branching ratios in the $N + CH_3$ reaction: Formation of the methylene amidogen (H_2CN) radical. *J. Chem. Phys.*, 91(6):3483–3491.

[349] B. Atakan, A. Jacobs, M. Wahl, R. Weller, and J. Wolfrum (1989). Kinetic studies of the gas-phase reactions of CN with O_2 and H_2 from 294 to 1000 K. *Chem. Phys. Lett.*, 154(5): 449–453.

[350] J. N. Mulvihill and L. F. Phillips (1975). Breakdown of cyanogen in fuel-rich $H_2/N_2/O_2$ flames. *Proc. Combust. Inst.*, 15(1):1113–1122.

[351] K. Natarajan and P. Roth (1988). A shock tube study of CN radical reactions with H_2 and NO verified by H, N and O atom measurements. *Proc. Combust. Inst.*, 21(1):729–737.

[352] J. A. Miller, M. C. Branch, W. J. McLean, D. W. Chandler, M. D. Smooke, and R. J. Kee (1985). The conversion of HCN to NO and N2 in H_2-O_2-HCN-Ar flames at low pressure. *Proc. Combust. Inst.*, 20(1):673–684.

[353] M. Y. Louge and R. K. Hanson (1985). Shock tube study of NCO kinetics. *Proc. Combust. Inst.*, 20(1):665–672.

[354] J. A. Miller and C. T. Bowman (1991). Kinetic modeling of the reduction of nitric oxide in combustion products by isocyanic acid. *Int. J. Chem. Kinet.*, 23(4):289–313.

[355] W. F. Cooper, J. Park, and J. F. Hershberger (1993). Product channel dynamics of the NCO + NO reaction. *J. Phys. Chem.*, 97(13):3283–3290.

[356] W. Tsang (1987). Chemical Kinetic Data Base for Combustion Chemistry. Part 2. Methanol. *J. Phys. Chem. Ref. Data*, 16(3):471–508.

[357] M. Perrin, A. Garnaud, F. Lasagni, S. Hasko, H. Levinsky, J. C. Rolon, et al. TOPDEC Final Report CEC Project CT95 0056 (1999).

[358] J. D. Mertens and R. K. Hanson (1996). A shock tube study of $H + HNCO \rightarrow H_2 + NCO$ and the thermal decomposition of NCO. *Proc. Combust. Inst.*, 26(1):551–555.

[359] W. Tsang (1992). Chemical Kinetic Data Base for Propellant Combustion. II. Reactions Involving CN, NCO, and HNCO. *J. Phys. Chem. Ref. Data*, 21(4):753–791.

[360] A. L. East and W. D. Allen (1993). The heat of formation of NCO. *J. Chem. Phys.*, 99(6): 4638–4650.

[361] M. S. Wooldridge, R. K. Hanson, and C. T. Bowman (1994). A shock tube study of the $OH + OH \rightarrow H_2O + O$ reaction. *Int. J. Chem. Kinet.*, 26(4):389–401.

[362] Y. He, M. Lin, C. Wu, and C. Melius (1992). The reaction of HNCO with NO_2 in shock waves. *Proc. Combust. Inst.*, 24(1):711–717.

[363] I. Stranic, D. P. Chase, J. T. Harmon, S. Yang, D. F. Davidson, and R. K. Hanson (2012). Shock tube measurements of ignition delay times for the butanol isomers. *Combust. Flame*, 159(2):516–527.

[364] J. D. Nauclér, Y. Li, E. J. Nilsson, H. J. Curran, and A. A. Konnov (2016). An experimental and modeling study of nitromethane + O_2 + N_2 ignition in a shock tube. *Fuel*, 186:629–638.

[365] M. Faghih and Z. Chen (2017). Two-stage heat release in nitromethane/air flame and its impact on laminar flame speed measurement. *Combust. Flame*, 183:157–165.

[366] P. Glarborg, A. B. Bendtsen, and J. A. Miller (1999). Nitromethane dissociation: Implications for the CH3 + NO2 reaction. *International Journal of Chemical Kinetics*, 31(9):591–602.

[367] J.-J. Weng, Z.-Y. Tian, K.-W. Zhang, L.-L. Ye, Y.-X. Liu, L.-N. Wu, et al. (2019). Experimental and kinetic investigation of pyrolysis and oxidation of nitromethane. *Combust. Flame*, 203: 247–254.

[368] United States Environmental Protection Agency (2020). Overview of Greenhouse Gases, 2020 Edition. *Tech. Rep.* URL: https://www.epa.gov/ghgemissions/understanding-global-warming-potentials. [Accessed 22 August 2023].

[369] M. Frenklach (2007). Transforming data into knowledge-Process Informatics for combustion chemistry. *Proc. Combust. Inst.*, 31 I(1):125–140.

[370] J. E. Dec (2009). Advanced compression-ignition engines—understanding the in-cylinder processes. *Proc. Combust. Inst.*, 32(2):2727–2742.

[371] F. Hampp and R. P. Lindstedt (2020). Quantification of fuel chemistry effects on burning modes in turbulent premixed flames. *Combust. Flame*, 218:134–149.

[372] F. Hampp. *Quantification of combustion regime transitions*. PhD thesis, Imperial College London (2016).

[373] K. R. McManus, T. Poinsot, and S. M. Candel (1993). A review of active control of combustion instabilities. *Prog. Energy Combust. Sci.*, 19(1):1–29.

[374] K. C. Schadow and E. Gutmark (1992). Combustion instability related to vortex shedding in dump combustors and their passive control. *Prog. Energy Combust. Sci.*, 18(2):117–132.

[375] S. R. De Zilwa, S. Sivasegaram, and J. H. Whitelaw (2000). Control of combustion oscillations close to stoichiometry. *Flow, Turbul. Combust.*, 63(1):395–414.

[376] N. A. Malik and R. P. Lindstedt (2010). The Response of Transient Inhomogeneous Flames to Pressure Fluctuations and Stretch: Planar and Outwardly Propagating Hydrogen/Air Flames. *Combustion Science and Technology*, 182(9):1171–1192.

[377] N. A. Malik and R. P. Lindstedt (2012). The Response of Transient Inhomogeneous Flames to Pressure Fluctuations and Stretch: Planar and Outwardly Propagating Methane/Air Flames. *Combustion Science and Technology*, 184(10-11):1799–1817.

[378] M. AlAbbad, T. Javed, F. Khaled, J. Badra, and A. Farooq (2017). Ignition delay time measurements of primary reference fuel blends. *Combust. Flame*, 178:205–216.

[379] H. Xiao, A. Valera-Medina, and P. J. Bowen (2017). Modeling Combustion of Ammonia/Hydrogen Fuel Blends under Gas Turbine Conditions. *Energy and Fuels*, 31(8):8631–8642.

[380] J. Li, S. Lai, D. Chen, R. Wu, N. Kobayashi, L. Deng, and H. Huang (2021). A Review on Combustion Characteristics of Ammonia as a Carbon-Free Fuel. *Frontiers in Energy Research*, 9:602.

[381] C. F. Melius, J. A. Miller, and E. M. Evleth (1992). Unimolecular reaction mechanisms involving C_3H_4, C_4H_4, and C_6H_6 hydrocarbon species. *Proc. Combust. Inst.*, 24(1):621–628.

[382] K. A. Rizos. *Detailed Chemical Kinetic Modelling of Homogeneous Systems*. PhD thesis, Imperial College London (2003).

[383] W. Boullart and J. Peeters (1992). Product distributions of the C_2H_2 + O and HCCO + H reactions. Rate constant of $CH_2(\tilde{X}\ ^3B_1)$+ H. *J. Phys. Chem.*, 96(24):9810–9816.

[384] T. Böhland and F. Temps (1984). Direct Determination of the Rate Constant for the Reaction $CH_2 + H \rightarrow CH + H_2$. *Berichte der Bunsengesellschaft für Phys. Chemie*, 88(5):459–461.

[385] J. Peeters, W. Boullart, and K. Devriendt (1995). $CH(a_4\Sigma^-$ and/or $X^2\Pi)$ formation in the reaction between ketenyl radicals and oxygen atoms. Determination of the CH yield between 405 and 960 K. *J. Phys. Chem.*, 99(11):3583–3591.

[386] C. Dombrowsky and H. G. Wagner (1992). Investigation of the $^3CH_2 + O_2$ reaction in shock waves. *Berichte der Bunsengesellschaft für Phys. Chemie*, 96(8):1048–1055.

[387] R. P. Lindstedt and G. Skevis (1997). Chemistry of acetylene flames. *Combust. Sci. Technol.*, 125(1-6):73–137.

[388] M. W. Markus, D. Woiki, and P. Roth (1992). Two-channel thermal decomposition of CH_3. *Proc. Combust. Inst.*, 24(1):581–588.

[389] H.-H. Grotheer, S. Kelm, H. S. T. Driver, R. J. Hutcheon, R. D. Lockett, and G. N. Robertson (1992). Elementary Reactions in the Methanol Oxidation System. Part I: Establishment of the Mechanism and Modelling of Laminar Burning Velocities. *Berichte der Bunsengesellschaft für Phys. Chemie*, 96(10):1360–1376.

[390] R. Humpfer, H. Oser, H. H. Grotheer, and T. Just (1994). The reaction system CH_3+OH at intermediate temperatures. Appearance of a new product channel. *Proc. Combust. Inst.*, 25 (1):721–731.

[391] A. M. Dean and P. R. Westmoreland (1987). Bimolecular QRRK analysis of methyl radical reactions. *Int. J. Chem. Kinet.*, 19(3):207–228.

[392] D. L. Baulch, M. J. Pilling, C. J. Cobos, R. A. Cox, P. Frank, G. Hayman, et al. (1994). Evaluated Kinetic Data for Combustion Modeling. Supplement I. *J. Phys. Chem. Ref. Data*, 23(6):847–848.

[393] C. L. Yu, C. Wang, and M. Frenklach (1995). Chemical kinetics of methyl oxidation by molecular oxygen. *J. Phys. Chem.*, 99(39):14377–14387.

[394] R. Quiceno, J. Pérez-Ramírez, J. Warnatz, and O. Deutschmann (2006). Modeling the high-temperature catalytic partial oxidation of methane over platinum gauze: Detailed gas-phase and surface chemistries coupled with 3D flow field simulations. *Appl. Catal. A Gen.*, 303(2): 166–176.

[395] M. J. Rabinowitz, J. W. Sutherland, P. M. Patterson, and R. B. Klemm (1991). Direct rate constant measurements for H + $CH_4 \rightarrow CH_3 + H_2$, 897-1729 K, using the flash photolysis-shock tube technique. *J. Phys. Chem.*, 95(2):674–681.

[396] R. S. Timonen, E. Ratajczak, D. Gutman, and A. F. Wagner (1987). The addition and dissociation reaction H + CO $\rightleftharpoons$ HCO. 2. Experimental studies and comparison with theory. *J. Phys. Chem.*, 91(20):5325–5332.

[397] C. C. Hsu, A. M. Mebel, and M. C. Lin (1996). Ab initio molecular orbital study of the HCO + O_2 reaction: Direct versus indirect abstraction channels. *J. Chem. Phys.*, 105(6):2346–2352.

[398] Y. Hidaka, T. Oki, H. Kawano, and T. Higashihara (1989). Thermal decomposition of methanol in shock waves. *J. Phys. Chem.*, 93(20):7134–7139.

[399] H. H. Grotheer, G. Riekert, D. Walter, and T. Just (1988). Non-Arrhenius behavior of the reaction of hydroxymethyl radicals with molecular oxygen. *J. Phys. Chem.*, 92(14):4028–4030.

[400] C. Dombrowsky, A. Hoffmann, M. Klatt, and H. Gg. Wagner (1991). An Investigation of the Methanol Decomposition Behind Incident Shock Waves. *Berichte der Bunsengesellschaft für Phys. Chemie*, 95(12):1685–1687.

[401] T. J. Held and F. L. Dryer (1994). An experimental and computational study of methanol oxidation in the intermediate-and high-temperature regimes. *Proc. Combust. Inst.*, 25(1): 901–908.

[402] S. K. Farhat, C. L. Morter, and G. P. Glass (1993). Temperature dependence of the rate of reaction of C_2H with H_2. *J. Phys. Chem.*, 97(49):12789–12792.

[403] B. J. Opansky, P. W. Seakins, J. O. P. Pedersen, and S. R. Leone (1993). Kinetics of the reaction $C_2H + O_2$ from 193 to 350 K using laser flash kinetic infrared absorption spectroscopy. *J. Phys. Chem.*, 97(33):8583–8589.

[404] S. A. Carl, H. Minh Thi Nguyen, R. M. Elsamra, M. Tho Nguyen, and J. Peeters (2005). Pulsed laser photolysis and quantum chemical-statistical rate study of the reaction of the ethynyl radical with water vapor. *J. Chem. Phys.*, 122(11):114307.

[405] J. V. Michael and A. F. Wagner (1990). Rate constants for the reactions O + C_2H_2 and O + $C_2D_2 \rightarrow$ products, over the temperature range $\sim$850-1950 K, by the flash photolysis-shock tube technique. Determination of the branching ratio and a further theoretical analysis. *J. Phys. Chem.*, 94(6):2453–2464.

[406] H. Wang and M. Frenklach (1994). Calculations of rate coefficients for the chemically activated reactions of acetylene with vinylic and aromatic radicals. *J. Phys. Chem.*, 98(44): 11465–11489.

[407] V. D. Knyazev, Á. Bencsura, S. I. Stoliarov, and I. R. Slagle (1996). Kinetics of the $C_2H_3 + H_2 \rightleftharpoons H + C_2H_4$ and $CH_3 + H_2 \rightleftharpoons H + CH_4$ reactions. *J. Phys. Chem.*, 100(27):11346–11354.

[408] S. J. Klippenstein, J. A. Miller, and L. B. Harding (2002). Resolving the mystery of prompt CO2: The HCCO + O_2 reaction. *Proc. Combust. Inst.*, 29(1):1209–1217.

[409] Y. Hidaka, K. Kimura, and H. Kawano (1994). High-temperature pyrolysis of ketene in shock waves. *Combust. Flame*, 99(1):18–28.

[410] J. Warnatz. Rate Coefficients in the C/H/O System. In *Combust. Chem.*, pages 197–360. Springer, New York, NY (1984).

[411] R. P. Lindstedt (2000). The modelling of direct chemical kinetic effects in turbulent flames. *Proc. Inst. Mech. Eng. Part G J. Aerosp. Eng.*, 214(3):177–189.

[412] C. E. Canosa-Mas, H. M. Frey, and R. Walsh (1984). Studies of methylene chemistry by pulsed laser-induced decomposition of ketene. Part 1. - Ketene in the presence of noble gases. *J. Chem. Soc. Faraday Trans. 2 Mol. Chem. Phys.*, 80(5):561–578.

[413] R. P. Lindstedt and G. Skevis (2000). Molecular growth and oxygenated species formation in laminar ethylene flames. *Proc. Combust. Inst.*, 28(2):1801–1807.

[414] R. O. Foelsche, J. M. Keen, and W. C. Solomon. University of Illionis report No. AAE9307. Technical report (1993).

[415] M. W. Slack (1976). Kinetics and thermodynamics of the CN molecule. III. Shock tube measurement of CN dissociation rates. *J. Chem. Phys.*, 64(1):228–236.

[416] A. R. Fairbairn (1969). The dissociation of carbon monoxide. *Proc. R. Soc. London. A. Math. Phys. Sci.*, 312(1509):207–227.

[417] S. L. Baughcum and R. C. Oldenborg. Measurement of the $C_2(a^3\Pi_u)$ and $C_2(X^1\Sigma_g^+)$ Disappearance Rates with O_2 from 298 to 1300 Kelvin. In *Chem. Combust. Process.*, volume 249 of *ACS Symposium Series*, pages 15–257. American Chemical Society (1983).

[418] D. L. Baulch, C. J. Cobos, R. A. Cox, P. Frank, G. Hayman, T. Just, et al. (1994). Summary table of evaluated kinetic data for combustion modeling: Supplement 1. *Combust. Flame*, 98 (1-2):59–79.

[419] W. Tsang and V. Mokrushin (2000). Mechanism and rate constants for 1,3-butadiene decomposition. *Proc. Combust. Inst.*, 28(2):1717–1723.

[420] T. B. Hunter, T. A. Litzinger, H. Wang, and M. Frenklach (1996). Ethane oxidation at elevated pressures in the intermediate temperature regime: Experiments and modeling. *Combust. Flame*, 104(4):505–523.

[421] R. Atkinson, D. L. Baulch, R. A. Cox, R. F. Hampson, J. A. Kerr, M. J. Rossi, and J. Troe (1997). Evaluated Kinetic and Photochemical Data for Atmospheric Chemistry: Supplement VI. IUPAC Subcommittee on Gas Kinetic Data Evaluation for Atmospheric Chemistry. *J. Phys. Chem. Ref. Data*, 26(6):1329–1499.

[422] I. A. Reid, C. Robinson, and D. B. Smith (1985). Spontaneous ignition of methane: Measurement and chemical model. *Proc. Combust. Inst.*, 20(1):1833–1843.

[423] P. D. Lightfoot, R. A. Cox, J. N. Crowley, M. Destriau, G. D. Hayman, M. E. Jenkin, et al. (1992). Organic peroxy radicals: Kinetics, spectroscopy and tropospheric chemistry. *Atmos. Environ. Part A, Gen. Top.*, 26(10):1805–1961.

[424] H. H. Carstensen, C. V. Naik, and A. M. Dean (2005). Detailed modeling of the reaction of $C_2H_5 + O_2$. *J. Phys. Chem. A*, 109(10):2264–2281.

[425] A. Laskin and H. Wang (1999). On initiation reactions of acetylene oxidation in shock tubes: A quantum mechanical and kinetic modeling study. *Chem. Phys. Lett.*, 303(1-2):43–49.

[426] Y. Hidaka, T. Nishimori, K. Sato, Y. Henmi, R. Okuda, K. Inami, and T. Higashihara (1999). Shock-tube and modeling study of ethylene pyrolysis and oxidation. *Combust. Flame*, 117(4): 755–776.

[427] P. Saxena and F. A. Williams (2007). Numerical and experimental studies of ethanol flames. *Proc. Combust. Inst.*, 31(1):1149–1156.

[428] S. L. Fischer, F. L. Dryer, and H. J. Curran (2000). Reaction kinetics of dimethyl ether. I: high-temperature pyrolysis and oxidation in flow reactors. *Int. J. Chem. Kinet.*, 32(12): 713–740.

[429] M. V. Johnson, S. S. Goldsborough, Z. Serinyel, P. O'Toole, E. Larkin, G. O'Malley, and H. J. Curran (2009). A shock tube study of n- and iso-propanol ignition. *Energy and Fuels*, 23(12): 5886–5898.

Appendix A | Base mechanisms

The hydrogen and C_1 – C_2 chemistry which the mechanisms presented in this work were appended to are shown in Tables A.1 and A.2, respectively.

Table A.1: Hydrogen oxidation sub-mechanism applied in the current work. Forward rate constants as $k_f = AT^n e^{-E_a/RT}$. Units: kg, m, s, kmol, kJ, K. Chaperon efficiencies used to evaluate M set to unity unless otherwise indicated.

No.	Reaction	A	n	E_a	Ref.
A1	$H + O_2 \rightleftharpoons O + OH$	1.040×10^{11}	0.00	6.396×10^{4}	[285]
A2	$O + H_2 \rightleftharpoons H + OH$	5.080×10^{1}	2.67	2.633×10^{4}	[286]
A3	$H_2 + OH \rightleftharpoons H_2O + H$	2.160×10^{5}	1.51	1.433×10^{4}	[286]
A4	$OH + OH \rightleftharpoons O + H_2O$	3.340×10^{1}	2.42	-8.065×10^{3}	[166]
A5	$H_2 + M \rightleftharpoons H + H + M$	4.577×10^{16}	-1.40	4.367×10^{5}	[286]
	H_2 = 2.50; H_2O = 12.0; Ar = 0.0				
A6	$H_2 + M \rightleftharpoons H + H + M$	5.840×10^{15}	-1.10	4.367×10^{5}	[286]
	Ar = 1.0; otherwise = 0.0				
A7	$O + O + M \rightleftharpoons O_2 + M$	6.165×10^{9}	-0.50	0	[286]
	H_2 = 2.50; H_2O = 12.0; Ar = 0.0				
A8	$O + O + M \rightleftharpoons O_2 + M$	1.886×10^{7}	0.00	-7.481×10^{3}	[286]
	Ar = 1.0; otherwise = 0.0				
A9	$O + H + M \rightleftharpoons OH + M$	4.714×10^{12}	-1.00	0	[286]
	H_2 = 2.50; H_2O = 12.0; Ar = 0.75				
A10	$H_2O + M \rightleftharpoons H + OH + M$	6.064×10^{24}	-3.32	5.054×10^{5}	[287]
	H_2 = 3.0; H_2O = 0.0; O_2 = 1.5; N_2 = 2.0				
A11	$H_2O + M \rightleftharpoons H + OH + M$	1.006×10^{23}	-2.44	5.028×10^{5}	[287]
	H_2O = 1.0; otherwise = 0.0				
A12	$H + O_2 \rightleftharpoons HO_2$	4.651×10^{9}	0.44	0	[288]
	k_0	6.366×10^{14}	-1.72	2.196×10^{3}	[286]
	F_c = 0.5				
	H_2 = 2.0; H_2O = 14.0; O_2 = 0.78; Ar = 0.67				
A13	$HO_2 + H \rightleftharpoons H_2 + O_2$	2.750×10^{3}	2.09	-6.071×10^{3}	[289]
A14	$HO_2 + H \rightleftharpoons OH + OH$	7.079×10^{10}	0.00	1.234×10^{3}	[286]
A15	$HO_2 + O \rightleftharpoons O_2 + OH$	1.750×10^{10}	0.00	-1.660×10^{3}	[158]

Table A.1 (Continued)

No.	Reaction	A	n	E_a	Ref.
A16	$HO_2 + OH \rightleftharpoons H_2O + O_2$	2.890×10^{10}	0.00	-2.079×10^{3}	[286]
A17	$HO_2 + HO_2 \rightleftharpoons H_2O_2 + O_2$	4.200×10^{11}	0.00	5.013×10^{4}	[286]
+		1.300×10^{8}	0.00	-6.817×10^{3}	[286]
A18	$H_2O_2 \rightleftharpoons OH + OH$	2.000×10^{12}	0.90	2.040×10^{5}	[290]
	k_0	2.490×10^{21}	-2.30	2.040×10^{5}	
	$F_c = 0.43$				
	$H_2 = 3.7$; $H_2O = 7.5$; $H_2O_2 = 7.7$; $N_2 = 1.5$; Ar = 0.65				
A19	$H_2O_2 + H \rightleftharpoons H_2O + OH$	2.410×10^{10}	0.00	1.661×10^{4}	[286]
A20	$H_2O_2 + H \rightleftharpoons HO_2 + H_2$	4.820×10^{10}	0.00	3.326×10^{4}	[286]
A21	$H_2O_2 + O \rightleftharpoons OH + HO_2$	9.630×10^{3}	2.00	1.661×10^{4}	[286]
A22	$H_2O_2 + OH \rightleftharpoons HO_2 + H_2O$	4.600×10^{10}	0.00	2.187×10^{4}	[285]

Table A.2: Carbon ($C_1 - C_2$) oxidation sub-mechanism applied in the current work. Forward rate constants as $k_f = AT^n e^{-E_a/RT}$. Units: kg, m, s, kmol, kJ, K. Chaperon efficiencies used to evaluate M set to unity unless otherwise indicated.

No.	Reaction	A	n	E_a	Ref.
A23	$C + OH \rightleftharpoons CO + H$	5.000×10^{10}	0.00	0	[381]
A24	$C + O_2 \rightleftharpoons CO + O$	1.200×10^{11}	0.00	1.671×10^{4}	[336]
A25	$CH + H \rightleftharpoons C + H_2$	3.000×10^{10}	0.00	0	[382]
A26	$CH + O \rightleftharpoons CO + H$	4.000×10^{10}	0.00	0	[165]
A27	$CH + OH \rightleftharpoons C + H_2O$	4.000×10^{4}	2.00	1.255×10^{4}	[381]
A28	$CH + OH \rightleftharpoons CHO + H$	3.000×10^{10}	0.00	0	[309]
A29	$CH + O_2 \rightleftharpoons CHO + O$	7.500×10^{10}	0.00	0	[181]
A30	$CH + H_2O \rightleftharpoons CH_2OH$	5.730×10^{9}	0.00	-3.150×10^{3}	[165]
A31	$CH + CO_2 \rightleftharpoons CO + CHO$	3.400×10^{9}	0.00	2.900×10^{3}	[165]
A32	$CH_2(S) + M \rightleftharpoons CH_2(T) + M$	1.000×10^{10}	0.00	0	[165]
	$C_2H_2 = 5.0$; $C_2H_4 = 1.40$; $C_2H_6 = 2.20$; $CH_4 = 0.70$; $CO = 0.36$; $CO_2 = 0.36$; $H_2O = 4.0$; $N_2 = 0.36$				
A33	$CH_2(S) + H \rightleftharpoons CH + H_2$	7.000×10^{10}	0.00	0	[383]
A34	$CH_2(S) + O \rightleftharpoons CO + H + H$	1.500×10^{10}	0.00	0	[158]
A35	$CH_2(S) + O \rightleftharpoons CO + H_2$	1.500×10^{10}	0.00	0	[158]
A36	$CH_2(S) + OH \rightleftharpoons CH_2O + H$	3.000×10^{10}	0.00	0	[158]
A37	$CH_2(S) + H_2 \rightleftharpoons CH_3 + H$	7.230×10^{10}	0.00	0	[158]
A38	$CH_2(S) + O_2 \rightleftharpoons CO + OH + H$	3.000×10^{10}	0.00	0	[158]
A39	$CH_2(S) + CO_2 \rightleftharpoons CH_2O + CO$	3.000×10^{9}	0.00	0	[158]
A40	$CH_2(T) + H \rightleftharpoons CH + H_2$	1.100×10^{11}	0.00	0	[384]
A41	$CH_2(T) + O \rightleftharpoons CO + H + H$	4.880×10^{10}	0.00	0	[385]
A42	$CH_2(T) + O \rightleftharpoons CO + H_2$	3.250×10^{10}	0.00	0	[385]

Table A.2 (Continued)

No.	Reaction	A	n	E_a	Ref.
A43	$CH_2(T) + OH \rightleftharpoons CH + H_2O$	1.130×10^{4}	2.00	1.256×10^{4}	[309]
A44	$CH_2(T) + OH \rightleftharpoons CH_2O + H$	2.500×10^{10}	0.00	0	[309]
A45	$CH_2(T) + C \rightleftharpoons C_2H + H$	5.000×10^{10}	0.00	0	[381]
A46	$CH_2(T) + CH \rightleftharpoons C_2H_2 + H$	4.000×10^{10}	0.00	0	[309]
A47	$CH_2(T) + CH_2(T) \rightleftharpoons C_2H_2 + H + H$	1.200×10^{11}	0.00	3.320×10^{3}	[165]
A48	$CH_2(T) + H_2 \rightleftharpoons CH_3 + H$	3.000×10^{6}	0.00	0	[158]
A49	$CH_2(T) + O_2 \rightleftharpoons CO + H + OH$	1.642×10^{18}	-3.30	1.200×10^{4}	[386]
A50	$CH_2(T) + O_2 \rightleftharpoons CO + H_2O$	2.240×10^{19}	-3.30	1.200×10^{4}	[386]
A51	$CH_2(T) + O_2 \rightleftharpoons CO_2 + H + H$	3.285×10^{18}	-3.30	1.200×10^{4}	[386]
A52	$CH_2(T) + O_2 \rightleftharpoons CO_2 + H_2$	2.630×10^{18}	-3.30	1.200×10^{4}	[386]
A53	$CH_2(T) + O_2 \rightleftharpoons CH_2O + O$	3.285×10^{18}	-3.30	1.200×10^{4}	[386]
A54	$CH_2(T) + CO \rightleftharpoons C_2H_2O$	6.020×10^{5}	0.00	0	[387]
A55	$CH_2(T) + CO_2 \rightleftharpoons CH_2O + CO$	1.100×10^{8}	0.00	4.180×10^{3}	[309]
A56	$CH_3 + M \rightleftharpoons CH_2(S) + H + M$	1.900×10^{13}	0.00	3.824×10^{5}	[388]
A57	$CH_3 + H \rightleftharpoons CH_4$	2.110×10^{11}	0.00	0	[387]
	k_0	6.300×10^{17}	-1.80	0	
	Troe form: α = 0.630; T^{*} = 3315.0; T^{***} = 61.000				
	H_2 = 2.00; O_2 = 1.50; CO = 1.50; H_2O = 6.00; CO_2 = 3.00;				
A58	$CH_3 + O \rightleftharpoons CH_2O + H$	8.430×10^{10}	0.00	0	[165]
A59	$CH_3 + OH \rightleftharpoons CH_2(S) + H_2O$	4.000×10^{10}	0.00	1.047×10^{4}	[389]
A60	$CH_3 + OH \rightleftharpoons CH_2O + H_2$	1.024×10^{9}	0.00	0	[390]
A61	$CH_3 + OH \rightleftharpoons CH_2OH + H$	1.500×10^{11}	0.00	3.446×10^{4}	[389]
A62	$CH_3 + OH \rightleftharpoons CH_3O + H$	5.740×10^{9}	-0.23	5.828×10^{4}	[391]
A63	$CH_3 + OH \rightleftharpoons CH_3OH$	6.000×10^{10}	0.00	0	[392]
	k_0	1.595×10^{38}	-8.20	0	
	Troe form: α = 0.180; T^{*} = 200.0; T^{***} = 1438.0				
A64	$CH_3 + HO_2 \rightleftharpoons CH_3O + OH$	1.800×10^{10}	0.00	0	[165]
A65	$CH_3 + C \rightleftharpoons C_2H_2 + H$	5.000×10^{10}	0.00	0	[381]
A66	$CH_3 + CH \rightleftharpoons C_2H_3 + H$	3.000×10^{10}	0.00	0	[309]
A67	$CH_3 + CH_2(S) \rightleftharpoons C_2H_4 + H$	1.800×10^{10}	0.00	0	[158]
A68	$CH_3 + CH_2(T) \rightleftharpoons C_2H_4 + H$	4.000×10^{10}	0.00	0	[165]
A69	$CH_3 + CH_3 \rightleftharpoons C_2H_5 + H$	5.000×10^{9}	0.10	4.436×10^{4}	[165]
A70	$CH_3 + CH_3 \rightleftharpoons C_2H_6$	3.600×10^{10}	0.00	0	[165]
	k_0	1.270×10^{35}	-7.00	1.155×10^{4}	
	Troe form: α = 0.380; T^{*} = 73.000; T^{***} = 1180.0				
	CO = 1.90; CO_2 = 3.30; H_2 = 1.10; H_2O = 5.70; O_2 = 1.90; N_2 = 1.60;				
A71	$CH_3 + O_2 \rightleftharpoons CH_2O + OH$	1.850×10^{9}	0.00	8.501×10^{4}	[393]
A72	$CH_3 + O_2 \rightleftharpoons CH_3O + O$	1.320×10^{11}	0.00	1.314×10^{5}	[165]
A73	$CH_3 + HO_2 \rightleftharpoons CH_4 + O_2$	3.600×10^{9}	0.00	0	[394]
A74	$CH_4 + H \rightleftharpoons CH_3 + H_2$	3.860×10^{3}	2.11	3.242×10^{4}	[395]
A75	$CH_4 + O \rightleftharpoons CH_3 + OH$	9.033×10^{5}	1.56	3.550×10^{4}	[165]

Table A.2 (Continued)

No.	Reaction	A	n	E_a	Ref.
A76	$CH_4 + OH \rightleftharpoons CH_3 + H_2O$	1.560×10^{4}	1.83	1.160×10^{4}	[165]
A77	$CH_4 + HO_2 \rightleftharpoons CH_3 + H_2O_2$	9.033×10^{9}	0.00	1.031×10^{5}	[165]
A78	$CH_4 + CH \rightleftharpoons C_2H_4 + H$	6.000×10^{10}	0.00	0	[309]
A79	$CH_4 + CH_2(S) \rightleftharpoons CH_3 + CH_3$	4.270×10^{10}	0.00	0	[158]
A80	$CO + O \rightleftharpoons CO_2$	1.800×10^{7}	0.00	9.950×10^{3}	[202]
	k_0	1.350×10^{18}	-2.79	1.750×10^{4}	
	F_c = 1.000				
	CO = 1.90; CO_2 = 3.80; H_2 = 2.50; H_2O = 12.00;				
A81	$CO + OH \rightleftharpoons CO_2 + H$	6.320×10^{3}	1.50	-2.079×10^{3}	[165]
A82	$CO + HO_2 \rightleftharpoons CO_2 + OH$	1.500×10^{11}	0.00	9.893×10^{4}	[158]
A83	$CO + O_2 \rightleftharpoons CO_2 + O$	2.500×10^{9}	0.00	2.000×10^{5}	[158]
A84	$CHO + M \rightleftharpoons CO + H + M$	1.860×10^{14}	-1.00	7.113×10^{4}	[396]
	CO = 2.50; CO_2 = 2.50; H_2 = 1.89; H_2O = 12.00;				
A85	$CHO + H \rightleftharpoons CO + H_2$	9.000×10^{10}	0.00	0	[165]
A86	$CHO + O \rightleftharpoons CO + OH$	3.000×10^{10}	0.00	0	[165]
A87	$CHO + O \rightleftharpoons CO_2 + H$	3.000×10^{10}	0.00	0	[165]
A88	$CHO + OH \rightleftharpoons CO + H_2O$	1.000×10^{11}	0.00	0	[165]
A89	$CHO + CH_3 \rightleftharpoons CO + CH_4$	1.200×10^{11}	0.00	0	[158]
A90	$CHO + O_2 \rightleftharpoons CO + HO_2$	1.200×10^{7}	0.81	-3.043×10^{3}	[397]
A91	$CH_2O + M \rightleftharpoons CHO + H + M$	1.260×10^{13}	0.00	3.260×10^{5}	[165]
A92	$CH_2O + H \rightleftharpoons CHO + H_2$	1.260×10^{5}	1.62	9.063×10^{3}	[165]
A93	$CH_2O + O \rightleftharpoons CHO + OH$	4.150×10^{8}	0.57	1.156×10^{4}	[165]
A94	$CH_2O + OH \rightleftharpoons CHO + H_2O$	3.430×10^{6}	1.18	-1.870×10^{3}	[165]
A95	$CH_2O + HO_2 \rightleftharpoons CHO + H_2O_2$	2.000×10^{9}	0.00	4.897×10^{4}	[389]
A96	$CH_2O + CH \rightleftharpoons C_2H_2O + H$	9.460×10^{10}	0.00	-2.160×10^{3}	[165]
A97	$CH_2O + CH_3 \rightleftharpoons CHO + CH_4$	4.090×10^{9}	0.00	3.700×10^{4}	[165]
A98	$CH_2O + O_2 \rightleftharpoons CHO + HO_2$	6.000×10^{10}	0.00	1.700×10^{5}	[165]
A99	$CH_2OH + M \rightleftharpoons CH_2O + H + M$	4.400×10^{12}	0.00	1.255×10^{5}	[398]
A100	$CH_2OH + H \rightleftharpoons CH_2O + H_2$	3.000×10^{10}	0.00	0	[73]
A101	$CH_2OH + O \rightleftharpoons CH_2O + OH$	4.220×10^{10}	0.00	0	[356]
A102	$CH_2OH + OH \rightleftharpoons CH_2O + H_2O$	2.400×10^{10}	0.00	0	[356]
A103	$CH_2OH + O_2 \rightleftharpoons CH_2O + HO_2$	4.560×10^{-9}	5.94	-1.899×10^{4}	[399]
A104	$CH_3O + M \rightleftharpoons CH_2O + H + M$	5.450×10^{10}	0.00	5.650×10^{4}	[389]
A105	$CH_3O + M \rightleftharpoons CH_2OH + M$	3.010×10^{8}	0.00	1.704×10^{4}	[356]
	CH_3OH = 1.00; otheriwse = 0.0				
A106	$CH_3O + H \rightleftharpoons CH_2O + H_2$	2.000×10^{10}	0.00	0	[158]
A107	$CH_3O + O \rightleftharpoons CH_2O + OH$	6.000×10^{9}	0.00	0	[158]
A108	$CH_3O + OH \rightleftharpoons CH_2O + H_2O$	1.800×10^{10}	0.00	0	[158]
A109	$CH_3O + O_2 \rightleftharpoons CH_2O + HO_2$	6.600×10^{7}	0.00	1.088×10^{4}	[158]
A110	$CH_3OH + M \rightleftharpoons CH_2(S) + H_2O + M$	7.000×10^{12}	0.00	2.780×10^{5}	[400]

Table A.2 (Continued)

No.	Reaction	A	n	E_a	Ref.
A111	$CH_3OH + M \rightleftharpoons CH_2OH + H + M$	2.000×10^{14}	0.00	3.159×10^{5}	[398]
A112	$CH_3OH + H \rightleftharpoons CH_2OH + H_2$	1.440×10^{10}	0.00	2.550×10^{4}	[401]
A113	$CH_3OH + H \rightleftharpoons CH_3O + H_2$	4.000×10^{9}	0.00	2.550×10^{4}	[389]
A114	$CH_3OH + O \rightleftharpoons CH_2OH + OH$	3.880×10^{2}	2.50	1.290×10^{4}	[389]
A115	$CH_3OH + O \rightleftharpoons CH_3O + OH$	1.000×10^{10}	0.00	1.959×10^{4}	[73]
A116	$CH_3OH + OH \rightleftharpoons CH_2OH + H_2O$	3.000×10^{1}	2.65	-3.700×10^{3}	[389]
A117	$CH_3OH + OH \rightleftharpoons CH_3O + H_2O$	5.300	2.65	-3.700×10^{3}	[389]
A118	$CH_3OH + CH_3 \rightleftharpoons CH_2OH + CH_4$	3.190×10^{-2}	3.20	3.000×10^{4}	[356]
A119	$C_2H + O \rightleftharpoons CO + CH$	1.000×10^{10}	0.00	0	[165]
A120	$C_2H + OH \rightleftharpoons C_2HO + H$	2.000×10^{10}	0.00	0	[309]
A121	$C_2H + H_2 \rightleftharpoons C_2H_2 + H$	5.680×10^{7}	0.90	8.340×10^{3}	[402]
A122	$C_2H + O_2 \rightleftharpoons CO + CO + H$	9.040×10^{9}	0.00	-1.910×10^{3}	[403]
A123	$C_2H + H_2O \rightleftharpoons C_2H_2O + H$	1.325	3.05	3.126×10^{3}	[404]
A124	$C_2H_2 + M \rightleftharpoons C_2H + H + M$	4.200×10^{13}	0.00	4.480×10^{5}	[73]
A125	$C_2H_2 + O \rightleftharpoons CO + CH_2(T)$	2.893×10^{3}	2.09	6.530×10^{3}	[405]
A126	$C_2H_2 + O \rightleftharpoons C_2HO + H$	4.339×10^{3}	2.09	6.530×10^{3}	[405]
A127	$C_2H_2 + OH \rightleftharpoons C_2H + H_2O$	3.370×10^{4}	2.00	5.857×10^{4}	[381]
A128	$C_2H_2 + OH \rightleftharpoons C_2H_2O + H$	3.750×10^{3}	1.70	4.180×10^{3}	[387]
A129	$C_2H_2 + HO_2 \rightleftharpoons C_2H_2O + OH$	6.000×10^{6}	0.00	3.352×10^{4}	[158]
A130	$C_2H_2 + O_2 \rightleftharpoons C_2H + HO_2$	1.200×10^{10}	0.00	3.117×10^{5}	[158]
A131	$C_2H_3 \rightleftharpoons C_2H_2 + H$	2.000×10^{14}	0.00	1.663×10^{5}	[165]
	k_0	4.160×10^{38}	-7.50	1.904×10^{5}	
	$F_c = 0.350$				
	$CO = 2.00$; $CO_2 = 3.00$; $H_2 = 2.00$; $H_2O = 5.00$; $O_2 = 1.50$;				
A132	$C_2H_3 + H \rightleftharpoons C_2H_2 + H_2$	3.000×10^{10}	0.00	0	[165]
A133	$C_2H_3 + O \rightleftharpoons C_2H_2O + H$	3.000×10^{10}	0.00	0	[309]
A134	$C_2H_3 + OH \rightleftharpoons C_2H_2 + H_2O$	2.000×10^{10}	0.00	0	[309]
A135	$C_2H_3 + HO_2 \rightleftharpoons CH_3CO + OH$	3.000×10^{10}	0.00	0	[158]
A136	$C_2H_3 + CH \rightleftharpoons C_2H_2 + CH_2(T)$	5.000×10^{10}	0.00	0	[309]
A137	$C_2H_3 + C_2H \rightleftharpoons C_2H_2 + C_2H_2$	3.000×10^{10}	0.00	0	[309]
A138	$C_2H_3 + O_2 \rightleftharpoons CH_2O + CHO$	1.640×10^{18}	-2.78	1.056×10^{4}	[406]
A139	$C_2H_3 + O_2 \rightleftharpoons C_2H_2 + HO_2$	1.660×10^{11}	-0.83	1.063×10^{4}	[406]
A140	$C_2H_3 + O_2 \rightleftharpoons CH_2CHO + O$	2.500×10^{9}	0.06	3.970×10^{3}	[406]
A141	$C_2H_4 + M \rightleftharpoons C_2H_3 + H + M$	2.600×10^{14}	0.00	4.040×10^{5}	[73]
A142	$C_2H_4 + H \rightleftharpoons C_2H_3 + H_2$	5.070×10^{4}	1.93	5.419×10^{4}	[407]
A143	$C_2H_4 + H \rightleftharpoons C_2H_5$	3.974×10^{6}	1.28	5.400×10^{3}	[392]
	k_0	4.714×10^{12}	0.00	3.159×10^{3}	
	Troe form: $\alpha = 0.240$; $T^{*} = 40.000$; $T^{***} = 1025.0$				
	$C_2H_2 = 5.00$; $C_2H_4 = 1.40$; $C_2H_6 = 2.20$; $CH_4 = 0.70$;				
	$CO = 0.36$; $CO_2 = 0.36$; $H_2O = 4.00$; $N_2 = 0.36$;				

Table A.2 (Continued)

No.	Reaction	A	n	E_a	Ref.
A144	$C_2H_4 + O \rightleftharpoons CHO + CH_3$	8.100×10^{3}	1.88	7.600×10^{2}	[165]
A145	$C_2H_4 + OH \rightleftharpoons C_2H_3 + H_2O$	2.050×10^{10}	0.00	2.486×10^{4}	[165]
A146	$C_2H_5 + O \rightleftharpoons CH_2O + CH_3$	6.600×10^{10}	0.00	0	[165]
A147	$C_2H_6 \rightleftharpoons C_2H_5 + H$	8.850×10^{20}	-1.23	4.277×10^{5}	[177]
	k_0	4.900×10^{39}	-6.43	4.484×10^{5}	
	SRI form: a = 47.6; b = 16182; c = 3371; d = 1.0				
	$CO = 1.90$; $CO_2 = 3.30$; $H_2 = 1.10$; $H_2O = 5.70$; $O_2 = 1.90$; $N_2 = 1.60$;				
A148	$C_2H_6 + H \rightleftharpoons C_2H_5 + H_2$	1.445×10^{6}	1.50	3.100×10^{4}	[165]
A149	$C_2H_6 + O \rightleftharpoons C_2H_5 + OH$	1.000×10^{6}	1.50	2.430×10^{4}	[165]
A150	$C_2H_6 + OH \rightleftharpoons C_2H_5 + H_2O$	7.226×10^{3}	2.00	3.610×10^{3}	[165]
A151	$C_2H_6 + CH_2(S) \rightleftharpoons C_2H_5 + CH_3$	1.140×10^{11}	0.00	0	[158]
A152	$C_2O + H \rightleftharpoons CO + CH$	5.000×10^{10}	0.00	0	[309]
A153	$C_2O + O \rightleftharpoons CO + CO$	5.000×10^{10}	0.00	0	[309]
A154	$C_2O + OH \rightleftharpoons CO + CO + H$	2.000×10^{10}	0.00	0	[309]
A155	$C_2O + O_2 \rightleftharpoons CO + CO + O$	2.000×10^{10}	0.00	0	[309]
A156	$C_2HO + H \rightleftharpoons CH_2(S) + CO$	1.000×10^{11}	0.00	0	[309]
A157	$C_2HO + O \rightleftharpoons CO + CO + H$	9.635×10^{10}	0.00	0	[165]
A158	$C_2HO + OH \rightleftharpoons C_2O + H_2O$	3.000×10^{10}	0.00	0	[309]
A159	$C_2HO + CH \rightleftharpoons C_2H_2 + CO$	5.000×10^{10}	0.00	0	[309]
A160	$C_2HO + CH_2(T) \rightleftharpoons C_2H_3 + CO$	3.000×10^{10}	0.00	0	[309]
A161	$C_2HO + C_2HO \rightleftharpoons C_2H_2 + CO + CO$	1.000×10^{10}	0.00	0	[309]
A162	$C_2HO + O_2 \rightleftharpoons CO + CO + OH$	1.909×10^{8}	-0.02	4.280×10^{3}	[408]
A163	$C_2HO + O_2 \rightleftharpoons CO_2 + CO + H$	4.782×10^{9}	-0.14	4.812×10^{3}	[408]
A164	$C_2H_2O + H \rightleftharpoons CO + CH_3$	1.110×10^{4}	2.00	8.360×10^{3}	[409]
A165	$C_2H_2O + H \rightleftharpoons C_2HO + H_2$	1.800×10^{11}	0.00	3.598×10^{4}	[409]
A166	$C_2H_2O + O \rightleftharpoons CO_2 + CH_2(T)$	2.000×10^{10}	0.00	9.600×10^{3}	[410]
A167	$C_2H_2O + O \rightleftharpoons C_2HO + OH$	2.000×10^{4}	2.00	4.168×10^{4}	[411]
A168	$C_2H_2O + OH \rightleftharpoons CH_2OH + CO$	1.020×10^{10}	0.00	0	[165]
A169	$C_2H_2O + CH_2(S) \rightleftharpoons C_2H_4 + CO$	1.260×10^{11}	0.00	0	[412]
A170	$C_2H_2O + CH_3 \rightleftharpoons C_2H_5 + CO$	9.000×10^{7}	0.00	0	[409]
A171	$C_2H_2O + CH_3 \rightleftharpoons C_2HO + CH_4$	7.500×10^{9}	0.00	5.439×10^{4}	[409]
A172	$CH_2CHO + CH_3 \rightleftharpoons C_2H_6 + CO$	6.100×10^{9}	0.00	0	[413]
A173	$CH_3CHO + M \rightleftharpoons CHO + CH_3 + M$	7.080×10^{15}	0.00	3.422×10^{5}	[165]
A174	$CH_3CHO + H \rightleftharpoons CH_3CO + H_2$	2.100×10^{6}	1.16	1.009×10^{4}	[414]
A175	$CH_3CHO + O \rightleftharpoons CH_3CO + OH$	5.000×10^{9}	0.00	7.500×10^{3}	[410]
A176	$CH_3CHO + OH \rightleftharpoons CH_3CO + H_2O$	2.300×10^{7}	0.73	-4.660×10^{3}	[414]
A177	$CH_3CHO + HO_2 \rightleftharpoons CH_3CO + H_2O_2$	3.000×10^{9}	0.00	4.987×10^{4}	[165]
A178	$CH_3CHO + CH_2(T) \rightleftharpoons CH_3CO + CH_3$	2.500×10^{9}	0.00	1.589×10^{4}	[414]

Table A.2 (Continued)

No.	Reaction	A	n	E_a	Ref.
A179	$CH_3CHO + CH_3 \rightleftharpoons CH_3CO + CH_4$	2.000×10^{-9}	5.64	1.031×10^{4}	[165]
A180	$CH_3CHO + O_2 \rightleftharpoons CH_3CO + HO_2$	4.000×10^{10}	0.00	1.642×10^{5}	[414]
A181	$C_2H + C_2H \rightleftharpoons C_2H_2 + C_2$	1.810×10^{9}	0.00	0	[158]
A182	$C_2H + H \rightleftharpoons C_2 + H_2$	3.610×10^{10}	0.00	1.183×10^{5}	[411]
A183	$C + C + M \rightleftharpoons C_2 + M$	1.800×10^{15}	-1.60	0	[415]
A184	$C_2 + O \rightleftharpoons CO + C$	3.610×10^{11}	0.00	0	[416]
A185	$C_2 + O_2 \rightleftharpoons CO + CO$	8.970×10^{9}	0.00	4.100×10^{3}	[417]
A186	$CH + M \rightleftharpoons C + H + M$	1.000×10^{11}	0.00	2.680×10^{5}	[411]
A187	$CH_2(T) + M \rightleftharpoons C + H_2 + M$	1.148×10^{11}	0.00	2.337×10^{5}	[384]
A188	$C_2H_2O + OH \rightleftharpoons C_2HO + H_2O$	1.000×10^{4}	2.00	1.256×10^{4}	[411]
A189	$C_2H_4 + O \rightleftharpoons CH_2CHO + H$	4.700×10^{3}	1.88	7.600×10^{2}	[392]
A190	$C_2H_4 + O \rightleftharpoons C_2H_2O + H_2$	6.750×10^{2}	1.88	7.600×10^{2}	[165]
A191	$C_2H_5 + O \rightleftharpoons CH_3CHO + H$	6.600×10^{10}	0.00	0	[158]
A192	$CH_2CHO \rightleftharpoons CH_3CO$	1.000×10^{13}	0.00	1.841×10^{5}	[203]
A193	$CH_2CHO \rightleftharpoons C_2H_2O + H$	1.580×10^{13}	0.00	1.967×10^{5}	[203]
A194	$CH_3CO \rightleftharpoons CH_3 + CO$	2.800×10^{13}	0.00	7.175×10^{4}	[418]
	k_0	6.030×10^{12}	0.00	5.886×10^{4}	
	$F_c = 1.000$				
A195	$H_2C_2 + O_2 \rightleftharpoons CHO + CHO$	1.000×10^{10}	0.00	0	[382]
A196	$CH_3OH + O_2 \rightleftharpoons CH_2OH + HO_2$	2.050×10^{10}	0.00	1.880×10^{5}	[419]
A197	$CH_3OH + HO_2 \rightleftharpoons CH_2OH + H_2O_2$	3.980×10^{10}	0.00	8.122×10^{4}	[401]
A198	$CH_2CHO + O_2 \rightleftharpoons CH_2O + CO + OH$	1.810×10^{7}	0.00	0	[165]
A199	$CH_2CHO + OH \rightleftharpoons C_2H_2O + H_2O$	1.000×10^{10}	0.00	0	[413]
A200	$CH_2CHO + O \rightleftharpoons C_2H_2O + OH$	1.000×10^{11}	0.00	0	[413]
A201	$CH_3CO + H \rightleftharpoons C_2H_2O + H_2$	1.150×10^{10}	0.00	0	[413]
A202	$CH_3CO + H \rightleftharpoons CH_3 + CHO$	2.150×10^{10}	0.00	0	[413]
A203	$CH_3CO + OH \rightleftharpoons C_2H_2O + H_2O$	1.210×10^{10}	0.00	0	[158]
A204	$CH_3CO + O \rightleftharpoons CH_3 + CO_2$	1.544×10^{11}	0.00	0	[382]
A205	$CH_3CO + O \rightleftharpoons C_2H_2O + OH$	3.860×10^{10}	0.00	0	[382]
A206	$C_2H_6 + O_2 \rightleftharpoons C_2H_5 + HO_2$	6.023×10^{10}	0.00	2.170×10^{5}	[165]
A207	$C_2H_6 + HO_2 \rightleftharpoons C_2H_5 + H_2O_2$	1.320×10^{10}	0.00	8.564×10^{4}	[165]
A208	$C_2H_4 + HO_2 \rightleftharpoons C_2H_3 + H_2O_2$	1.120×10^{10}	0.00	1.273×10^{5}	[420]
A209	$C_2H_4 + HO_2 \rightleftharpoons CH_3CHO + OH$	6.030×10^{6}	0.00	3.326×10^{4}	[158]
A210	$C_2H_4 + O_2 \rightleftharpoons C_2H_3 + HO_2$	4.220×10^{10}	0.00	2.411×10^{5}	[158]
A211	$C_2H_3 + O_2 \rightleftharpoons CH_3CO + O$	1.500×10^{8}	0.00	-9.980×10^{2}	[387]
A212	$CH_3 + O_2 \rightleftharpoons CH_3OO$	2.060×10^{6}	1.10	0	[421]
	k_0	5.310×10^{19}	-3.30	0	
	$F_c = 0.270$				
A213	$CH_3OO + CH_4 \rightleftharpoons CH_3OOH + CH_3$	3.000×10^{9}	0.00	9.500×10^{4}	[422]

Table A.2 (Continued)

No.	Reaction	A	n	E_a	Ref.
A214	$CH_3OO + CH_2O \rightleftharpoons CH_3OOH + CHO$	3.000×10^{9}	0.00	5.200×10^{4}	[382]
A215	$CH_3OO + HO_2 \rightleftharpoons CH_3OOH + O_2$	2.470×10^{8}	0.00	-6.568×10^{3}	[423]
A216	$CH_3OO + CH_3OO \rightleftharpoons CH_3O + CH_3O + O_2$	5.480×10^{7}	0.00	-3.492×10^{3}	[392]
A217	$CH_3OO + CH_3 \rightleftharpoons CH_3O + CH_3O$	1.000×10^{10}	0.00	0	[382]
A218	$CH_3OOH \rightleftharpoons CH_3O + OH$	6.000×10^{14}	0.00	1.771×10^{5}	[422]
A219	$CH_3OO + C_2H_6 \rightleftharpoons CH_3OOH + C_2H_5$	3.000×10^{8}	0.00	6.250×10^{4}	[158]
A220	$C_2H_4O \rightleftharpoons CH_3 + CHO$	3.400×10^{13}	0.00	2.419×10^{5}	[420]
A221	$C_2H_4O \rightleftharpoons CH_3CHO$	5.840×10^{11}	0.00	2.191×10^{5}	[420]
A222	$C_2H_4O + H \rightleftharpoons CHCH_2O + H_2$	7.900×10^{10}	0.00	4.100×10^{4}	[420]
A223	$C_2H_4O + OH \rightleftharpoons CHCH_2O + H_2O$	1.780×10^{10}	0.00	1.510×10^{4}	[420]
A224	$C_2H_4O + HO_2 \rightleftharpoons CHCH_2O + H_2O_2$	1.120×10^{10}	0.00	1.273×10^{5}	[420]
A225	$C_2H_5O \rightleftharpoons CH_2O + CH_3$	1.000×10^{15}	0.00	9.040×10^{4}	[420]
A226	$C_2H_5O \rightleftharpoons CH_3CHO + H$	2.510×10^{14}	0.00	9.790×10^{4}	[420]
A227	$C_2H_5O + O_2 \rightleftharpoons CH_3CHO + HO_2$	6.030×10^{7}	0.00	6.900×10^{3}	[420]
A228	$C_2H_5OO \rightleftharpoons C_2H_4OOH$	4.554×10^{51}	-13.3	1.845×10^{5}	[424]
A229	$C_2H_5OO + HO_2 \rightleftharpoons C_2H_5OOH + O_2$	1.630×10^{8}	0.00	-8.314×10^{3}	[420]
A230	$C_2H_5OO + CH_2O \rightleftharpoons C_2H_5OOH + CHO$	2.000×10^{9}	0.00	4.880×10^{4}	[420]
A231	$C_2H_5OO + CH_4 \rightleftharpoons C_2H_5OOH + CH_3$	1.120×10^{10}	0.00	1.032×10^{5}	[420]
A232	$C_2H_5OO + C_2H_4 \rightleftharpoons C_2H_4O + C_2H_5O$	2.820×10^{9}	0.00	7.160×10^{4}	[420]
A233	$C_2H_5OO + C_2H_4 \rightleftharpoons C_2H_5OOH + C_2H_3$	1.120×10^{10}	0.00	1.273×10^{5}	[420]
A234	$C_2H_5OO + C_2H_6 \rightleftharpoons C_2H_5OOH + C_2H_5$	1.700×10^{10}	0.00	8.560×10^{4}	[420]
A235	$C_2H_4OOH \rightleftharpoons C_2H_4O + OH$	1.490×10^{41}	-9.51	9.447×10^{4}	[424]
A236	$C_2H_4OOH \rightleftharpoons C_2H_4 + HO_2$	6.580×10^{41}	-9.70	9.628×10^{4}	[424]
A237	$C_2H_4OOH \rightleftharpoons C_2H_4 + HO_2$	5.650×10^{41}	-10.9	1.108×10^{5}	[424]
A238	$C_2H_5OOH \rightleftharpoons C_2H_5O + OH$	4.000×10^{15}	0.00	1.796×10^{5}	[420]
A239	$C_2H_5OOH + CH_2OH \rightleftharpoons C_2H_5OO + CH_3OH$	3.011×10^{15}	0.00	1.080×10^{4}	[420]
A240	$C_2H_4O + CH_3OO \rightleftharpoons CHCH_2O + CH_3OOH$	1.120×10^{10}	0.00	1.273×10^{5}	[420]
A241	$C_2H_5OO + C_2H_4O \rightleftharpoons CHCH_2O + C_2H_5OOH$	1.120×10^{10}	0.00	1.273×10^{5}	[420]
A242	$C_2H_4O + CH_3 \rightleftharpoons CHCH_2O + CH_4$	1.070×10^{9}	0.00	4.950×10^{4}	[420]

Table A.2 (Continued)

No.	Reaction	A	n	E_a	Ref.
A243	$C_2H_4O + CH_3O \rightleftharpoons CHCH_2O + CH_3OH$	1.200×10^{8}	0.00	2.830×10^{4}	[420]
A244	$C_2H_2 + M \rightleftharpoons H_2C_2 + M$	2.500×10^{12}	-0.64	2.080×10^{5}	[425]
	H_2O = 6.50; Ar = 0.40;				
A245	$H_2C_2 + O_2 \rightleftharpoons CH_2(T) + CO_2$	5.000×10^{10}	0.00	0	[425]
A246	$H_2C_2 + O \rightleftharpoons CH_2(T) + CO$	3.000×10^{10}	0.00	0	[425]
A247	$H_2C_2 + OH \rightleftharpoons CH_2(T) + CHO$	2.000×10^{10}	0.00	0	[425]
A248	$CH_3CO + CH_3 \rightleftharpoons C_2H_6 + CO$	5.000×10^{10}	0.00	0	[414]
A249	$C_2H_4 + HO_2 \rightleftharpoons C_2H_4O + OH$	2.230×10^{9}	0.00	7.190×10^{4}	[165]
A250	$C_2H_6 + CH_3 \rightleftharpoons C_2H_5 + CH_4$	1.500×10^{-10}	6.00	2.527×10^{4}	[165]
A251	$C_2H_5 + O_2 \rightleftharpoons CH_3CHO + OH$	1.946×10^{9}	-0.48	3.247×10^{4}	[424]
A252	$CHCH_2O \rightleftharpoons CH_3CO$	8.500×10^{14}	0.00	5.860×10^{4}	[420]
A253	$CHCH_2O \rightleftharpoons CH_2CHO$	1.000×10^{14}	0.00	5.860×10^{4}	[420]
A254	$C_2H_5 + H \rightleftharpoons C_2H_4 + H_2$	4.500×10^{10}	0.00	0	[177]
A255	$C_2H_5 + O \rightleftharpoons C_2H_4 + OH$	3.060×10^{10}	0.00	0	[177]
A256	$C_2H_4 + C_2H_4 \rightleftharpoons C_2H_3 + C_2H_5$	5.010×10^{11}	0.00	2.710×10^{5}	[426]
A257	$C_2H_4O + HO_2 \rightleftharpoons CH_3 + CO + H_2O_2$	4.000×10^{9}	0.00	7.120×10^{4}	[165]
A258	$C_2H_5 + O_2 \rightleftharpoons C_2H_4 + HO_2$	1.020×10^{17}	-2.97	3.613×10^{4}	[424]
A259	$C_2H_5 + O_2 \rightleftharpoons C_2H_5OO$	9.420×10^{33}	-8.01	2.550×10^{4}	[424]
A260	$C_2H_5OO \rightleftharpoons C_2H_4 + HO_2$	6.463×10^{30}	-6.06	1.470×10^{5}	[424]
A261	$C_2H_5OO \rightleftharpoons C_2H_4 + HO_2$	4.470×10^{42}	-10.1	1.871×10^{5}	[424]
A262	$C_2H_5 + O_2 \rightleftharpoons C_2H_4OOH$	8.840×10^{34}	-9.33	4.248×10^{4}	[424]
A263	$C_2H_4OOH \rightleftharpoons CH_3CHO + OH$	3.100×10^{37}	-10.1	1.196×10^{5}	[424]
A264	$C_2H_5 + O_2 \rightleftharpoons C_2H_4O + OH$	1.939×10^{17}	-3.08	3.613×10^{4}	[424]
A265	$C_2H_5OO \rightleftharpoons C_2H_4O + OH$	3.015×10^{42}	-10.0	1.887×10^{5}	[424]
A266	$C_2H_5OO \rightleftharpoons CH_3CHO + OH$	2.134×10^{41}	-9.81	1.920×10^{5}	[424]
A267	$C_2H_2 + CH_3 \rightleftharpoons C_2H + CH_4$	1.810×10^{8}	0.00	7.234×10^{4}	[158]
A268	$C_2H_5OH \rightleftharpoons CH_2OH + CH_3$	5.000×10^{15}	0.00	3.428×10^{5}	[427]
	k_0	3.000×10^{13}	0.00	2.424×10^{5}	
	F_c = 0.500				
	H_2 = 2.00; H_2O = 6.00; CO = 1.50; CO_2 = 2.00; CH_4 = 2.00; Ar = 0.70;				
A269	$C_2H_5OH \rightleftharpoons C_2H_5 + OH$	2.400×10^{23}	-1.62	4.165×10^{5}	[428]
	k_0	5.110×10^{82}	-18.80	4.969×10^{5}	
	Troe form: α = 0.500; T^{*} = 650.0; T^{***} = 800.0				
	H_2 = 2.00; H_2O = 5.00; CO = 2.00; CO_2 = 3.00;				
A270	$C_2H_5OH \rightleftharpoons C_2H_4 + H_2O$	8.000×10^{13}	0.00	2.717×10^{5}	[427]
	k_0	1.000×10^{14}	0.00	2.257×10^{5}	
	F_c = 0.500				
	H_2 = 2.00; H_2O = 6.00; CO = 1.50; CO_2 = 2.00; CH_4 = 2.00; Ar = 0.70;				
A271	$C_2H_5OH \rightleftharpoons CH_3CHO + H_2$	7.240×10^{11}	0.10	3.808×10^{5}	[428]

Table A.2 (Continued)

No.	Reaction	A	n	E_a	Ref.
	k_0	4.460×10^{84}	-19.42	4.836×10^{5}	
	Troe form: α = 0.900; T^* = 900.0; T^{***} = 1100.0; T^{**} = 3500.0;				
	H_2 = 2.00; H_2O = 5.00; CO = 2.00; CO_2 = 3.00;				
A272	$C_2H_5OH + O_2 \rightleftharpoons C_2H_4OH + HO_2$	2.000×10^{10}	0.00	2.209×10^{5}	[428]
A273	$C_2H_5OH + O_2 \rightleftharpoons CH_3CHOH + HO_2$	1.500×10^{10}	0.00	2.098×10^{5}	[428]
A274	$C_2H_5OH + OH \rightleftharpoons C_2H_4OH + H_2O$	1.740×10^{8}	0.27	2.511×10^{3}	[428]
A275	$C_2H_5OH + OH \rightleftharpoons CH_3CHOH + H_2O$	4.640×10^{8}	0.15	0	[428]
A276	$C_2H_5OH + H \rightleftharpoons C_2H_4OH + H_2$	1.230×10^{4}	1.80	2.133×10^{4}	[428]
A277	$C_2H_5OH + H \rightleftharpoons CH_3CHOH + H_2$	2.580×10^{4}	1.65	1.183×10^{4}	[428]
A278	$C_2H_5OH + HO_2 \rightleftharpoons C_2H_4OH + H_2O_2$	1.230×10^{1}	2.55	6.590×10^{4}	[428]
A279	$C_2H_5OH + HO_2 \rightleftharpoons CH_3CHOH + H_2O_2$	8.200	2.55	4.498×10^{4}	[428]
A280	$C_2H_5OH + HO_2 \rightleftharpoons C_2H_5O + H_2O_2$	2.500×10^{9}	0.00	1.004×10^{5}	[428]
A281	$C_2H_5OH + O \rightleftharpoons C_2H_4OH + OH$	9.410×10^{4}	1.70	2.284×10^{4}	[428]
A282	$C_2H_5OH + O \rightleftharpoons CH_3CHOH + OH$	1.880×10^{4}	1.85	7.632×10^{3}	[428]
A283	$C_2H_5OH + CH_3 \rightleftharpoons C_2H_4OH + CH_4$	1.330×10^{-1}	3.18	3.917×10^{4}	[428]
A284	$C_2H_5OH + CH_3 \rightleftharpoons CH_3CHOH + CH_4$	4.440×10^{-1}	2.90	3.218×10^{4}	[428]
A285	$C_2H_5OH + C_2H_5 \rightleftharpoons C_2H_4OH + C_2H_6$	5.000×10^{7}	0.00	5.607×10^{4}	[428]
A286	$C_2H_5OH + C_2H_5 \rightleftharpoons CH_3CHOH + C_2H_6$	5.000×10^{7}	0.00	4.352×10^{4}	[428]
A287	$C_2H_4OH \rightleftharpoons C_2H_4 + OH$	1.293×10^{12}	-0.37	1.123×10^{5}	[428]
A288	$CH_3CHOH + M \rightleftharpoons CH_3CHO + H + M$	1.000×10^{11}	0.00	1.046×10^{5}	[428]
A289	$C_2H_5OH + OH \rightleftharpoons C_2H_5O + H_2O$	7.460×10^{8}	0.30	6.837×10^{3}	[428]
A290	$C_2H_5OH + H \rightleftharpoons C_2H_5O + H_2$	1.500×10^{4}	1.60	1.271×10^{4}	[428]
A291	$C_2H_5OH + O \rightleftharpoons C_2H_5O + OH$	1.580×10^{4}	2.00	1.861×10^{4}	[428]
A292	$C_2H_5OH + CH_3 \rightleftharpoons C_2H_5O + CH_4$	1.340×10^{-1}	2.92	3.118×10^{4}	[428]
A293	$CH_3CHOH + O_2 \rightleftharpoons CH_3CHO + HO_2$	3.810×10^{3}	2.00	6.866×10^{3}	[428]
A294	$C_2H_5 + HO_2 \rightleftharpoons C_2H_5O + OH$	3.200×10^{10}	0.00	0	[428]
A295	$CH_3OO + C_2H_5 \rightleftharpoons CH_3O + C_2H_5O$	7.000×10^{9}	0.00	-4.184×10^{3}	[428]
A296	$CH_3OCH_3 \rightleftharpoons CH_3 + CH_3O$	4.860×10^{55}	-11.5	4.272×10^{5}	[428]
A297	$CH_3OCH_3 + OH \rightleftharpoons CH_3OCH_2 + H_2O$	9.350×10^{2}	2.29	-3.264×10^{3}	[428]
A298	$CH_3OCH_3 + H \rightleftharpoons CH_3OCH_2 + H_2$	7.720×10^{3}	2.09	1.416×10^{4}	[428]
A299	$CH_3OCH_3 + O \rightleftharpoons CH_3OCH_2 + OH$	1.860×10^{-6}	5.29	-4.560×10^{2}	[428]

Table A.2 (Continued)

No.	Reaction	A	n	E_a	Ref.
A300	$CH_3OCH_3 + HO_2 \rightleftharpoons CH_3OCH_2 + H_2O_2$	1.680×10^{10}	0.00	7.402×10^{4}	[428]
A301	$CH_3OCH_3 + CH_3 \rightleftharpoons CH_3OCH_2 + CH_4$	1.450×10^{-9}	5.73	2.385×10^{4}	[428]
A302	$CH_3OCH_3 + O_2 \rightleftharpoons CH_3OCH_2 + HO_2$	4.100×10^{10}	0.00	1.879×10^{5}	[428]
A303	$CH_3OCH_3 + CH_3O \rightleftharpoons CH_3OCH_2 + CH_3OH$	6.020×10^{8}	0.00	1.705×10^{4}	[428]
A304	$CH_3OCH_2 \rightleftharpoons CH_2O + CH_3$	1.600×10^{13}	0.00	1.067×10^{5}	[428]
A305	$CH_3OCH_2 + CH_3O \rightleftharpoons CH_3OCH_3 + CH_2O$	2.410×10^{10}	0.00	0	[428]
A306	$CH_3OCH_2 + CH_2O \rightleftharpoons CH_3OCH_3 + CHO$	5.490	2.80	2.453×10^{4}	[428]
A307	$CH_3OCH_2 + CH_3CHO \rightleftharpoons CH_3OCH_3 + CH_3CO$	1.260×10^{9}	0.00	3.556×10^{4}	[428]
A308	$C_2H_3OH + H \rightleftharpoons CH_2CHO + H_2$	9.810×10^{-1}	3.37	1.480×10^{4}	[429]
A309	$C_2H_3OH + OH \rightleftharpoons CH_2CHO + H_2O$	3.330×10^{6}	1.10	2.261×10^{3}	[429]
A310	$C_2H_3OH + O \rightleftharpoons CH_2CHO + OH$	1.875×10^{3}	1.90	-3.598×10^{3}	[429]
A311	$C_2H_3OH + CH_3 \rightleftharpoons CH_2CHO + CH_4$	2.030×10^{-11}	5.90	4.402×10^{3}	[429]
A312	$C_2H_3OH + O_2 \rightleftharpoons CH_2CHO + HO_2$	5.310×10^{8}	0.21	1.666×10^{5}	[429]
A313	$C_2H_3OH + HO_2 \rightleftharpoons CH_2CHO + H_2O_2$	3.400	2.50	3.733×10^{4}	[429]
A314	$CH_2CHO \rightleftharpoons CH_3 + CO$	1.000×10^{13}	0.00	1.840×10^{5}	[202]
A315	$HO_2 + C_2H_4 \rightarrow CH_3 + CHO + OH$	0.603×10^{7}	0.00	3.326×10^{4}	[202]